Model-Driven Reconstruction in Atom Probe Tomography



Charles Fletcher

Oriel College

University of Oxford

Thesis submitted for the degree of

Doctor of Philosophy

Trinity Term 2021

Supervisors: Dr Daniel Haley and Professor Michael Moody

Abstract

This thesis presents a new continuum model for predicting results from atom probe tomography (APT) experiments. Unlike previous atomic-scale approaches, this continuum approach makes realistic specimen simulation computationally tractable, enabling direct quantitative comparison with experiment. Here, specimen evaporation resembles a moving boundary problem, where the electrostatic field at the surface and in the surrounding vacuum must be solved throughout time. Tracking the surface implicitly as a contour in a scalar field ensures numerical stability of surface faceting and evaporation of voids (cavities). The electric field is efficiently solved by a boundary integral equation. Proof-of-concept submodels for laser-assisted evaporation, crystallographic faceting, and material dielectricity are also considered. Predictions are shown to agree well with experiment.

The application of the model to directly performing data reconstruction is also considered. A protocol is proposed where the specimen model for an APT analysis is calibrated against experimental data by solving a generalised image registration problem. Here, model parameters are constrained by maximising the similarity between the model and experimental data, measured using mutual information (MI). Through this proposed method, large-scale trajectory distortions are shown to be corrected for two experimental semiconductor devices: a multilayer structure and a fin field-effect transistor (FinFET) structure.

Preface

This thesis comprises of the author's own work in the Department of Materials, University of Oxford, under the supervision of Dr Daniel Haley and Professor Michael Moody. No part of this work has previously been submitted for a degree.

Funding and Acknowledgements

My studentship was financially sponsored by CAMECA. Support was also received via postgraduate scholarships from Oriel College, Oxford.

Firstly, I would like to thank Dr Daniel Haley and Professor Michael Moody as, without their support and guidance, this work would have surely been impossible.

Secondly, I would like to express my gratitude to Claudia Fleischmann and Jeroen Shreeder from IMEC/KU Leuven, and Thomas Slater from Diamond Light Source, for providing data that proved essential to completing this work. I also would like to thank Ian Griffiths at the Oxford Centre for Industrial Mathematics for assisting with the time-dependent trajectory mapping continuity proof.

Thirdly, I wish to thank Brian Geiser and David Larson at CAMECA, and Thomas Kelly at Steam Instruments for their support and insight.

Finally, I thank all my amazing family (including Flora the dog), friends, colleagues, and girlfriend for their unwavering support and encouragement. I dedicate this work to my incredible grandfather John Anstice Brown.

Source Code

A large part of the work unseen in this thesis is the following open-source code:

- 2D simulator (CASRA): `https://gitlab.com/fletchie/casra`
- 3D simulator (CASRA 3D): `https://gitlab.com/fletchie/casra-3d`

Contents

1 Introduction **8**

2 Background to Atom Probe Tomography **11**

2.1 Theory of Field Evaporation 11

2.2 The Modern APT Instrument 15

2.3 APT Mass Spectra 17

2.4 Image Formation and Reconstruction 19

2.4.1 Imaging Distortions 19

2.4.2 The Point-Projection Reconstruction 20

2.4.3 Parameter Tuning 26

2.4.4 Dynamic Reconstruction 26

2.4.5 Density Relaxation 27

2.4.6 Projection Model Summary 27

2.5 Historical Simulation and Reconstruction Efforts 28

2.5.1 Early Analytic Models 28

2.5.2 Atomic-Scale Simulation 28

2.5.3 Analytical Models 30

2.5.4 Continuum Models 31

2.5.5 Reverse Projection Protocols 32

2.5.6 Summary 33

2.6 Independent Measuring of Specimen Shapes 34

2.6.1 Electron Tomography 34

2.6.2 Correlative Reconstruction 35

2.6.3 Electron Tomography Surface Thresholding 36

2.6.4 Atomic Force Microscopy 37

3 Methodology **38**

3.1 Predicting Field Evaporation in APT 38

3.2 Specimen Surface Tracking 41
3.3 The Level Set Method 43
3.3.1 The Level Set Framework 43
3.3.2 Field Reinitialisation 48
3.4 Mesh processing 51
3.4.1 Contour Extraction 51
3.4.2 Adaptive Isotropic Remeshing 51
3.4.3 Shank Extension 54
3.5 Electrostatics 57
3.5.1 The Curvature Flow Approximation 57
3.5.2 The Boundary Element Method 61
3.5.3 Solving the Boundary Matrix Equation 69
3.5.4 Conductor Model 71
3.5.5 Incorporating Dielectric Phases 72
3.5.6 Solving the FEM-BEM Coupled System 74
3.5.7 Calculating Ion Trajectories 74
3.5.8 Acceleration via Panel Clustering 76
3.6 Model Testing 82
3.6.1 Electrostatic Tests 82
3.6.2 Surface Collapse Tests 86
3.7 Evaporation Model Extensions 89
3.7.1 Specimen Faceting 89
3.7.2 Laser-Matter Interaction 92
3.8 The Trajectory Mapping 98
3.8.1 The Spatial Continuity of Ion Trajectories 98
3.8.2 Temporal Continuity 101
3.8.3 Local Stability Behaviour 102
3.8.4 Constructing the Inverse Trajectory Mapping 108

3.9 Data Simulation and Processing 112
3.9.1 Local Evaporation Rate 112
3.9.2 Realistic Launching of Ions 114
3.9.3 Calculating Density and Trajectory Overlap Detector Maps 116
3.9.4 Calculating Composition Detector Maps 120
3.9.5 Model Depth Calibration 120
3.9.6 Local Density and Composition Estimation for Point Clouds 122
3.10 Specimen-Independent Trajectory Compression 123
3.10.1 Additional Instrument Components 123
3.10.2 An Instrument Transfer Function 125
3.10.3 Deriving a Model Cutoff 127
3.10.4 Specimen Voltage Correction 129
3.11 A Model-Driven Reconstruction 130
3.11.1 The Reconstruction Protocol 130
3.11.2 Landmark Depth Calibration 132
3.11.3 Model Parameter Tuning 135
3.11.4 Specimen Alignment and Image Compression 136
3.11.5 Physical Parameters 137
3.11.6 Parameter Optimisation 137
3.11.7 Data Preprocessing 138
3.11.8 Measuring Similarity: Mutual Information 139
3.11.9 Test Alignment 143
3.11.10 Generalised Alignment Transformations 145
3.12 Methodology Conclusions 149

4 Two Dimensional Model **150**

4.1 Summary of the 2D Model 150
4.2 Initialisation 150
4.3 Implementation 152

4.4 Multilayer Structures 154
4.5 High and Low Field Precipitates 158
4.6 The Fin Field-Effect Transistor 160
4.7 Dielectric Microstructures 163
4.8 Crystallographic Simulation 166
4.9 Incorporating Voids 170
4.10 Conclusions 172

5 Three Dimensional Model 174

5.1 Initialisation 174
5.2 Implementation 175
5.3 Multiphase Evaporation 177
5.4 Laser-Assisted Evaporation 181
5.5 Three Dimensional Crystallography 184
5.6 Void Structures 188
5.7 Electron Tomography Initialisation 191
5.8 Towards Data-Driven Evaporation 194
5.9 Conclusions 196

6 Exploring Model-Driven Reconstruction 199

6.1 Setup and Workflow 199
6.2 Reconstruction of a Synthetic Dataset 201
6.3 The Multilayer Reconstruction 205
6.4 The FinFET Reconstruction 211
6.5 Discussion and Conclusions 221

7 General Conclusions and Future Work 222

8 Appendix A: Variation in Evaporation Parameters 253

9 Appendix B: The Exterior BEM Problem 256

10 Appendix C: 3D BEM Analytic Integrals **257**

11 Appendix D: 3D BEM Numerical Integrals **258**

12 Appendix E: The FEM-BEM Coupling **259**

13 Appendix F: The Multipole Expansion **264**

14 Appendix G: BEM System for Mixed Boundary Conditions **266**

15 Appendix H: Continuity of Laplace's Equation under Boundary Perturbations **267**

1 Introduction

Since 1975, the density of devices within integrated circuits (ICs) has approximately doubled every one to two years - an empirical observation coined Moore's law [1]. However, over the last few years this previously steady increase in device density has declined due to limits imposed on device operation and manufacturing by decreasing device scales [2]. In order to try and maintain Moore's law, the semiconductor industry is resorting to designs of increasing structural complexity [3].

Silicon fabrication follows the planar process [4]. Here, individual transistors are etched out on doped silicon wafer. Initially, a photoresist coating is applied such that, on exposure to ultraviolet light, particular wafer regions can be shielded from etching. Ion implantation is used to create p-wells and n-wells forming the source and drain, while a thin SiO_2 layer separating the gate and bulk is applied through thermal oxidation.

Traditional analysis techniques used for performing failure analysis - the process of identifying the mechanisms behind an IC malfunction - are becoming limited by increasingly sophisticated device architectures. A typical failure analysis workflow involves localising the failure site, followed by a physical analysis of the failure region [5]. The localising step uses techniques such as X-Ray, scanning acoustic microscopy and charged-coupled device detection of photoemission caused by recombination from current leaks. If the fault region cannot be identified through observation, then circuit components must be probed to locate faults by anomalous results. A number of unit tests are performed and their output compared to results for a portfolio of simulated fault models [6] - each containing the predicted output under failure at different sites. A match between the unit test outputs and a fault model successfully identifies the failure site.

Once the failure site has been localised, physical analysis of the region can be performed to determine a cause for failure. Currently, a typical analysis

process [5] could involve sample preparation, either in planar through IC layer removal by etching or polishing, or in cross-section through focused ion beam (FIB). This would be followed by scanning or transmission electron microscopy (SEM/TEM) to obtain higher-level structural information, and finally secondary-ion mass spectrometry (SIMS) to perform depth profiling of low concentration dopants. With the shrinking sizes of IC components such techniques provide only limited information regarding sample morphology and spatial chemistry, and as a result the cause of failure cannot always be identified. Examples are insufficient SiO_2 fin thickness or conductive defects building up during the etching stage of the manufacturing process, triggering dielectric breakdown through electrostatic discharge [5, 7]. Crystallographic defects and dopant distribution fluctuations in the bulk can also result in out of specification properties and unanticipated behaviour.

Traditionally IC transistor designs have followed the MOSFET structure (see Figure 1a). However, recent developments have shifted towards the fin field-effect transistor (FinFET) design where the source and drain rise out of the wafer in finlike structures (see Figure 1b). While such a design improves energy efficiency and gate switching speeds, the floating fins result in increased vulnerability to dielectric breakdown across the gate [8]. Decreased dopant levels present within FinFETs also result in dopant fluctuations increasingly limiting device minimisation [9, 10]. Given these developments, there is increasing demand for new analysis tools of higher chemical and spatial resolution.

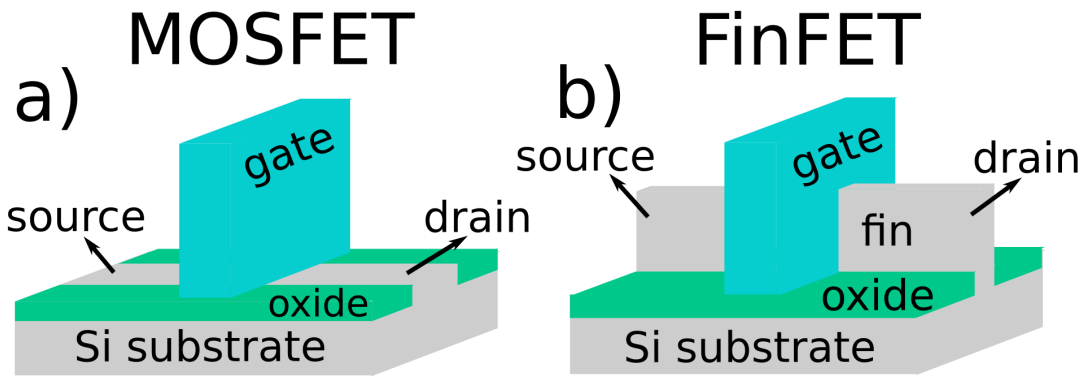


Figure 1: (a) Diagram showing MOSFET transistor structure. (b) The FinFET transistor structure. Note its more complex 3D raised fin structure.

Atom probe tomography (APT) is a materials characterisation technique capable of measuring the three dimensional (3D) positions and ion chemistry at a near atomic scale. This high chemical and spatial resolution makes APT the perfect candidate for analysing next-generation semiconductor devices [11]. However, several unsolved technical challenges are limiting its wider uptake within industry. One major problem is the presence of spatial distortions in APT images of multiphase material systems, such as semiconductor devices. These distortions directly impact the atomic density and microstructural shapes reported. Even more challenging are local composition artefacts that arise near interfaces due to the crossover or overlap of ion trajectories. In order to enable the wider uptake of APT in both industry and academia, there is strong demand for new reconstruction algorithms capable of reducing or eliminating these distortions. The development of such a reconstruction algorithm will be the focus of this thesis.

2 Background to Atom Probe Tomography

2.1 Theory of Field Evaporation

The fundamental physical mechanism behind Atom Probe Tomography (APT) is field evaporation. Here, application of an electric field to the specimen surface removes and ionises surface exposed atoms. In APT this surface field is pulsed, with the magnitude of the pulse finely controlled to ensure a fixed evaporation rate per pulse. This evaporation rate is typically kept relatively low (below 1%) to avoid an increased probability of multiple ions evaporating during the same pulse.

Without the application of an external field, atoms remain bonded together within a material lattice. Unless sufficient energy is put into the system, these bonds cannot be broken. This is exactly what is observed at the macroscale when a solid is heated to the point of melting or sublimation. The energy required to break these bonds is phase dependent, and defined to be the material's sublimation energy (Λ). Additionally, during the field evaporation process, removed atoms are also ionised. This ionisation requires an energy I_n, where n corresponds to the degree of ionisation. During surface atom ionisation, there is also the addition of n free electrons to the solid, which contributes an energy change given by the material-dependent work function (Θ). Therefore, surface atom evaporation can occur if it gains sufficient energy to overcome the combined energy contribution from these three terms, given by a total energy barrier Q_0.

$$Q_0 = \Lambda + I_n - n\Theta \tag{1}$$

During field evaporation, this energy barrier is modified due to the presence of an applied electric field. A simple model by Müller attempts to predict this

contribution by considering the electric potential energy of the newly produced ion (see Figure 2). The ion is considered positioned at a normal distance a from the emitter surface. In Müller's image hump model, the local specimen surface is considered as an infinite plane, whilst liberated electrons are left behind on this surface. The field-modified energy barrier is given by Eq. (2). The maximum height of this barrier $Q_E(a_{max})$ is then given by Eq. (4), occurring at a distance a_{max} above the surface.

$$Q_E(a) = Q_0 - ne||E(a))||a - \frac{n^2e^2}{16\pi\epsilon_0 a} \tag{2}$$

$$a_{max} = \sqrt{\frac{ne}{16\pi\epsilon_0}\frac{1}{||E(a)||}} \tag{3}$$

$$Q_E(a_{max}) = Q_0 - \sqrt{\frac{n^3e^3}{4\pi\epsilon_0}||E(a)||} \tag{4}$$

Here e is the electron charge and ϵ_0 is the vacuum permittivity. Finally, a critical material-dependent evaporation field (F_e) can be defined at which the energy barrier maximum becomes zero (Eq. (5)).

$$F_e = \frac{4\pi\epsilon_0}{n^3e^3}Q_0^2 \tag{5}$$

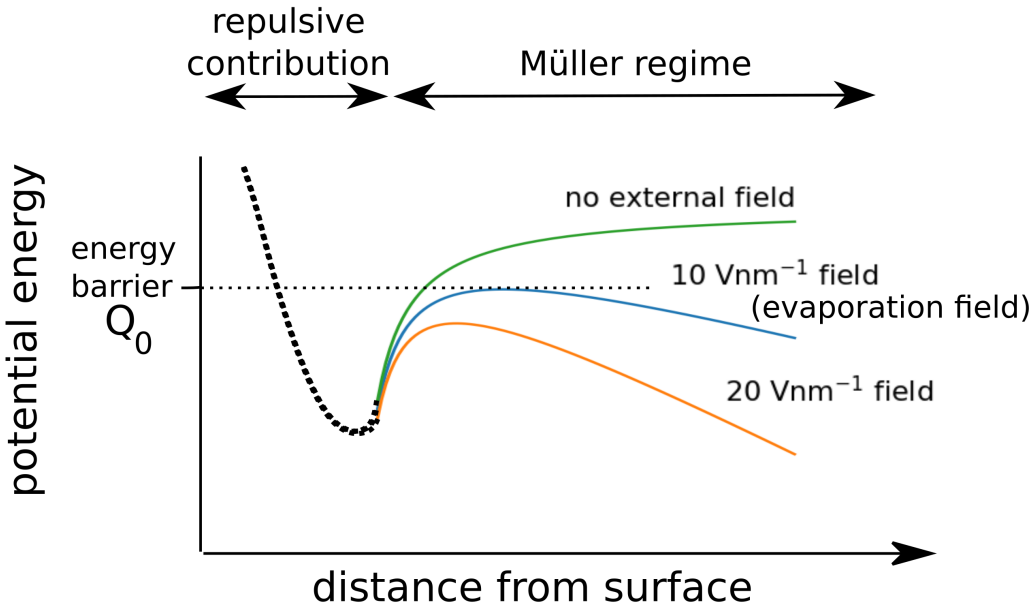


Figure 2: Post-ionisation energy curve under Müller's model (immediate ionisation at surface). The curve region, marked Müller regime, indicates approximately where Eq. (2) is valid, whilst the repulsive region contains repulsive forces unaccounted for by Müller's model. In this example, field evaporation is shown to occur at the critical field of 10 Vnm^{-1}.

Ironically, while Müller's model is a good predictor of metal evaporation fields, the current consensus is that its assumption that ionisation occurs well before crossing the energy barrier is unphysical, with predictions mostly agreeing chance. In reality, the true mechanism behind field evaporation requires a quantum mechanical interpretation, with the electron charge slowly being drained throughout the evaporation process [12]. However, Müller's model serves as a simplified classical model for understanding the process.

At temperatures above 40 K, the physical mechanism behind field evaporation is known to be largely thermally driven due to experimental evaporation rates obeying Arrhenius plots in this region [13]. Below 40 K, Arrhenius plot linearity breaks down, implying that the primary mechanism behind evaporation is no longer thermal. This is typically assumed to be due to quantum tunnelling effects becoming dominant. In the thermal regime, the average time until evaporation for a surface atom (τ) can be described through the Arrhenius law in Eq. (6).

$$\tau = \tau_0 \; e^{\frac{Q_E}{kT}} \tag{6}$$

Here $\tau_0 = 1/\nu_0$, where ν_0 is the vibrational frequency of the atom within the lattice, and can be effectively interpreted as the time between the surface atom trialling its evaporation barrier Q_E. Assuming a surface region with atoms of constant vibrational frequency, the local evaporation rate at surface position $\mathbf{s}$ is approximated by Eq. (7).

$$R_e = A \; e^{\frac{-\bar{Q}_E(\mathbf{s})}{kT(\mathbf{s})}} \tag{7}$$

Here A is some global prefactor related to surface density, and $\bar{Q}_E \sim Q_E$ is some surface-averaged energy barrier as observed in experiment. The Eq. (7) has been empirically validated in numerous studies [14, 13, 15]. This macroscale law for local evaporation rate raises the possibility of building continuum models capable of predicting specimen shape changes under evaporation. Later, by introducing ion optics into such a model, spatial distortions as observed in APT experiments will be modelled and corrected for.

2.2 The Modern APT Instrument

The original atom probe was a modification of the earlier field ion microscope (FIM). A small pinhole in the FIM fluorescent screen detector allowed for field evaporated surface ions to enter a mass spectrometer. This early FIM-atom probe enabled individual surface atoms to be observed via an inert imaging gas, and characterised via the mass spectrometer.

Modern atom probes appeared in the 1980s with the invention of the 3D atom probe (3DAP). These instruments were capable of detecting evaporated atoms directly over some specimen surface patch without any imaging gas. With the introduction of a two-dimensional position-sensitive detector [16] following a mass spectrometer, the initial positions of millions of specimen atoms could be directly estimated by projecting back from their detected coordinates onto a geometric model for the specimen [17]. Through this back-projection of detected ions, a tomographic image of detected ions and their initial positions can be generated in a process called reconstruction. This breakthrough allowed 3D heterogeneities within materials to be investigated at near-atomic resolutions [18].

Experiments throughout the 1970s investigating laser-assisted field evaporation culminated in the invention of the pulsed-laser atom probe (PLAP) [14]. PLAP allowed for analysis of insulators and semiconductors, where previously their low conductivities had prevented field evaporation under only an electrostatic field. However, problems at the time, including the laser's high expense and its alignment, led to the technique being largely forgotten until the 2000s, where it gathered renewed interest due to increasing demands for the analysis of dielectric materials [19]. The vast majority of semiconductor device analyses use laser-assisted field evaporation.

The culmination of these advances was the invention of the local electrode atom probe (LEAP) [20]. Here, a funnel shaped local electrode is placed in front of the sample, and its voltage pulsed to generate a fluctuating electric field on

the specimen surface. This fluctuating surface field allows accurate control over atom evaporation times. Through the local electrode, instrument field-of-view (FOV) could be significantly expanded [21], pulse rates increased one hundred fold [19], and mass resolution significantly increased. However, a side effect of this expanded FOV is the presence of more severe spatial distortions. In order to take full advantage of modern commercial instruments, new imaging algorithms are required that can correct these distortions.

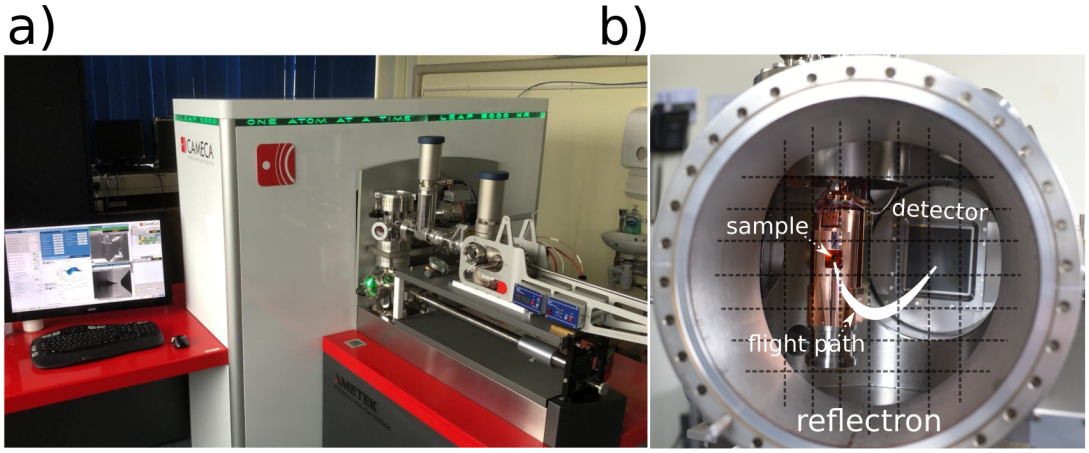


Figure 3: (a) Photo of a modern LEAP 5000 instrument showing the sample loading arm and enclosed analysis chamber. (b) Inside a 3DAP analysis chamber showing sample location, detector, and a typical ion flight path. When operational, The presence of a reflectron mesh (removed here) deflects ion trajectories back onto the detector, increasing mass resolution [22].

2.3 APT Mass Spectra

The raw data produced from a 3D atom probe experiment consists of a detector event sequence, with each sequenced event possessing a time-of-flight (TOF), 2D detected coordinates, and the instrument evaporation pulse voltage. For a specific event's TOF (t_{event}), its mass-to-charge-state ratio (m/c) can be estimated via Eq. (8), which arises from considering energy conservation [23].

$$m/c = 2eV\frac{t_{\text{event}}^2}{L^2} \tag{8}$$

Here V is the total instrument voltage, e is the electron charge, and L is the instrument flight path. The detector event sequence represents the order in which events triggering the detector are registered and recorded. Contained in this sequence are events describing the detection of evaporated ions. However, a fraction of these events will also represent background noise. Current instrument detectors are also not 100% efficient (modern straight flight path instruments have detection efficiencies $\eta \sim 80\%$). As a result, evaporated ions within the instrument FOV can go undetected.

Assuming a detection event is real, its ionic species can be assigned based off its mass-to-charge-state ratio. This is performed through labelling regions of the mass spectrum known as peak ranging. During ranging, detector events are assigned to single fitted mass-spectrum peaks associated with particular ionic species. All detector events within a peak are assigned its associated species. Events outside any ranged peaks are discarded as background noise. Accurate ranging is an essential prerequisite to reconstruction.

Following species ranging, we obtain a filtered sequence of detector events, each with an associated 2D detector position and species type. This ranged data is now ready for spatial reconstruction.

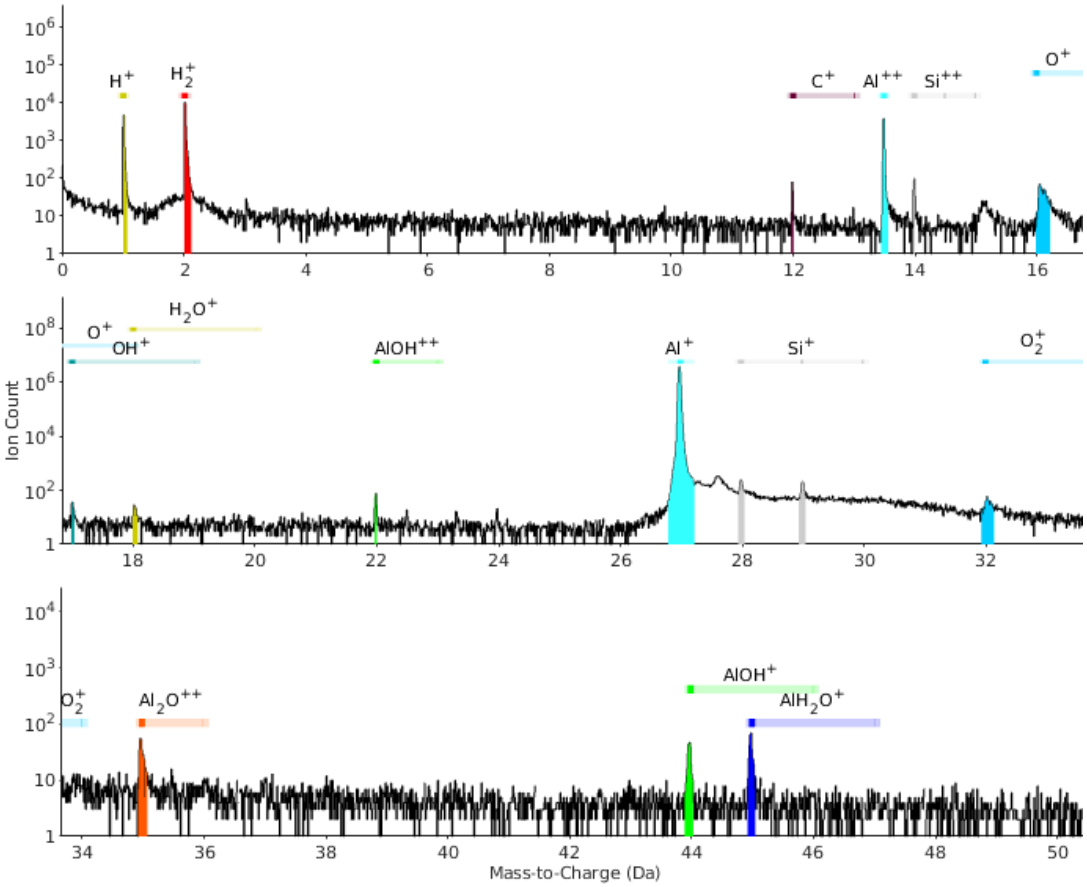


Figure 4: An example mass spectrum for an electropolished aluminium wire, analysed on a LEAP 3000 instrument. The ranged peaks have been coloured, with their associated species labelled above. Note here that certain peaks, e.g. H^+ and H_2^+, are known chamber contaminants and should be ignored from any analysis. (data courtesy of Martin Meier, Department of Materials, University of Oxford)

2.4 Image Formation and Reconstruction

2.4.1 Imaging Distortions

In an ideal case, the specimen apex would remain near hemispherical throughout evaporation. This is the expected equilibrium shape by purely considering its evolution as a function of surface electric field. The resulting trajectories of evaporated ions are then well approximated by a mathematical projection. However, in practise this is rarely realised. Instead physical phenomena, working over various length scales, prevent such an equilibrium shape from being reached.

During the evaporation of crystallographic specimens, the emitter evolves towards a steady-state shape resembling the underlying crystallographic structure. Facets form at local surface orientations corresponding to the lattice symmetries. Variation in local curvature, due to increasing distances between terraces at facets, then results in changes in local magnification. This gives rise to low density cylindrical and planar artefacts (pole structure) in the detected data and subsequent reconstruction, with a symmetry dependent on the underlying crystal structure.

The local evaporation barrier on the specimen surface is also known to be material specific. As a result, when held at the same electric field strength, certain phases evaporate preferentially compared to others. These differing evaporation mechanics drive the specimen apex away from being hemispherical. The exact evolution of the specimen surface depends on the internal phase structure. In terms of ion emission, these differences disrupt the ordering of evaporation, and introduce local deflections into ion trajectories.

Finally, the anisotropic incidence of a laser on the specimen apex results in a non-uniform temperature distribution over its surface. This in turn drives the apex away from being hemispherical, due to the evaporation rate's dependence on temperature [24].

2.4.2 The Point-Projection Reconstruction

The concept of atom probe tomographic reconstruction dates back to the invention of position-sensitive detectors [16, 25, 18]. These early protocols considered atomic positions within a cylindrical scaled stack of $X-Y$ detected coordinates, and depths given by detected ion sequence positions [18]. While a reasonable approximation given the initially small instrument FOVs, development of wide-angle FOV instruments [18] demanded more sophisticated protocols to account for specimen surface curvature.

With specimen surface curvature no longer being negligible, simple models for the field emitter assuming a hemispherical apex were proposed [26, 27, 28]. Under these geometric assumptions, a reconstruction method was developed based off a mathematical projection between a hemisphere (emitter apex) and plane (detector) [17]. This point-projection approach proved incredibly successful and has formed the basis of almost every APT reconstruction algorithm since [29, 30, 31].

The assumed point-projection geometry is shown in Figure 5. Instrument-specific parameters include the detector radius (R_{det}) and flight path (L). The emitter-specific parameters depend on the model assumptions, typically falling into two separate modes of operation. The first mode attempts to constrain the emitter geometry based off user input. This requires parameters defining the initial apex radius ($R_{\mathrm{apex}} = R_0$) and shank angle (α). Typically, its assumed that α remains constant throughout the analysis. Defining the hemispherical apex centre (z_{apex}), these parameters can be used to constrain the radius evolution throughout an experiment via Eq. (9).

$$R_{\mathrm{apex}}(z_{\mathrm{apex}}) = R_0 + \frac{\sin(\alpha)}{1-\sin(\alpha)} z_{\mathrm{apex}} \tag{9}$$

The second operational mode attempts to constrain the apex radius throug-

hout reconstruction by considering the experimental voltage data. This is based off the assumption that the instantaneous specimen voltage (V) and apex electric field (E_{apex}) are related by Eq. (10).

$$E_{\text{apex}} = \frac{V}{k_f \ R_{\text{apex}}} \tag{10}$$

Here k_f is an emitter-specific parameter. Throughout experiment, the voltage changes to ensure that a constant evaporation flux is maintained [32]. Therefore, assuming that the surface electric field is close to the material-specific evaporation field (F_0), the apex radius can be constrained via Eq. (11) throughout the reconstruction.

$$R_{\text{apex}} = \frac{V}{k_f F_0} \tag{11}$$

Once the specimen geometry has been constrained, ion optics are modelled through the mathematical projection. The most commonly applied projection is derived from a modified stereographic projection [17]. Here, a projection point is set to some parameterised distance from the hemispherical apex centre ($p = z_{\text{apex}} - (\xi - 1)R_{\text{apex}}(z_{\text{apex}})$), where ξ is a dimensionless specimen-dependent parameter referred to as the image compression factor (ICF). This point-projection defines a unique invertible mapping between the specimen apex and detector plane, given by Eq. (12). Here, $(R_{\text{apex}}, \theta, \psi)$ defines an apex position in local spherical polar coordinates, which is transformed into Cartesian coordinates through Eq. (13). The model geometry and parameters are visualised in Figure 5.

$$\theta' = \arctan\Big(\frac{\sqrt{x_d^2 + y_d^2}}{L}\Big)$$
$$\theta = \theta' + \arcsin\big((\xi - 1)\ \sin(\theta')\big)$$
$$\psi = \arctan\Big(\frac{x_d}{y_d}\Big) \tag{12}$$

$$\begin{pmatrix} x \\ y \\ z \end{pmatrix} = R_{\text{apex}}(z_{\text{apex}}) \begin{pmatrix} \cos(\psi)\ \sin(\theta) \\ \sin(\psi)\ \sin(\theta) \\ \cos(\theta) \end{pmatrix} + \begin{pmatrix} 0 \\ 0 \\ z_{\text{apex}} \end{pmatrix} \tag{13}$$

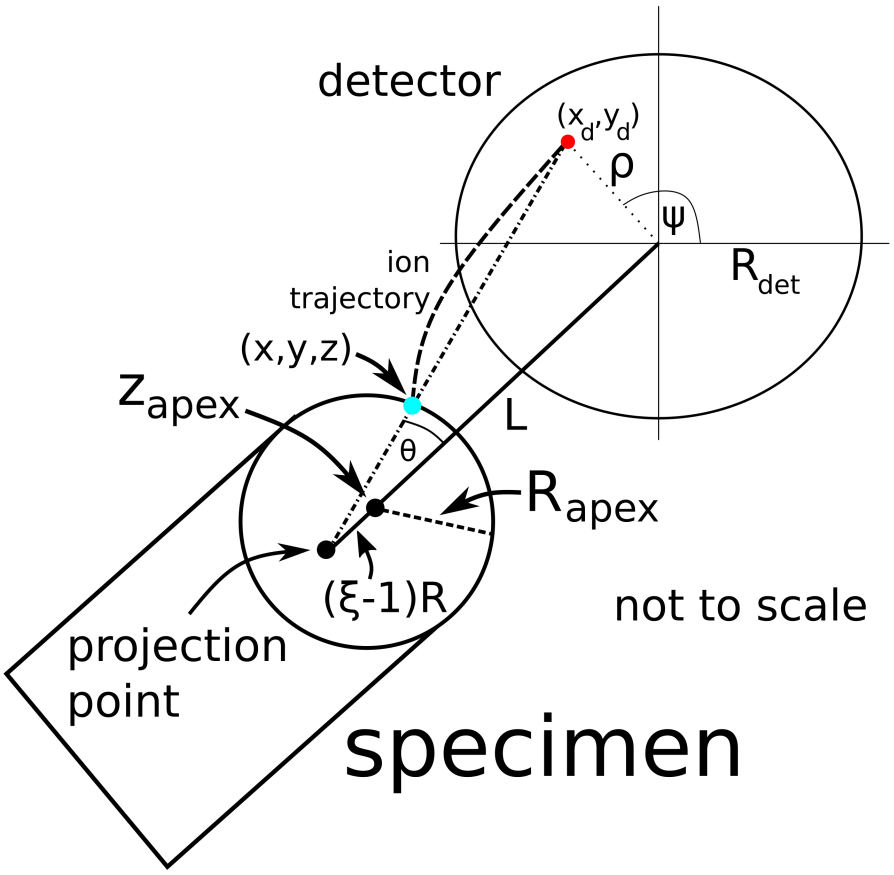


Figure 5: Geometric setup for the Bas point-projection model.

While the Bas model is the most popular mathematical projection model, alternative models also exist (e.g. linear projection models [33, 31]). However, all these mathematical projections largely rely on the same geometric assumptions, and so all breakdown for multiphase systems (Section 2.4.1).

Now that a projection approximating ion optics has been defined, the standard reconstruction protocol can be outlined. Due to APT's destructive nature, this reconstruction process has to be performed iteratively as the state of the specimen geometry must be updated after each ion placement. For the i-th ion to be reconstructed with detected coordinates (x_d, y_d), given the current model specimen state (defined by apex radius (R_i) and centre depth (z_i)), its reconstructed coordinates are estimated via Eqs. (12) and (13). The ion's final position within the reconstruction is then given by (x, y, z).

Following an ion's placement, the model specimen state must then be updated. In order to ensure that the model specimen remains calibrated to experiment, the total evaporated volume in the model is constrained by the total number of detected ions. Following the i-th ion's placement, the model apex is shifted downwards by dz_i (see Figure 6). This shift is calculated using Eqs. (15) and (16), estimating the specimen volume removed under evaporation (approximated as a cylindrical volume).

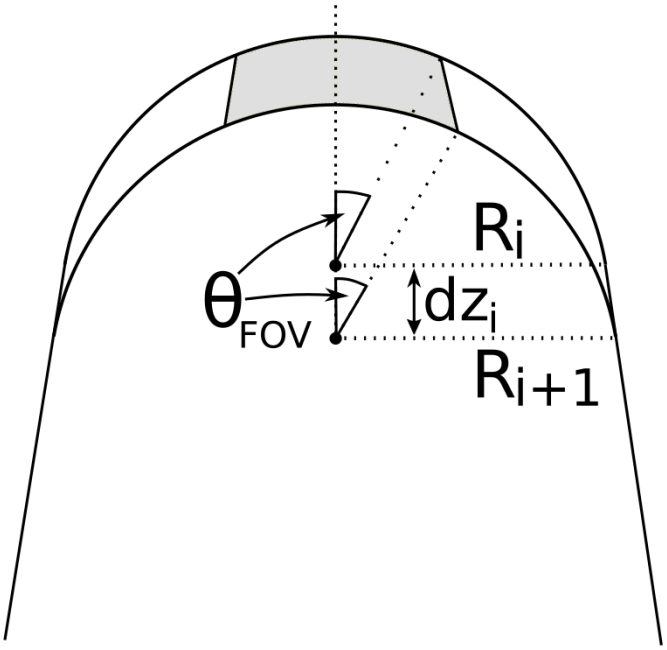


Figure 6: Diagram illustrating the depth incrementation of the hemispherical apex. The shaded region corresponds to the evaporated volume within the FOV (estimated in Eqs. (15) and (16)).

$$\theta_{FOV} = \arctan\left(\frac{R_{det}}{L}\right) + \arcsin\left(\left(\xi - 1\right)\,\sin\left(\arctan(\frac{R_{det}}{L})\right)\right) \tag{14}$$

$$A(z_i) = \pi R^2 \sin^2\left(\theta_{\mathrm{FOV}}\right) \tag{15}$$

$$dz_i = \frac{\Omega_i}{\eta \cdot A(z_i)} \tag{16}$$

Here θ_{FOV} is the angular FOV, η is the detection efficiency, and Ω_i is the ionic volume taken up by the i-th reconstructed ion. A more accurate volume increment formula accounting for the shank angle can be found in [30]. Once this shift is calculated, the specimen state is updated prior to the next ion placement.

$$z_{i+1} = z_i - dz_i - (R_{i+1} - R_i)\,\cos(\theta_{FOV}) \tag{17}$$

The apex radius is updated either via Eq. (9), or Eq. (11) using the pulse voltage at the i-th ion's evaporation. The additional radially-dependent term in Eq. (17) ensures approximate model volume conservation during the radius update.

2.4.3 Parameter Tuning

A number of methods have been proposed to experimentally calibrate the free parameters within projection models. In circumstances where the specimen material gives rise to a clear pole structure due to surface faceting, and the lattice cell structure is known, the ICF (ξ) can be estimated by considering the crystallographic pole structure artefacts (Section 2.4.1) [34, 31]. Model parameters can also be estimated directly from SEM micrographs of pre-evaporated specimens.

Several methods aim to constrain parameters through periodicity signals within the reconstructed atomic positions. Due to crystallographic terracing, the evaporation of atoms is most probable at the edge of terraces where the electrostatic field is highest and evaporation fields weakest [17]. The result is a preferential evaporation sequence from the outside of terraces inwards, giving rise to spatial periodicity in detected ion positions [35, 36]. A number of techniques have been developed that aim to maximise this atomic periodicity, and calibrate it against the true material lattice structure [37, 38, 39, 40, 41].

While there exist numerous reconstruction calibration methods, these are all limited by the geometric assumptions of the projection model, and as a result are highly material dependent.

2.4.4 Dynamic Reconstruction

Previous studies have attempted to relax the constraint for constant projection parameters. One study by Larson et al. [42] relaxed the ICF (ξ) to allow its variation over the apex, correcting for changing magnification surrounding poles [43]. Another study by Gault et al. [44] assumed ξ and k_f can temporally vary throughout an experiment as a function of the detection event sequence. However, both these methods fail for specimens containing complex microstructures, where projection assumptions breakdown. A spatially varying ICF for multilayer structures has also been derived using simulation [45]. However, the derived function holds

only for this specific microstructure. All these methods attempt to correct local magnification changes by introducing additional degrees of freedom into what is fundamentally an unphysical and invalid model. Therefore, their utility is limited.

2.4.5 Density Relaxation

Density correction methods have been proposed that use reconstruction postprocessing to correct density fluctuations arising from imaging artefacts [46, 47]. By identifying microstructure through clustering, an iterative relaxation algorithm is applied to reconstructed atoms until local ion densities become homogenised [47]. However, its relatively arbitrary repositioning of atoms raises questions regarding the fidelity and physicality of the resulting reconstruction. Additionally, such density relaxation algorithms are incapable of correcting for ion trajectory crossover [48].

2.4.6 Projection Model Summary

Mathematical projection models assume a specimen apex that remains hemispherical throughout experiment. However, real specimens observed during experiment are inhomogeneous, non-axisymmetric, and have evolving apex shapes [49, 50, 51]. Therefore the underlying geometric approximations of these projections frequently breakdown. As a result, there is strong demand for new general models predicting specimen shape changes under field evaporation that are capable of relaxing these geometric constraints.

2.5 Historical Simulation and Reconstruction Efforts

2.5.1 Early Analytic Models

Early models for the electrostatic field were developed by approximating the specimen analytically via a paraboloid [52, 53] or hyperboloid [54, 55]. One study [56] even considered the effect of surface protrusions and concavities, revealing that the local crossing over of ion trajectories can occur. These very early analytical models considered the emitter a continuum. Trajectory calculations from a crystallographic geometry under a paraboloidal model's field solution revealed pole structure characteristic of FIM images [55]. It was identified that varying an ion's mass-to-charge-state ratio results in the same trajectory, assuming an initial launch velocity of near zero. Another group of studies [26, 27], motivated by empirical results, modelled ion trajectories analytically via mathematical projections. These studies laid the foundations for the development of projection-based reconstruction protocols.

2.5.2 Atomic-Scale Simulation

These early analytic models didn't consider specimen shape changes under field evaporation. The first models to consider atomic-scale evolution were created by Dimond et al. [57] and Vurpillot et al. [58, 59, 60, 61]. While Dimond's model invoked a curvature based approximation for surface electrostatics, Vurpillot's model incorporated both electrostatic calculations through a finite difference method and ion trajectory calculations. Vurpillot's framework is capable of capturing a wide range of evaporation physics, and introduced many of the concepts behind modern atomic-scale models. An extension to Vurpillot's model introduced an adaptive grid, allowing the simulation of body-centred cubic (BCC) and face-centred cubic (FCC) crystallographies [62]. Another extension incorporated material dielectricity [63].

An alternative approach solved the electric field via a boundary integral equation over the specimen surface, rather than having to mesh the entire domain [64]. The proposed algorithm also incorporated a Barnes-Hut compression technique [65], where distant charges are grouped and approximated together, reducing computational complexity.

A major advance in the atomic-scale modelling of field emitters came from using a Voronoi simulation mesh for the emitter lattice structure and surrounding vacuum by Oberdorfer et al. [66, 67, 68]. The electric field was solved over this mesh via an irregular grid finite difference method [69]. This generalised mesh allowed for the simulation of arbitrary lattice orientations, grain boundaries, and amorphous material. Further extensions to this model have included evaporation field variation due to bonding [70], and direct coupling with molecular dynamics [71, 72, 73].

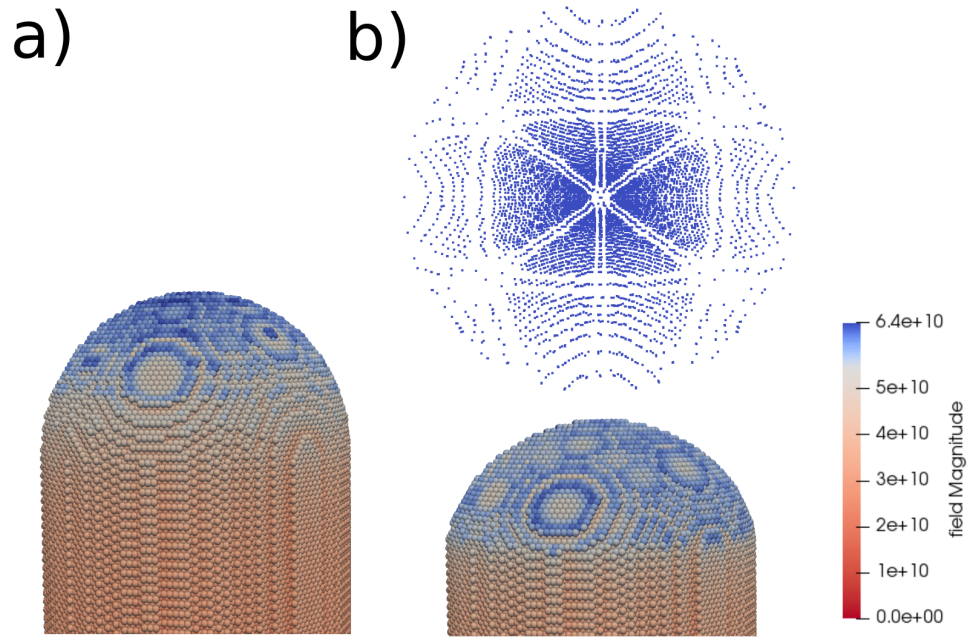


Figure 7: Example simulation of a pure tungsten specimen using TAPSim [67]. (a) Initial specimen state following relaxation. (b) Specimen after a period of evaporation. Its simulated detector hitmap, constructed from the previous ten thousand evaporated ions, is shown above.

However, while reproducing a high level of accuracy, simulation of full-scale experiments (typically tens of millions of ions) with these current atomic-scale models would take $20-40$ days given their evaporation rates of $200-300$ atoms per minute [64, 74]. Here, a fundamental communications bottleneck due to thread-joining limits their potential acceleration through parallelisation [74]. There's also a question of whether such accuracy is always necessary? Frequently, experimental data is too noisy to identify the very features predicted by modelling at this scale. This is particularly true for laser-assisted evaporation, which is required for the analysis of non-metallics.

2.5.3 Analytical Models

The most widely used model is that developed by Bas et al. [28, 17] (Section 2.4.2). While the captured level of detail represents the complete opposite from atomic-scale approaches, its simplicity allows it to form the basis of every widely used APT reconstruction protocol [29].

Attempts have been made to formulate more general analytical models capable of modelling multiphase structures. Currently, the only successful published attempt is by Rolland et al. [75, 76, 77]. Rolland's semi-analytical model successfully relaxes the hemispherical approximation for multilayer systems. By approximating the specimen surface electric field via its mean surface curvature, assuming Eq. (10) and surface field continuity, the specimen is modelled as a stack of constant-mean-curvature Delaunay surfaces. Ion trajectories are then modelled using a mathematical projection law. The model has been applied to reconstructing synthetic and experimental data [77]. Like with the Bas model, the total evaporated FOV volume in the model and experiment are matched, with the evaporated volume throughout experiment being estimated by summing all preceding detected ionic volumes. While the model successfully improves the accuracy of measured multilayer widths, it still makes many unphysical assump-

tions.

2.5.4 Continuum Models

By modelling the emitter as a continuum, Rolland's model has sufficient computational efficiency to reconstruct experimental data. However, its assumptions restrict its application to multilayer systems. This constraint can be relaxed through numerical surface tracking techniques. These include both explicit surface parameterisation methods that discretise and update the specimen surface via marker points, and implicit methods that embed the specimen surface within scalar fields [78].

Applying the implicit level set method to modelling field evaporation was originally proposed by Haley et al. [79, 80]. Haley's original model approximated the local evaporation rate via surface curvature (further discussed in Section 3.5.1). The approximation of phase evaporation field differences through a local rescaling of mean surface curvature was demonstrated, as well as the ability to initialise the specimen geometry through electron microscopy. However, the curvature approximation invoked is unphysical, and results in erroneous evaporation of microstructures and the shank.

A 2D level set model was later considered where the electrostatic field is solved via a finite difference solver [81]. The derived electric field is then used to evolve the level set field, resolving erroneous evaporation effects predicted by curvature flow. However, this implementation had a low computational efficiency (taking $8-10$ hours on a 120×120 grid [81]). Additionally, by using the local electric field solution to update the level set field away from the specimen surface, numerical accuracy will rapidly degrade due to level set bunching [82].

A surface parameterisation method is currently being developed by Hatzoglou et al. [83] that can handle differing evaporation fields and non-uniform temperature distributions. However, due to a current lack of publication details, its exact

numerical implementation, stability, and efficiency is unknown.

2.5.5 Reverse Projection Protocols

The final approach discussed is purely a data reconstruction scheme. The proposed protocol initially relied on Oberdorfer's TAPSim model [67] to perform the back projection of detected ions [84]. By considering the reversed evaporation sequence, detected ions are placed back one-by-one onto the emitter surface. This new approach builds up the reconstruction from last-to-first ion detected, removing the requirement for prior information regarding the specimen geometry. Later implementations switched to a continuum surface representation, enabling application to experimental data [85, 86].

While early results look promising [86], unphysical assumptions remain such as a requirement for convex emitter shapes. Both experiment and modelling has shown this convexity assumption to be invalid (see Figure 8). The protocol also currently assumes that ion trajectories obey a mathematical projection law, and imposes continuity assumptions regarding the specimen surface outside of the FOV. Due to APT data being directly coupled to the specimen model under this protocol, there is a concern that local positioning errors and ranging inconsistencies might propagate and grow throughout the reconstruction. Residual distortions to microstructures are still present under the new protocol [85, 86], likely arising due to remaining geometric assumptions.

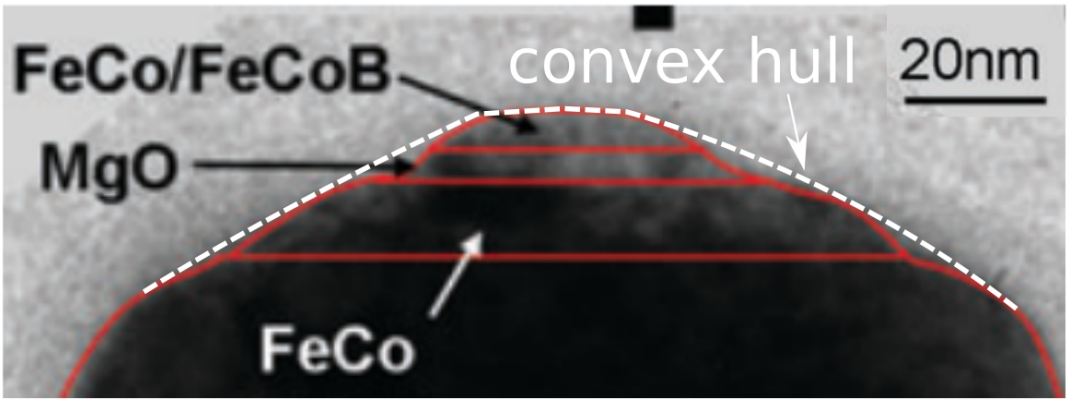


Figure 8: TEM of a multilayer structure following field evaporation. The surface convex hull has been fitted, identifying regions where convexity breaks down. (image reprinted and edited from E. A. Marquis, B. P. Geiser, T. J. Prosa, and D. J. Larson. Journal of Microscopy, 241:225–233, 2011., with the permission of John Wiley & Sons, Inc.).

2.5.6 Summary

While significant progress has been made, currently no existing model or reconstruction protocol can accurately correct for general multiphase distortions. While atomic-scale modelling has been very successful in accurately reproducing observed distortions and phenomena, these models are too slow to directly drive the reconstruction of experimental datasets. Alternative geometric-based protocols are also currently limited in their applications. With regards to achieving full-scale experiment simulation, continuum modelling approaches such as the level set method show particular promise by balancing accuracy, flexibility, and computational efficiency. Indeed, the simulation times given by Haley et al. [80] strongly imply that, if combined with an efficient electrostatic solver, level set models might be efficient enough to replace the Bas model in directly driving reconstruction. It is the development of such a model that this thesis sets out to achieve.

2.6 Independent Measuring of Specimen Shapes

In order to predict the field evaporation of realistic APT specimen shapes, and compare its simulated results to experiment, its surface and internal phase geometries must be known prior to analysis. One technique capable of obtaining this required geometry information is Electron Tomography (ET).

2.6.1 Electron Tomography

Electron tomography (ET) is a non-destructive technique where a 3D image is reconstructed from TEM micrographs obtained at differing tilts. During ET reconstruction, it can be assumed that the specimen geometry remains unchanged between TEM measurements. By approximating the electron beam as experiencing zero attenuation, the ET reconstruction problem can be defined as the linear inverse problem [87] in Eq. (18).

$$\mathbf{A} \cdot \mathbf{x} = \mathbf{b} \tag{18}$$

Here $\mathbf{x}$ is the desired vector of tomogram voxel values, $\mathbf{b}$ is the vector of projected voxel values (the inputted tilt series pixel contrasts), and $\mathbf{A}$ is a sparse projection operator describing the imaging process (i.e. how particular tomogram voxel densities contribute to the detected TEM pixel contrasts).

A number of ET algorithms exist [88, 89, 87, 90, 91]. The achievable resolution depends on the material, specimen geometry, and algorithm used. In this thesis, the Simultaneous Iterative Reconstruction Technique (SIRT) algorithm has been applied [88]. The resulting tomogram $\mathbf{x}_f$ consists of local contrast values giving imaging mode dependent information regarding local electron transmission properties.

In this thesis, the HAADF-STEM imaging mode has been used. Under

HAADF-STEM, voxel contrast depends on local atomic number. Therefore local contrast differences identify regions of differing composition. However, specimen thickness means that imaging resolution falls far short of APT, and lacks atomic-scale sensitivity. This is where correlative methods between ET and APT can account for these shortfalls.

2.6.2 Correlative Reconstruction

Several correlative studies compare microstructures within ET and APT reconstructions [92, 93, 94, 95]. Of particular interest is the work by Mouton et al. [96, 97]. Mouton proposes an approach for computationally tuning APT reconstruction parameters to maximise ET and APT data overlap. The protocol overlays a voxel grid onto the APT reconstruction conforming with the ET voxels. The local APT composition is calculated within each voxel. Finally, a rigid body transformation and APT reconstruction parameter optimisation is performed that maximises the cross-correlation between the APT composition and ET contrast. This method surpasses previously qualitative approaches [94, 98] by automatically maximising overlap under some similarity function. In theory, there is nothing preventing such a quantitative method from performing parameter optimisation for more advanced models.

It has been previously noted that APT and TEM could be combined into a single instrument [99]. A study by Haley et al. [100] demonstrated such an instrument's potential by numerically calculating ion trajectories from specimen surfaces measured via ET. Using these trajectories, a mapping was derived describing how final detector positions correspond to initial positions on the specimen surface. If this information was available throughout an APT analysis, such a mapping could be used to position ions within the reconstruction. The successful development of such a microscope would allow for in-situ ET-APT correlation throughout experiment [101].

2.6.3 Electron Tomography Surface Thresholding

As described in Section 2.6.1, the SIRT algorithm produces a 3D scalar field of local contrast values, dependent on the local phase. In order to extract model phase boundaries from this voxel field, the marching cubes contour extraction algorithm can be applied (see Section 3.4.1). This requires user-defined threshold values for phases (see Figure 9). Choosing appropriate thresholds, although minor, remains an unresolved problem and is left to the user.

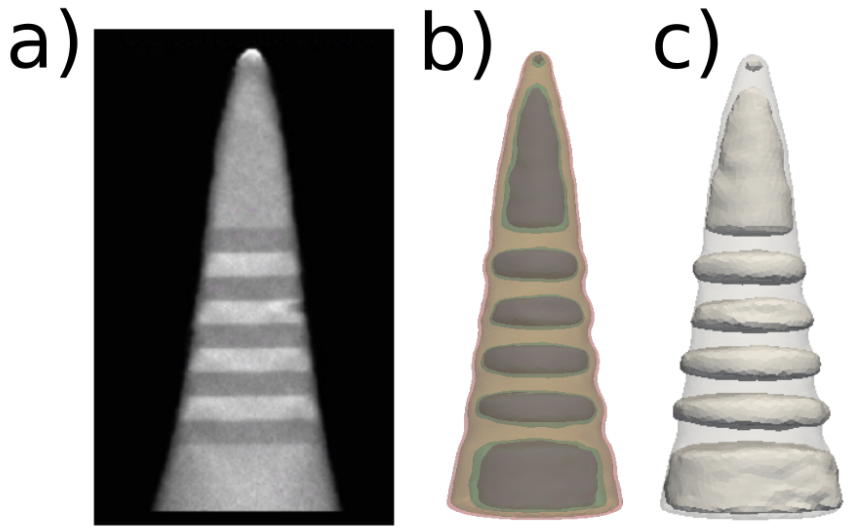


Figure 9: (a) Transverse slice of a multilayer specimen. (b) Isosurface plot showing different surface thresholdings. (c) Extrapolation of internal microstructure layers to intersect with the specimen surface, correcting for edge artefacts.

In addition, microstructure contrast can be lost close to the specimen surface. Local histogram equalisation also fails to resolve these edge microstructures (Figure 10). This contrast loss might arise both from ET reconstruction artefacts due to the changing thickness [102], but also from Ga implantation and subsequent material amorphisation during Focused Ion Beam (FIB) sample preparation [103]. The former could potentially be corrected through more sophisticated reconstruction or phase segmentation approaches [104], whilst the latter could be avoided by using a Plasma FIB. While microstructure extrapolation within these regions might be possible given system-specific knowledge, such as for multilayer

structures (see Figure 9c), this will not always be the case.

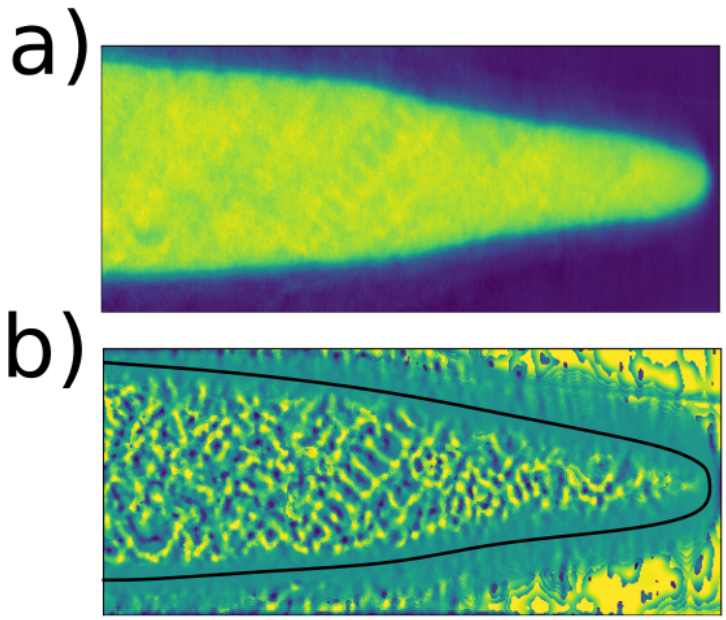


Figure 10: (a) ET reconstruction transverse slice of an APT specimen. Faint blurring artefacts can be observed at the edges. (b) Same slice following 3D local histogram equalisation. Microstructure close to the specimen edge still cannot be resolved. Data obtained by Thomas Slater, Diamond Light Source.

Finally, the extracted specimen surface and internal phase boundaries define the specimen geometry. The obtained initial specimen geometry could now be used to set up an evaporation model.

2.6.4 Atomic Force Microscopy

Another technique known as Atomic Force Microscopy (AFM) can directly measure both the specimen surface and surface electric field during experiment [105]. While such work looks promising, and could have future uses in constraining evaporation models, technical challenges must be solved to avoid multiple instrument transfers. In addition, its surface data output cannot directly initialise model internal phases. Therefore, only model initialisation via ET has been explored here.

3 Methodology

The following chapter will outline the concepts, theory, and methods making up a new continuum evaporation model for simulating APT experiments, and a model-driven reconstruction algorithm capable of correcting multiphase distortions.

3.1 Predicting Field Evaporation in APT

In order to predict surface evolution, a model is required for the local surface evaporation rate. It is known from both theory and experiment (see Section 2.1) that the rate of field evaporation is well described by the Arrhenius equation in Eq. (19).

$$R_e(\mathbf{s}) = Ae^{-\frac{\bar{Q}_E(\mathbf{s})}{kT}} \tag{19}$$

Here $\bar{Q}_E$ is some surface-averaged evaporation barrier. It is worth noting that in the underlying microscopic theory, an atom's evaporation barrier (Q_E) is specific to its surface site configuration. The derivation in Appendix A indicates how this law can incorporate a distribution of Q_E. These derivations also show that, assuming a well-behaved (normal) distribution for Q_E, a macroscopic Arrhenius law still holds.

Obtaining a general relationship for $\bar{Q}_E$ is more challenging. A number of different theories exist proposing equations for $\bar{Q}_E(\mathbf{s})$ featuring various material and temperature specific terms [106, 107, 12, 108]. However, Forbes proposed a useful approximation for the evaporation barrier around a local evaporation field F_0 via a Taylor expansion [109, 108]. Truncating this expansion to first order, we arrive at an approximate form for $\bar{Q}_E$ in Eq. (20). This law has been assumed in a wide number of models [110, 70, 81], and is known to agree reasonably well with experiment for surface fields close to F_0 [14, 13, 15].

$$\begin{aligned}\bar{Q}_E(\mathbf{s}) &= Q'_0\left(1-\frac{||\mathbf{E}(\mathbf{s})||}{F_0(\mathbf{s})}\right)+Q'_1\left(1-\frac{||\mathbf{E}(\mathbf{s})||}{F_0(\mathbf{s})}\right)^2+... \\ &\approx Q'_0\left(1-\frac{||\mathbf{E}(\mathbf{s})||}{F_0(\mathbf{s})}\right)\end{aligned} \tag{20}$$

It is this linear form for the evaporation barrier that will be assumed here. While the validity of such a law for field strengths differing from F_0 is unclear, there is also nothing preventing modifications or additional terms being later incorporated into the developed model framework. The complete local evaporation rate equation and specimen voltage constraint is given below.

$$R_e(\mathbf{s}) = Ae^{-\frac{C}{k_B T(\mathbf{s})}(1-\frac{||\mathbf{E}(\mathbf{s})||}{F_0(\mathbf{s})})} \tag{21}$$

$$F_R = \max_{\mathbf{s}\in\Gamma}\left(\frac{||\mathbf{E}(\mathbf{s})||}{F_0(\mathbf{s})}\right) \tag{22}$$

Here A is the global prefactor related to atomic surface density, $\beta(\mathbf{s})$ is a temperature-like parameter (or distribution when modelling the applied laser pulse) with an approximate experiment range from 40 to 400, $||\mathbf{E}(\mathbf{s})||$ is the surface electric field strength, $F_0(\mathbf{s})$ is the isotropic local evaporation field, and $\mathbf{s} \in \Gamma$ defines a point on the specimen surface Γ.

Throughout this thesis, the field reduction rate has been held constant at $F_R = 1$ through rescaling the specimen voltage. It is worth briefly noting that this constraint is not entirely realistic of the voltage control in modern APT experiments, with the true voltage controlled by an algorithm based off the incident detector flux [32]. However, assuming sufficiently fast voltage controller response times, this constraint shouldn't be too unreasonable. At the macroscale, $F_R > 1.0$ likely corresponds to a complete breakdown in evaporation sequence ordering and a high multiple hit rate (as multiple surface patches are now above the

critical evaporation barrier). Such a regime would be extremely undesirable in typical APT experiments. The Figure 11 shows the form of Eq. (21) with varying temperature.

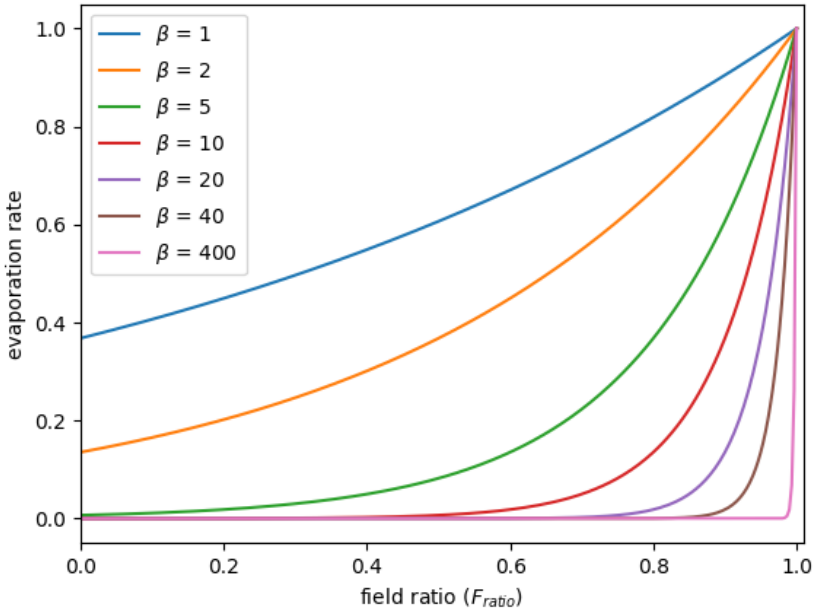


Figure 11: Plot showing how the evaporation rate varies with the field ratio F_{ratio} for different values of β.

In conclusion, we have obtained a macroscale law for predicting surface evaporation rate (Eq. (21)). This law will form a core component of the model by providing the surface velocity for specimen evolution.

3.2 Specimen Surface Tracking

Once this evaporation rate can be calculated, surface evolution can be considered. The specimen surface is discretised as a closed surface mesh. For this study, a line segment mesh was used for the 2D implementation, and a triangle surface mesh for the 3D implementation. In both models, the elements are by default stored as a triangle or edge list. These data structures are given in Figure 12, along with some example meshes.

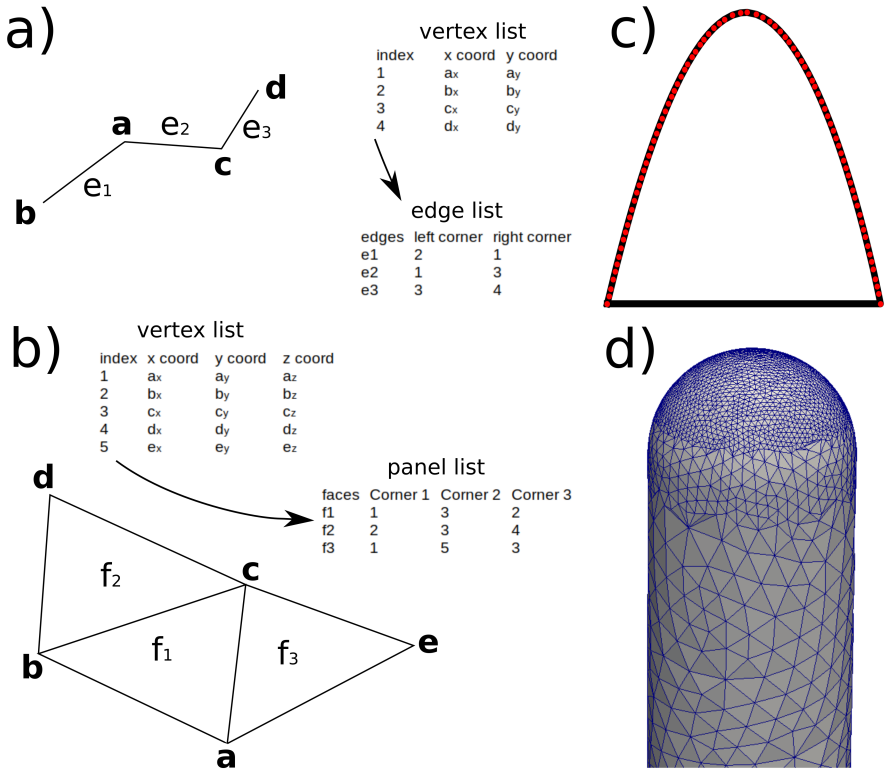


Figure 12: a) The edge list data structure for an example line segment mesh (2D model). b) The face list data structure for an example triangle mesh (3D model). (c) Example closed specimen line segment mesh. (d) Example closed specimen triangle mesh.

Once the specimen surface mesh has been defined, a method is required to track this surface under its evolution. The obvious approach is to evolve the mesh explicitly by moving its vertices (marker points). However, in such direct methods, vertices can spread out or bunch together, and can even cross over to

produce an invalid mesh. This is particularly problematic at corner discontinuities that can form during faceting, e.g. Figure 13. Handling the joining and separation of disconnected meshes is also non-trivial.

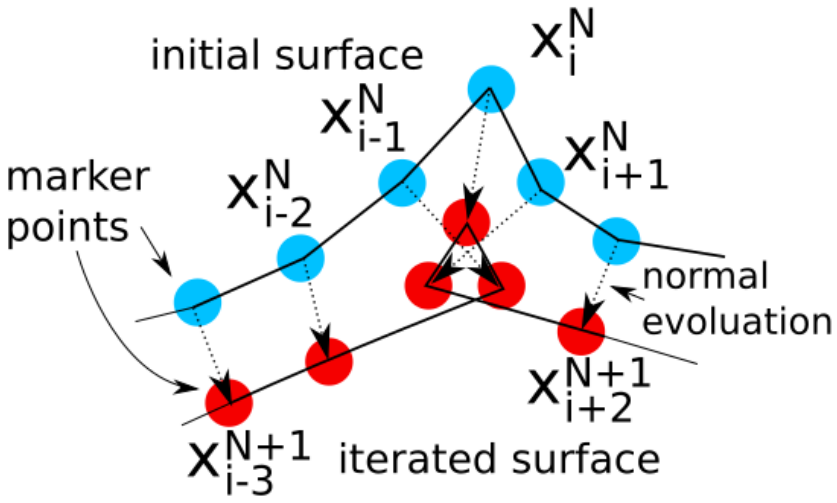


Figure 13: Example surface evolution under a marker point method where vertices are shifted normal to the surface. If the iteration time step is too large, marker points can bunch and cross over, resulting in surface element inversions.

An alternative group of methods can be constructed by considering an Eulerian reference frame: where the surface position is gauged by tracking its motion with respect to static domain points. These methods tend to track the evolving surface implicitly through the evolution of discretised field(s) on a static grid. While the tracked surface must be extracted from these fields when required, the static grid means that many of the numerical problems encountered by marker point methods can be avoided. The model developed in this work uses one such group of methods, known as level set methods, the theory for which will be developed in the following section.

3.3 The Level Set Method

The level set method is a mathematical framework for tracking surfaces via an embedding as a contour within a higher dimensional function: the level set field [78]. This implicit approach avoids numerical issues that arise in explicit approaches, whilst allowing for the merging and separation of surfaces, and formation of surface discontinuities. These properties make the framework appealing for modelling APT specimen evaporation, where both specimen faceting [50] and voids [111] (specimen cavities) have been experimentally observed. The following section will outline the method's theory.

3.3.1 The Level Set Framework

The specimen surface is tracked as an N dimensional closed surface (Γ) within an $N+1$ dimensional scalar field (ϕ). Conventionally, the surface is defined as the zero level set, as given in Eq. (23).

$$\Gamma = \{\mathbf{x} \mid \phi(\mathbf{x}) = 0\} \tag{23}$$

Here $\mathbf{x} \in \mathbf{\Omega}$, where $\mathbf{\Omega}$ is the problem domain, and Γ is the set of all points on the surface. From this definition alone, the exact form of ϕ over $\mathbf{\Omega}/\Gamma$ is unconstrained, and an additional constraint regarding the initial form of ϕ over all $\mathbf{\Omega}$ is required. The most common constraint is to define ϕ by a signed distance field (Eq. (24)). A signed distance form for ϕ has contours that are evenly spaced surrounding the embedded surface, ensuring that numerical accuracy is maintained following field discretisation. From this field definition, the outer surface normal vector is defined via Eq. (25).

$$\phi(\mathbf{x}) = \begin{cases} +d(\mathbf{x}, \Gamma) & \mathbf{x} \in \mathbf{\Omega}^+ \\ -d(\mathbf{x}, \Gamma) & \mathbf{x} \in \mathbf{\Omega}^- \\ 0 & \mathbf{x} \in \Gamma \end{cases} \tag{24}$$

$$\mathbf{n}(\mathbf{s}) = -\nabla\phi(\mathbf{s}) \tag{25}$$

Here $d(\mathbf{x}, \Gamma)$ defines the minimum Euclidean distance between point $\mathbf{x} \in \mathbf{\Omega}$ and the specimen surface Γ. The subdomain inside the tracked surface is given by $\mathbf{\Omega}^+$, $\mathbf{\Omega}^-$ is the subdomain outside the tracked surface, and $\mathbf{s} \in \Gamma$. Note that the level set normal definition in Eq. (25) holds only for signed distance functions. For general ϕ, the outer normal is given by $\mathbf{n}(\mathbf{s}) = -\frac{\nabla\phi(\mathbf{s})}{||\nabla\phi(\mathbf{s})||}$. An example signed distance field for a closed 2D surface is shown in Figure 14.

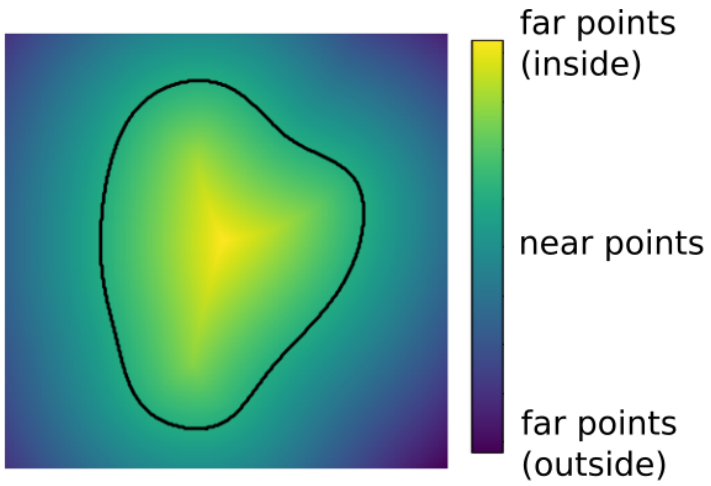


Figure 14: Visualisation of a closed surface embedding as the zero contour within a signed distance field. In the level set framework, this signed distance field is modified between iterations such that the zero contour moves over time.

In the level set method, the propagation of the embedded surface under a general velocity field $\nu(\mathbf{x})$ normal to the embedded surface is achieved by evolving $\phi(\mathbf{x})$ according to an equation of motion. In order to derive this equation, the condition that $\phi = 0$ at the embedded surface throughout time is considered.

We can consider a particle following a curve $\mathbf{x}(t)$ that moves with this embedded surface (Eq. (26)).

$$\phi(\mathbf{x}(t), t) = 0 \tag{26}$$

Applying the total derivative and chain rule to Eq. (26) results in the material derivative given by Eq. (27).

$$\begin{aligned} \frac{d\ \phi(\mathbf{x}(t), t)}{dt} &= 0 \\ \frac{\partial \phi}{\partial t} + \nabla \phi \cdot \frac{\partial \mathbf{x}}{\partial t} &= 0 \end{aligned} \tag{27}$$

Here $\frac{\partial \mathbf{x}}{\partial t}$ is the velocity field of particles moving with the embedded surface. Note that this expression must hold for any particle following the embedded surface. Recalling that the embedded surface normal is given by $\mathbf{n} = -\frac{\nabla \phi}{||\nabla \phi||}$, and taking $\nu = \frac{\partial \mathbf{x}}{\partial t} \cdot \mathbf{n}$, where ν is the normal component of the velocity, Eq. (27) can be rewritten in terms of the normal velocity component (Eq. (28)).

$$\frac{\partial \phi(\mathbf{x}, t)}{\partial t} - \nu(\mathbf{x}, t)||\nabla \phi(\mathbf{x}, t)|| = 0 \tag{28}$$

This is known as the *level set equation*. Taking Eq. (28) to hold for all $\mathbf{x} \in \mathbf{\Omega}$ ensures that the zero level set always identifies with the embedded surface. The $\nu(\mathbf{x})$ velocity term, referred to as the velocity extension field, must be defined for all $\mathbf{x} \in \mathbf{\Omega}$. However, the surface evaporation rate only defines the normal velocity at the embedded surface, and not over $\mathbf{\Omega}/\Gamma$. By again considering a particle moving with the front, it can be seen that the velocity extension field ν should converge at the embedded specimen surface to the calculated material evaporation rate (Eq. (29)).

$$\lim_{||\mathbf{x}-\mathbf{s}||\to 0} \nu(\mathbf{x},t) = -R_e(\mathbf{s},t) \tag{29}$$

where $R_e(\mathbf{s})$ is the calculated local evaporation rate at $\mathbf{s}$. Similar to ϕ, an additional condition is required to define ν over the rest of $\mathbf{\Omega}$ away from the embedded surface. Multiple methods exist to construct such velocity extensions [82, 112]. Here a closest-point method is used, where $\nu(\mathbf{x})$ takes the same R_e value as the closest point on the embedded surface. This velocity extension method obeys Eq. (30), and can be understood as projecting the velocity from the closest points on the embedded surface onto the grid points throughout the domain.

$$\nu(\mathbf{x},t) = -R_e(\mathbf{s}_m) \quad \text{where} \quad \mathbf{s}_m = \text{argmin}_{\mathbf{s}\in\Gamma}||\mathbf{x}-\mathbf{s}|| \tag{30}$$

In this work, the level set field has been discretised via a finite difference method on a Cartesian grid. Discretisation of Eq. (28) was performed according to a first-order normal upwind scheme previously used in coupled level set-boundary integral models [113, 82, 114]. The second-order upwind scheme described in [78] was also implemented in the 3D model, but was found in practice to have little effect on the solution. In this work, only the first-order scheme is shown due to its simpler form. Its formulation is omitted from this thesis due to unnecessary complexity. Temporal integration has largely been performed using adaptive Euler's method, and while the second order Heun's method was implemented for the 2D model, it was found to provide little improvement in accuracy. The resulting first-order 3D update equation is given by Eq. (31).

$$\phi_{ijk}^{n+1} = \phi_{ijk}^{n} + \delta t^{n}\ \nu_{ijk}^{n}\ [\max(\partial_x^+ \phi_{ijk}^n, 0)^2 + \min(\partial_x^- \phi_{ijk}^n, 0)^2 + \max(\partial_y^+ \phi_{ijk}^n, 0)^2 + \min(\partial_y^- \phi_{ijk}^n, 0)^2 \max(\partial_z^+ \phi_{ijk}^n, 0)^2 + \min(\partial_z^- \phi_{ijk}^n, 0)^2]^{1/2} \quad (31)$$

$$\partial_x^+ \phi_{ijk}^n = \frac{\phi_{i+1jk}^n - \phi_{ijk}^n}{h} \qquad \partial_x^- \phi_{ijk}^n = \frac{\phi_{ijk}^n - \phi_{i-1jk}^n}{h}$$
$$\partial_y^+ \phi_{ijk}^n = \frac{\phi_{ij+1k}^n - \phi_{ijk}^n}{h} \qquad \partial_y^- \phi_{ijk}^n = \frac{\phi_{ijk}^n - \phi_{ij-1k}^n}{h}$$
$$\partial_z^+ \phi_{ijk}^n = \frac{\phi_{ijk+1}^n - \phi_{ijk}^n}{h} \qquad \partial_z^- \phi_{ijk}^n = \frac{\phi_{ijk}^n - \phi_{ijk-1}^n}{h}$$

Here h is the level set grid cell width, ϕ_{ijk}^n is the field value for voxel ijk at time step n, δt is the update time step, and ν_{ijk}^n is the velocity extension field that has been discretised on the same Cartesian grid as ϕ. The min/max operations ensure the correct direction of upwinding according to the surface normal velocity field. Due to the velocity direction ν_{ijk}^n being inward flowing, a Neumann boundary condition ($\partial\phi = 0$) has been implemented at the domain edge such that ∂^+ and ∂^- are defined. When updating ϕ under Eq. (31), an adaptive time stepping has been used, with an appropriate time step calculated via the CFL condition in Eq. (32).

$$\delta t^n = C\frac{h}{\max_{\mathbf{\Omega}}(|\nu_{ijk}^n|)} \quad (32)$$

Here C is a user-defined parameter known as the CFL fraction, and $\max_{\mathbf{\Omega}}(|\nu_{ijk}^n|)$ indicates the maximum absolute value for ν_{ijk}^n in the computational domain.

3.3.2 Field Reinitialisation

To ensure no degradation in numerical accuracy, the signed distance form of ϕ should be maintained as it evolves under Eq. (29). This is not guaranteed under the closest-point method due to $\mathbf{s}_m$ in general not being continuous with respect to variations in $\mathbf{x}$ [82]. As a result, the field ϕ can drift from a signed distance form throughout the simulation. To restore ϕ to signed distance form, a number of different reinitialisation methods exist. These consist of direct methods that rebuild the signed distance field from the embedded surface, and iterative methods that aim to restore the signed distance form by relaxing the level set field [78].

In the 2D model, the signed distance field is directly rebuilt from the extracted $\phi = 0$ surface. However, direct reinitialisation in 3D is slow and instead an implicit iterative approach has been implemented based on the method originally proposed by Sussman et al. [115]. The method proceeds by solving Eq. (33) until the steady-state solution is reached, i.e. $\frac{\partial \phi(\mathbf{x},\tau)}{\partial \tau} = 0$. It can be seen that the steady-state solution for this PDE obeys a signed distance form $||\nabla \phi(\mathbf{x}, \tau)|| = 1$.

$$\frac{\partial \phi(\mathbf{x},\tau)}{\partial \tau} = \text{sgn}(\phi^0)(1 - ||\nabla \phi(\mathbf{x},\tau)||) \tag{33}$$

$$\text{sgn}(\phi^0)(\mathbf{x}) = \frac{\phi(\mathbf{x},0)}{\sqrt{\phi(\mathbf{x},0)^2 + \zeta^2}} \tag{34}$$

Here ζ is a small numerical perturbation to ensure convergence. The Eq. (33) has been discretised via a finite difference first-order upwind scheme given in Eq. (35) [116].

$$G_{ijk} = \begin{cases} \sqrt{\sum_{\alpha}^{D} \max\big(\max(\partial_{\alpha}^{-}\phi_{ijk}^{t}, 0)^2, \min(\partial_{\alpha}^{+}\phi_{ijk}^{t}, 0)\big)} - 1 & \text{for } \phi_{ijk}^{0} > 0 \\ \sqrt{\sum_{\alpha}^{D} \max\big(\min(\partial_{\alpha}^{-}\phi_{ijk}^{t}, 0)^2, \max(\partial_{\alpha}^{+}\phi_{ijk}^{t}, 0)\big)} - 1 & \text{for } \phi_{ijk}^{0} < 0 \\ 0 & \text{otherwise} \end{cases}$$

$$\phi_{ijk}^{t+1} = \phi_{ijk}^{t} + \mathrm{sgn}(\phi^{0})_{ijk}\; G_{ijk}\; \delta t \tag{35}$$

$$\frac{\sum_{ijk}^{N} |\phi_{ijk}^{t+1} - \phi_{ijk}^{t}|}{N} < \gamma\; \delta t \tag{36}$$

Here D is the problem dimensionality (either 2 or 3), and $\alpha \in \{x, y, z\}$. When solving this system, a constant iteration time step of $\delta t = 0.1$ has been used. The Eq. (36) describes the termination condition (with a termination threshold parameter γ). Parameter values of $\zeta = 0.5$ and $\gamma = 0.4$ were empirically found to ensure good convergence. The total number of level set grid cells is given by N.

In order to validate and assess the performance of the implemented scheme, two test cases were considered (see Figures 15). For both cases, the initial level set field ϕ_{initial} is that for a sphere of radius 10, centred within a $40 \times 40 \times 40$ field grid. In both cases, the convergence of the field back to signed distance form is investigated following a perturbation. In these examples, to ensure additional zero contours are not introduced under perturbation, the narrowband $|\phi_{\text{initial}}| < 1$ is left unchanged. When applying this reinitialisation scheme in practice however, this locking is not applied.

The first case (Figure 15b) considers a smooth sinusoidal perturbation $\phi_{\text{pert}} = \phi_{\text{initial}} + 0.95\, \sin(\frac{\pi}{5}(x+y+z))$. Under the criterion given in Eq. (36), convergence was achieved in 99 iterations, with a signed distance field being largely restored (Figure 15c).

The second case (Figure 15d) considers the addition of Random Gaussian noise $\phi_{\text{pert}} = \phi_{\text{initial}} + N(\mu = 0,\ \sigma = 0.5)$. Despite the perturbation's roughness, convergence was achieved in 59 iterations, with a signed distance field also being

largely restored (Figure 15e).

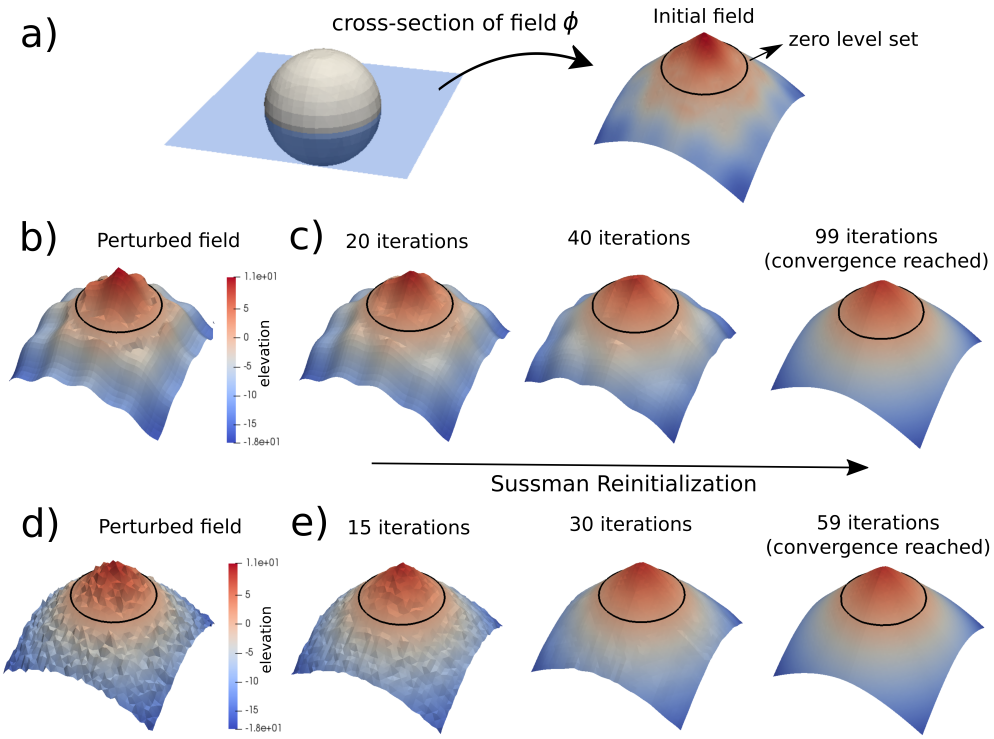


Figure 15: Iterative reinitialisation examples in 3D. (a) The initial zero level set surface and cross-sectional level set field. (b) The cross-sectional level set field perturbed via a smooth sinusoid. (c) The same field after various Sussman iterations. (d) The cross-sectional level set field perturbed via discontinuous Gaussian noise. (e) The same field after various Sussman iterations.

While the signed distance form was restored in both test cases, this was not without some drift of the zero level set. While this numerical drift was found to be much smaller than the level set grid width, such reinitialisation should not be performed too frequently or unnecessarily. This drift when solving the reinitialisation equation could also be reduced through higher-order discretisation schemes, e.g. essentially non-oscillatory (ENO) schemes [117]. It is worth noting that these examples are extreme cases in the context of the numerical drift present in simulation. For drifts observed in practice, iterative reinitialisation typically converged in a few iterations.

3.4 Mesh processing

3.4.1 Contour Extraction

The level set method tracks the specimen surface implicitly as the zero contour within a voxel field (ϕ). However, in order to calculate the electric field, this contour must be located and extracted from ϕ as a surface mesh. In this work, contour extraction is performed using Lewiner's Marching Cubes algorithm [118, 119] (known as Marching Squares in 2D). Lewiner's marching cubes introduces additional case checks and topological tests to ensure that the extracted mesh is a manifold. The output of this algorithm is a triangle surface mesh (or a line segment mesh in the 2D model) corresponding to the embedded specimen surface. The structures of the generated meshes are the same as those in Figure 12.

3.4.2 Adaptive Isotropic Remeshing

While the extracted 1D edge mesh in the 2D model can be directly inputted into the electrostatic solver, this is not the case for the 3D triangle mesh due to the solver's sensitivity to the surface mesh quality. For a particular linear system $\mathbf{A} \cdot \mathbf{x} = \mathbf{b}$, its conditioning depends on the size of the resulting solution perturbation $\mathbf{A}^{-1} \cdot \mathbf{e}$ from an input perturbation $\delta\mathbf{b} = \mathbf{e}$. From this definition, a scalar quantity known as the condition number can be defined that measures the relative stability of the system to its inputs. This number is calculated via Eq. (37).

$$C = ||\mathbf{A}^{-1}||_2 \; ||\mathbf{A}||_2 \tag{37}$$
$$\mathbf{A} = \mathbf{F}^{-1} \cdot \mathbf{P}$$

Note that under the conductor approximation, $\mathbf{A}$ is given by the BEM problem matrices $\mathbf{F}$ and $\mathbf{P}$ (Section 3.5.2). Here we use the matrix spectral norm $||...||_2$

(fraction of the smallest and largest singular values of $\mathbf{A}$), which is typically applied when considering BEM conditioning [120]. In practical terms, a poorer conditioned system (lower C) will result in larger solution errors.

To investigate the 3D BEM conditioning, we consider a spherical geometry with radius $R = 8$ m as extracted from a signed distance field. The geometry in Figure 16a shows the mesh immediately following isosurface extraction. This is compared to the mesh in Figure 16b where an additional isotropic remeshing step has been applied [121]. This algorithm aims for similarly sized surface panels by performing edge splits, edge collapses, edge flips, and vertex relocations, whilst minimising the error between the new and original mesh. In this work, the isotropic remesh algorithm within the C++ mesh processing library *CGAL* is used [122].

Applying Eq. (37) to the BEM systems for the meshes in Figure 16a and Figure 16b, we obtain condition numbers of $C_{\text{raw}} = 309$ and $C_{\text{remesh}} = 119$. These values imply that the remeshing has improved system conditioning. The effect of this improvement on panel fluxes can be seen in Figure 16c. Here the variation in fluxes from the analytical solution (green) for the unremeshed solution (orange) can be seen to be significantly greater than the remeshed solution (blue). It is also seen in Figure 16d that there is a larger flux spread for smaller panels. This is due to both the lower relative weighting of smaller panels within the linear system, and that smaller panels are more likely to be skinny triangles, which frequently give poor results in numerical calculations [123].

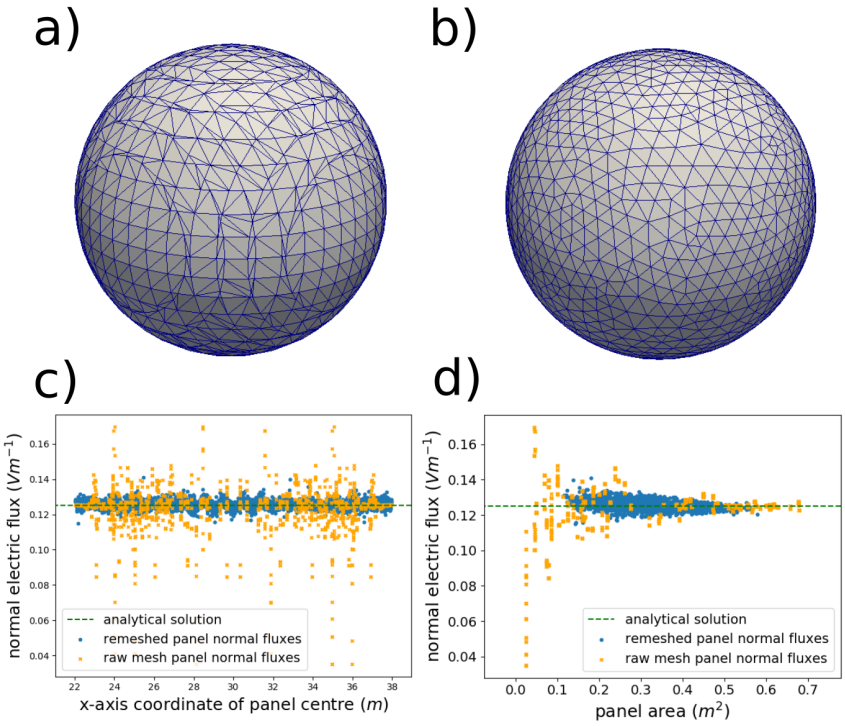


Figure 16: (a) Raw mesh immediately following extraction via Marching Cubes. Note the panel size variation. (b) Mesh following isotropic remeshing [122]. (c) The panel fluxes for the raw mesh (orange) and remeshed (blue) geometries. (d) The distribution of panel fluxes with respect to panel areas.

For the 3D model, this isotropic remeshing step was required to produce well-behaved surface fluxes. Without this remeshing step, large spikes in panel fluxes were found to regularly occur. These spikes result in a non-smooth velocity field, which in turn can result in the simulation time step (Eq. (32)) becoming infinitesimal, effectively freezing the simulation. Isotropic remeshing prior to solving the field prevented this freezing.

Finally, the CGAL isotropic remeshing algorithm also enables adaptive remeshing. Here the algorithm's target panel size can be increased with distance away from the specimen apex. By performing this remeshing such that elements further from the apex increase in size, the total number of elements can be reduced, whilst ensuring that high mesh resolution at the apex is maintained. By reducing the total number of panels, the linear system size is also reduced, allo-

wing for more rapid solution. The end result of this adaptive remeshing is shown in Figure 17. The parameters of this adaptive remeshing algorithm have been manually tuned, with the exact tunings found in the source code.

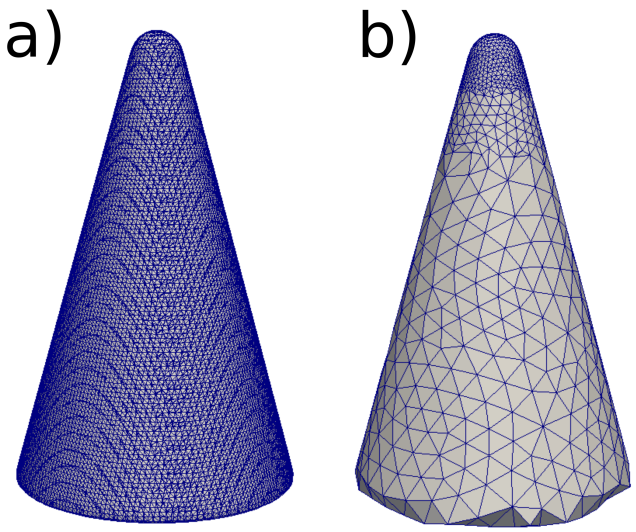


Figure 17: (a) A raw specimen mesh immediately following extraction. (b) The same specimen geometry following adaptive isotropic remeshing.

3.4.3 Shank Extension

In both the 2D and 3D models, there is an option to extend the shank geometry beyond that extracted from the level set field. The shank geometry affects the field solution, in turn impacting both the predicted evaporation rate and ion trajectories. Therefore, it is desirable to model both a sufficient shank length to minimise discrepancy, as well as maintain a consistent length throughout simulations.

For the 2D model, mesh elements are clockwise ordered within the edge list (see Figure 12a). Therefore, the shank can be extended by temporarily removing base elements, and appending additional elements before the first element and after the final element. The number and size of these appended elements is governed by a user-defined parameter. The angle (α) at which to orient these appended elements is calculated by considering the average angle of neighbouring

non-appended elements.

In the 3D model, this extension is performed by shifting mesh vertices located at the extracted mesh base down by displacement δD according to Eq. (38).

$$\begin{bmatrix} x_{ex} \\ y_{ex} \\ z_{ex} \end{bmatrix} = \begin{bmatrix} x_i \\ y_i \\ z_i \end{bmatrix} + \delta D \begin{bmatrix} \cos\theta \ \tan\alpha \\ \sin\theta \ \tan\alpha \\ -1 \end{bmatrix} \tag{38}$$
$$\theta = \arctan(\frac{y_i - y_c}{x_i - x_c})$$

Here α is the shank angle to extend by, $\mathbf{x}_i = (x_i, y_i, z_i)$ are an initial base vertex's coordinates, $\mathbf{x}_{ex} = (x_{ex}, y_{ex}, z_{ex})$ are an extended base vertex's coordinates, and $\mathbf{x}_c = (x_c, y_c, z_c)$ is the initial centroid position of all base vertices. An appropriate angle for α can be estimated via a Least Squares fit of a truncated cone to the initial specimen geometry (Figure 18a). Following this extension, the isotropic remeshing step is performed. An example multilayer system simulation is shown in Figures 18b-d, maintaining a constant total specimen length at each iteration.

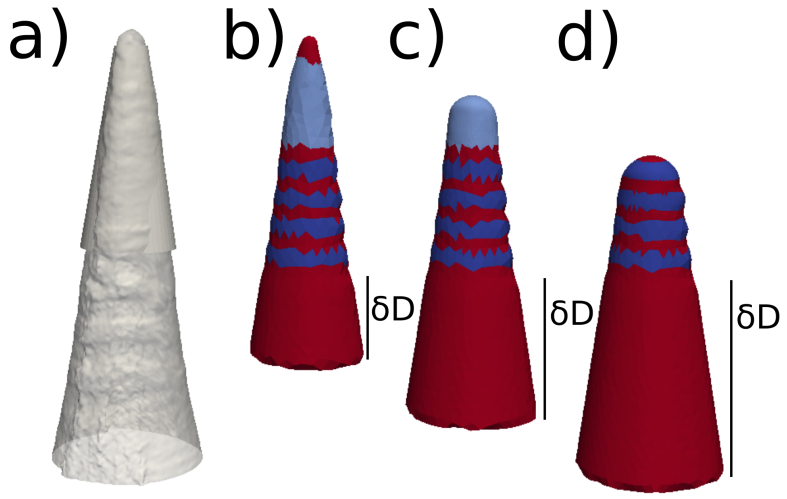


Figure 18: (a) A truncated cone fitted via least squares to a specimen geometry obtained from ET. (b-d) Frames from its simulated evaporation, whilst maintaining a constant specimen length.

3.5 Electrostatics

In order to predict the evaporation rate (Eq. (21)) and ion optics, accurate calculation of the electric field at both the specimen surface and at points in the surrounding vacuum is critical. A typical assumption made when modelling APT experiments is to treat the problem via classical electrostatics. Here the voltage pulse applied to the specimen (or local electrode) is approximated as a step function, with all field evaporation and ion flight assumed to occur within this pulse duration. A study to assess this assumption's validity predicted detector positioning errors of only $1-3$ % [124].

Under these electrostatic assumptions, Maxwell's equations reduce to Poisson's equation with zero free charges (Eq. (39)).

$$\begin{aligned} -\nabla \cdot \big(\epsilon(\mathbf{x})\nabla u(\mathbf{x})\big) = 0 \qquad \forall \mathbf{x} \in \mathbf{X} \\ \mathbf{E}(\mathbf{x}) = -\nabla u(\mathbf{x}) \end{aligned} \tag{39}$$

Here $u(\mathbf{x})$ is the electric potential, $\mathbf{E}(\mathbf{x})$ is the electric field, $\epsilon(\mathbf{x})$ is the dielectric permittivity, and $\mathbf{X}$ is the electrostatic problem domain. Note that this is not equivalent to the level set domain $\mathbf{\Omega}$, which is only local to the tracked surface. The value of $\mathbf{E}$ over $\mathbf{X}$ determines ion trajectories from the emitter surface to detector, whilst its value at Γ determines the local evaporation rate.

3.5.1 The Curvature Flow Approximation

It has long been known that there exists a fundamental connection between the surface electric field and surface curvature of a conductor. This connection is formalised through the following equation [125]:

$$\nabla E \cdot \mathbf{n} = -2\kappa_M E \tag{40}$$

Here $\kappa_M = \frac{1}{2}(\frac{1}{R_1} + \frac{1}{R_2})$ is the local surface mean curvature, where R_1 and R_2 are the local principle radii of curvature, $E = ||\mathbf{E}||$ is the electric field magnitude, and $\mathbf{n}$ is the surface normal. While there exists no direct equation between $\mathbf{E}$ and κ_M, a qualitative relation is well established where greater surface curvature implies a higher surface charge density (σ). For a conductor, the surface charge can then be related to the surface field magnitude via $E = \epsilon_0\sigma$ through Gauss's law, where ϵ_0 is the vacuum permittivity. This relation has led to the idea that $||\mathbf{E}||$ can be approximated as some function of κ, an assumption that has been widely applied throughout APT literature [57, 79, 76].

In the level set framework, the embedded surface's mean curvature can be directly calculated from the level set field (ϕ) via Eq. (41). Haley et al. [79, 80] approximated the evaporation rate as positively-capped mean curvature flow, where a suitable extension velocity can be defined via Eq. (42).

$$\kappa_M = \nabla \cdot \frac{\nabla\phi}{||\nabla\phi||} \tag{41}$$

$$\nu(\mathbf{x}) = I(\mathbf{x})\ \max\big(\kappa_M(\mathbf{x}), 0\big) \quad \forall \mathbf{x} \in \mathbf{\Omega} \tag{42}$$

Here $I(\mathbf{x})$ is a local modifier approximating differences in material evaporation fields. When discretising Eq. (41), the upwind scheme outlined in Eq. (31) cannot be applied for parabolic terms such as κ_M [78]. Instead the central difference scheme in Eq. (43) is applied [113].

$$\phi_{ijk}^{n+1} = \phi_{ijk}^{n} + \delta t^{n}\ \nu_{ijk}^{n}\ \left[(\partial_x^0 \phi_{ijk}^{n})^2 + (\partial_y^0 \phi_{ijk}^{n})^2 + (\partial_z^0 \phi_{ijk}^{n})^2\right]^{1/2} \tag{43}$$

$$\partial_x^0 = \frac{\partial_x^+ + \partial_x^-}{2}$$

$$\partial_y^0 = \frac{\partial_y^+ + \partial_y^-}{2}$$

$$\partial_z^0 = \frac{\partial_z^+ + \partial_z^-}{2}$$

$$\kappa_M = \sum_{\alpha}^{D} \partial_\alpha^0 \left(\frac{\partial_\alpha^0 \phi_{ijk}^{n}}{|| \sum_{\gamma}^{D} \partial_\gamma^0 \phi_{ijk}^{n} ||} \right) \tag{44}$$

Here D is the dimensionality (either 2 or 3). Curvature flow evolution has been implemented in the 2D model to allow for direct comparison with electrostatic-driven evolution (Section 4).

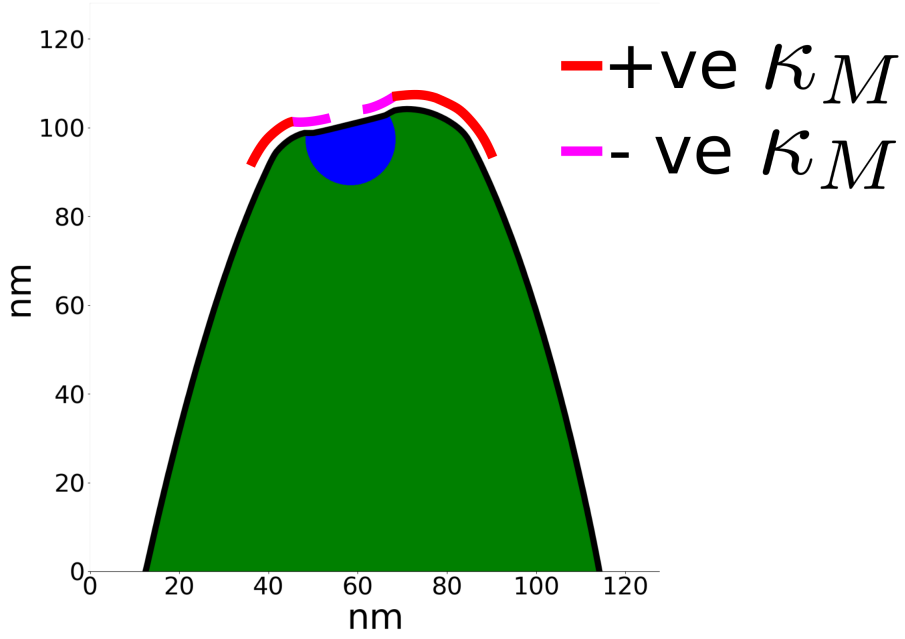


Figure 19: An instance from the electrostatic-driven evolution of a low-field precipitate in the 2D model. The regions of positive (red) and negative (purple) apex surface curvatures are shown.

The curvature approximation breaks down for concave surface features. Such features arise during the evaporation of low field phases and voids (see Figure 19).

In such cases the velocity field definition in Eq. (42) would simply assign an evaporation rate of zero. Therefore, under curvature flow concave specimen shapes cannot form, and all initially concave shapes become convex over time. For isotropic curvature flow evolution, this is formalised by Grayson's theorem [126, 127].

While non self-crossing closed shapes tend to circles or spheres under curvature flow, a self-similar solution also exists for open curves known as the grim reaper curve [128]. This open curve is shown in Figure 20. Under curvature flow, the curve remains self-similar and is translated along the axis of symmetry. Its evolution can be considered a 'toy' model for understanding steady-state apex behaviour under field evaporation, demonstrating why mathematical projection models work well for homogeneous materials.

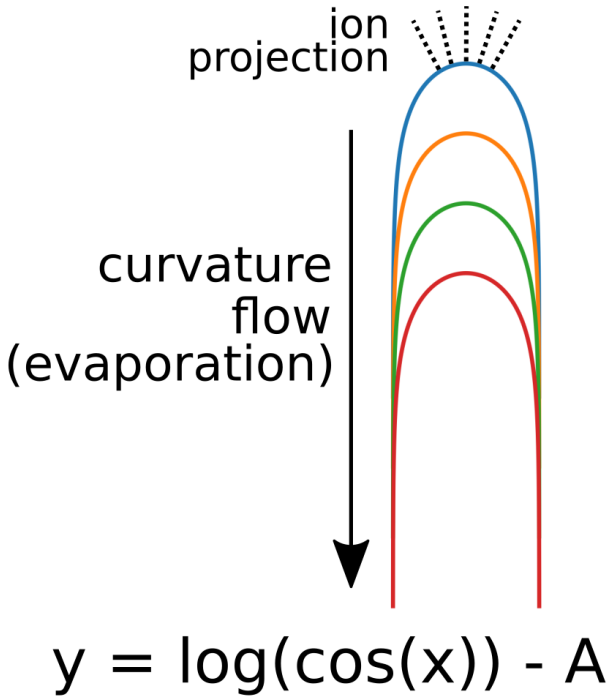


Figure 20: The grim reaper curve [128] is an open curve that remains self-similar under curvature flow.

The mean curvature flow approximation can also result in unphysical evaporation of the shank [80]. This shank evaporation phenomenon is most apparent in 3D, where the shank's curvature is always non-zero. As will be seen, mean

curvature flow can not accurately reproduce electrostatic-driven flow (Section 4).

It is worth noting that for paraboloidal and hyperboloidal conductors, which were frequently used as early models for field emitters [55], the surface electric field can be analytically expressed in terms of the 0.25th power of Gaussian curvature, $\kappa_G = \frac{1}{R_1 R_2}$ [129]. Therefore, κ_G might prove a better approximation than κ_M.

3.5.2 The Boundary Element Method

It will become clear in Section 4, as well as from previous studies' results [79, 80], that curvature flow is incapable of accurately modelling general specimen evaporation. Curvature flow also does not provide the electric field in the surrounding vacuum that's needed for ion trajectory calculation. Therefore, accurate calculation of both local evaporation and ion trajectories requires evaluation of the electric field. Previous APT experiments have used both domain-based [130, 62, 66] and boundary integral [64] solvers. Boundary integral methods have the advantage of solving the electric field only where required, i.e. the specimen surface and specific domain points during trajectory integration, and also only require meshing of the problem boundary rather than the entire computational domain. As a result, their computational complexity depends only on the size of the boundary rather than the domain. Boundary integral approaches can efficiently solve system electrostatics over the vast length scale differences in APT. For these reasons, a boundary integral approach has been opted for, with the electric field being solved via a direct boundary element method (as opposed to indirect formulations [131]).

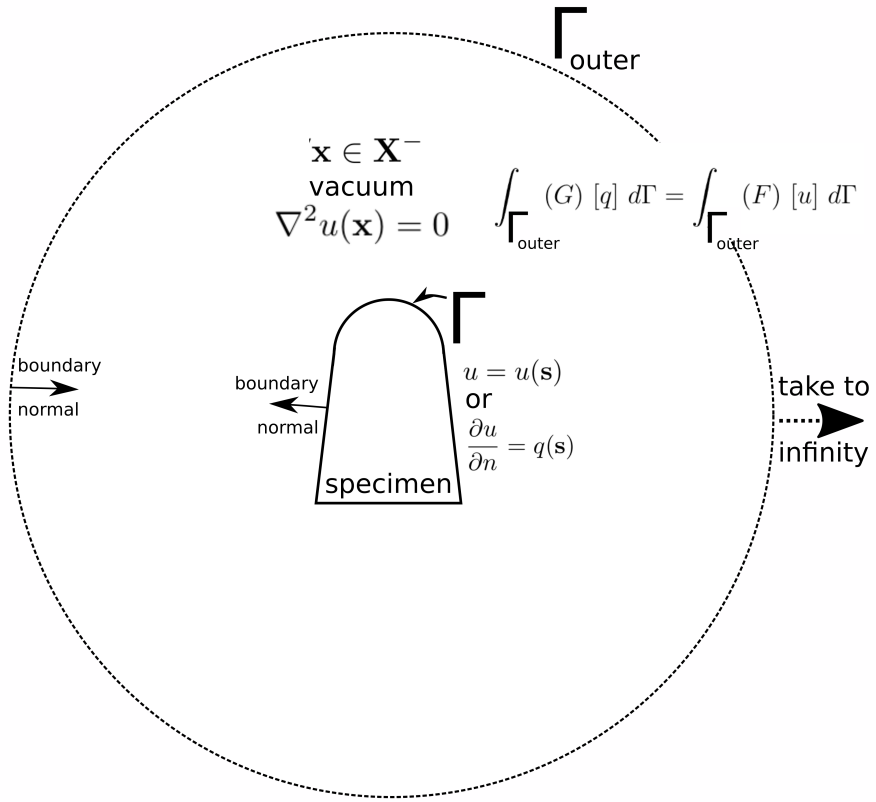


Figure 21: Diagram showing the electrostatic problem within the vacuum domain $\mathbf{X}^-$. The inner boundary represents the specimen surface. The outer boundary is taken away to infinity during the boundary integral formulation.

The direct boundary element method formulation starts by rearrangement of Laplace's equation with mixed boundary conditions (Eq. (45)). The electrostatic problem is visualised in Figure 21.

$$\nabla^2 u(\mathbf{x}) = 0 \qquad \forall \mathbf{x} \in \mathbf{X}^- \tag{45}$$

$$u = u(\mathbf{s}) \quad \mathbf{s} \in \Gamma_D \tag{46}$$

$$\frac{\partial u}{\partial n} = q(\mathbf{s}) \quad \mathbf{s} \in \Gamma_N \tag{47}$$

Here $\mathbf{X}^-$ is the open domain for the free space electrostatics problem bounded by Γ, Γ_D is the boundary subset of Γ over which Dirichlet boundary conditions apply, Γ_N is the subset over which Neumann boundary conditions apply, and $\frac{\partial}{\partial n}$

implies the directional derivative on the surface normal to the boundary Γ. For the following derivation we consider the Green's function to Laplace's equation:

$$\nabla^2 G(\mathbf{x}, \mathbf{y}) = -\delta(\mathbf{x} - \mathbf{y}) \tag{48}$$

$$G(\mathbf{x}, \mathbf{y}) = -\frac{1}{2\pi} \log(||\mathbf{x} - \mathbf{y}||) \quad \text{for two dimensions} \tag{49}$$

$$G(\mathbf{x}, \mathbf{y}) = \frac{1}{4\pi ||\mathbf{x} - \mathbf{y}||} \quad \text{for three dimensions} \tag{50}$$

The boundary integral derivation proceeds by multiplying Eq. (48) by a test function $\psi \in C^2$, and integrating $\mathbf{y}$ over $\mathbf{X}^-$ to give Eq. (51). Here C^2 refers to second-degree smoothness (the set of functions with well-defined second derivatives). Integration by parts is then performed twice, giving Eq. (53). Finally, the divergence theorem is applied to give Eq. (54).

$$\int_{\mathbf{X}^-} \psi(\mathbf{y})\ \nabla^2 G(\mathbf{x}, \mathbf{y})\ d^3\mathbf{y} = -\psi(\mathbf{x}) \qquad \psi \in C^2 \tag{51}$$

$$\int_{\mathbf{X}^-} \nabla \cdot (\psi(\mathbf{y}) \nabla G(\mathbf{x}, \mathbf{y}))\ d^3\mathbf{y} - \int_{\mathbf{X}^-} \nabla \psi(\mathbf{y}) \cdot \nabla G(\mathbf{x}, \mathbf{y})\ d^3\mathbf{y} = -\psi(\mathbf{x}) \tag{52}$$

$$\int_{\mathbf{X}^-} \nabla \cdot (\psi(\mathbf{y}) \nabla G)\ d^3\mathbf{y} - \int_{\mathbf{X}^-} \nabla \cdot (\nabla \psi(\mathbf{y}) \cdot G)\ d^3\mathbf{y} + \int_{\mathbf{X}^-} \nabla^2 \psi(\mathbf{y}) \cdot G\ d^3\mathbf{y} = -\psi(\mathbf{x}) \tag{53}$$

$$\int_{\Gamma} (\psi(\mathbf{y})\ \nabla G) \cdot d\Gamma(\mathbf{y}) - \int_{\Gamma} (G\ \nabla \psi(\mathbf{y})) \cdot d\Gamma(\mathbf{y}) + \int_{\mathbf{X}^-} \nabla^2 \psi(\mathbf{y})\ G\ d^3\mathbf{y} = -\psi(\mathbf{x}) \tag{54}$$

As ψ can be any C^2 function, we are free to choose ψ such that it is harmonic, i.e. satisfies Eq. (45). Therefore, by assigning ψ to be the electric potential (u), we arrive at a boundary integral equation for Laplace's equation.

$$u(\mathbf{x}) = \int_\Gamma G(\mathbf{x},\mathbf{y})\frac{\partial u(\mathbf{y})}{\partial n}d\Gamma(\mathbf{y}) - \int_\Gamma \frac{\partial G(\mathbf{x},\mathbf{y})}{\partial n}u(\mathbf{y})d\Gamma(\mathbf{y}) \quad \forall \mathbf{x} \in \mathbf{X}^-, \mathbf{y} \in \Gamma \quad (55)$$

The Eq. (55) holds only for interior problems within a closed boundary. However, in our problem, the problem domain $\mathbf{X}^-$ (the vacuum) is bounded only by the specimen surface (excluding the instrument chamber). A boundary integral equation for this exterior problem can be derived, given in Eq. (56), by considering an outer boundary (Γ_{outer}) that is taken outward to infinity, where its associated integral vanishes (see Appendix B).

$$u(\mathbf{x}) = \int_\Gamma \frac{\partial G(\mathbf{x},\mathbf{y})}{\partial n}u(\mathbf{y})d\Gamma(\mathbf{y}) - \int_\Gamma G(\mathbf{x},\mathbf{y})\frac{\partial u(\mathbf{y})}{\partial n}d\Gamma(\mathbf{y}) \qquad \forall \mathbf{x} \in \mathbf{X}^-, \mathbf{y} \in \Gamma \quad (56)$$

So far only the solution at points $\mathbf{x} \in \mathbf{X}^-$ has been considered (note that $\mathbf{X}^-$ is open and does not include Γ). However, a modified equation can be derived which holds on the boundary [132] where instead $\mathbf{x} \in \Gamma$. In the case where Γ is smooth at $\mathbf{x}$, the integral equation valid at the boundary is Eq. (57).

$$-\frac{3}{2}u(\mathbf{x}) + \int_\Gamma \frac{\partial G(\mathbf{x},\mathbf{y})}{\partial n}u(\mathbf{y})d\Gamma(\mathbf{y}) = \int_\Gamma G(\mathbf{x},\mathbf{y})\frac{\partial u(\mathbf{y})}{\partial n}d\Gamma(\mathbf{y}) \quad \forall \mathbf{x}, \mathbf{y} \in \Gamma \quad (57)$$

Together Eq. (56) and Eq. (57) make up the boundary integral equations used in formulating the direct boundary element method. Following surface discretisation into k panels $\Gamma_i \subset \Gamma$, a constant panel collocation scheme [131] is invoked. Here Eq. (57) is enforced at the centre point of each panel (x_i), with u and q taken to be piecewise constant over each Γ_i. Defining u_j and q_j to be the constant potential and normal flux on Γ_j, we arrive at Eq. (58).

$$\sum_{j}^{k} u_j \underbrace{\Big[-\frac{3}{2}\,\delta_{ij} + \int_{\Gamma_j} \frac{\partial G(\mathbf{x}_i, \mathbf{y})}{\partial n}\, d\Gamma(\mathbf{y}) \Big]}_{F_{ij}} = \sum_{j}^{k} q_j \underbrace{\Big[\int_{\Gamma_j} G(\mathbf{x}_i, \mathbf{y})\, d\Gamma(\mathbf{y}) \Big]}_{P_{ij}} \quad \forall i \in (1, k) \tag{58}$$

$$\sum_{j}^{k} F_{ij} u_j = \sum_{j}^{k} P_{ij} q_j \quad \forall i \in (1, k) \tag{59}$$

Here δ_{ij} is the Kronecker delta. The Eq. (59) describes a matrix equation relating $\mathbf{u}$ and $\mathbf{q}$ in Eq. (60).

$$\mathbf{F} \cdot \mathbf{u} = \mathbf{P} \cdot \mathbf{q} \tag{60}$$

The term $\mathbf{F}$ corresponds to a $k \times k$ matrix populated by elements F_{ij}, $\mathbf{P}$ is a $k \times k$ matrix populated by P_{ij}, $\mathbf{u}$ is the length-k vector of panel potentials u_j, and $\mathbf{q}$ is a length-k vector of panel fluxes q_j. The exact form of F_{ij} and P_{ij} depends on the discretised boundary geometry. In 2D, the analytical solutions for these matrix elements are relatively straightforward, given in Eq. (61) and Eq. (62).

$$F_{ij} = F(\mathbf{x}_i, \mathbf{y}_j) = -\frac{1}{2\pi}\Big(\arctan(\frac{s_b}{n}) - \arctan(\frac{s_a}{n})\Big) \tag{61}$$

$$\begin{aligned} P_{ij} = P(\mathbf{x}_i, \mathbf{y}_j) = -\frac{1}{4\pi}\Big(& s_b\, (\ln(n^2 + s_b^2) - 2) + 2n \arctan(\frac{s_b}{n}) \\ & - s_a\, (\ln(n^2 + s_a^2) - 2) - 2n \arctan(\frac{s_a}{n})\Big) \end{aligned} \tag{62}$$

Here the scalars (n, s_a, s_b) define a local coordinate system in Eq. (63), dependent on the field coordinate $\mathbf{x}_i$, and panel Γ_j on which the node $\mathbf{y}_j$ is centred.

$$
\begin{aligned}
n &= \frac{1}{||\mathbf{y}_j^R - \mathbf{y}_j^L||} \begin{vmatrix} (\mathbf{x} - \mathbf{y}_j^R)_y & (\mathbf{x} - \mathbf{y}_j^R)_y \\ (\mathbf{y}_j^L - \mathbf{y}_j^R)_x & (\mathbf{y}_j^L - \mathbf{y}_j^R)_y \end{vmatrix} \\
s_a &= \frac{(\mathbf{x} - \mathbf{y}_j^L) \cdot (\mathbf{y}_j^L - \mathbf{y}_j^R)}{||\mathbf{y}_j^R - \mathbf{y}_j^L||} \\
s_b &= \frac{(\mathbf{x} - \mathbf{y}_j^R) \cdot (\mathbf{y}_j^L - \mathbf{y}_j^R)}{||\mathbf{y}_j^R - \mathbf{y}_j^L||}
\end{aligned} \tag{63}
$$

The terms $\mathbf{y}_j^L$ and $\mathbf{y}_j^R$ define the coordinate vectors of the left-hand and right-hand corners of panel segment Γ_j, $|...|$ is the matrix determinant, and $||...||$ is the Euclidean norm. These local panel coordinates are visualised in Figure 22a. The matrix elements corresponding to a pair of surface panels are shown in Figure 22b.

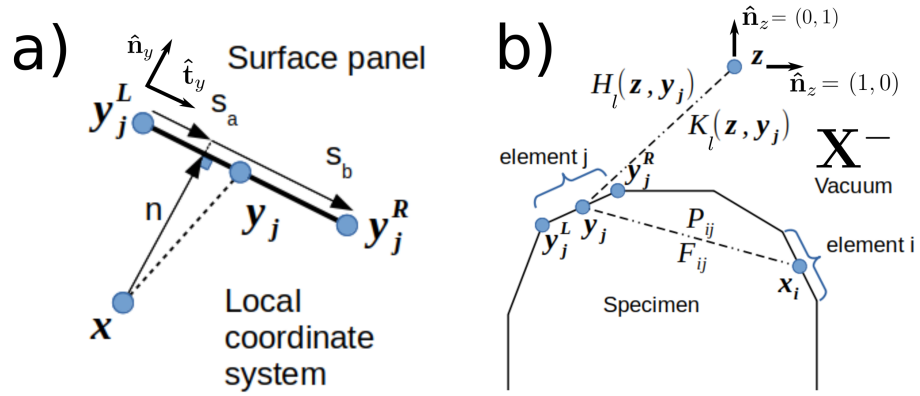


Figure 22: Diagrams outlining the 2D BEM. (a) Shows the local coordinate system in Eq. (63) for a particular surface panel with centre $\mathbf{y}_j$. (b) Shows the matrix elements and integration associated with a panel pairing, and a domain evaluation. Adapted from [133].

In 3D, the analytical forms of P_{ij} and F_{ij} are more complicated. Formulas for the diagonal elements can be found in Appendix C. The off-diagonal elements are calculated numerically via a 7-point integration scheme described in Appendix D [134]. Such numerical integration is more computationally efficient than analytical solutions in 3D [135]. Particular matrix element calculations for an example mesh is illustrated in Figure 23.

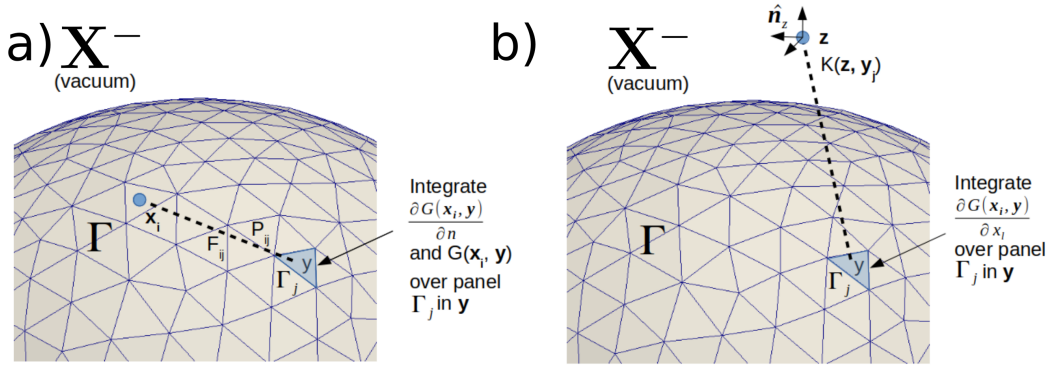


Figure 23: Diagrams outlining the 3D BEM. (a) Shows the matrix element integration between two surface panels. (b) Shows the integral calculation between a panel pairing, and a field evaluation at domain point $\mathbf{z}$. Adapted from [136].

While Eq. (56) allows for calculation of u within $\mathbf{X}^-$, in order to calculate ion trajectories it is the electric field $\mathbf{E}(\mathbf{z})$ that is required. This can be determined directly through the hypersingular boundary integral equations in Eq. (64).

$$E_l = \frac{\partial u(\mathbf{z})}{\partial x_l} = \int_\Gamma \frac{\partial^2 G(\mathbf{z},\mathbf{y})}{\partial n\, \partial z_l} u(\mathbf{y}) d\Gamma(\mathbf{y}) - \int_\Gamma \frac{\partial G(\mathbf{z},\mathbf{y})}{\partial z_l} \frac{\partial u(\mathbf{y})}{\partial n} d\Gamma(\mathbf{y}) \tag{64}$$

$$\forall \mathbf{z} \in \mathbf{X}^-, \mathbf{y} \in \Gamma \text{ and } l \in \{1,2,3\} \quad \text{where } \mathbf{E} = (E_1, E_2, E_3) \quad \mathbf{z} = (z_1, z_2, z_3)$$

Again, the exact form of the integration kernels depends on the boundary geometry and problem dimensionality. In 2D, these integrals are efficiently calculated by the analytical expressions in Eqs. (65 - 67).

$$H_l(\mathbf{z},\mathbf{y}_j) = \int_{\Gamma_j} \frac{\partial^2 G(\mathbf{z},\mathbf{y})}{\partial n\ \partial z_l} d\Gamma(\mathbf{y}) \tag{65}$$

$$= -\frac{1}{2\pi}\Bigg[\Big(\frac{sa}{n^2+sa^2} - \frac{sb}{n^2+sb^2}\Big)\hat{\mathbf{n}}_y \cdot \hat{\mathbf{n}}_z + \Big(\frac{n}{n^2+sb^2} - \frac{n}{n^2+sa^2}\Big)\hat{\mathbf{t}}_y \cdot \hat{\mathbf{n}}_z\Bigg]$$

$$K_l(\mathbf{z},\mathbf{y}_j) = \int_{\Gamma_j} \frac{\partial G(\mathbf{z},\mathbf{y})}{\partial z_l} d\Gamma(\mathbf{y}) \tag{66}$$

$$= -\frac{1}{2\pi}\Bigg[\Big(\arctan(\frac{s_b}{n}) - \ \arctan(\frac{s_a}{n})\Big)\hat{\mathbf{n}}_y \cdot \hat{\mathbf{n}}_z - \Big(\frac{1}{2}\ln(n^2+s_b^2) + \frac{1}{2}\ln(n^2+s_a^2)\Big)\hat{\mathbf{t}}_y \cdot \hat{\mathbf{n}}_z\Bigg]$$

$$\frac{\partial u}{\partial z_l} = \sum_j^k H_l(\mathbf{z},\mathbf{y}_j)u_j - \sum_j^k K_l(\mathbf{z},\mathbf{y}_j)q_j \tag{67}$$

Here $\hat{\mathbf{n}}_y$ is the normalised normal vector of panel Γ_j, $\hat{\mathbf{t}}_y = \frac{\mathbf{y}_j^R - \mathbf{y}_j^L}{||\mathbf{y}_j^R - \mathbf{y}_j^L||}$ is the normalised tangent vector of panel Γ_j, and $\hat{\mathbf{n}}_z$ is the normalised normal vector of the desired field component at $\mathbf{z}$.

In 3D, the boundary integral components are numerically integrated via the 7-point integration scheme (Appendix D). However, in 3D only panels close to domain point $\mathbf{x}$ will be evaluated directly, whilst panels further from $\mathbf{x}$ are grouped and evaluated in clusters (Section 3.5.8). This clustering approach reduces the total operations required.

The takeaway results are a matrix equation (Eq. (60)) relating surface panel potentials to fluxes, and integral equations that can calculate the electric field at arbitrary points in the vacuum (Eqs. 64). However, as the locally known problem boundary conditions are either the potential or flux, this matrix equation must be solved prior to vacuum field point evaluations.

3.5.3 Solving the Boundary Matrix Equation

In the previous section, a matrix equation relating the boundary potential ($\mathbf{u}$) and normal electric field flux ($\mathbf{q}$) was constructed (Eq. (68)).

$$\mathbf{F} \cdot \mathbf{u} = \mathbf{P} \cdot \mathbf{q} \tag{68}$$

Here $\mathbf{F}$ and $\mathbf{P}$ are the problem matrices depending on the boundary. As will be seen, regardless of any mixed boundary conditions, Eq. (68) can be rearranged into a linear system (Eq. (69)).

$$\mathbf{A} \cdot \mathbf{x} = \mathbf{b} \tag{69}$$

Here $\mathbf{A}$ is the rearranged problem matrix, $\mathbf{x}$ is the desired solution vector (a mix of the unknown $\mathbf{u}$ and $\mathbf{q}$ elements), and $\mathbf{b}$ is the loading vector (a mix of the $\mathbf{u}$ and $\mathbf{q}$ elements fixed by the boundary condition). While Eq. (69) can be solved directly via lower-upper (LU) decomposition, direct methods requires $O(k^3)$ arithmetic operations for an $k \times k$ system. A faster iterative method for solving the linear system of type Eq. (69) is the generalised minimal residual method (GMRES). In comparison to LU decomposition, the GMRES algorithm solves the same system in $O(mk^2)$ arithmetic operations, where m is the required number of iterations to achieve convergence. Here m can be reduced by appropriate preconditioning [137].

$$\boldsymbol{\mathcal{P}}^{-1} \cdot \mathbf{A} \cdot \mathbf{x} = \boldsymbol{\mathcal{P}}^{-1} \cdot \mathbf{b} \tag{70}$$

The BEM problem matrices are dense and diagonally dominant (with diagonal

elements representing panel self-interactions). An appropriate preconditioner for such systems is the Jacobi preconditioner, with matrix elements given by $\mathcal{P}_{ij}^{-1} = \frac{\delta_{ij}}{A_{ij}}$. Using the Jacobi preconditioner reduced the convergence time by around 50% for practical system sizes in the 3D model (Figure 24).

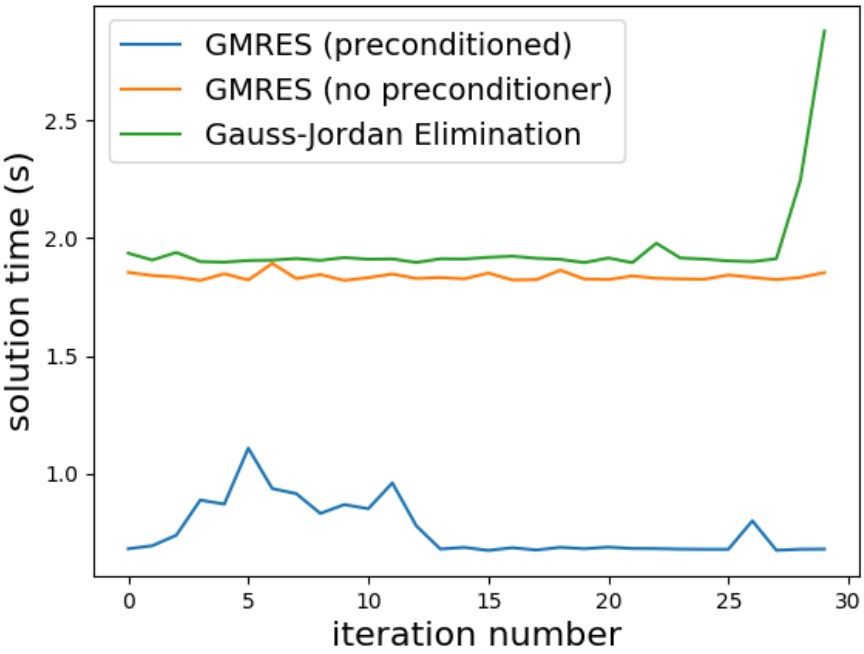


Figure 24: Comparison of LU decomposition, non-preconditioned GMRES, and preconditioned GMRES for the same 5434×5434 linear system. Such a system size is typical of the 3D model. The pre-conditioned GMRES used a Jacobi preconditioner. In this work, the GMRES implementation in the Python package *Scipy* has been used.

3.5.4 Conductor Model

The electrostatic problem in Eq. (39) can be simplified by assuming the specimen behaves as a conductor, such that its surface is equipotential (constant u). In this case, the electrostatic problem simplifies to Laplace's Equation (Eq. (45)) over the domain $\mathbf{X}^-$ (vacuum) with the Dirichlet boundary condition $u_j = V(t) \quad \forall u_j \in \mathbf{u}$. This can be solved using the boundary element method outlined in Section 3.5.2. The resulting linear system is given in Eq. (71).

$$\underbrace{\mathbf{P}}_{\mathbf{A}} \cdot \underbrace{\mathbf{q}}_{\mathbf{x}} = \underbrace{\mathbf{F} \cdot (\mathbf{1}V)}_{\mathbf{b}} \tag{71}$$

In the case where Γ is a closed surface, the following integral identity holds [138]:

$$\mathbf{w} \cdot \int_C \nabla \left(\frac{\partial G(\mathbf{x}, \mathbf{y})}{\partial n} \right) d\Gamma(\mathbf{y}) = 0 \tag{72}$$

Here $\mathbf{w}$ is an arbitrary direction vector. Therefore, the first integral term in Eqs. 64 vanishes as long as the boundary is equipotential.

Typical insulator dielectric breakdown voltages are around three orders of magnitude less than the surface fields reached during APT [139], suggesting that the conductor approximation could also be reasonable for dielectrics. However, a study by Oberdorfer et al. [63] implies there might be some sort of dielectric field enhancement effects. While further experimental research is required to validate to what extent the classical electrostatic approximation for dielectrics holds in APT, having the flexibility to extend the BEM framework to incorporate dielectric and other nonlinear effects is an important prerequisite.

3.5.5 Incorporating Dielectric Phases

To account for dielectric phases, the specimen surface can no longer be assumed equipotential, and the electrostatics must be solved both inside and outside of the specimen. The specimen base is held at a constant voltage ($u_{\text{tip}} = V$). In order to solve this system, a FEM-BEM coupling scheme has been implemented [140]. Here the internal solution is solved via a Finite Element Method (FEM), coupled to a BEM at the specimen surface that handles the solution in the vacuum. The FEM-BEM approach is more flexible than alternative multidomain BEM methods [141], and so is better equipped to handle any future nonlinear extensions [142]. The problem setup is in Figure 25.

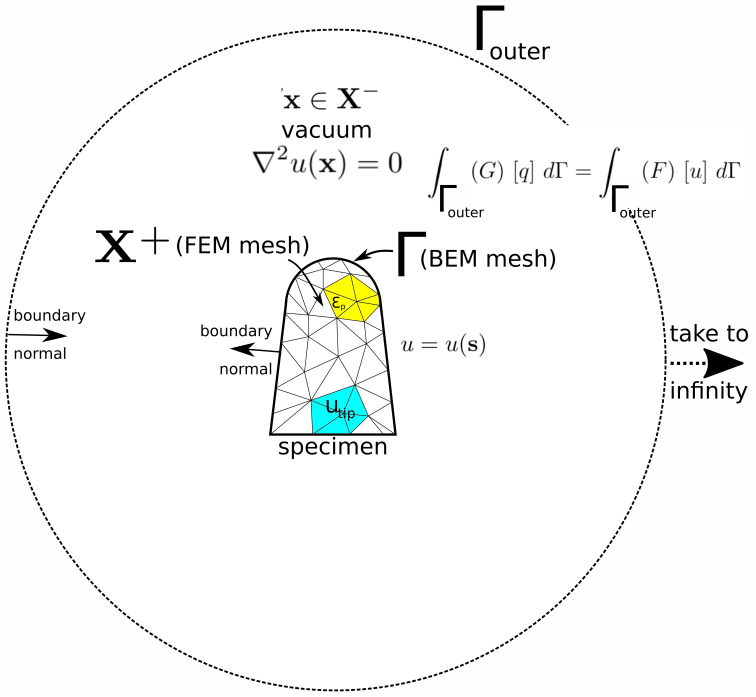


Figure 25: Diagram showing the setup for the full electrostatic solution over $\mathbf{X} = \mathbf{X}^+ \cup \Gamma \cup \mathbf{X}^-$. The example specimen contains a precipitate with dielectric constant ϵ_p.

Unlike the collocation BEM in Section 3.5.2, the FEM is typically discretised from the weak form of Poisson's equation [143]. To obtain this formulation, Eq. (39) is rearranged into the weak form through multiplication by some arbitrary function, and then integrating over its domain.

$$\int_{\mathbf{X}^+} \nu(\mathbf{x})\ \nabla \cdot (\epsilon(\mathbf{x})\nabla u(\mathbf{x}))\ d^2\mathbf{x} = 0$$

$$\int_{\mathbf{X}^+} \epsilon(\mathbf{x})\ \nabla\nu(\mathbf{x}) \cdot \nabla u(\mathbf{x})\ d^2\mathbf{x} = \int_{\mathbf{X}^+} \nabla \cdot (\nu(\mathbf{x})\ \epsilon(\mathbf{x})\nabla u(\mathbf{x})) \cdot d^2\mathbf{x} \tag{73}$$

$$\int_{\mathbf{X}^+} \epsilon(\mathbf{x})\ \nabla\nu(\mathbf{x}) \cdot \nabla u(\mathbf{x})\ d^2\mathbf{x} = \int_{\Gamma} \nu(\mathbf{x})\ \epsilon(\mathbf{x})\nabla u(\mathbf{x}) \cdot d\Gamma \tag{74}$$

where $\nu(\mathbf{x})$ is some arbitrary test function, $\mathbf{X}^+ \equiv \mathbf{\Omega}^+$ is the FEM problem domain (inside specimen), and Γ is the domain boundary (specimen surface). Here Eq. (73) is obtained via the product rule, and Eq. (74) obtained by invoking the divergence theorem.

Proceeding with Galerkin discretisation [143], the domain is divided into 2D triangle elements with nodes at element corners. This triangle mesh is constructed such that BEM elements conform with FEM element edges on the boundary (Appendix E). Using triangle basis functions centred on these corner FEM nodes, a linear system can be obtained (Eq. (75)).

$$\mathbf{A}' \cdot \mathbf{u}^{\text{fem}} = \mathbf{b} \tag{75}$$

Here $\mathbf{u}^{\text{fem}} = (\mathbf{u}^{\text{fem}}_{\mathbf{X}^+}, \mathbf{u}^{\text{fem}}_{\Gamma})$, where $\mathbf{u}^{\text{fem}}_{\mathbf{X}^+}$ is the set of interior FEM node potentials, and $\mathbf{u}^{\text{fem}}_{\Gamma}$ is the set of FEM boundary (specimen surface) node potentials. Derivation of Eq. (75) can be found in Appendix E. The boundary normal fluxes can then be calculated by solving Eq. (76).

$$\mathbf{P} \cdot \mathbf{q}^{\text{bem}} = \mathbf{F} \cdot \mathbf{T} \cdot \mathbf{u}^{\text{fem}}_{\Gamma} \tag{76}$$

The interpolation matrix $\mathbf{T}$ is defined in Appendix E. Due to uncertainty regarding the physics of dielectric phases in APT, the coupling has only been implemented in 2D to serve as proof-of-concept. Previous APT studies have found that classical electrostatics fails to correctly capture APT dielectric behaviour due

to high voltages and laser interactions [144, 145, 146, 147]. However, the wide applicability of FEM implies that with discretisation of the correct physics, fast and accurate modelling of dielectrics could be possible through such a coupling framework.

3.5.6 Solving the FEM-BEM Coupled System

In order to calculate $\mathbf{q}^{\text{bem}}$, first $\mathbf{u}^{\text{fem}}$ must be solved. This requires solving the coupled system in Eq. (75). Similar to the BEM in Section 3.5.3, there exist a number of applicable numerical solvers. The non-symmetric problem matrix $\mathbf{A}'$ contains a dense block associated with BEM, as well as a symmetric sparse block associated with FEM. These submatrices can be decoupled and iteratively solved using specialised solvers (GMRES for BEM and the conjugate gradient method for FEM) [140]. However, as efficiency was not a problem in 2D, the total coupled system has typically been solved via LU decomposition.

3.5.7 Calculating Ion Trajectories

To compare model results with experiment, evaporated ion trajectories must be calculated. These are described via Eq. (77).

$$\frac{d^2\mathbf{z}}{dt^2} = \frac{ne}{m}\,\mathbf{E}(\mathbf{z}) \tag{77}$$

Here $\mathbf{z} \in \mathbf{X}^-$ is the ion's position. This can be rewritten as a system of first-order equations:

$$\begin{bmatrix} \frac{d\mathbf{v}}{dt} \\ \frac{d\mathbf{z}}{dt} \end{bmatrix} = \begin{bmatrix} \frac{ne}{m} & 0 \\ 0 & 1 \end{bmatrix} \cdot \begin{bmatrix} \mathbf{E}(\mathbf{z}) \\ \mathbf{v} \end{bmatrix} \tag{78}$$

Here m is the ion's mass, $\mathbf{E}(\mathbf{z})$ is the electric field, ne is the ion's charge, and

$\mathbf{v}$ is its velocity.

In this work, trajectories have been calculated from Eq. (78) via a fifth-order Runge-Kutta (RK5) adaptive scheme [148]. Throughout trajectory integration, $\mathbf{E}(\mathbf{x})$ is determined through evaluation of Eq. (64). The integrator time step is determined adaptively within a user-defined error tolerance. Integration of a trajectory continues until intersection with the detector or simulation bounding box.

A property of Eq. (77) is that for a rescaling of the mass-to-charge-state (m-c) ratio $\frac{ne}{m} \rightarrow a\frac{ne}{m}$, the original differential equation can be obtained under the time reparameterisation $t \rightarrow t'$, where $t' = a^{-\frac{1}{2}}t$ and a is a rescaling constant. Therefore, assuming an initial velocity $\mathbf{v} = \mathbf{0}$, the exact path of ion trajectories should be independent of m-c, with trajectories only needing to be calculated for one particular value of m-c. The implication is that the same calculated trajectories can be applied regardless of m-c. While chromatic aberrations can occur in experiment, these are understood to be due to atomic-scale surface evaporation ordering effects of the emitter rather than charged optics [149]. Such effects cannot be captured through continuum scale modelling alone.

In order to calculate ion trajectories, the electric field $\mathbf{E}(\mathbf{z})$ must be evaluated via Eq. (64) at each RK5 integrator iteration. While it turns out that performing the required number of evaluations for accurate trajectory calculations is computationally slow, a clustering method described in Section 3.5.8 allows for its acceleration, ensuring practical computation times.

3.5.8 Acceleration via Panel Clustering

When calculating ion trajectories, the electric field must be evaluated at multiple points $\mathbf{z}$ for each integrator step. These evaluations are performed by calculating the integrals in Eq. (64). Practically, direct evaluation of these integrals through a standard quadrature scheme (Appendix D) is slow, taking hours for surface projection off specimen apices with ion launch positions spaced $1 - 4$ nm apart.

This evaluation can be accelerated by leveraging approximate group solutions for clusters of adjacent panels. Such a panel clustering method was first described by Hackbusch et al. [150]. The method proceeds by initially determining cluster candidates using an octree grid structure [151]. Coefficients for a finite series approximating the solution of these clusters are then calculated. When evaluating a particular field point, panel clusters are selected to reduce the required number of clusters within a given error tolerance. Panels sufficiently close to the field point $\mathbf{z}$ are computed exactly without approximation. Each cluster's approximating finite series is obtained from a truncated multipole expansion [152]. The series converges to the true solution as the distance between the cluster centre and the field point increases (with truncated higher-order terms more rapidly tending to zero). An example panel cluster consisting of four surface panels is illustrated in Figure 26.

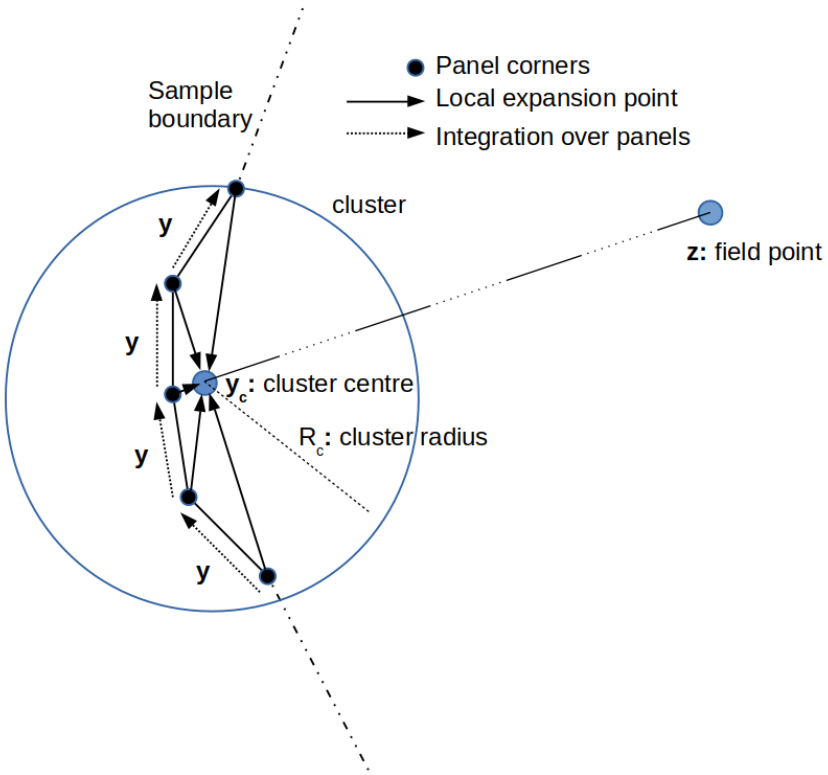


Figure 26: Diagram showing how a particular group of panels contained within a cluster of radius R_c and centre point $\mathbf{y}_c$ can be approximated by a local expansion around $\mathbf{y}_c$. Reprinted from C. Fletcher, M. P. Moody, and D. Haley. Journal of Physics D: Applied Physics, 53(475303), 2020., with the permission of IOP Publishing.

Each cluster has an associated centroid $\mathbf{y}_c$ (centre averaged position) and enclosing sphere radius R_c. Let C_{Γ^c} be the unique set of panel corner points within the cluster Γ^c. The cluster's centroid and radius can be defined by Eqs. (79) and (80).

$$\mathbf{y}_c = \frac{1}{N_{\Gamma^c}} \sum_{i}^{C_{\Gamma^c}} \mathbf{v}_i, \quad \mathbf{v}_i \in C_{\Gamma^c} \tag{79}$$

$$R_c = \max_{C_{\Gamma^c}} ||\mathbf{v}_i - \mathbf{y}_c||, \quad \mathbf{v}_i \in C_{\Gamma^c} \tag{80}$$

Here $\mathbf{v}_i$ is a panel corner point, and N_{Γ^c} is the number of cluster panels. The radius R_c defines the minimum sphere around the centroid that includes all of

the cluster's panels.

Our implementation proceeds by first building the octree in space. This is constructed recursively, with parent nodes being equally split into eight children nodes. Panels which have centres' falling within a particular octree node are grouped into a cluster candidate (Γ^c) associated with that node. A tree node is no longer split once its associated cluster size falls below a user-defined panel number (M_c). Such nodes are known as the tree's leaf nodes. A visualisation of octree nodes with $M_c = 1$ for a typical specimen mesh is shown in Figure 27.

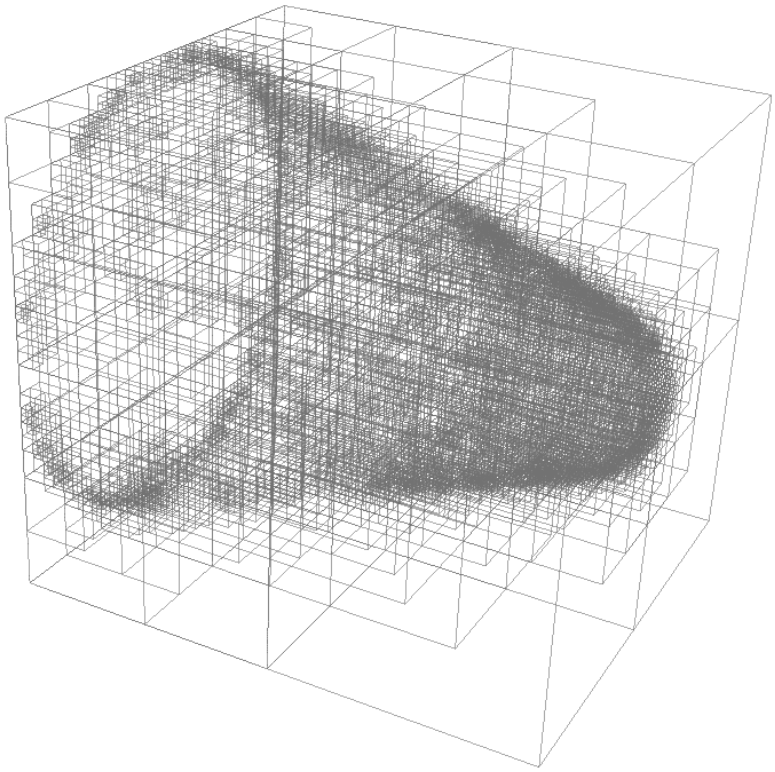


Figure 27: Octree visualisation for a typical specimen mesh.

During field evaluations, the octree will be traversed in a downward pass (recursively from the top (root) to the bottom (leaf) nodes), and a particular cluster grouping will be determined for efficiently calculating Eq. (64). This cluster group defines a partition of the boundary element panels (P_Γ), such that every panel in the specimen surface must be in exactly one cluster of the grouping. In order to

construct this clustering, the clusters associated with nodes are checked against the admissibility criterion $||\mathbf{z}-\mathbf{y}_c||\epsilon_t > R_c$, where ϵ_t is a user-defined parameter ($\epsilon_t = 0.1$ has been used). As will be seen, this criterion is used to assess the validity of the cluster's approximating series. On successfully passing the criterion, the cluster candidate is described as being admissible and appended to the cluster grouping. On failing the criterion, the algorithm proceeds down the octree to check the admissibility of its children nodes' clusters. The downward pass terminates once each surface panel is contained within exactly one cluster in the assembled grouping, i.e. satisfies Eqs. (81).

$$\bigcup_{c}^{P_\Gamma} \Gamma^c = \Gamma \tag{81}$$

$$\Gamma^c \cap \Gamma^\nu = \Phi \quad \forall \Gamma^c, \Gamma^\nu \in P_\Gamma \qquad \text{where } c \neq \nu$$

With Φ being the null set. For a particular panel partitioning P_Γ, the solution to Eq. (64) can be split into a number of partial sums associated with each cluster (Eqs. (82)). The aim is to find approximate series solutions for these partial sums that hold in the far-field regime $||\mathbf{z}-\mathbf{y}_c|| >> R_c$. These approximate truncated multipole series are denoted by $M_l(\mathbf{z}, \mathbf{y}_c, R_c)$ (Eqs. (82) and (83)). The exact form of $M_l(\mathbf{z}, \mathbf{y}_c, R_c)$ is derived in Appendix F.

$$E_l(\mathbf{z}) = -\frac{1}{4\pi}\sum_{j}^{k} q_j \int_{\Gamma_j} \frac{\partial G(\mathbf{z},\mathbf{y})}{\partial z_l} d^2\mathbf{y} = -\frac{1}{4\pi}\sum_{\Gamma^c}^{P_\Gamma}\left[\sum_{j}^{\Gamma^c}\int_{\Gamma_j}\frac{\partial G(\mathbf{z},\mathbf{y})}{\partial z_l} q_j d^2\mathbf{y}\right] \tag{82}$$

$$\sum_{j}^{\Gamma^c}\int_{\Gamma_j}\frac{\partial G(\mathbf{z},\mathbf{y})}{\partial z_l} q_j d^2\mathbf{y} \approx M_l(\mathbf{z}, \mathbf{y}_c, R_c) \quad \text{for } ||\mathbf{z}-\mathbf{y}_c|| > \frac{R_c}{\epsilon_t} \tag{83}$$

$$\text{where } l \in \{1,2,3\} \quad \mathbf{E} = (E_1, E_2, E_3) \quad \mathbf{z} = (z_1, z_2, z_3)$$

Critically the series coefficients for $M_l(\mathbf{z}, \mathbf{y}_c, R_c)$ are independent of the field

point $\mathbf{z}$, and can be precomputed. Therefore, the same expansion can be used to compute the field at multiple positions, without having to re-evaluate the series coefficients (Appendix F).

The series coefficients are calculated prior to ion projection via an upward octree pass (from leaf nodes up to root node). The series expansion coefficients in Appendix F are solved via the integration scheme in Appendix D. Calculation of the series coefficients has a combined computational complexity of $\mathcal{O}(k \cdot log(k))$, where k is the total number of mesh panels.

Once this octree has been constructed and coefficients calculated, the ion trajectory calculation step is undertaken. During this stage, Eq. (64) must be solved at points determined sequentially by the previous step of the trajectory integrator. The partial sums of any leaf node clusters in the partition are directly evaluated by summing and integrating over cluster panels. Meanwhile, the partial sums of non-leaf node clusters are calculated by its approximate truncated multipole series. An example partitioning of panels for a particular field point $\mathbf{z}$ is illustrated for a simplified 2D quadtree case in Figure 28.

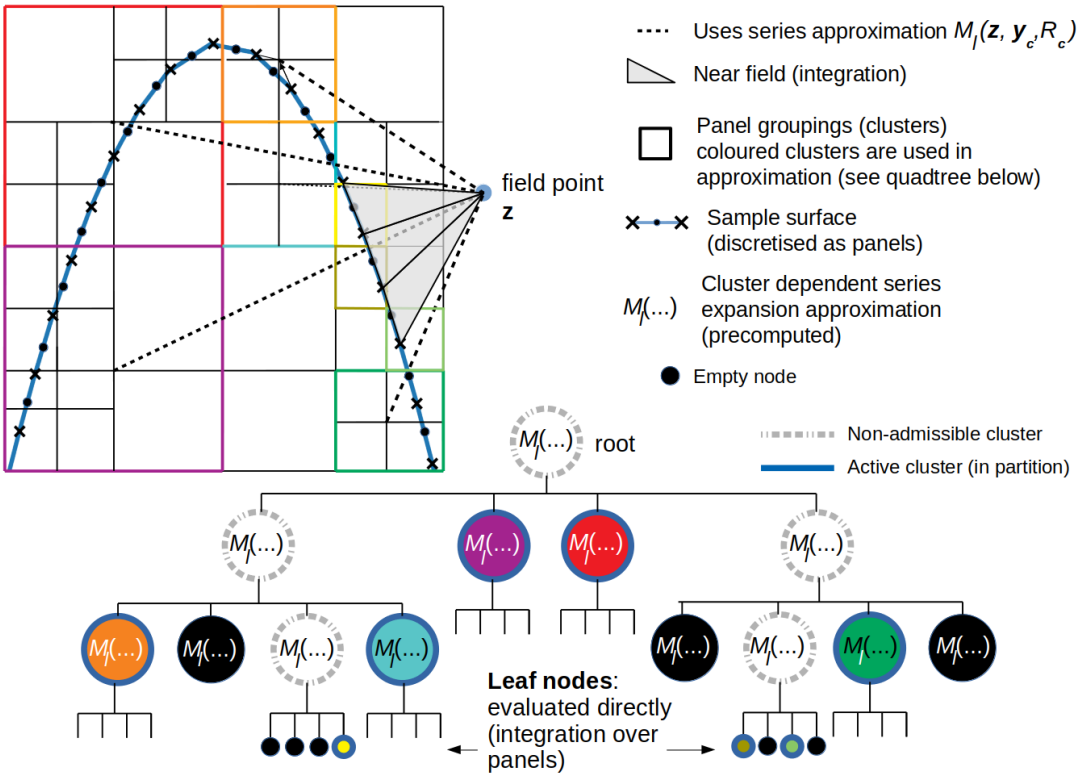


Figure 28: 2D clustering example showing nodes contained in a particular partition. Coloured tree nodes show the clusters used in the field evaluation at point **z**. The integrals for panels in leaf node clusters are directly evaluated. Modified from [136].

Direct evaluation of Eq. (64) has a computational complexity of $\mathcal{O}(k)$, whilst under the panel clustering approach this is reduced to $\mathcal{O}(log(k))$. Assuming that the number of launched ions is proportional to surface panels k, panel clustering reduces the total computational complexity from $\mathcal{O}(k^2)$ to $\mathcal{O}(k \cdot log(k))$, whilst increasing memory complexity from $\mathcal{O}(k)$ to $\mathcal{O}(k \cdot log(k))$. In practice, panel clustering reduced the projection time for 1000 ions off a typical geometry from around 60 minutes to a few seconds. Its accuracy compared to direct integral evaluation will be investigated in Section 3.6.1.

3.6 Model Testing

3.6.1 Electrostatic Tests

To check the accuracy of the BEM solver, the numerical solution can be checked against systems with analytical solutions. In particular, the analytical solution of radially symmetric systems can be readily derived. The form of Laplace's equation, and its general solution, for radially symmetric problems in 2D (left) and 3D (right) is given in Eq. (84).

$$\begin{array}{ll} \text{2D Problems} & \text{3D Problems} \\ \dfrac{\partial^2 u}{\partial r^2} + \dfrac{1}{r}\dfrac{\partial u}{\partial r} = 0 & \dfrac{1}{r^2}\dfrac{\partial}{\partial r}\left(r^2 \dfrac{\partial u}{\partial r}\right) = 0 \\ u = A \log r + B & u = \dfrac{A}{r} + B \end{array} \tag{84}$$

Here r is the radial distance, and A and B are solution-dependent constants. Comparison of the 3D BEM and analytical solutions for a radially symmetric exterior and interior problem are shown in Figure 29. In the following, the 'H-integral' refers to the integral sums associated with u in Eqs. (64). The plot shows the analytical solution (red), the standard BEM with H-integral evaluation (blue), the standard BEM without H-integral evaluation (green), and the cluster accelerated BEM (orange). The BEM including the H-integral shows significant divergence close to the boundary. This large inaccuracy is not unexpected due to the H-integral becoming near hypersingular as the field point $\mathbf{x}$ is brought towards the boundary [153]. Mathematical solutions have been proposed in the literature [153], although a higher-order or adaptive quadrature integration scheme should help reduce divergence. However, under the conductor approximation, any H-integral integrals can be omitted due to Eq. (72).

It can be seen that without the H-integral evaluation, the standard BEM

(orange) and panel clustered (green) solutions agree well with the analytical solution (red) until up close to the boundary. It is worth noting that there is still a minor divergence between the numerical solutions and analytical solution when very close to the boundary meshes. However, such divergence is not unphysical due to surface discretisation resulting in only near-spherical meshes. Given the current uncertainty in surface evaporation physics, the degree of divergence is certainly acceptable.

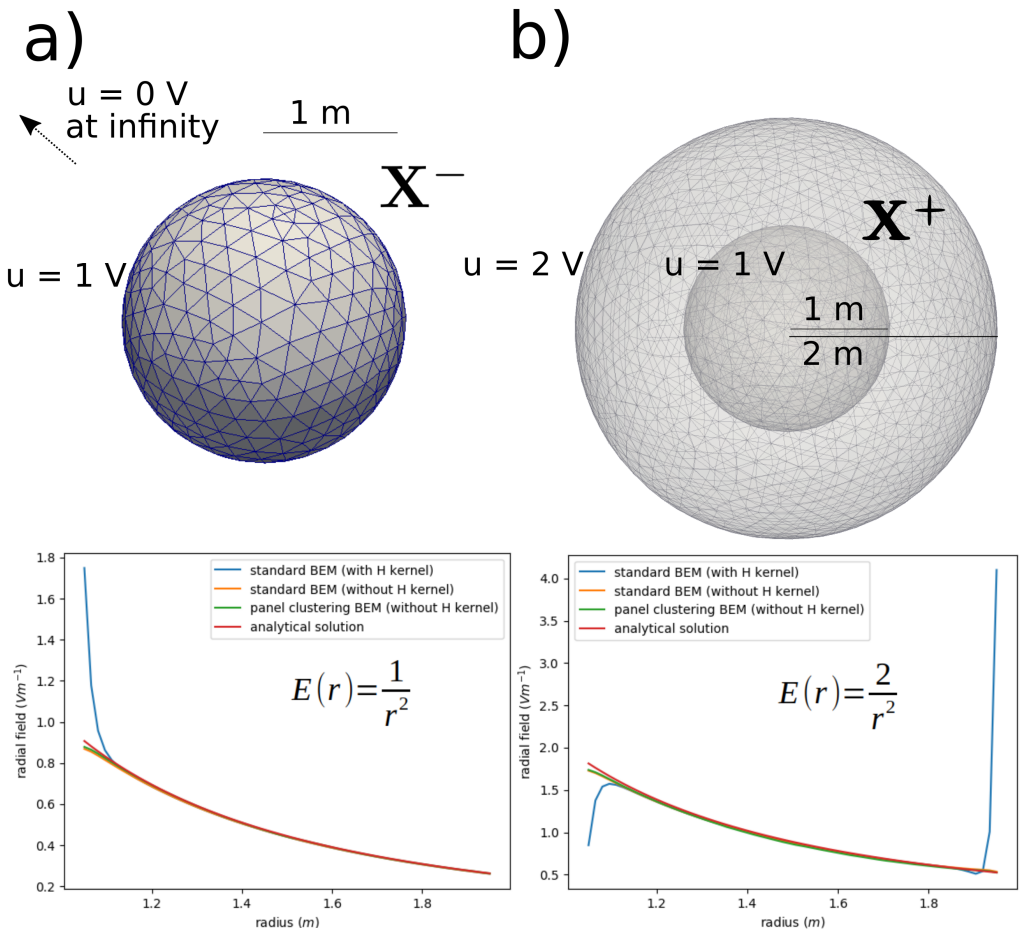


Figure 29: (a) Test geometry for the exterior BEM problem with a single closed equipotential boundary. (b) Test geometry for the interior BEM problem, solved between inner and outer equipotential boundaries. Note that some error is expected due to boundary mesh discretisation.

The 2D model contains both a pure BEM and FEM-BEM coupling scheme for capturing dielectrics. To verify the accuracy of these, the cylindrical test geometry in Figure 30 can be considered. Due to its cylindrical symmetry, an analytical

solution for the electric potential ($u(r)$) can be constructed by considering Gauss's theorem, and the BEM integral condition imposed at infinity (Eq. (139)). This piecewise solution is given in Eq. (85).

$$u(r) = \begin{cases} V_0 & \text{for } r < r_0 \\ A \log r + B & \text{for } r_0 < r < r_1 \\ A \log r_1 + B & \text{for } r_1 < r < r_2 \\ A \log r & \text{for } r > r_2 \end{cases} \tag{85}$$

$$\text{where } A = \frac{B}{\log r_2 - \log r_1} \text{ and}$$

$$B = V_0 \left[\frac{\log r_0}{\log r_2 - \log r_1} + 1 \right]^{-1}$$

A test mesh shown in Figure 30a was generated using Triangle [154] (with a fixed minimum internal angle of 21°). The electric potential is visualised in Figure 30b, and its cross-section in Figure 30c, where $V_0 = -1$ V shows good agreement between the FEM-BEM and analytical solutions. The Figure 30d shows that as the mesh resolution increases, errors tend to zero, implying these are largely caused by domain discretisation.

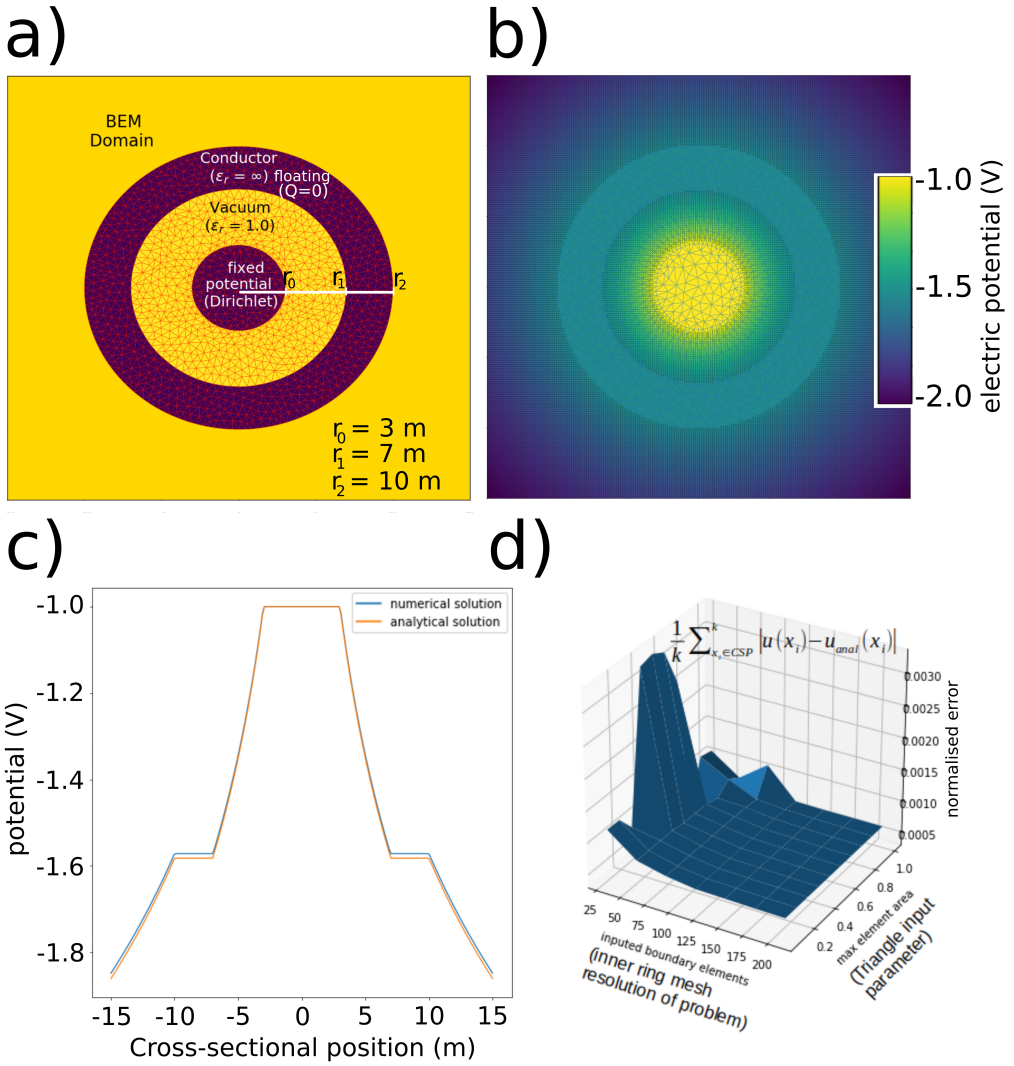


Figure 30: The cylindrical capacitor FEM-BEM test problem with $V_0 = -1$ V. (a) The test problem geometry showing the triangular FEM mesh (red). Colour indicates local dielectricity, where yellow implies vacuum permittivity and purple implies perfect conductivity. (b) Local electric potential. (c) Comparison between the FEM-BEM and analytical cross-sectional electric field strength. (d) Error between FEM-BEM and analytical solutions across mesh generation parameter space. The error formula sums the numerical ($u(x_i)$) and analytical field ($u_a(x_i)$) difference at 120 cross-sectional positions x_i. Figure modified from [133].

These tests show that the implemented electrostatic solvers are accurate until very close to the boundary. Now that solver accuracy has been verified, its coupling to the level set method can be investigated.

3.6.2 Surface Collapse Tests

In order to check the correctness and numerical accuracy of the coupling, simple collapse tests can be performed in which a sphere (circle) is collapsed according to particular velocity functions (see Figure 32). Due to the problem's spherical symmetry, analytical solutions for the collapsing surface can be obtained.

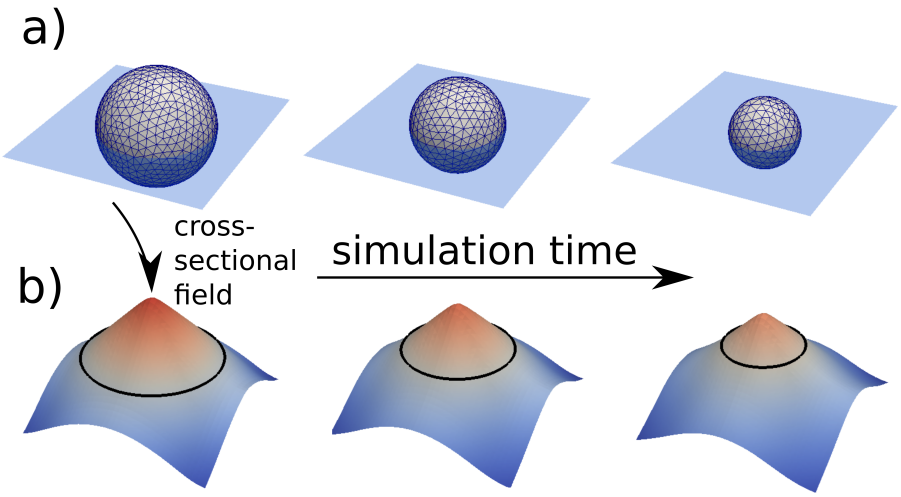


Figure 31: Visualisation of the 3D Arrhenius-driven spherical front collapse at different instances. (a) The collapsing front. (b) Cross-section of the level set field showing the restricted zero level set.

Considering first the 2D model, a collapse test was performed using a linear (Eq. (86)) and Arrhenius (Eq. (87)) velocity law, with the evolving geometry held at constant potential u_c.

$$\nu_{\text{linear}}(\mathbf{s}) = \frac{dR(t)}{dt} = -B\,\frac{E(R)}{F_0} \tag{86}$$

$$\nu_{\text{Arrh}}(\mathbf{s}) = \frac{dR(t)}{dt} = -Ae^{-\beta\left(1-\frac{E(R)}{F_0}\right)} \tag{87}$$

Here $R(t)$ is the circle radius as a function of time, B is a global constant, $E(R)$ is the surface electric field strength, and F_0 is an isotropic material evaporation field. The analytical expression for the surface electric field of a circle with an

instantaneous charge Q is given by $E = \frac{Q}{2\pi R}$. This test system is similar to the mean curvature collapse [80], but not identical, as here the surface is held at a constant potential u_c. The mean curvature flow case is equivalent to the surface having constant charge. Therefore, given that the electric field can be expressed as $E(R) = \frac{u_c}{R\ \log(R)}$, the differential equation governing the collapse test is Eq. (88).

$$\frac{dR}{dt} = -\frac{B\ u_c}{F_0}\frac{1}{R\ \log(R)} \tag{88}$$

A similar expression can be constructed in 2D for the evolution of a circle at constant potential under an Arrhenius law (Eq. (89)). Solving Eqs. (88) and (89) numerically, these solutions are compared with the level set solution in Figure 32. The tests reveal a slightly faster collapse for the Arrhenius-driven level set solution. This divergence was found to decrease when reducing the CFL fraction C controlling the time step.

$$\frac{dR}{dt} = -Ae^{-\beta\left(1-\frac{u_c}{F_0}\frac{1}{R\ \log(R)}\right)} \tag{89}$$

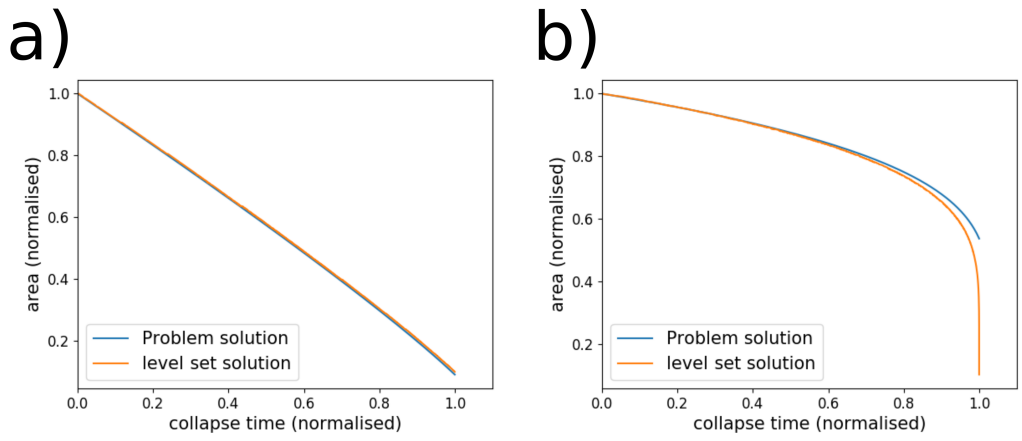


Figure 32: Level set solution in comparison to the true solution for a circle collapse test under (a) a Linear law (Eq. (88)) and (b) an Arrhenius law (Eq. (89)). Collapse was defined to occur at 5% of the initial area. Reprinted from C. Fletcher, M. P. Moody, and D. Haley. Journal of Physics D: Applied Physics, 52(435305), 2019., with the permission of IOP Publishing.

Via a similar approach, the differential equation governing the solution for a collapsing 3D sphere under an Arrhenius law can also be constructed (Eq. (90)).

$$\frac{dR}{dt} = -Ae^{-\beta}e^{\frac{\beta u_c}{F_0}\frac{1}{R(t)}} \tag{90}$$

For the subsequent 3D test, $A = 1$ ms^{-1}, $\beta = 10$, $u_c = 1$ V and $F_0 = 10$ Vm^{-1}. The spherical front has an initial radius of $R_0 = 30$ m. The Eq. (90) has again been solved numerically. The results of the collapse test is shown in Figure 33. The test terminated once the sphere volume had reached 5% of its initial volume. It can be seen from Figure 33 that the 3D Arrhenius-driven front collapse remained closer to the numerical solution. This collapsing front is visualised in Figure 31.

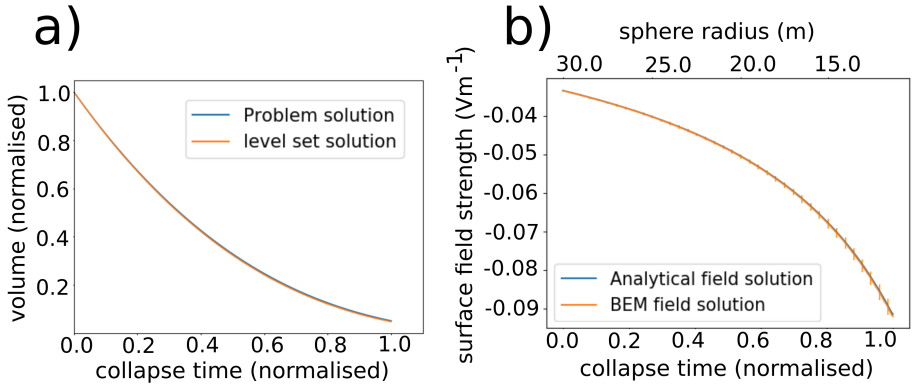


Figure 33: (a) Comparison of the level set and numerical solutions for a 3D spherical front collapse. (b) Comparison of the analytical vs BEM solution for the surface electric field. Error bars for the BEM surface field have been derived from the standard deviation of panel fluxes. Collapse was defined to occur at 5% of the initial volume. Reprinted from C. Fletcher, M. P. Moody, and D. Haley. Journal of Physics D: Applied Physics, 53(475303), 2020., with the permission of IOP Publishing.

It was found that a CFL fraction of $C = 0.2$ and field reinitialisation every 30 iterations was sufficient to minimise numerical drift in both the 2D and 3D models. These simulation parameters have been used henceforth, unless otherwise stated. Collapse tests for more complex initial fronts could potentially be performed by deriving theoretical collapse times through Biaocchi-type transformations [155].

3.7 Evaporation Model Extensions

Now that the model's accuracy has been established, the incorporation of additional physics can be considered. Up until now the evaporation model has only considered isotropic material with constant evaporation fields. However, two additional anisotropy sources are present within experiment: specimen faceting due to its underlying crystallography, and asymmetric blunting due to laser-assisted evaporation. While the exact underlying physics of these processes is not sufficiently understood at the macroscale to enable direct quantitative comparison with experimental data, it is important that the continuum model can incorporate such anisotropy for when satisfactory physical theories are developed.

3.7.1 Specimen Faceting

The underlying crystallographic structure of the field emitter can result in surface faceting for a wide range of materials (particularly metallics). This faceting can be observed both directly through electron microscopy [50, 68], but also indirectly through pole structure artefacts in APT data (Figure 34). While pole structures are technically artefacts of the imaging process, they can benefit analyses by revealing local crystallography [156], creating higher magnification regions, and constraining reconstruction parameters [139].

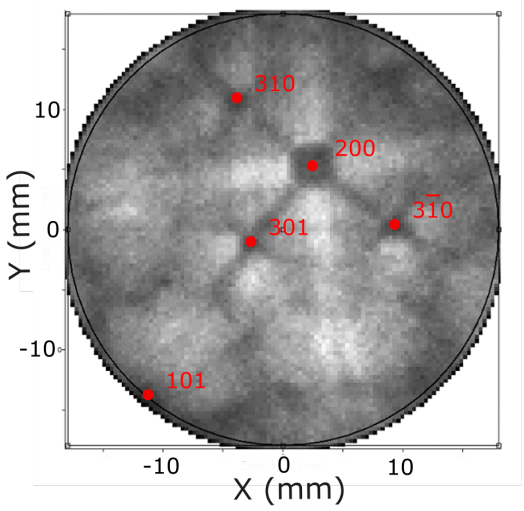


Figure 34: Example of an APT detector hitmap for a Reactor Pressure Vessel steel (courtesy of Megan Carter, Department of Materials, University of Oxford). Low hit-density pole structure (the darker contrast pattern), labelled by Miller indices, arises due to the underlying material crystallography (here face-centred cubic).

Through atomic-scale modelling, poles and zone lines are well understood to arise due to specimen faceting driven by its underlying crystallographic structure [58, 66]. Therefore, it is desirable to incorporate faceting into the model's framework. As discussed in Section 3.2, a significant advantage of the level set framework over explicit surface tracking is its ability to handle surface discontinuities [78].

The physically correct macroscopic law for predicting field-driven faceting currently remains unknown, although research into similar anisotropic curvature flow problems might reveal appropriate forms [157, 158]. However, faceting can be qualitatively reproduced by generalising the material-specific evaporation fields to be functions of surface normal angle. Some angular dependence of evaporation field is predicted, with exact material values expected to vary between crystallographic planes [70]. However, it should be noted that faceting also arises from electrostatics on crystallographic geometries, without anisotropic variation of the atomic-scale evaporation field [58].

Specifying a set of parameters for a particular material grain $\mathbb{F} = \{\gamma, \mathbf{f}_0, \mathbf{f}_1, \ldots, \mathbf{f}_N\}$,

where $\mathbf{f}_i$ are oriented vectors corresponding to evaporation fields of N fundamental facets (specified by Miller indices), and γ is an isotropic constant, a heuristic law can be defined that qualitatively reproduces faceting (Eq. (91)). This law has been motivated by assuming an approximate linear relationship between the evaporation field and surface free energy [159].

$$F_0(\mathbf{s}, \theta) = ||\mathbf{f}_{min}|| + \gamma \ |\tan(\theta_{min})| \tag{91}$$

$$\tan \theta_{min}(\mathbf{s}) = \min_{\mathbb{F}/\{\gamma\}} \left|\left| \frac{\hat{\mathbf{n}}(\mathbf{s}) \times \mathbf{f}_i}{\hat{\mathbf{n}}(\mathbf{s}) \cdot \mathbf{f}_i} \right|\right|$$

$$f_{min}(\mathbf{s}) = \underset{\mathbb{F}/\{\gamma\}}{\operatorname{argmin}} \left|\left| \frac{\hat{\mathbf{n}}(\mathbf{s}) \times \mathbf{f}_i}{\hat{\mathbf{n}}(\mathbf{s}) \cdot \mathbf{f}_i} \right|\right|$$

where θ_{min} defines the smallest angle between the surface normal $\hat{\mathbf{n}}$ and the closest facet normal $\mathbf{f}_{min}$. The closest facet is determined by identifying the facet giving the smallest angle $\theta_{min}(\mathbf{s})$ between surface normal and facet normal. Examples showing specimen faceting in both the 2D and 3D models for the anisotropy law in Eq. (91) can be seen in Figure 35.

A comparison between the faceting behaviour and ion optics for this anisotropic continuum model, and an atomic-scale model [67], is performed in Section 5.5.

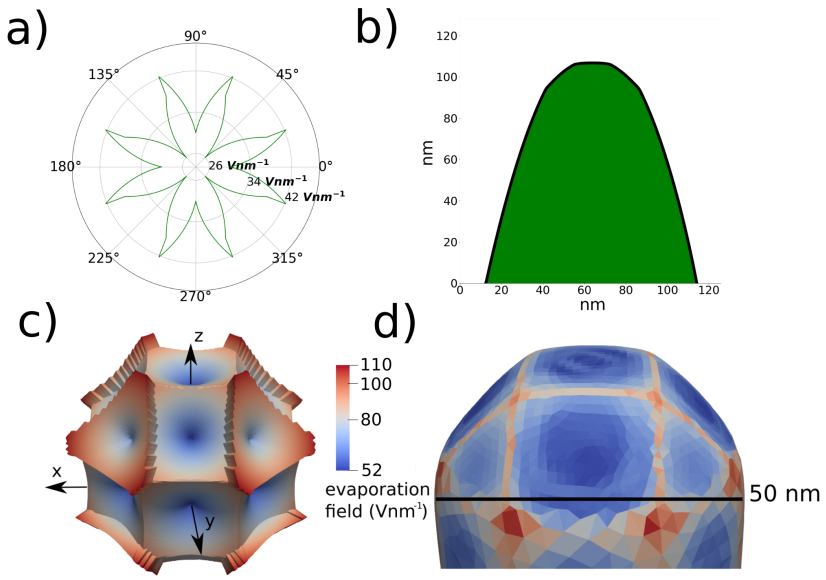


Figure 35: Examples for specimen faceting under Eq. (91). (a) A polar plot of an example 2D model anisotropy function. (b) Corresponding steady-state emitter shape. (c) Polar plot of an example 3D model anisotropy function. (d) Corresponding steady-state emitter shape.

3.7.2 Laser-Matter Interaction

So far the application of specimen laser pulsing during evaporation has been omitted from the model. However, its incidence is known to introduce anisotropy into specimen evolution that can be observed as apex blunting [24].

In order to serve as a proof-of-concept demonstration, two simple models for the laser are proposed. The first steady-state model assumes that the temperature distribution over the specimen surface can be calculated by solving the steady-state heat equation (Eq. (92)), with the specimen base acting as a heat sink. As will be shown, it is safe to assume that any radiative cooling is negligible. Here different specimen phases have been approximated as having the same thermal conductivity.

$$\nabla^2 T = 0 \tag{92}$$

$$T(\mathbf{x}) = T_0 \quad \forall \mathbf{x} \in \Gamma_{\text{base}}$$

$$q(\mathbf{x}) = \max\big(-\mathbf{P} \cdot \mathbf{n}(\mathbf{x}),\ 0\big) \quad \forall \mathbf{x} \in \Gamma / \Gamma_{\text{base}}$$

Here $\mathbf{P}$ is the Poynting vector associated with the incident laser, and $\mathbf{n}$ is the surface normal. The diagram in Figure 36 shows the laser flux through a surface element. This steady-state equation is Laplace's equation, and therefore can be solved via the BEM method in Section 3.5.2. However, due to a mix of Dirichlet and Neumann boundary conditions, the BEM matrix equation must first be re-arranged (see Appendix G). This model effectively assumes that the specimen cooling time (τ_{cool}) is significantly faster than the laser pulse duration (τ_{pulse}), resulting in the specimen reaching a steady-state temperature. In addition, this simplistic model does not account for shadowing, and ignores phase-specific transparency/absorption effects (phenomena which would require ray tracing).

The second surface heating model considered is based off the opposite assumption that the specimen cools significantly slower than the laser pulse duration. Instead the surface temperature is considered to be locally proportional to the incident laser flux (Figure 36). An expression motivated from the previous work of Vurpillot et al. [160] is given in Eq. (93).

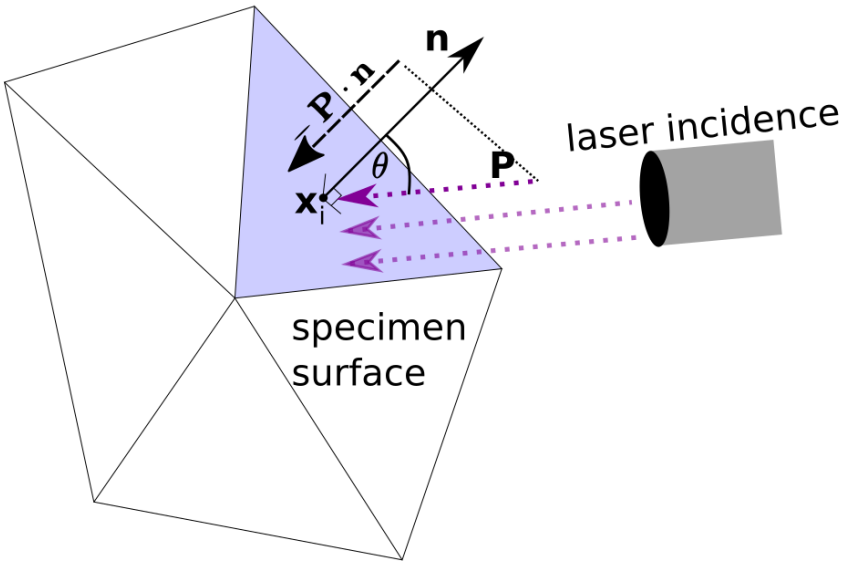


Figure 36: Diagram showing the laser intensity component (flux) passing through a specimen surface panel.

$$T(\mathbf{x}) = T_{\text{base}} + (T_{\text{max}} - T_{\text{base}}) \max\left(-\frac{\mathbf{P} \cdot \mathbf{n}(\mathbf{x})}{||\mathbf{P}||},\ 0 \right) \tag{93}$$

Here T_{max} is the surface maximum temperature reached, and $\mathbf{n}$ is the surface normal. Note that in the second model, the exact magnitude of $\mathbf{P}$ is unimportant (its dependence has been absorbed into T_{max}). This second model is equivalent to considering all the energy from a given a laser pulse as heating a thin shell of material close to the specimen surface. All evaporation has been assumed to occur during this initial surface heating period.

Typical values for the model parameters can be determined from the experiment details. For these simple models, the laser is assumed to have a Gaussian intensity beam profile focused on its apex. The power $P(r, z)$ passing through a ring of radius r normal to the beam, at position z, is given by Eq. (94).

$$P(r,z) = P_0\left[1 - e^{\frac{-2r^2}{w^2(z)}}\right] \tag{94}$$

$$P_0 = \frac{1}{2}\pi I_0 w_0^2 \tag{95}$$

Here $w(z)$ is the beam spot size at position z, P_0 is the total transmitted power, I_0 is the maximum intensity, and $w_0 = w(0)$. The LEAP 5000 has a spot size of $w_0 \sim 3$ μm and a typical total power value of $P_0 = 5$ μW (assuming a 10 pJ pulse energy and 500 kHz repetition rate) [161]. Defining the apex to be at $z = 0$, the maximum intensity at the surface can be calculated via Eq. (95) to be $I_0 = 0.35$ MWm^{-2}s^{-1}. Dividing $P(r,0)$ by $2\pi r$, the average intensity at a particular radius can also be calculated. This intensity distribution is shown in Figure 37.

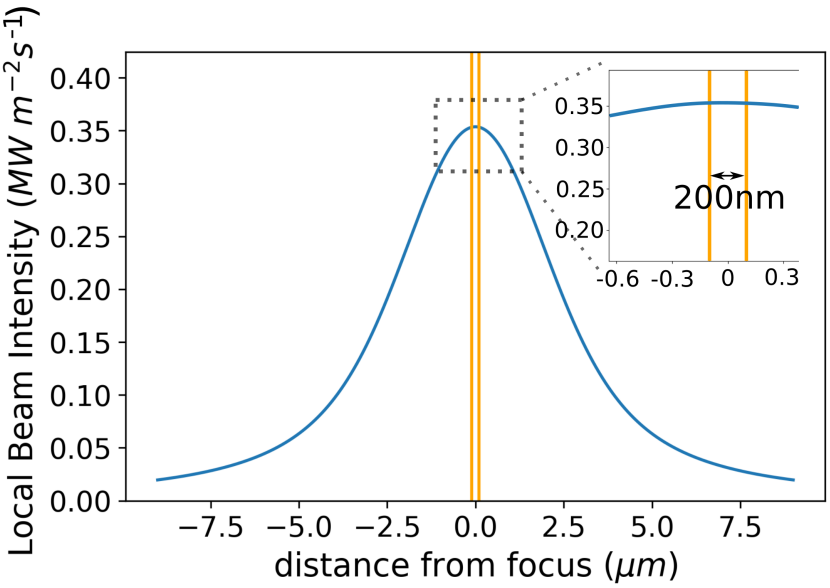


Figure 37: plot of the average intensity through a ring of radius r normal to the beam direction for a 3 μm spot size laser. The orange lines represent a diameter of 200 nm, typical of a specimen apex. If a true Gaussian beam, laser intensity could be assumed near uniform at the apex.

The gap between the two orange lines represents a diameter of 200 nm, typical of an APT specimen apex. This implies that the laser intensity, and therefore the

Poynting vector $\mathbf{P}$ magnitude, can be considered constant in the vicinity of the apex. Note that in reality, a Gaussian profile is almost certainly a poor assumption due to experimental observations of nodes with locally enhanced absorption along the specimen shank [162].

The LEAP 5000 laser parameters [161] give a typical time-averaged value of $||\mathbf{P}|| = 0.35$ MWm^{-2} for the steady-state model. Typical temperature values for the surface heating model are $T_{\text{base}} = 40$ K and $T_{\text{max}} = 300$ K, as estimated via experiment for a tungsten specimen [160]. For comparison, using the black body surface power density equation $\rho_p = \sigma_s T^4$, where σ_s is the Stefan-Boltzmann constant, a perfect black body emitter at 300 K would radiate at a maximum power density of 460 Wm^{-2} $<<$ $||\mathbf{P}||$. Therefore, any radiative emission of the specimen can be assumed negligible.

Experimental studies [160] imply that the surface heating model might be the more valid of the two proposed, and could even make reasonable qualitative predictions for metallics, where skin depths are typically only a few nanometres (implying the majority of absorption near the surface). However, previous theoretical studies have shown accurately modelling the laser to be non-trivial [163]. In reality, the skin depth for dielectric materials is greater than the thickness of typical APT specimens ($\sim$ 100 nm). Therefore, internal laser reflection can occur. This is further complicated by the similarity of the wavelength (355 nm or 532 nm depending on the LEAP system) to specimen dimensions, which can result in complex diffraction behaviour similar to Mie scattering [164]. However, these simplistic models demonstrate how laser thermal heating can be readily incorporated into the simulation. Example temperature profiles generated by the two laser models on a homogeneous specimen surface are shown in Figure 38.

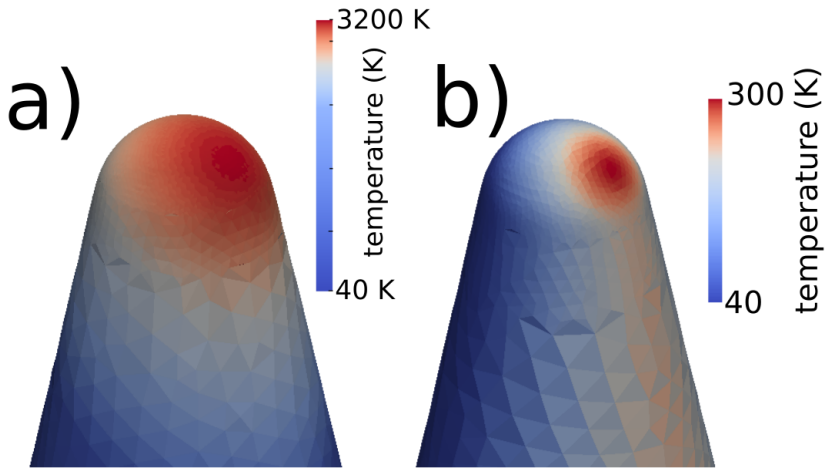


Figure 38: (a) Example temperature distribution under the steady-state model. (b) Example distribution under the surface heating model. Model results will be discussed in Section 5.4.

In conclusion, the previous sections have demonstrated how crystallographic and laser anisotropy can be incorporated into the continuum model. None of these extensions are expected to be physically accurate beyond first order. Correlative experiment, combined with more fundamental modelling approaches, will likely be required to further constrain the theory.

3.8 The Trajectory Mapping

3.8.1 The Spatial Continuity of Ion Trajectories

So far the theoretical groundwork for a continuum evaporation model allowing calculation of charged ion optics has been laid out. However, if the aim is to directly compare with, or to reconstruct, experimental data, this would typically involve estimating the initial specimen positions and final detector positions for millions of evaporated ions, each having followed an individual trajectory. Thankfully, as we will now show, mathematical properties of the trajectory solutions ensure that only a small sample of trajectories need to be calculated. These sampled trajectories can then be used to estimate arbitrary ions' trajectories through interpolation.

The concept of formalised trajectory or reconstruction mappings has been previously hinted at [100, 165]. This notion of a reconstruction mapping ($\mathcal{R}$) was further formalised in [165] as a function or mapping from positions in the sample space of real atomic coordinates ($\mathbb{S} = \mathbb{R}^3$) to positions in detector space ($\mathbb{D} = \mathbb{R} \times \mathbb{R} \times \mathbb{N}$), where $\mathbb{R}$ is the set of real numbers and $\mathbb{N}$ the set of natural numbers representing the detector event sequence. APT reconstruction can then be considered as the process of attempting to estimate this mapping $\mathcal{R} \approx \mathcal{T}$, particularly its inverse $\mathcal{R}^{-1}$, where $\mathcal{T} : \mathbb{S} \rightarrow \mathbb{D}$ is the true trajectory mapping as present in experiment. While a complete experimental trajectory mapping should also really consider the space of initial and final velocities, i.e. $\mathcal{T}_{\mathbf{v}} : \mathbb{S} \times \mathbb{R}^3 \rightarrow \mathbb{D} \times \mathbb{R}^3$, this velocity information is currently unavailable to both theory and experiment. Therefore any initial velocity spread will have to be assumed negligible (with initial velocities approximated as zero). Future technologies, such as the development of superconducting detectors for APT analysis [166], might allow for partial constraint of this momentum.

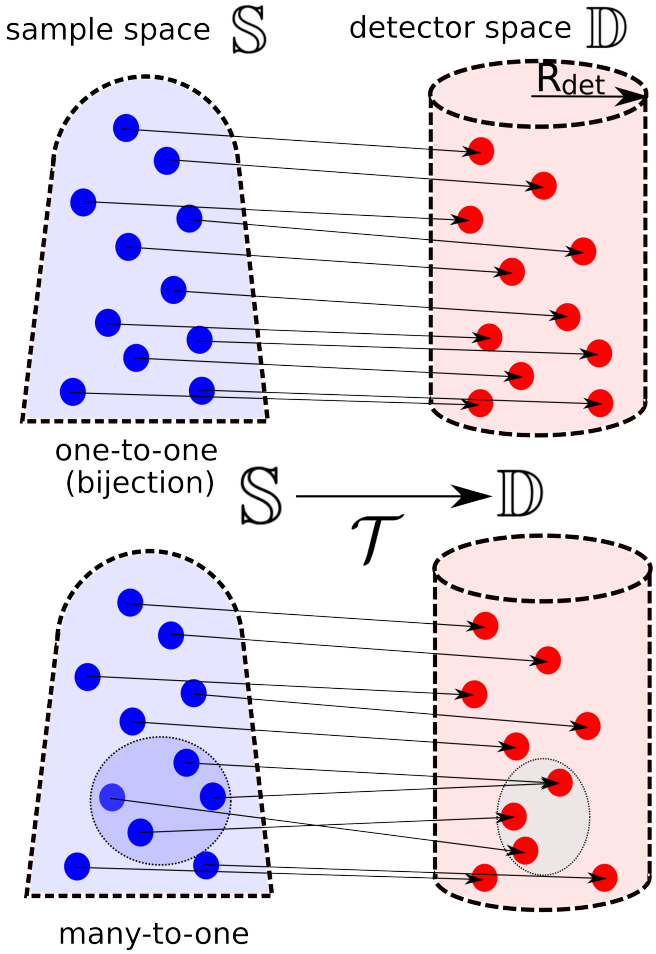


Figure 39: Diagram illustrating the differences between a one-to-one and many-to-one mapping. For a many-to-one mapping, multiple points in $\mathbb{S}$ can map to the same point in $\mathbb{D}$ (trajectories can cross over). The true forward trajectory mapping is generally many-to-one.

An assumption of projection-based reconstruction approaches is to assume that the estimated forward mapping ($\mathcal{R}$) is bijective or one-to-one [165]. This enables $\mathcal{R}^{-1}$ to be uniquely defined. In reality however, bijectivity of the experiment mapping ($\mathcal{T}$) cannot be assumed (Figure 39). Ion trajectories can crossover or spatially overlap from the emitter to detector, resulting in regions of $\mathcal{T}^{-1}$ within the detector space $\mathbb{D}$ that cannot be uniquely defined. However, we can prove the continuity of $\mathcal{T}$, at least under the continuum approximation, which is critical for its numerical calculation.

In order to prove the forward trajectory mapping's continuity, it is enough to

show that the dependence of the ion trajectory solution is continuous with respect to initial launch conditions. As shown in Section 3.5.7, an ion's motion is governed by a system of first-order equations (Eq. (78)). Following the ion's evaporation from the specimen surface, it is accelerated by the electric field ($\mathbf{E}$), governed by Poisson's equation (Eq. (39)), towards the detector. Weyl's lemma [167] tells us that the solution to Eq. (39) within the vacuum is smooth. To avoid potential field discontinuities on the specimen surface (e.g. facet corners), ion launch positions can be set to be some small distance away from the surface.

Finally, in order to prove the forward mapping's continuity, there exists the following theorem for first-order differential equations, as proven in [168].

Theorem 1 *For a first-order differential equation* $\frac{d\mathbf{y}}{dt} = \mathbf{f}(\mathbf{y}, \mathbf{k}, t, \mathbf{s})$*, where* $\mathbf{s}$ *are the initial conditions and* $\mathbf{k}$ *are parameters, assuming that* $\frac{\partial f_i}{\partial \mathbf{y}} \in C$*,* $\frac{\partial f_i}{\partial \mathbf{k}} \in C$*,* $\frac{\partial f_i}{\partial \mathbf{s}} \in C$*, then at any point* $\mathbf{y}'$ *where the solution exists, the solution is continuous in* $\mathbf{y}$ *with respect to* $\mathbf{s}$ *and* t*.*

Here C is the set of continuous functions. In our case, $\mathbf{y} = (\mathbf{z}, \mathbf{v})$ in Eq. (78). Therefore, on applying this theorem, if ions originating from the specimen impact the detector within the neighbourhood of a specific detector coordinate $\mathbf{z}'_D$, then an ion trajectory's solution at $\mathbf{z}'_D$ must be continuous in $\mathbf{z}$ with respect to variations in its initial surface launch position $\mathbf{s}$. Therefore, the trajectory mapping ($\mathcal{T}$) is also continuous in this neighbourhood region on the detector. This property of the mapping directly validates its estimation computationally via the spatial interpolation of sampled ion trajectories, converging to the true solution as trajectory sampling is increased.

Once again, it is important to note that this continuity condition for $\mathcal{T}$ does not imply bijectivity. In fact the spatial overlap of ion trajectories is a well reported phenomenon in APT literature [56, 51]. Instead, $\mathcal{T}$ should be considered in general continuous and many-to-one (where multiple apex positions can correspond to the same detector position). Nearer the atomic-scale, additional

trajectory overlaps should also be expected due to the atomic roughness of the specimen surface (e.g. at terraces) [60, 68]. However, these atomic-scale overlaps cannot be captured by a continuum model.

3.8.2 Temporal Continuity

Unlike spatial continuity, temporal continuity of the trajectory mapping cannot always be guaranteed where there is a change in specimen topology, e.g. field evaporation into a cavity. During these topological changes, there is a discontinuous jump in the specimen surface, and therefore $\mathcal{T} : \mathbb{S} \to \mathbb{D}$ cannot in general be continuous throughout time. However, assuming that the boundary is evolving smoothly throughout time (no discontinuous jumps), its temporal continuity within these smooth evolution time intervals can be guaranteed. It is possible to prove that the electric potential throughout the domain is continuous with respect to smooth parameterised perturbations of the domain boundary (Appendix H). Reconsidering Theorem 1, we can see that as the electric field is continuous with respect to these perturbation parameters (elements of $\mathbf{k}$ in Theorem 1), the inhomogeneous term $\mathbf{f}$ is also continuous, implying the condition $\frac{\partial f_i}{\partial \mathbf{k}} \in C$ in Theorem 1 holds. Therefore, ion trajectories are also continuous under smooth surface evolution. Similar problems for which continuity proofs exist include Hele-Shaw flow [169].

3.8.3 Local Stability Behaviour

As we have shown, the forward trajectory mapping can be considered continuous. However, it is the model's inverse mapping estimate ($\mathcal{R}^{-1}$) that is required for reconstruction. If trajectory overlap is occurring within a detector region, the continuity proof in Section 3.8.1 tells us that the inverse mapping within this entire region cannot be uniquely defined. However, projection-based reconstruction assumes a unique one-to-one mapping over the entire detector, resulting in composition artefacts [51, 170]. By considering the APT data alone, these artefacts can be difficult to separate from physical changes in composition, especially as both trajectory overlaps and composition changes typically occur at interfaces between material phases. Therefore, being able to quantify the local behaviour of the trajectory mapping throughout a reconstruction, and in particular whether trajectory overlap is occurring, could prove invaluable information for APT users.

In the 3D model, the specimen surface (Γ) is described by a piecewise surface mesh of triangular panels ($\Gamma_j \in \Gamma$). By launching ions from panel corners, the image of an individual triangle element can be considered on the detector (Figure 40). If an element inverts under the mapping, then due to the proven continuity of the forward mapping, trajectory overlap must be occurring within its regional neighbourhood on the detector.

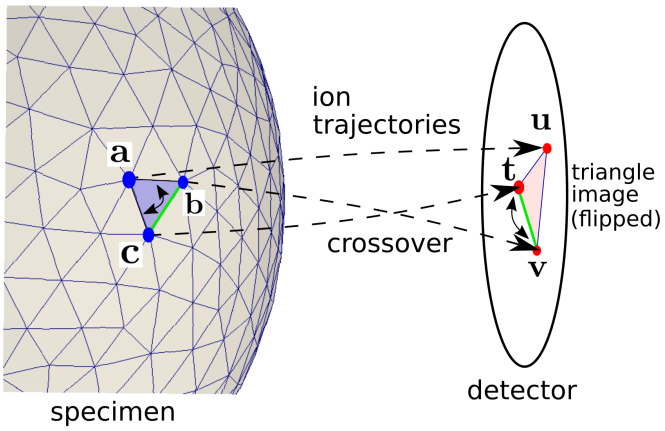


Figure 40: Diagram showing the projection of a surface panel onto the detector. Trajectory crossover results in the projected panel inverting (flipping).

The Jacobian matrix ($\mathbf{J}$) and its determinant ($||\mathbf{J}||$) for the forward mapping provide exactly this information. The magnitude of the determinant gives the ratio of the projected triangle panel to its original area. This can be considered a local scalar magnification. A more complete vector description containing anisotropy information can be found by considering the elements of $\mathbf{J}$ [1]. Meanwhile, the sign of $||\mathbf{J}||$ indicates whether the orientation of the projected panel is preserved (positive), or is inverted (negative) as in Figure 40. An inversion implies that in this panel's neighbourhood projected onto the detector, $\mathcal{R}^{-1}$ is multivalued. The Jacobian is also used to describe magnification in gravitational lensing [171].

The local Jacobian for $\mathcal{R}$ is defined in Eq. (96). Here (x_t, y_t) are local coordinates tangential to the specimen surface, whilst (d_x, d_y) are coordinates on the detector.

$$||\mathbf{J}|| = \begin{vmatrix} \frac{\partial d_x}{\partial x_t} & \frac{\partial d_x}{\partial y_t} \\ \frac{\partial d_y}{\partial x_t} & \frac{\partial d_y}{\partial y_t} \end{vmatrix} \tag{96}$$

Performing linear interpolation for our model's mapping estimate ($\mathcal{R}$) over panels, $\mathbf{J}$ will be constant over each panel. In order to calculate $||\mathbf{J}||$ on a specific panel, defined by corner positions $(\mathbf{a}, \mathbf{b}, \mathbf{c})$ on the surface mesh and projected positions $(\mathbf{u}, \mathbf{v}, \mathbf{t})$ on the detector, a local coordinate system tangential to this panel is defined. To allow direct comparison of $\mathbf{J}$ between elements, the orientation of the local coordinate system with respect to the global coordinate system, defined by unit vectors $\hat{\mathbf{x}} = (1, 0, 0)$ and $\hat{\mathbf{y}} = (0, 1, 0)$ (Figure 41), must be preserved. The local tangent unit vectors $(\hat{\mathbf{x}}_\mathbf{t}, \hat{\mathbf{y}}_\mathbf{t})$ are then calculated through Eqs. (97).

[1] Strictly, a negative sign for $||\mathbf{J}||$ only occurs for a single panel inversion (a single edge flip under projection), as opposed to a double inversion (a negative panel rescaling under projection). A stronger condition for both single and double inversions would require considering both the signs of the $\frac{\partial d_x}{\partial x_t}$ and $\frac{\partial d_y}{\partial y_t}$ Jacobian matrix elements. However, due to the forward mapping continuity, considering $||\mathbf{J}||$ alone should be enough to determine the projected crossover region on the detector.

$$
\begin{aligned}
\hat{\mathbf{n}} &= \frac{(\mathbf{b}-\mathbf{a})\times(\mathbf{c}-\mathbf{a})}{||(\mathbf{b}-\mathbf{a})\times(\mathbf{c}-\mathbf{a})||} \\
\hat{\mathbf{x}}_\mathbf{t} &= \frac{\hat{\mathbf{x}}-(\hat{\mathbf{x}}\cdot\hat{\mathbf{n}})\hat{\mathbf{n}}}{||\hat{\mathbf{x}}-(\hat{\mathbf{x}}\cdot\hat{\mathbf{n}})\mathbf{n}||} \\
\hat{\mathbf{y}}_\mathbf{t} &= \frac{\hat{\mathbf{y}}-(\hat{\mathbf{y}}\cdot\hat{\mathbf{n}})\hat{\mathbf{n}}-(\hat{\mathbf{y}}\cdot\hat{\mathbf{x}}_\mathbf{t})\hat{\mathbf{x}}_\mathbf{t}}{||\hat{\mathbf{y}}-(\hat{\mathbf{y}}\cdot\hat{\mathbf{n}})\hat{\mathbf{n}}-(\hat{\mathbf{y}}\cdot\hat{\mathbf{x}}_\mathbf{t})\hat{\mathbf{x}}_\mathbf{t}||}
\end{aligned}
\tag{97}
$$

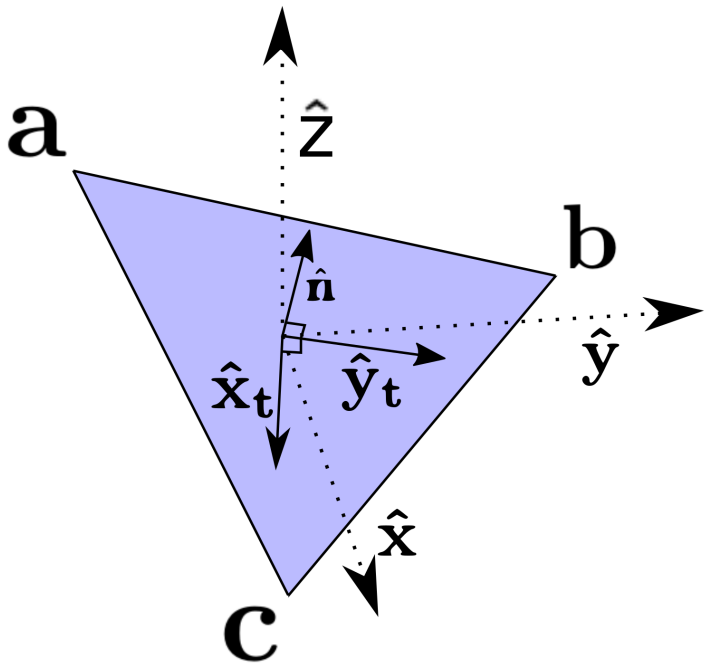


Figure 41: Diagram showing the local tangential coordinate system $(\hat{\mathbf{x}}_t, \hat{\mathbf{y}}_t)$ for a surface panel with normal $\hat{\mathbf{n}}$, with respect to a global coordinate system $(\hat{\mathbf{x}}, \hat{\mathbf{y}}, \hat{\mathbf{z}})$.

The corner points $(\mathbf{a}, \mathbf{b}, \mathbf{c})$ are labelled such that $\hat{\mathbf{n}}$ is the outer unit normal of the surface mesh. Finally, the corner points are transformed into the local coordinate system via Eqs. (98). The Jacobian matrix can then be calculated through Eq. (99) [172].

$$a'_x = 0 \quad b'_x = (\mathbf{b} - \mathbf{a}) \cdot \hat{\mathbf{x}}_\mathbf{t} \quad c'_x = (\mathbf{c} - \mathbf{a}) \cdot \hat{\mathbf{x}}_\mathbf{t}$$
$$a'_y = 0 \quad b'_y = (\mathbf{b} - \mathbf{a}) \cdot \hat{\mathbf{y}}_\mathbf{t} \quad c'_y = (\mathbf{c} - \mathbf{a}) \cdot \hat{\mathbf{y}}_\mathbf{t} \tag{98}$$

$$\mathbf{J}^T = \frac{1}{2A} \begin{pmatrix} b'_y - c'_y & c'_y - a'_y & a'_y - b'_y \\ c'_x - b'_x & a'_x - c'_x & b'_x - a'_x \end{pmatrix} \cdot \begin{pmatrix} u_x & u_y \\ v_x & v_y \\ t_x & t_y \end{pmatrix} \tag{99}$$

Here $\mathbf{a}' = (a'_x, a'_y)$, $\mathbf{b}' = (b'_x, b'_y)$, $\mathbf{c}' = (c'_x, c'_y)$, $\mathbf{u} = (u_x, u_y)$, $\mathbf{v} = (v_x, v_y)$, $\mathbf{t} = (t_x, t_y)$, and A is the panel area.

We can now calculate $\mathbf{J}$ over the specimen surface, and consider its projection onto the detector. An example specimen surface featuring a concavity is given in Figure 42. The mapping stability values on the specimen surface are shown in Figure 42a, and their projection shown in Figure 42b. As expected, a decreased magnification (blue-yellow) can be observed within the concavity compared to the surrounding bulk (orange-red). A blue ring can also be observed, showing where $||\mathbf{J}||$ is negative and local image inversion is occurring. In order to estimate the detector region where $\mathcal{R}^{-1}$ is multivalued, we must consider the projection of $||\mathbf{J}||$ onto the detector (Figure 42b). The region of mixed positive and negative stability values in Figure 42b indicates the detector region where trajectory overlap is occurring. The origin of any detected ion on the specimen within this overlap region cannot be unambiguously determined.

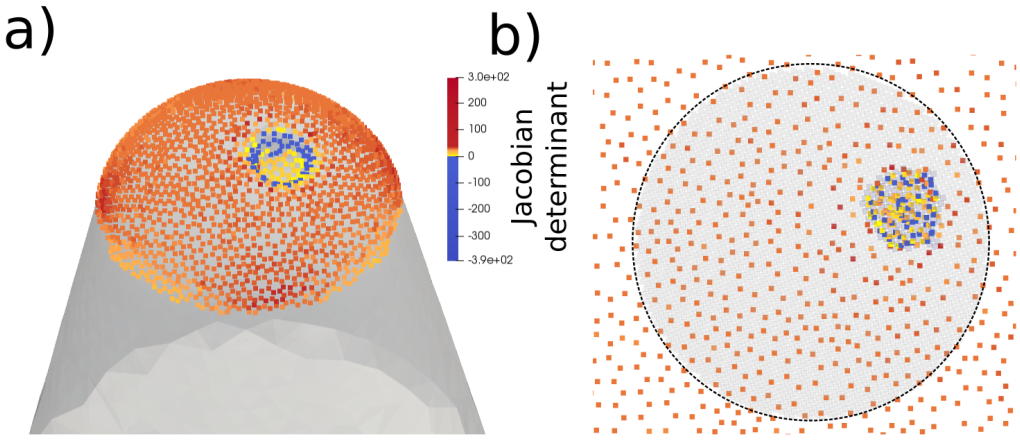


Figure 42: a) Local panel stability on the specimen surface featuring a concavity. Blue points indicate a local image inversion. b) Corresponding image of local stabilities following projection onto the detector. Spatial mixing of positive (yellow) and negative (blue) projected panel stabilities indicates that trajectory overlap is occurring within the dark grey detector region (calculated via the method in Section 3.9.3).

Finally, by invoking the continuity theorem in Section 3.8.1, in order to restore the mapping monotonicity outside of a detector region containing negative $||\mathbf{J}||$ values, this region must also contain positive $||\mathbf{J}||$ values. Therefore, any region of local image inversion on the detector is also a region of trajectory overlap, where $\mathcal{R}^{-1}$ is multivalued (Figure 43).

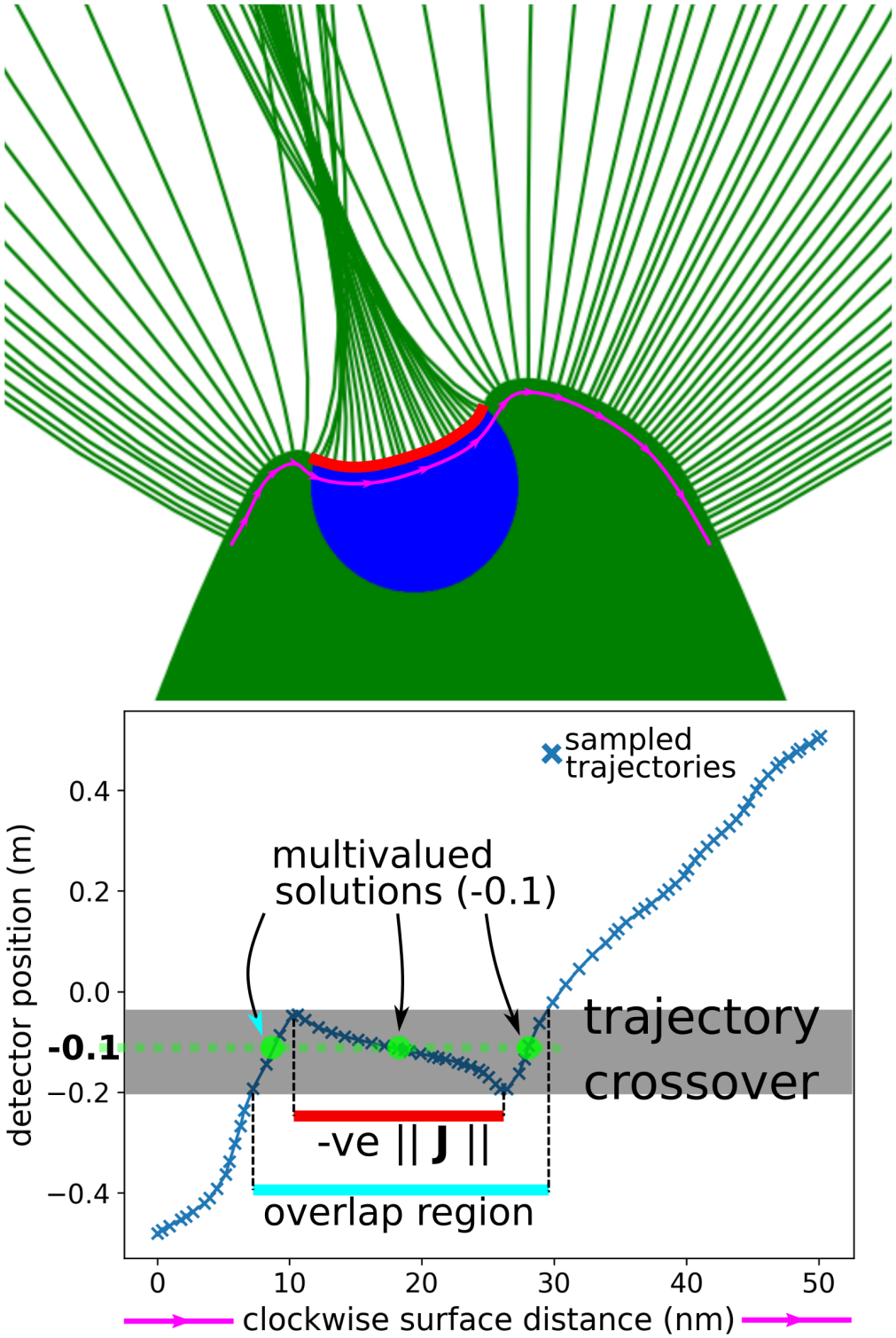


Figure 43: Visualisation of results from 2D model showing how local ion trajectory crossover, and the forward mapping's continuity, leads to a locally multivalued inverse mapping.

3.8.4 Constructing the Inverse Trajectory Mapping

We know from these continuity proofs that the estimated forward trajectory mapping ($\mathcal{R}$) is continuous in the absence of topological changes (e.g. evaporation of cavities). However, this does not ensure that $\mathcal{R}^{-1}$ is always single-valued. In fact, $\mathcal{R}$ continuity only implies that ion trajectory overlaps will result in $\mathcal{R}^{-1}$ becoming multivalued within some region. Within these multivalued regions, positioning of reconstructed ions would become ambiguous (although probabilistic assignment by relative evaporation probabilities might be possible).

In the remainder of this work, it is largely assumed that, for the systems considered, such multivalued regions are very limited (verified by mapping stability), and that the inverse mapping typically remains one-to-one. However, as will be seen in Section 4.9, multivalued forms of the mapping can be constructed and so local information on ion positioning ambiguity could be incorporated into future reconstruction schemes.

For now let's proceed under the global bijectivity assumption, which should be valid for the majority of analysed systems. Both the 2D and 3D model produces a set of surface meshes $\{..., \Gamma^n, ...\}$, where Γ^n is the specimen mesh at the n-th model iteration (instance). To construct the inverse mapping, ions are launched from the corners of mesh elements for a subset of these surface meshes, and their trajectories calculated up to the detector (Section 3.5.7). It should be noted that the function $\mathcal{R}^{-1}$ maps to a position vector on the specimen surface. Therefore, $\mathcal{R}^{-1}$ really has multiple components corresponding to each surface position coordinate (dimension). These components will be distinguished by the index $\alpha \in \{x, y\}$ in 2D and $\alpha \in \{x, y, z\}$ in 3D, with mapping components denoted $\mathcal{R}_\alpha^{-1}$.

Initially, the static time-independent inverse mapping $(\mathcal{R}_\alpha^{-1})_j$ associated with each surface mesh Γ^n are calculated by spatial interpolation of its sampled trajectories. Here, the initial ion launch coordinates are linearly interpolated over

each projected surface element onto a regular grid over the detector (shown in Figure 44 for 3D). Note that the interpolated initial surface position for a particular regular grid coordinate can only be single-valued (bijective) if it is contained within just one of the projected surface elements, i.e. projected elements do not flip and overlap. The regular detector grid used is identical for each static mapping $(\mathcal{R}_\alpha^{-1})_j$.

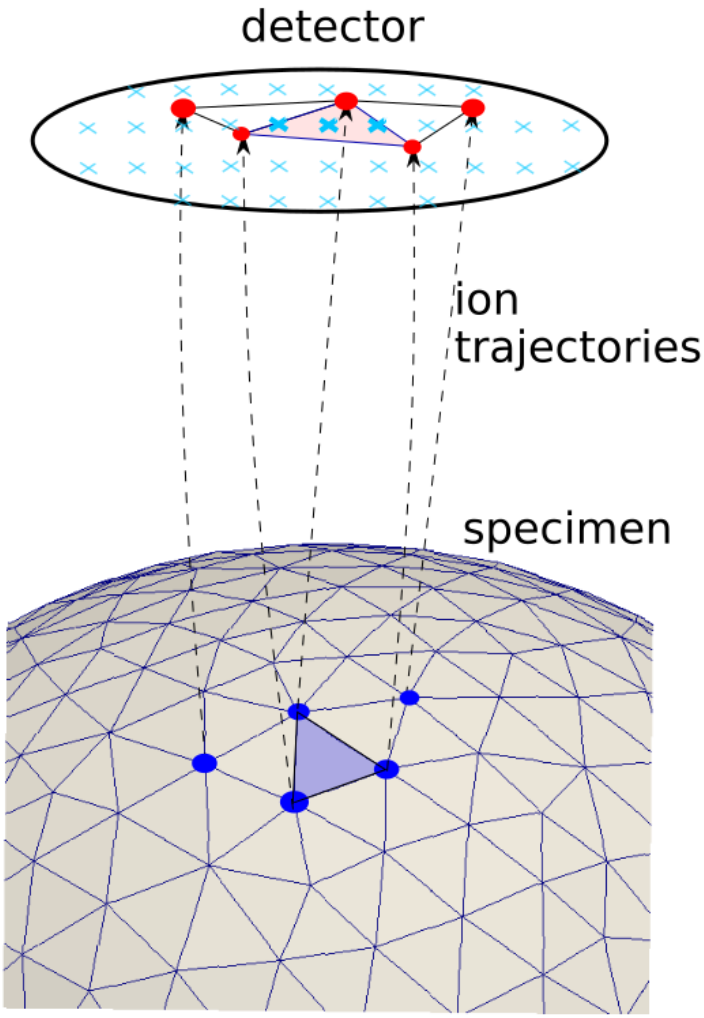


Figure 44: Diagram showing the ion projection from panel corners for a particular surface mesh. A panel and its corresponding projection has been highlighted. The cyan crosses indicate the detector grid coordinates where initial launch positions are calculated via interpolation. Crosses in bold indicate where these grid values are calculated via linear interpolation over the highlighted panel.

Once estimates for the static inverse mappings $(\mathcal{R}_\alpha^{-1})_j$ have been constructed,

these can be used to estimate the time-dependent inverse mapping $\mathcal{R}_\alpha^{-1}(\tau)$ by interpolating between the static inverse mappings. Assuming no topological change, the forward mapping is continuous in both space and time. Therefore, under the bijective assumption, $\mathcal{R}_\alpha^{-1}(\tau)$ is also bijective and continuous. This mapping is constructed for all time by linear interpolation between neighbouring $(\mathcal{R}_\alpha^{-1})_j$, which have all been discretised on the same regular detector grid. This linear interpolation at a grid point $\mathbf{x}_{\gamma,\delta}$, where γ and δ index the detector grid points, between the neighbouring static mappings $(\mathcal{R}_\alpha^{-1})_j$ and $(\mathcal{R}_\alpha^{-1})_{j+1}$ is parameterised by a temporal parameter $\tau_j \leq \tau \leq \tau_{j+1}$ (Eq. (100)).

$$\mathcal{R}_\alpha^{-1}(\mathbf{x}_{\gamma,\delta},\tau) = \frac{\tau_{j+1}-\tau}{\tau_{j+1}-\tau_j}(\mathcal{R}_\alpha^{-1})_j(\mathbf{x}_{\gamma,\delta}) + \frac{\tau-\tau_j}{\tau_{j+1}-\tau_j}(\mathcal{R}_\alpha^{-1})_{j+1}(\mathbf{x}_{\gamma,\delta}) \tag{100}$$

Having performed this temporal linear interpolation, the inverse mapping at time τ and detector position $\mathbf{x} = (x, y)$ can be calculated via bilinear interpolation for the 3D model (linear interpolation for the 2D model). For a detector position $\mathbf{x}$, bounded by the rectangle of detector grid coordinates $\mathbf{x}_{\gamma,\delta} = (x_1, y_1)$, $\mathbf{x}_{\gamma+1,\delta} = (x_2, y_1)$, $\mathbf{x}_{\gamma,\delta+1} = (x_1, y_2)$, and , $\mathbf{x}_{\gamma+1,\delta+1} = (x_2, y_2)$, the inverse mapping in the 3D model at a general $(\mathbf{x}, \tau)$ is given by Eq. (101).

$$\mathcal{R}_\alpha^{-1}(\mathbf{x},\tau) = \frac{1}{(x_2-x_1)(y_2-y_1)}\begin{bmatrix} x_2-x & x-x_1 \end{bmatrix} \cdot \begin{bmatrix} \mathcal{R}_\alpha^{-1}(\mathbf{x}_{\gamma,\delta},\tau) & \mathcal{R}_\alpha^{-1}(\mathbf{x}_{\gamma,\delta+1},\tau) \\ \mathcal{R}_\alpha^{-1}(\mathbf{x}_{\gamma+1,\delta},\tau) & \mathcal{R}_\alpha^{-1}(\mathbf{x}_{\gamma+1,\delta+1},\tau) \end{bmatrix} \cdot \begin{bmatrix} y_2-y \\ y-y_1 \end{bmatrix} \tag{101}$$

A diagram illustrating the construction of this mapping at a constant detector grid coordinate (red line) from the projected surface panels is shown in Figure 45.

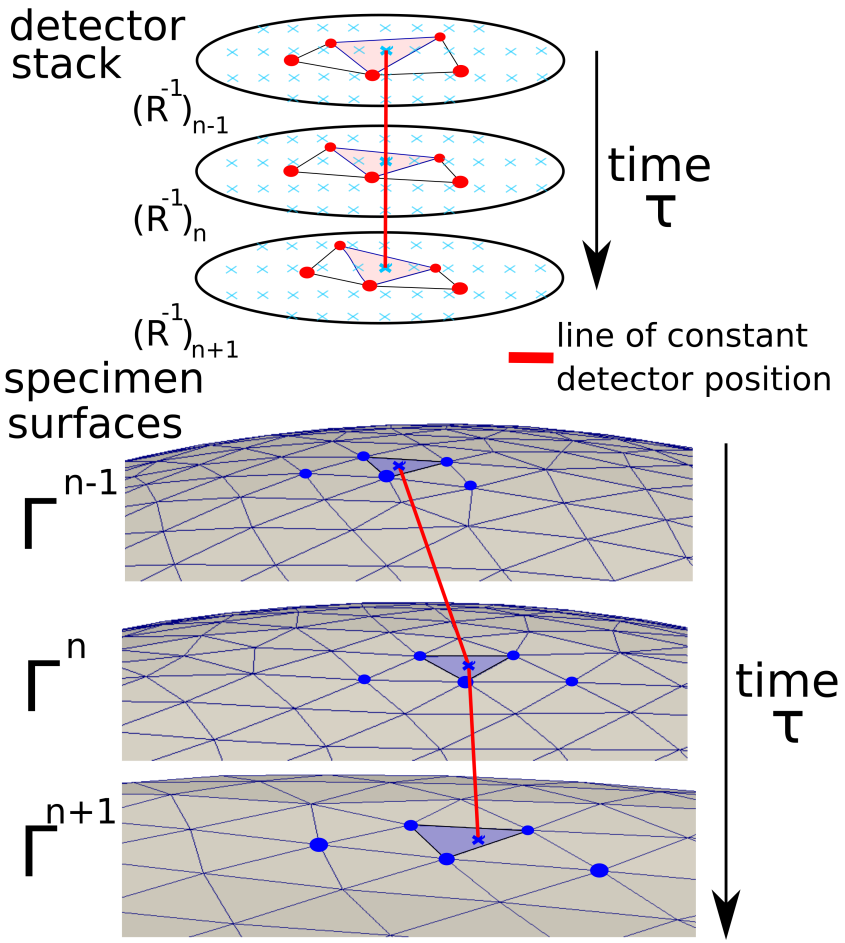


Figure 45: The construction of the temporal inverse mapping $\mathcal{R}_{\alpha}^{-1}(\tau)$ is shown at a particular detector grid position. The panel this point falls within is highlighted at each model instance. Finally, by interpolation, the corresponding specimen surface position can be derived throughout time (red line).

In later thesis chapters, examples of specimen geometries will be considered where these bijectivity and continuity assumptions for the inverse mapping can locally breakdown. If attempting to reconstruct such systems, the model can aid in potentially identifying these regions.

3.9 Data Simulation and Processing

So far, the theoretical groundwork behind the continuum evaporation model has been outlined. However, in order to leverage the model, it must be capable of making predictions directly comparable to experiment. The following section will outline how this comparative data can be generated. As only the 3D model can be directly compared with experiment, these methods are constructed here only for 3D.

3.9.1 Local Evaporation Rate

In order to consider physically realistic evaporated ion fluxes, the local evaporation rate of material must be determined. One method is to use the output from the local evaporation rate equation (Eq. (3.1)). However, a more stable and accurate approach is to directly estimate the true local volume of evaporated material between iterations. Recalling that Γ^n is the specimen surface at the n-th model iteration, a backward-difference-estimated closest distance ($v_-^n(\mathbf{s})$) can be constructed via Eq. (102) using the specimen surfaces at neighbouring model iterations. Assuming evaporation is occurring normal to the surface, $v_-^n(\mathbf{s})$ should approximately give the locally evaporated volume of material per unit area at surface position $\mathbf{s}$, between the previous model state $\Gamma^{n-\gamma}$ and the current model state Γ^n. Via this backward difference approximation, an estimate for the total volume of evaporated material between model states $\Gamma^{n-\gamma}$ and Γ^n can then be obtained using Eq. (103), and an estimate for the local relative evaporation probability density at $\mathbf{s} \in \Gamma^n$ can be constructed using Eq. (104).

$$v_{-}^{n}(\mathbf{s}) = \min_{\mathbf{s}' \in \Gamma^{n-\gamma}} ||\mathbf{s} - \mathbf{s}'|| \tag{102}$$

$$\mathcal{V}_{-}^{n} = \int_{\Gamma^n} v_{-}^{n}(\mathbf{s}) \; d^2\mathbf{s} \tag{103}$$

$$p_e^n(\mathbf{s}) \; d^2\mathbf{s} = \frac{v_{-}^{n}(\mathbf{s})}{\mathcal{V}_{-}^{n}} \; d^2\mathbf{s} \tag{104}$$

Here $\mathcal{V}_{-}^{n}$ is an estimate for the total evaporated volume between model states $\Gamma^{n-\gamma}$ and Γ^n, $p_e^n(\mathbf{s})$ is the local evaporation probability density (estimated via closest distance), and γ is the considered spacing between neighbouring model projection states (in this work $\gamma = 5$). Finally, performing discretisation, whilst assuming the evaporation probability over a panel to be constant, an estimate for the relative probability of ion evaporation from panel Γ_i^n can be obtained by Eq. (107).

$$(\bar{R}_e)_i^n = v_{-}^{n}(\mathbf{x}_i) \; A_i^n \tag{105}$$

$$\mathcal{V}_{-}^{n} = \sum_{j}^{\Gamma^n} v_{-}^{n}(\mathbf{x}_j) \; A_j^n \tag{106}$$

$$p_i^n = \frac{v_{-}^{n}(\mathbf{x}_i) \; A_i^n}{\mathcal{V}_{-}^{n}} \tag{107}$$

Here $\mathbf{x}_i$ is the centre point of panel Γ_i^n, p_i^n is its evaporation probability, A_i^n is its area, and $(\bar{R}_e)_i^n$ is the estimated evaporated volume over Γ_i^n between $\Gamma^{n-\gamma}$ and Γ^n.

Using the closest surface distance approach provides a more stable measure of evaporation rate that is averaged over iterations, compared to the Arrhenius predicted rate in Eq. (3.1). These two measures are compared for the same model in Figure 46. Throughout the rest of this thesis, it is this closest distance method that has been applied whenever synthetic data generation is considered.

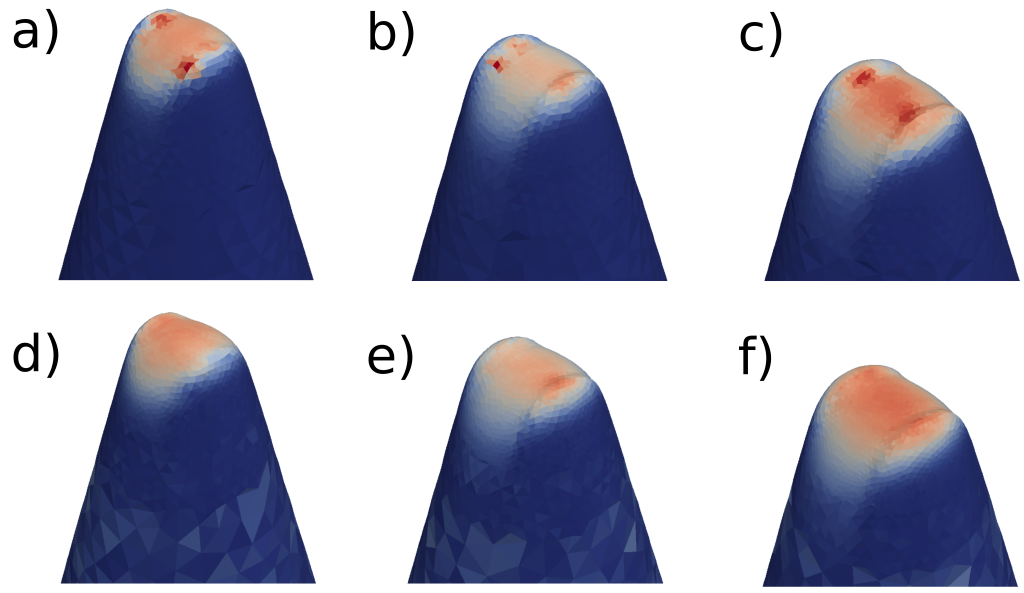


Figure 46: Evaporation of a vertical multilayer structure. (a-c) Instantaneous evaporation rate predicted by Eq. (3.1). (d-f) Evaporation rate estimated by closest distance. This closest distance rate can be seen to be less noisy at the apex where ion projection is performed.

3.9.2 Realistic Launching of Ions

Now that a stable local evaporation rate can be calculated over the model surface, ions can be launched proportional to this rate, ensuring that the resulting simulated data is physically comparable to experiment.

Initially the surface panel of origin can be determined by a residence-time algorithm [110]. First a cumulative function of panel probabilities in Eq. (104) is determined $P_i^n = \sum_j^i p_i^n$ (the exact ordering of panels here is irrelevant). Noting that p_i^n are normalised, a random real number r between 0 and 1 is generated. The panel selected for evaporation Γ_k^n then satisfies the condition $P_{k-1}^n < r \leq P_k^n$. Once a launch panel has been chosen, an exact ion launch position can be selected by generating some random position on this panel.

In the 3D model, internal material phases are defined by bounding triangle surface meshes. Therefore, a launched ion's phase is determined via a point-in-polygon test (here performed through ray casting [173] using the even-odd

rule [174]) of its initial launch position with respect to these phase meshes. Launched ion trajectories can then be calculated up to the detector (Section 3.5.7).

If only the hitmap is required, then some user-defined fixed number of ions can be launched off the surface. However, a synthetic dataset directly comparable to experimental data can be obtained by defining an ionic volume v_{ion} for the model (future models could extend this to allow for species-specific volumes). A total number of ions (I^n) can then be determined that should be launched at the model projection state Γ^n (Eq. (108)).

$$I^n = \text{round}\left(\eta \, \frac{\sum_j^{\Gamma^n} v_-^n(\mathbf{x}_j) \; A_j^n}{v_{\text{ion}}}\right) \tag{108}$$

Here η is the instrument detection efficiency, taking a value between 0 and 1. In practice, ions are only launched from panels that are a user-defined distance from the apex, reducing the calculation of ions outside of the FOV.

The resulting data is a synthetic point cloud of simulated ionic evaporation events in detector space ($\mathbb{D} = \mathbb{R}^2 \times \mathbb{N}$), each with a 2D detector position and evaporation sequence position. Each ion is also labelled by its phase of origin (determined by point-in-polygon testing [174, 173]). User-assigned compositions for model phases then allows for the calculated evaporation events to be randomly assigned particular ion types, with assignments weighted by the inputted composition. This species assignment process allows synthetic data to be directly compared with the experimental data both prior or post reconstruction.

3.9.3 Calculating Density and Trajectory Overlap Detector Maps

In APT, the raw data from an analysis is the detector sequence data. Taking a detector sequence interval, and visualising ions' detection x-y coordinates within this slice concurrently, is known as an ion detector hitmap. An example experimental hitmap is visualised for a similar structure to that in Figure 47a. A common data processing method is to bin this data and calculate the density distribution over the detector (Figure 47b). These distributions are known as density hitmaps. Local fluctuations in density can provide insight into a specimen's local magnification.

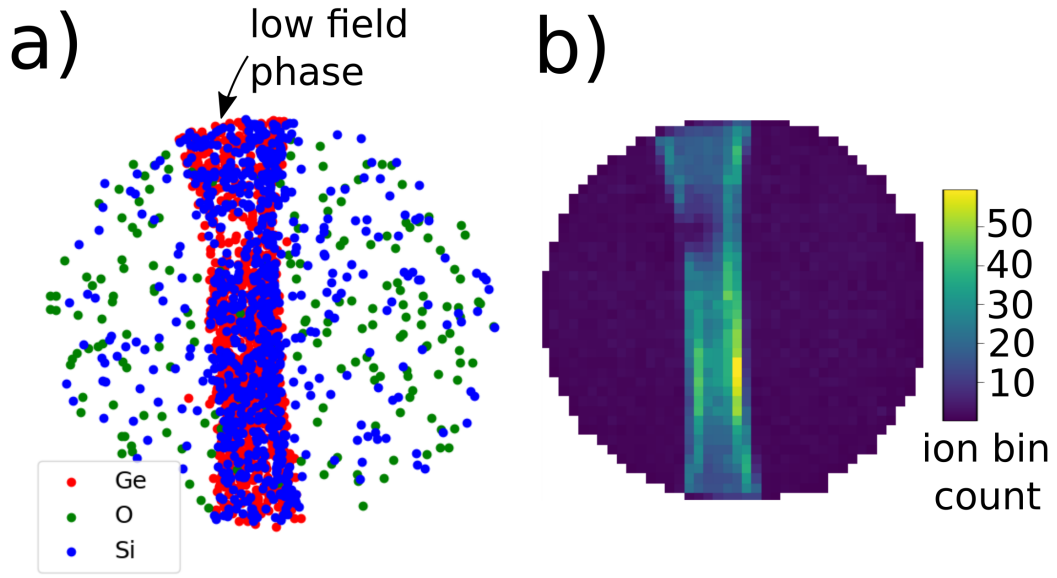


Figure 47: (a) Detector hitmap of 1000 ions in an experimental semiconductor device dataset (FinFET). (b) Corresponding density hitmap generated by spatially binning these points. The higher density region implies demagnification. This density histogram can be interpreted as the probability of finding an ion within a particular bin.

In order to compare model results to experiment, this hitmap data should be simulated. However, unlike with atomic models where individual atoms within the emitter are modelled, the continuum model does not directly simulate individual atoms. However, as discussed in Section 3.9.1, synthetic hitmap data comparable with experiment can still be generated by considering surface evapo-

ration rates.

The most obvious generation method is by directly launching ions from the specimen surface according to the Monte Carlo (MC) approach in Section 3.9.2. Once a sufficient number of simulated ions have been evaporated, a density hit-map comparable to experiment can be constructed by calculating a multidimensional histogram or through Kernel Density Estimation (Section 3.9.6). While this method is the most comparable to the underlying physical process, it requires a relatively costly trajectory evaluation for every ion in our synthetic dataset.

Therefore, a more computationally efficient method is proposed where densities can instead be directly constructed from evaporation fluxes via the Jacobian Determinant $||\mathbf{J}||$ (defined in Section 3.8.3). Assume that at some time, the specimen mesh is given by Γ. An exact density $\rho_d(\mathbf{x}_d)$ at detector position $\mathbf{x}_d = (x_d, y_d)$ can be calculated by considering the model static forward mapping ($\mathcal{R}_\alpha(\mathbf{s})$) at this same time.

$$\rho_d(\mathbf{x}_d) = \int_\Gamma R_e(\mathbf{s})\ \delta\big(\mathcal{R}_x(\mathbf{s}) - x_d\big)\delta\big(\mathcal{R}_y(\mathbf{s}) - y_d\big)\ d^2\mathbf{s} \tag{109}$$

$$= \sum_i^k (\bar{R}_e)_i \int_{\Gamma_i} \delta\big(\mathcal{R}_x(\mathbf{s}) - x_d\big)\delta\big(\mathcal{R}_y(\mathbf{s}) - y_d\big)\ d^2\mathbf{s} \tag{110}$$

Here $\delta(.)$ is the Dirac delta function, $R_e(\mathbf{s})$ is the local surface evaporation rate, $(\bar{R}_e)_i$ is the estimated evaporated volume over panel Γ_i by Eq. (105), $||\mathbf{J}_i||$ is the estimated Jacobian determinant over panel Γ_i, and $\mathbf{s}$ is a surface position. The quantity $\rho_d(\mathbf{x}_d)$ defines an exact density at a point on the detector. However, experiment does not have access to this exact detector point density. Instead, the detector density is obtained by averaging over some detector region B, typically individual pixels on a discretised grid. This averaging over a particular region is given in Eq. (111).

$$< \rho_d >_B = \frac{1}{A_B} \int_B \rho_d(\mathbf{x}_d)\ d^2\mathbf{x}_d \tag{111}$$

$$= \frac{1}{A_B} \sum_i^k (\bar{R}_e)_i \cdot \int_B \int_{\Gamma_i} \delta\big(\mathcal{R}_x(\mathbf{s}) - x_d\big)\delta\big(\mathcal{R}_y(\mathbf{s}) - y_d\big)\ d^2\mathbf{s}\ d^2\mathbf{x}_d \tag{112}$$

$$= \frac{1}{A_B} \sum_i^k (\bar{R}_e)_i \cdot \big|||\mathbf{J}||_i\big|^{-1} \int_{\boldsymbol{\mathcal{R}}(\Gamma_i)\cap B} d^2\mathbf{x}_d \tag{113}$$

$$= \frac{1}{A_B} \sum_i^k (\bar{R}_e)_i \cdot \big|||\mathbf{J}||_i\big|^{-1} \cdot A_{\boldsymbol{\mathcal{R}}(\Gamma_i)\cap B} \tag{114}$$

The inverse Jacobian determinant term ($\big|||\mathbf{J}||_i\big|^{-1}$) arises from the integral over Γ_i on transformation into detector coordinates. Here $A_{\boldsymbol{\mathcal{R}}(\Gamma_i)\cap B}$ is the area within the intersection of the projected panel Γ_i and the averaged detector region B (Figure 48), and A_B is the area of B.

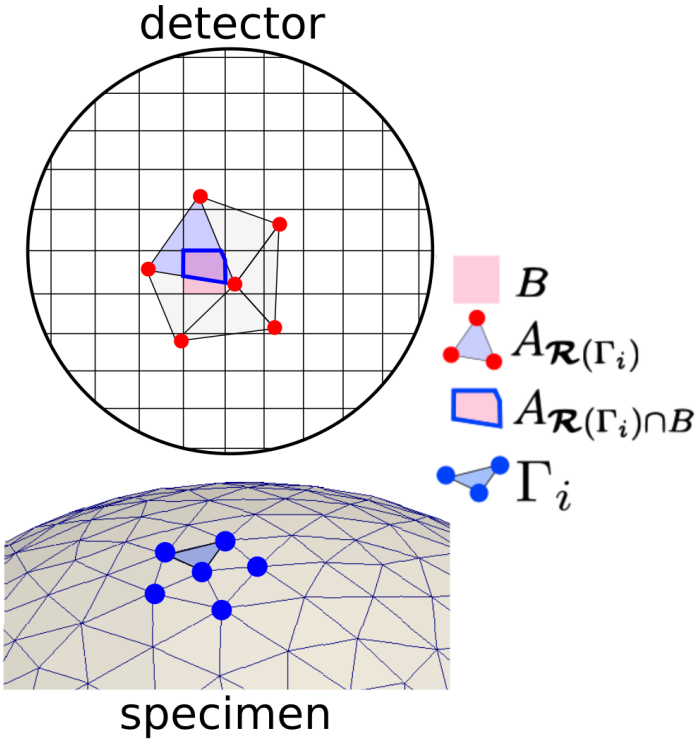


Figure 48: Diagram showing the density hitmap calculation within a particular pixel (highlighted pink). Considering the contribution for a particular panel (blue), the intersection area $A_{\boldsymbol{\mathcal{R}}(\Gamma_i)\cap B}$ can be identified (blue border), allowing its calculation via Eq. (114). This is performed for all panels. In this example, the mapping is locally bijective so that projected panels do not flip and overlap.

For a detector discretised into N pixels, we can construct the following matrix system describing the transfer of evaporation fluxes onto the detector. This system is given via Eq. (115).

$$\mathbf{M} \cdot \mathbf{R_e} = \boldsymbol{\rho} \qquad \text{where } M_{ij} = \frac{1}{A_{B_i}} \left| ||\mathbf{J}||_j \right|^{-1} \cdot A_{\boldsymbol{\mathcal{R}}(\Gamma_j) \cap B_i} \tag{115}$$

Here $\mathbf{R_e}$ is the vector of the evaporated volumes over each surface panel, B_i is a detector pixel, $\rho_{B_i} = A_{B_i} < \rho_d >_{B_i}$, where $\rho_{B_i} \in \boldsymbol{\rho}$, records the ion hit count within B_i, and $\mathbf{M}$ is the $N \times k_{\text{FOV}}$ rectangular transfer matrix. The integer k_{FOV} is the total number of surface panels whose projections intersect with the detector.

The intersection area $A_{\boldsymbol{\mathcal{R}}(\Gamma_i) \cap B}$ can be calculated by determining the bounding polygon of $A_{\boldsymbol{\mathcal{R}}(\Gamma_i) \cap B}$ via the Cohen-Sutherland line clipping algorithm [174], and then calculating its area. This is performed for each detector pixel (Figure 48). By also recording whether a voxel contains an inverted panel section due to trajectory crossover, the presence of any trajectory overlap and multivalued inverse mapping regions can be determined (Figure 42b).

The Figure 49 compares the simulated density hitmaps generated by these two methods for the vertical layer structure in Figure 47.

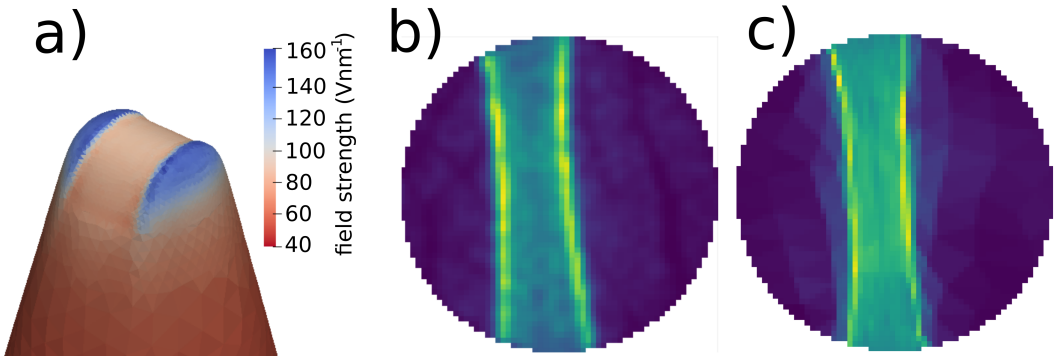


Figure 49: (a) The model surface that ions are launched off. (b) Density hitmap simulation by an MC approach (95681 ions launched in 19 minutes 10 s). (c) Density hitmap simulation via the flux method (calculated in 3.6 s).

3.9.4 Calculating Composition Detector Maps

As well as density, determining the local phase and composition throughout the model estimated detector space is useful data for experimental comparison. While this local composition data can be obtained by applying histogram or KDE methods (Section 3.9.6) to a MC generated synthetic point cloud dataset (see Section 3.9.2), as explained in Section 3.9.3, the generation of such datasets is slow. Instead, a good estimate for the local phase can be constructed by launching ions from the corners of surface panels.

Like with the previous density calculations, the detector is discretised on a pixellated grid. For simplicity, each pixel has been assigned only a single projected model phase using nearest-neighbour interpolation of panel trajectory data (see Figure 50a).

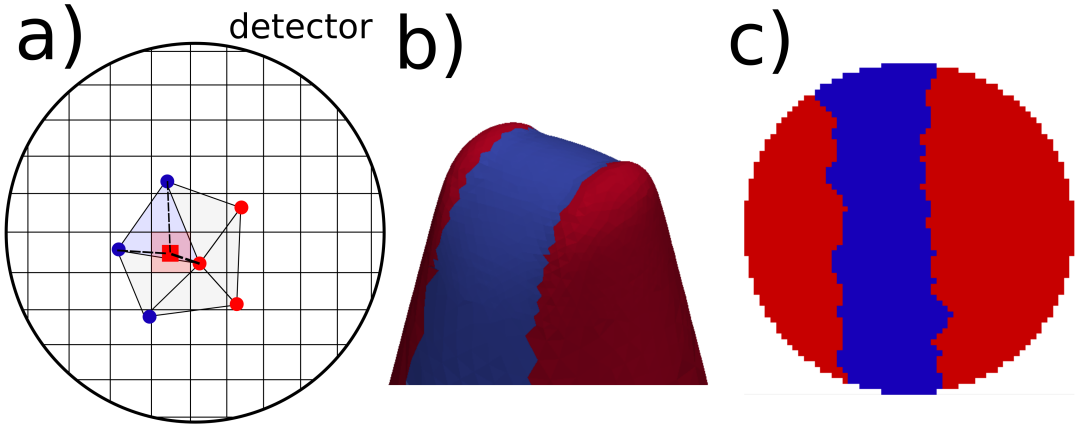


Figure 50: (a) Diagram illustrating the nearest-neighbour interpolation of projected phases onto the detector grid. (b) Specimen surface showing local material phase. (c) Its corresponding predicted local detector phase map.

3.9.5 Model Depth Calibration

While the MC method described in Section 3.9.2 generates directly comparable data to experiment, the density and phase detector maps are currently only defined at particular model surface instances. In order to also directly compare these to experimental data, detector maps must be proportionally spaced and

interpolated throughout the detector space.

The key to calculating this spacing is to consider the total volume of evaporated material within the model FOV. At the atomic scale, it is individual ions (originally specimen atoms) that are being detected during experiment. Each of these detected ions takes up some average ionic volume ν_{ion} within the original specimen. In experiment, these ionic volumes are phase specific.

Therefore, detector maps are assigned depth coordinates in detector space ($z_{\text{d}}^{\gamma\cdot l} \in \mathbb{N}$) equal to the total number of ions evaporated prior to the model projection state $\Gamma^{\gamma\cdot l}$. This number is proportional to the total associated volume of evaporated material within the FOV prior to this model state (see Eq. (116)).

$$z_{\text{d}}^{\gamma\cdot l} = -\sum_{n=p_i+1}^{l} \text{round}\left(\eta\,\frac{\sum_i^N \rho_{B_i}^{\gamma\cdot n}}{\nu_{\text{ion}}^{\gamma\cdot n}}\right) \quad \text{for } l \text{ from } \{\Gamma^{\gamma\cdot p_i}, \Gamma^{\gamma\cdot p_i+\gamma}, ..., \Gamma^{\gamma\cdot l}, ...\Gamma^{\gamma\cdot p_f}\} \tag{116}$$

Here $\{\Gamma^{\gamma\cdot p_i}, \Gamma^{\gamma\cdot p_i+\gamma}..., \Gamma^{\gamma\cdot l}, ...\Gamma^{\gamma\cdot p_f}\}$ represents the subset of model projection states being compared with experiment, and from which ion projection is performed. The $\rho_{B_i}^{\gamma\cdot n}$ is the ion hit counts in detector pixel B_i (with total pixels N) between model projection states $\Gamma^{\gamma\cdot n-\gamma}$ and $\Gamma^{\gamma\cdot n}$ (as defined in Section 3.9.3). The species-averaged ionic volume is given by $v_{\text{ion}}^{\gamma\cdot n}$. For reasons that will become clearer in Section 3.11.1, this ionic volume is set to depend on the model state.

Finally, assuming the same detector grid has been used, interpolation over the entire voxelised detector space can be performed via similar interpolation schemes to those in Eq. (100). This same depth calibration procedure will be revisited when calibrating $\mathcal{R}_\alpha^{-1}$ to experimental data for performing model-driven reconstruction.

3.9.6 Local Density and Composition Estimation for Point Clouds

The previous sections have outlined how local density and phase (relating to composition) can be predicted by the model throughout detector space (Section 3.9.5). However, raw experimental data is a point cloud, with individual points corresponding to particular mass-ranged ions. In order to allow quantitative comparison, analogous voxel fields for local density $\rho(\mathbf{x})$ and composition $\sigma_p(\mathbf{x})$, where p indexes the different ranged ions, must be calculated from this experimental data. These can be calculated within either the detector space or reconstruction via Eqs. (117) and (118).

$$\sigma_p(\mathbf{x}) = \frac{\rho_p(\mathbf{x})}{\rho(\mathbf{x})} \tag{117}$$

$$\rho(\mathbf{x}) = \sum_{p}^{P} \rho_p(\mathbf{x}) \tag{118}$$

Here $\sum_p^P$ is the sum over all ion types. Therefore, calculation of $\sigma_p(\mathbf{x})$ and $\rho(\mathbf{x})$ comes down to estimation of $\rho_p(\mathbf{x})$.

While the simplest method is to estimate each $\rho_p(\mathbf{x})$ via a multidimensional histogram, a smoother estimation for point cloud densities can be obtained through Kernel Density Estimation (KDE). Throughout this work, visualised ion densities have been calculated via KDE using an Epanechnikov kernel [175].

3.10 Specimen-Independent Trajectory Compression

So far the model specimen has been assumed to be floating in free space (see Figure 21). However, this setup does not accurately resemble the true electrostatic domain as present in experiment. In reality the problem domain is bounded by the atom probe chamber, which is typically held at some bias voltage [176]. Additionally, in LEAP instruments a local electrode is positioned just above the specimen apex to increase FOV (see Figure 51). The resultant effect of these additional instrument components is an enhanced compression of ion trajectories. The flexibility to adapt the model and incorporate their effects is critical for enabling direct comparison to experiment data.

3.10.1 Additional Instrument Components

It is straightforward to include additional equipotential boundary meshes into the BEM solver when solving the electrostatics. This allows for additional instrument components can be accounted for in the field solution, such as a local electrode (Figure 51). However, for predicted surface fields and ion trajectories that are directly comparable with experiment, simulation of the true specimen shank geometry and specimen holder would also be required [176]. A full-scale simulation of the specimen apex, shank, holder, and instrument chamber was found to be computationally impractical given the current computational efficiency of the implemented BEM solver. This is further complicated by the presence of the voltage biased detector (a typical bias being -2.2 kV [176]). This detector bias breaks the scale invariance of the electrostatic problem, such that the field can no longer be solved for an arbitrary specimen voltage and then rescaled (see Section 3.1). Given these challenges, it is unlikely that electrostatic simulation of a fully realistic problem domain is practically achievable without further method optimisation [177, 131].

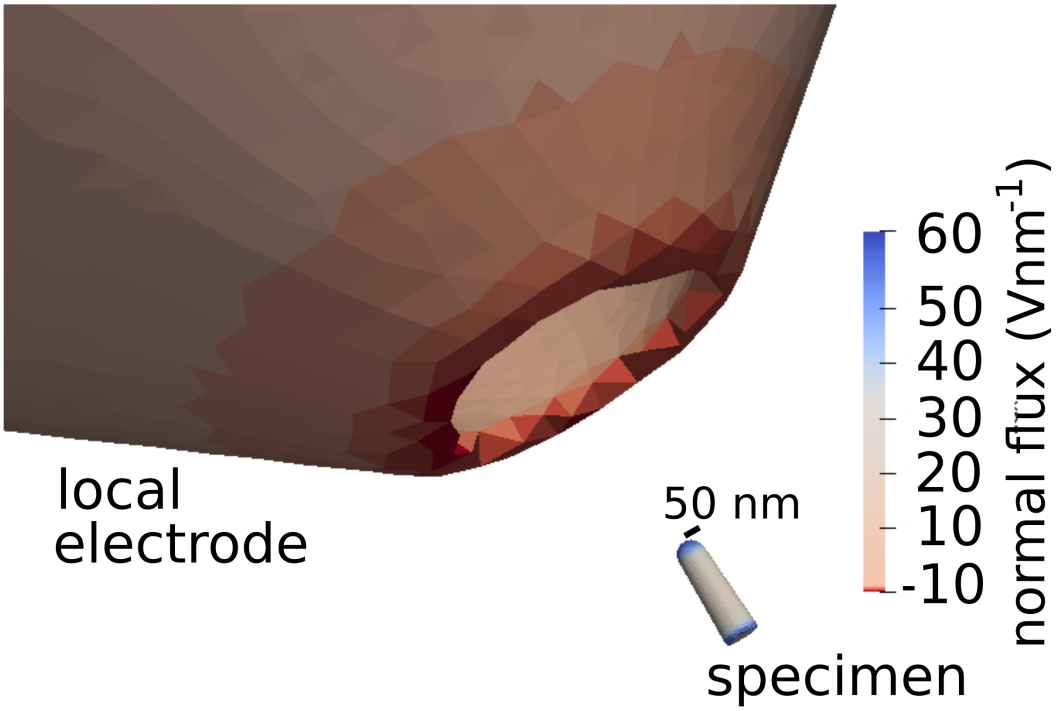


Figure 51: Proof-of-concept simulation of specimen electrostatics involving a local electrode (not to scale). Note that the specimen shank is still truncated and floating in free space. Therefore, even with the local electrode, results cannot be directly compared with experiment.

As discussed in Section 2.4.2, it is known from both modelling and experiment that ion trajectories from steady-state evaporating emitters of homogeneous material can be well approximated by mathematical projections [55, 33, 31]. It will therefore be assumed that at some sufficient distance from the specimen apex, surface protrusions and pits due to multiphase evaporation are comparatively small, and the specimen apex can be reasonably approximated as near hemispherical. Due to the radial symmetry of this approximated specimen geometry, it is likely that ion trajectories beyond this distance from the surface can be reasonably described by some mathematical projection function. In this work, a linear projection similar to that used in [63] has been applied.

3.10.2 An Instrument Transfer Function

Due to a number of approximations being made by the currently modelled electrostatics (e.g. lack of a biased APT detector and chamber), model predictions of ion trajectories cannot directly be compared to experimental data. However, experiment has shown that trajectory compression can often be well approximated by a linear relation between the angle of detector incidence (θ_{Det}), and the angle of surface evaporation (θ_{Tip}). These angles are taken with respect to the detector normal ($\mathbf{n}_{Det}$). This relation is given in Eq. (119).

$$\theta_{Det} = \kappa \cdot \theta_{Tip} \tag{119}$$

In this work, a linear compression law up to the detector is assumed once ions have reached a particular distance from the specimen surface (d). The majority of ion trajectory deflection due to the influence of apex surface features on the surrounding field occur close to these features. Therefore, the majority of these deflections should be accounted for through an appropriate choice for d.

The linear projection of a particular ion trajectory is equivalent to the problem of solving the intersection between a line and plane (Eqs. (120)).

$$\begin{aligned} \mathbf{p} &= \mathbf{p}_0 + l\ \boldsymbol{\kappa}'(\hat{\mathbf{v}}_0) \\ l &= \frac{(\mathbf{p}_{Det} - \mathbf{p}_0) \cdot \hat{\mathbf{n}}_{Det}}{\boldsymbol{\kappa}'(\mathbf{v}_0) \cdot \hat{\mathbf{n}}_{Det}} \\ \boldsymbol{\kappa}'(\hat{\mathbf{v}}_0) &= (\cos\phi\ \sin\theta, \sin\phi\ \sin\theta, \cos\theta) \\ \theta &= \kappa\ \arccos(\hat{\mathbf{n}}_{Det} \cdot \hat{\mathbf{v}}_0) \\ \phi &= \arctan(\frac{v_0^x}{v_0^y}) \end{aligned} \tag{120}$$

Here $\mathbf{p}$ is the detection coordinate, $\mathbf{p}_0$ is the position to where the ion trajec-

tory has been directly calculated, $\hat{\mathbf{v}}_0 = (v_0^x, v_0^y, v_0^z)$ is the ion velocity direction at point $\mathbf{p}_0$, $\hat{\mathbf{n}}_{Det} = (0, 0, -1)$ is the detector normal, $\mathbf{p}_{Det} = (0, 0, L)$ is a point on the detector, and κ is the linear compression factor (a model parameter). The setup for this linear projection is shown in Figure 52.

This linear projection can be considered as a transfer function, taking model calculated ion trajectories as inputs, and mapping these to detector positions directly comparable with experiment. Alternatively, a potentially more accurate transfer function could be obtained by physically solving for the electrostatics of the instrument chamber just once [176], and then assuming that the field away from the evaporating specimen apex remains approximately unchanged throughout time.

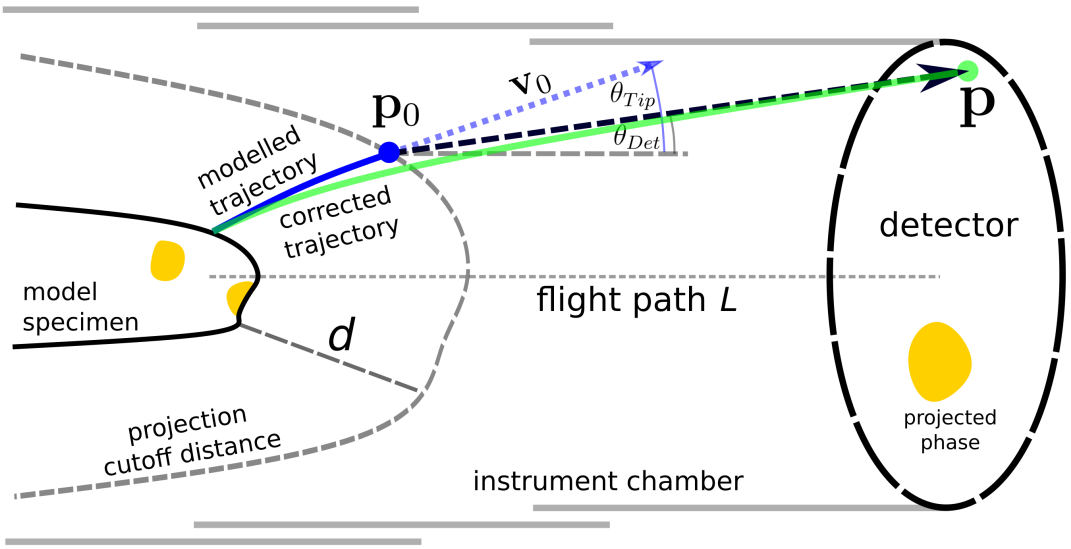


Figure 52: The geometric setup for the linear transfer projection. Ion trajectories are calculated up to a distance (d) from the specimen surface (terminating at the blue point). Beyond this distance, a linear projection is performed onto the detector plane (the green point) to account for any additional instrument trajectory compression.

3.10.3 Deriving a Model Cutoff

Alongside the compression parameter (κ), the linear transfer function also contains an additional parameter d: the distance cutoff beyond which to apply the mathematical projection (Section 3.10.2). Too small a value for d could result in trajectory deflections due to surface structures being underestimated. However, too large a value and the projection might not correctly capture the additional instrument compression.

A suitable value for d can be determined by considering both a homogeneous apex shape and an extreme multiphase apex shape, and investigating at what distance from the specimen surface their field solutions converge. The apex geometries, and their field solutions with distance from the surface, are shown in Figure 53. All specimen geometries considered have an apex radius of $R_{\text{apex}} = 35$ nm, and precipitates a radius of $R_{\text{precipitate}} = 6.25$ nm. The evaporation field ratio is $F_{\text{precipitate}} : F_{\text{apex}} = 1 : 2$ in the low-field example (Figure 53a), and $F_{\text{precipitate}} : F_{\text{apex}} = 2 : 1$ in the high-field example (Figure 53b). The field differences for these example microstructures are fairly extreme, and so the derived cutoff distance should provide a reasonable upper bound for further simulations.

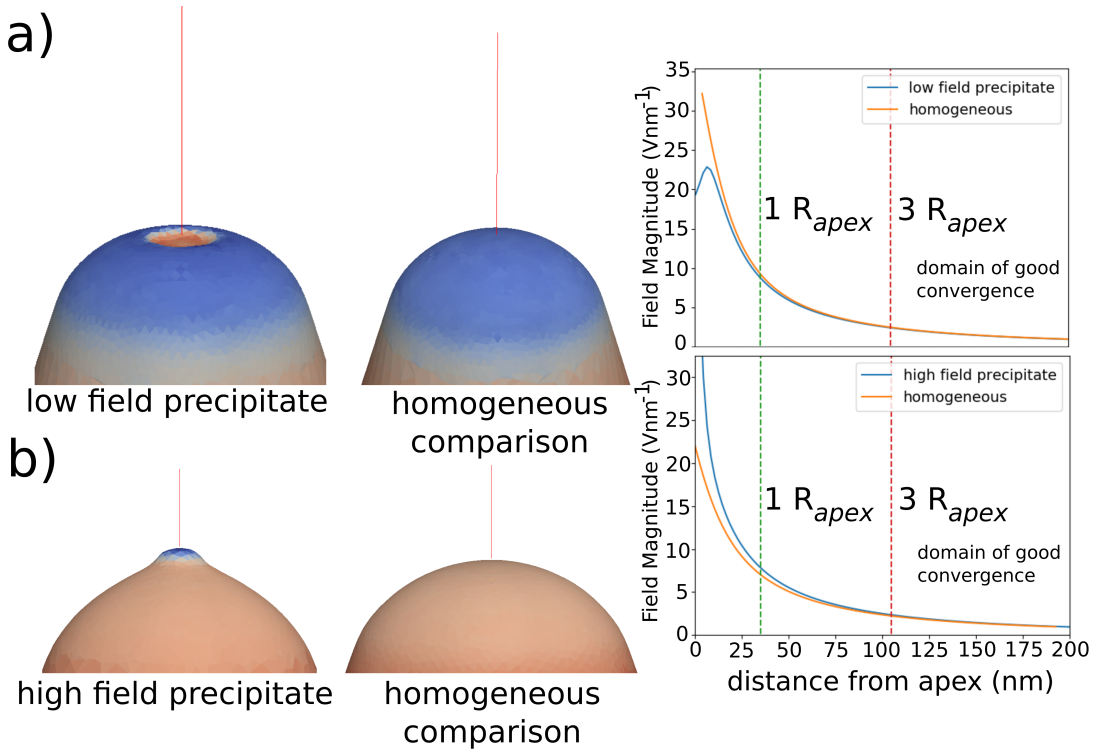


Figure 53: Field solutions along a vertical profile away from the apex for (a) a low-field precipitate and (b) a high-field precipitate. The plotted fields converge beyond a distance of $\sim$ 100 nm, or three apex radii (3 R_{apex}), from the surface.

In Figure 53, the electric field solutions converges with increasing distance from the specimen surface, with good convergence achieved around 3 R_{apex} from the surface. By considering these field solutions, a cutoff distance for performing the linear projection has been chosen of $d = 5\ R_{\text{apex}}$. This cutoff is well into the region displaying good convergence between the multiphase and homogeneous specimen fields, but still before the vast majority of the 0.102 m flight path. It is this cutoff that has been used throughout the rest of this work.

Now that an instrument transfer function has been defined, it is possible to make direct quantitative comparisons between model predictions and experimental data. In particular, the model's high computational efficiency raises the possibility of using its trajectory mapping to directly perform image reconstruction.

3.10.4 Specimen Voltage Correction

Before moving onto discussing model-driven reconstruction, it should be briefly noted that due to unphysical geometric assumptions (e.g. the lack of specimen holder), the determined applied voltage (see Eq. (22)) will likely not correlate well with experiment. While a solution for resolving this discrepancy is not presented here, a possible correction could consider some sort of field factor modification to the predicted voltages, similar to k_f in Eq. (11). This correction would only be required to directly compare the simulated and experiment voltage curves, and under current model assumptions such a correction would leave ion trajectories and relative surface evaporation rates unaffected.

3.11 A Model-Driven Reconstruction

With the definition of an instrument transfer function, the developed model can now be used to estimate an experiment's trajectory mapping $\mathcal{R}$. This mapping is a function of the initial specimen geometry, phase-specific evaporation parameters, the transfer function compression parameter (κ), and specimen alignment with respect to the detector. The following section will detail a protocol for how an estimated $\mathcal{R}^{-1}$ can drive reconstruction, and outline methods for calibrating this mapping to ensure that the generated reconstruction best matches our prior knowledge of the specimen structure. This calibration will be performed through model parameter optimisation and constrained spatial transformations.

3.11.1 The Reconstruction Protocol

A method for constructing $\mathcal{R}^{-1}$ has previously been described in Section 3.8.4. This inverse mapping estimate assumes bijectivity, thereby transforming a single position from detector space to a single position in sample space ($\mathcal{R}^{-1} : \mathbb{D} \rightarrow \mathbb{S}$). A particular experimental dataset consisting of e ranged ions can be described by $\hat{\mathbf{X}^D} = \{\mathbf{x}^0, ..., \mathbf{x}^e\}$. Here, a particular ion has coordinates $\mathbf{x}^i = (d_x^i, d_y^i, N^i, r^i)$, such that $(d_x^i, d_y^i, N^i) \in \mathbb{D}$ is its detector space position, and r^i is its ranged ion type. By transforming each ranged ion's detector space position under $\mathcal{R}^{-1}$, the reconstruction ($\hat{\mathbf{X}^D}$) can be constructed iteratively within sample space ($\mathbb{S}$). Here, a reconstructed ion is represented by coordinates $(x^i, y^i, z^i, r^i) \in \hat{\mathbf{X}}^{\mathcal{R}}$, such that $(x^i, y^i, z^i) \in \mathbb{S}$ is its 3D position, and r^i is its ranged ion type.

Before attempting reconstruction, depth calibration of the experimental ions and model states within detector space must be performed. Throughout this work, the 'depth' dimension has been measured by the set of integers $\mathbb{N}$, describing ion positions in the experiment's detected evaporation sequence. By considering the total evaporated volume of material throughout the model's evolution, detector space positions for particular model states can be determined via

Eq. (116) (Section 3.9.5). Following this depth calibration, reconstruction can be performed under $\mathcal{R}^{-1}$ via Eqs. (100) and (101) (Figure 54b). In these equations, the inverse mapping's temporal parameter τ is equivalent to ion's detector space depth position.

However, in order to perform this depth calibration of model states, a valid species-averaged ionic volume must be determined between each of the adjacent model projection states (see Section 3.9.5). Together these ionic volumes are described by the set $\{\nu_{ion}^{p_i}, ..., \nu_{ion}^{i-\gamma}, \nu_{ion}^{i}, ..., \nu_{ion}^{p_f}\}$, where ν_{ion}^{i} is the ionic volume between the neighbouring model projection states $\Gamma^{i-\gamma}$ and Γ^{i}. Ideally, these ionic volumes should be near identical. However, a large number of possible sources of variation exist, including numerical errors, ranging errors and biases between phases, and physical errors. Additionally, in real systems the atomic volume can vary between species and material phase, variation that the current protocol does not account for. Therefore, to avoid these errors accumulating during the reconstruction procedure, the ionic volume has been adaptively adjusted according to detector space depth. This ensures that recognisable microstructural events in both the experiment and model data align at known depth positions within the evaporation sequence.

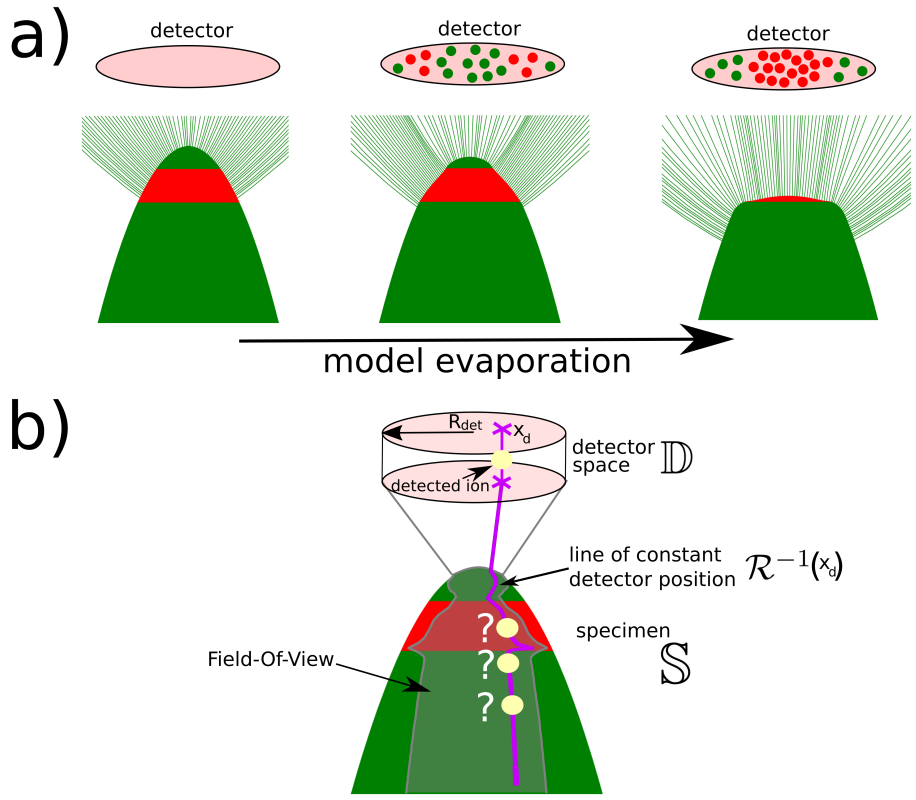


Figure 54: Diagram outlining the protocol and requirement for depth calibration. (a) Simulation of specimen evaporation (2D model). (b) Visualisation of a line of constant detector position x_d in sample space. Without depth calibration between the model and experiment, the correct positioning of ions along this line would be ambiguous.

3.11.2 Landmark Depth Calibration

In order to correct for multiphase distortions, the same microstructure must be present in both the APT dataset and the specimen model. This same microstructural 'event', where a microstructure appears or disappears from the FOV, can then be identified both within the experimental data and model (Figure 55). Therefore, these events can provide fixed depth landmarks for which both the model and experiment should align.

Assuming there is a compositional or density signal within the experimental data that uniquely identifies this event, an exact depth coordinate - a position in the detected evaporation sequence - for the event within detector space can

be determined. By considering the same event during the model evolution, and noting that particular model surface state instances correspond to constant depth positions within detector space, surface states can be identified that should match to these depth coordinates (Figure 55). The exact surface states can then be identified by considering when microstructural phases appear or disappear from the model's detector phase maps (see Section 3.9.4).

The species-averaged ionic volumes between these landmark states can then be calculated. For example, assume that two adjacent landmarks are defined by the model surface states Γ^{S} and $\Gamma^{S+\gamma\cdot l}$, where there are $l-1$ distinct model projection states between these landmark states. Using the terms defined in Section 3.9.5, the ionic volumes for states between these landmarks are given by Eq. (121).

$$v_{\text{ion}}^{S\rightarrow S+\gamma\cdot l} = \eta\ \frac{\sum_{n=S/\gamma+1}^{S+\gamma\cdot l}\sum_{i}^{N}\rho_{B_i}^{\gamma\cdot n}}{I^{S+\gamma\cdot l}-I^{S}} \tag{121}$$

Here $v_{\text{ion}}^{S\rightarrow S+\gamma\cdot l}$ defines the species-averaged ionic volumes to use between model states Γ^{S} and $\Gamma^{S+\gamma\cdot l}$, I^{S} is the total number of experimental ions detected prior to model landmark S, and $\rho_{B_i}^{\gamma\cdot n}$ is the ion hit count within detector pixel B_i (total pixels N) for the model projection state $\Gamma^{\gamma\cdot n}$ (as defined in Section 3.9.3). These ionic volumes allow for assignment of detector space depth coordinates to all model surface states via Eq. (116).

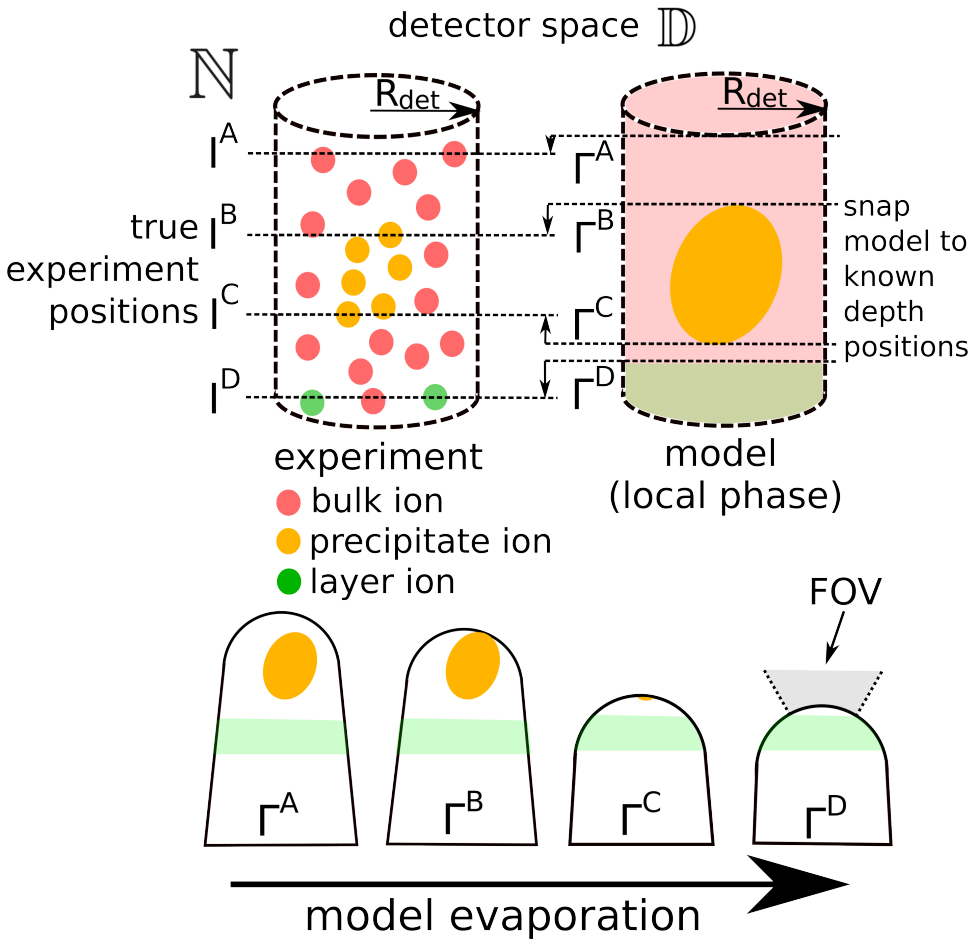


Figure 55: Diagram outlining the landmarking procedure. Landmarked detector space depth positions are aligned to corresponding model states by selecting appropriate ionic volumes (ν^i_{ion}) for states between landmarks. Particular model states (simulation times) correspond to constant depth slices of detector space.

Now that the model states have been depth calibrated to the experiment detector event sequence, placement of detected ions within the sample space can be performed under $\mathcal{R}^{-1}$ via Eqs. (100) and (101). This way, the reconstruction point cloud can be generated. However, as highlighted in Section 3.11, the model still contains a number of free parameters that must be tuned in order to ensure the best quality reconstruction.

3.11.3 Model Parameter Tuning

In order to measure our specimen-specific model's accuracy, the resulting model-driven reconstruction can be compared back to the assumed specimen microstructure. Differences between the location of model phases and the as-reconstructed microstructure imply there to be some inaccuracy or miscalibration in our assumed model. Ideally, compositional differences throughout the reconstruction should correlate well with the model's assumed phase positions. This similarity comparison can be performed both in sample space ($\mathbb{S}$) or detector space ($\mathbb{D}$) (see Figure 56), using the model trajectory mapping ($\mathcal{R}$ and $\mathcal{R}^{-1}$) to transform between these spaces.

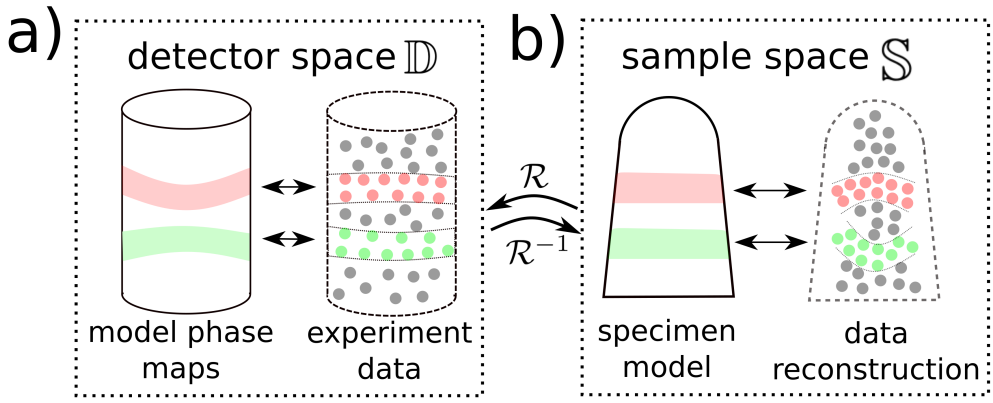


Figure 56: An example comparison between model predictions and experimental data for a multilayer structure. Differences between model predictions and experiment imply model miscalibration. This comparison can be performed in both (a) detector space or (b) sample (reconstruction) space.

Assuming that our initial model phase structure is accurate, we can aim to constrain our model parameters by quantitatively measuring this similarity between experimental composition and model phases. By exploring an ensemble of models with differing parameters, the best fit parameters and corresponding optimised models can be identified.

3.11.4 Specimen Alignment and Image Compression

In order to calibrate the model, the spatial alignment and orientation of our model specimen with respect to the detector must be constrained. This alignment is a rigid body transformation, with degrees of freedom including a horizontal translation ($\vec{\mathbf{r}}$) in the detector plane, and specimen orientation (ϕ, θ, ψ) with respect to the detector (Figure 57). In addition, there is also the additional degree of freedom due to image compression (see Section 3.10), described by parameter κ.

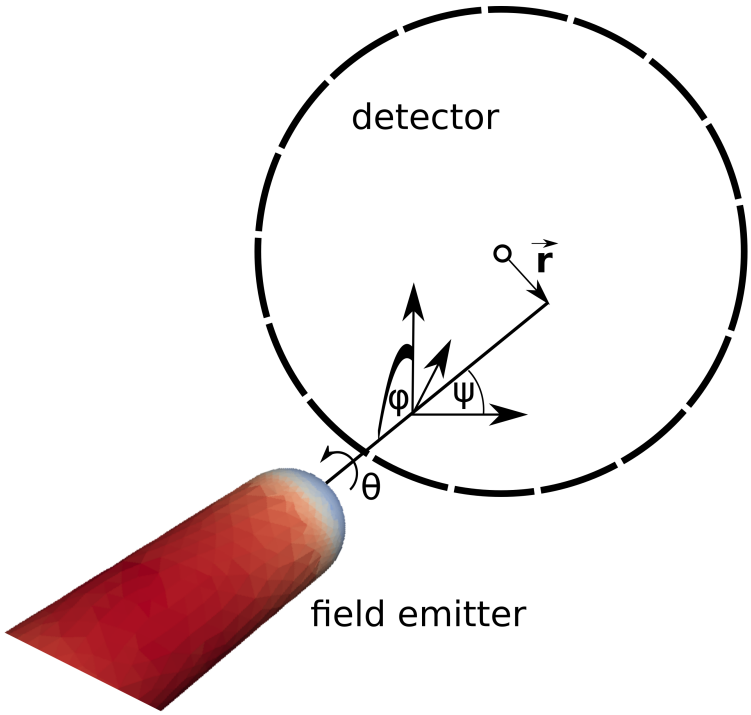


Figure 57: The degrees of freedom in the model spatial alignment with respect to the detector. This includes both translation ($\vec{\mathbf{r}}$) and orientation (ϕ, θ, ψ).

During this work, in order to reduce the size of the explored parameter space, the specimen tilt parameters, given by (ϕ, ψ) in Figure 57, will be assumed as zero. Experimental studies considering the misorientation of grain boundaries [178] imply that, assuming careful specimen holder mounting, this tilt is typically only a few degrees. Future implementations could also constrain this tilt.

3.11.5 Physical Parameters

Alongside the spatial alignment and image compression, there are also the phase-specific parameters governing material evaporation. The isotropic Arrhenius evaporation law, defined in Eq. (21), considers each phase as having a constant evaporation field (F_0). The relative values of these evaporation fields governs model evolution. While theory suggests that the β term in this law likely exhibits some material dependence [73], this has been assumed negligible here. Collectively the independent phase evaporation fields within the model can be described by the set $\mathbf{F}_0 = \{F_0^1, ..., F_0^P\}$. The optimisation method to be described here would still apply to modified evaporation laws.

3.11.6 Parameter Optimisation

Now that the free parameters have been identified, the optimisation problem can be defined. For a set of model parameters ($\dot{\boldsymbol{\theta}} = \{\vec{\mathbf{r}}, \theta, \kappa, \mathbf{F}_0\}$), we obtain a particular model for the experiment ($\boldsymbol{\Gamma} = \{\mathcal{G}, (\Gamma^{p_i}, ...\Gamma^n, ...\Gamma^{p_f}), \mathcal{I}\}$), where $\mathcal{G}$ represents the initially assumed specimen and phase geometries, Γ^n is the specimen surface state at the n-th model iteration, and $\mathcal{I}$ represents the geometries of the simulated detector and other instrument components.

When optimising the model, the alignment parameters $(\vec{\mathbf{r}}, \theta, \kappa)$ at fixed evaporation parameters can be tuned without having to rerun the physical evaporation model. Therefore, their optimisation is practically less computationally intensive. In this work, their optimisation is performed within detector space: this being the physical space in which specimen alignment actually occurs in experiment. Optimisation of $\mathbf{F}_0$ requires rerunning the physical evaporation model and so is more computationally intensive. However, these optimisations can be separated into two stages, such that the model must only be rerun whilst tuning $\mathbf{F}_0$. The optimisation problem can then be defined via Eqs. (122-124), where Eq. (122) refers to a partial optimisation at fixed $\mathbf{F}_0$.

$$\dot{\boldsymbol{\theta}}_{\mathrm{pmax}}(\mathbf{F}_0) = \underset{(\vec{\mathbf{r}},\theta,\kappa)}{\operatorname{argmax}}\ S_{\mathbb{D}}\left(\boldsymbol{\Gamma}(\vec{\mathbf{r}},\theta,\kappa,\mathbf{F}_0),\hat{\mathbf{X}}^{\mathcal{D}}\right) \tag{122}$$

$$\dot{\boldsymbol{\theta}}^{\mathbb{S}}_{\mathrm{max}} = \underset{\mathbf{F}_0}{\operatorname{argmax}}\ S_{\mathbb{S}}\left(\mathcal{G},\hat{\mathbf{X}}^{\mathcal{R}}\big(\dot{\boldsymbol{\theta}}_{\mathrm{pmax}}(\mathbf{F}_0)\big)\right) \tag{123}$$

$$\dot{\boldsymbol{\theta}}^{\mathbb{D}}_{\mathrm{max}} = \underset{\mathbf{F}_0}{\operatorname{argmax}}\left(\dot{\boldsymbol{\theta}}_{\mathrm{pmax}}(\mathbf{F}_0)\right) \tag{124}$$

Here $S_{\mathbb{D}}\big(\boldsymbol{\Gamma}(\dot{\boldsymbol{\theta}}),\hat{\mathbf{X}}^{\mathcal{R}}\big)$ is the to-be-defined similarity measure between the projected model phases and experimental data in detector space, and $S_{\mathbb{S}}\big(\mathcal{G},\hat{\mathbf{X}}^{\mathcal{R}}(\dot{\boldsymbol{\theta}})\big)$ is the same similarity measure between the initially assumed model phases and reconstruction in sample space. This similarity metric will be defined in Section 3.11.8. Note that two different optimisations of physical parameters can be performed: one in sample space ($\dot{\boldsymbol{\theta}}^{\mathbb{S}}_{\mathrm{max}}$), and one in detector space ($\dot{\boldsymbol{\theta}}^{\mathbb{D}}_{\mathrm{max}}$).

3.11.7 Data Preprocessing

Initially the model and experimental data must be preprocessed to provide local composition information. In sample space, the space is voxelised with dimensions $V_x \times V_y \times V_z$. The local model phase is determined within each voxel by a point-in-polygon test [173, 174] between the voxel centre and the model phase meshes. The local experimental composition is calculated for the reconstruction ($\hat{\mathbf{X}}^{\mathcal{R}}$) over the same grid via KDE (Section 3.9.6). If measuring detector space similarity, this space is also voxelised. The local model phase over this voxel grid is determined via phase maps (Section 3.9.4). The experiment composition is determined via binning the detector data ($\hat{\mathbf{X}}^{\mathcal{D}}$) on the grid. Each voxel now has an associated model phase ($\mathcal{M}_{ijk}$) and experimental composition ($\mathcal{E}^c_{ijk}$), where c indexes the composition channels (C) corresponding to the ranged ionic species. These resulting voxel grids of intensities can be considered 3D images: the model image ($\boldsymbol{\mathcal{M}}$) being unimodal, and the experiment image ($\boldsymbol{\mathcal{E}}^c$) being multimodal.

3.11.8 Measuring Similarity: Mutual Information

Now that the data has been discretised and processed, the similarity between these two images can be measured. Numerous methods exist for solving such template matching problems [179]. These methods each require definition of a metric capable of collapsing both multidimensional images down to a single scalar quantity that can effectively measure their similarity.

The simplest similarity measure is the sum of squared differences (SSD). Here the absolute square difference between the two images is taken for each image voxel, and these differences summed over the entire voxel grid to produce a single scalar similarity measure. SSD is both straightforward to interpret, easy to implement, and efficient to calculate. However, the metric requires significant image preprocessing through semi-accurate guesses for model phase compositions. Poor guesses can result in SSD failing to identify the true maximum during matching. However, alternative metrics can avoid these constraints.

Previous studies by Mouton et al. [96, 97] measured the similarity between APT reconstructions and electron microscopy data for the same specimen via the cross-correlation (CC) metric. CC considers sum of the product of voxel values between the two images. While initial compositional guesses for model image voxels are not required by CC, some prior knowledge of how model phases should match to experiment compositions is required.

However, a third metric called mutual information (MI) promises a similarity measure without requiring any such preprocessing [179]. Instead of calculating image similarity directly from the specific voxel intensities, MI measures the degree of mutual dependence between the two intensity fields. This considers the closeness of the two images' joint probability distribution for intensities ($P^c(\boldsymbol{\mathcal{M}}, \boldsymbol{\mathcal{E}})$) to the product of their marginal probability distributions for intensities ($P(\boldsymbol{\mathcal{M}}) \cdot P^c(\boldsymbol{\mathcal{E}})$). MI can also be interpreted as the information gained in predicting the experimental composition in a voxel, given knowledge of the model

phase in that same voxel. For discretised probability distributions, the MI metric is defined by Eq. (125).

$$MI = \frac{1}{C}\sum_{c}^{C}\sum_{i}^{N_{\boldsymbol{\mathcal{M}}}}\sum_{j}^{N_{\boldsymbol{\mathcal{E}}}^{c}} P^{c}(\boldsymbol{\mathcal{M}},\boldsymbol{\mathcal{E}}^{c})_{i,j}\log\left(\frac{P^{c}(\boldsymbol{\mathcal{M}},\boldsymbol{\mathcal{E}}^{c})_{i,j}}{P(\boldsymbol{\mathcal{M}})_{i}\cdot P^{c}(\boldsymbol{\mathcal{E}}^{c})_{j}}\right) \tag{125}$$

$$P^{c}(\boldsymbol{\mathcal{M}},\boldsymbol{\mathcal{E}}^{c})_{i,j} = \frac{H^{c}(\boldsymbol{\mathcal{M}},\boldsymbol{\mathcal{E}}^{c})_{i,j}}{(V_x V_y V_z)^2}$$

$$P(\boldsymbol{\mathcal{M}})_{i} = \frac{H(\boldsymbol{\mathcal{M}})_{i}}{V_x V_y V_z} \qquad P^{c}(\boldsymbol{\mathcal{E}}^{c})_{j} = \frac{H^{c}(\boldsymbol{\mathcal{E}}^{c})_{j}}{V_x V_y V_z}$$

Here i indexes the model histogram axis bins, j indexes the composition histogram axis bins, $P^{c}(\boldsymbol{\mathcal{M}},\boldsymbol{\mathcal{E}}^{c})_{i,j}$ is the binned joint probability distribution for ion type c, $P(\boldsymbol{\mathcal{M}})$ is the binned marginal probability distribution over $\boldsymbol{\mathcal{M}}$, and $P^{c}(\boldsymbol{\mathcal{E}}^{c})$ is the marginal probability distribution over $\boldsymbol{\mathcal{E}}^{c}$ for ion type c. These joint and marginal probability distributions are numerically estimated by calculating the joint 2D histogram of image voxel intensities $H^{c}(\boldsymbol{\mathcal{M}},\boldsymbol{\mathcal{E}})$, the 1D histogram of model phase voxels $H(\boldsymbol{\mathcal{M}})$, and the 1D histogram of experiment composition voxels $H^{c}(\boldsymbol{\mathcal{E}}^{c})$. These distributions and histograms have $N_{\boldsymbol{\mathcal{M}}}$ bins along model phase axes, and $N_{\boldsymbol{\mathcal{E}}}^{c}$ bins along experiment composition axes. An example of these calculated histograms for 2D model and experiment composition images are visualised in Figure 58.

It can be seen from Eq. (125), an MI of zero implies that the probability distributions are completely independent, i.e. $P^{c}(\boldsymbol{\mathcal{M}},\boldsymbol{\mathcal{E}}^{c})_{i,j} = P(\boldsymbol{\mathcal{M}})_{i}\cdot P^{c}(\boldsymbol{\mathcal{E}}^{c})_{j}$, and that there is no spatial correlation between image voxel intensities. Larger values for MI imply a greater spatial correlation or dependence between image voxel intensities, and therefore indicates greater similarity between model phases and experiment compositions.

In order to construct discretised estimates for the probability distributions, an appropriate number of bins for $N_{\boldsymbol{\mathcal{M}}}$ and $N_{\boldsymbol{\mathcal{E}}}^{c}$ must be determined. As the local model phase data is categorical, model image voxels are assigned integer labels

corresponding to their local phase. Setting the number of bins for the model phase histogram axes ($N_{\boldsymbol{\mathcal{M}}}$) equal to the number of distinct model phases ensures that each histogram bin corresponds to a particular phase. The appropriate number of bins to use for the experimental composition histogram axes ($N^c_{\boldsymbol{\mathcal{E}}}$) is less clear. In this work, $N^c_{\boldsymbol{\mathcal{E}}}$ has been estimated via Sturges' formula ($N^c_{\boldsymbol{\mathcal{E}}} = 1 + \log_2 N$) [180], where $N = V_x \times V_y \times V_z$ is the total number of voxels.

Unlike SSD and CC, the MI metric can be directly applied to the binned model phase and experiment composition data without any further preprocessing. Due to its generality as a metric, it is MI that has been applied in this work when evaluating image similarity.

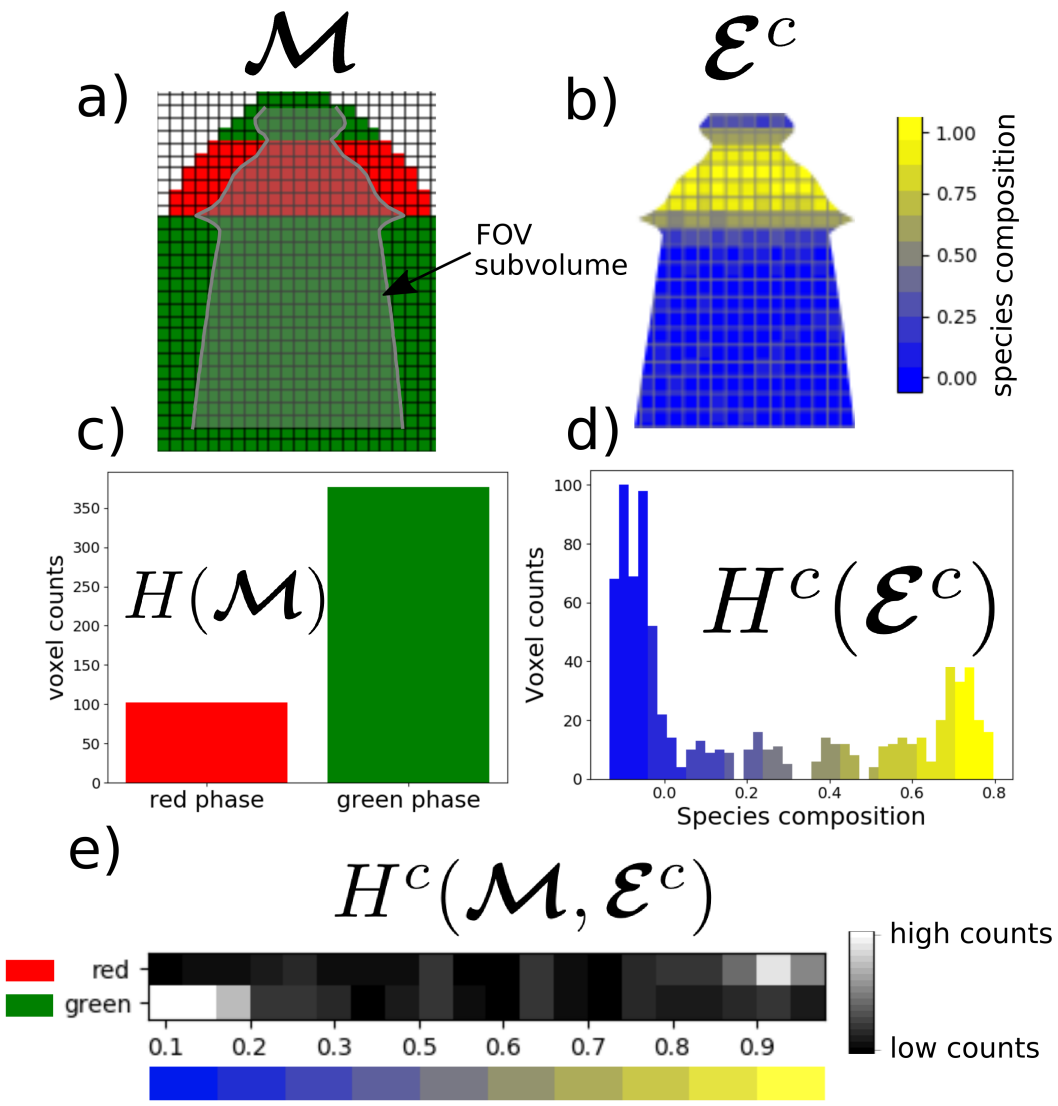


Figure 58: Example model-experiment image similarity measurement within reconstruction space showing a) Specimen model highlighting the FOV subvolume. b) Corresponding reconstruction showing a particular composition channel. c) 1D histogram of model phase voxels ($H(\boldsymbol{\mathcal{M}})$). d) 1D histogram of composition channel voxel values ($H^c(\boldsymbol{\mathcal{E}}^c)$). e) 2D histogram of the two images' voxels ($H^c(\boldsymbol{\mathcal{M}}, \boldsymbol{\mathcal{E}}^c)$).

3.11.9 Test Alignment

In order to test the image registration implementation using MI, an alignment test has been performed. Here a multichannel RGB input image (Figure 59a), generated using the 2D model, has been modified and transformed to generate a second image (Figure 59b), offset via a rigid body transformation (rotated anticlockwise by 25^o and rescaled by $1 : 1.3$). To test performance under modality differences, only the second image's G channel was used, which was inverted, and noise added through random sampling from a Poisson distribution. The original image will serve as the target image, whilst the second image will serve as the source image requiring alignment.

The final result of the image registration is shown in Figure 59c. It can be seen that the algorithm has managed to successfully realign the source and target images. The change in MI with respect to variations in individual parameters can be observed in Figures 59d and 59e. In both visualisations, the variation of MI with respect to all other parameters has been maximised. The plots show that MI has successfully identified the inverse transformation to reverse that originally applied.

This test confirms that the implementation for multichannel image alignment using MI is working.

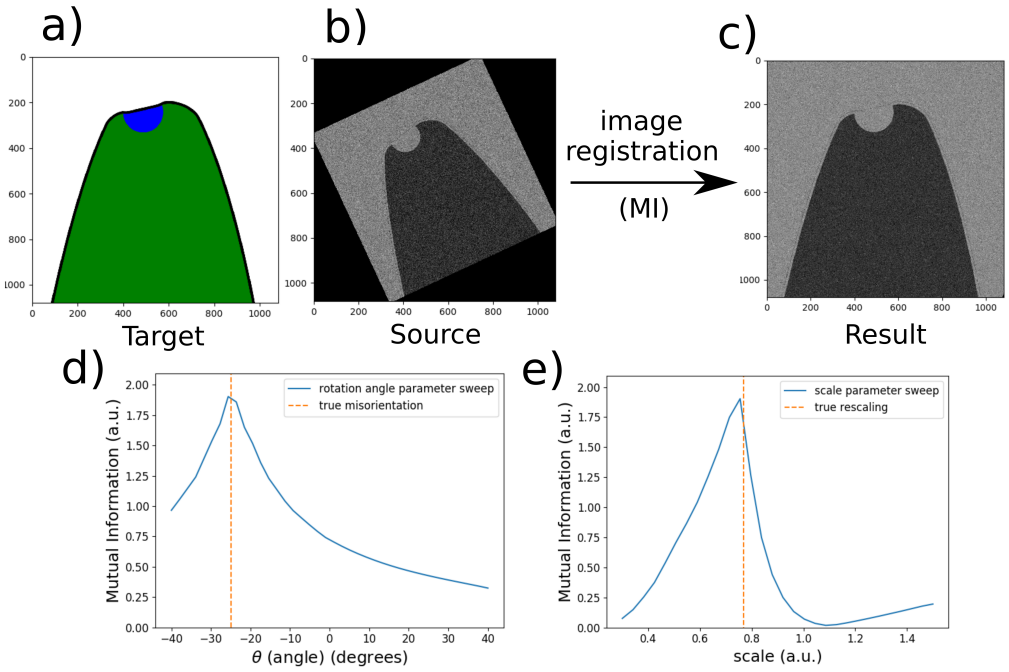


Figure 59: A test image registration problem using the MI metric. (a) The target image with three channels (corresponding to RGB). (b) The perturbed source image. (c) Target image matching following automated alignment. (d) The visualised marginal parameter sweep showing the change in MI under rotation (maximised for -25^o). The visualised marginal parameter sweep showing the change in MI under rescaling (maximised for 0.77). For both plots, all other parameters have been maximised throughout.

3.11.10 Generalised Alignment Transformations

Even following model parameter tuning, residual misalignment errors will almost certainly remain between the model and reconstruction. These errors should be expected to arise due to artefacts in the assumed model geometry, inaccuracies in the modelled evaporation physics, and unaccounted for instrument optics. It will be seen that these distortions are particularly severe at vertical interfaces, where sudden changes occur in both the specimen surface geometry and subsequent trajectory mapping. Within these regions where the trajectory mapping changes rapidly, even small misalignments can produce severe distortions. Correcting these distortions by varying phase boundaries would likely prove computationally challenging. In addition, this approach could introduce undetectable positioning errors, with distortions arising due to inaccuracies in assumed evaporation physics and electrostatics, rather than incorrectly assumed model geometries.

However, assuming the initial model for the specimen is known to relatively high accuracy, e.g. through electron microscopy, another alternative approach could be taken. Instead of attempting to constrain the specimen model entirely from the APT data, we could instead locally transform the experimental data to better match the model. The local magnitude of the required matching transformation would then directly provide information regarding the model's local predictive error. A similar approach is widely applied in the field of Computational Anatomy, where image data is typically matched up to standard computer models for organs [181]. These matching methods perform smooth and well-behaved deformations of image data through the diffeomorphic metric mapping algorithms.

At the point of transformation, the specimen model is already expected to be well calibrated to the experimental data. However, due to the mapping instability at vertical interfaces, small misalignments on the detector between corresponding model-experiment features can introduce localised interface distortions

in reconstructions. Application of the diffeomorphic metric mapping aims to snap experiment interfaces onto their corresponding model interfaces in detector space. The transformation is smooth (has well-defined derivatives), and so by applying it within detector space, any trajectory overlap regions predicted by the model should be preserved (by maintaining trajectory mapping topology and differentiable structure).

It should be noted here that diffeomorphic metric mappings are applied here only as a proof-of-concept, and due to their complexity, their provided background will be brief. Further details on these algorithms can be found in the literature [182, 183, 181, 184].

An important prerequisite is the concept of diffeomorphisms. A diffeomorphism ($\Theta(\mathbf{x}) : \mathbf{X} \to \mathbf{Y}$) is a one-to-one mapping that is smooth, i.e. both $\frac{\partial^r \Theta(\mathbf{x})}{\partial \mathbf{x}^r}$ and $\frac{\partial^r \Theta^{-1}(\mathbf{y})}{\partial \mathbf{y}^r}$ are well-defined for all $\mathbf{x} \in \mathbf{X}$, $\mathbf{y} \in \mathbf{Y}$, and $r \in \mathbb{N}$. A fundamental property of diffeomorphisms is that if $\Theta_0(\mathbf{x})$ and $\Theta_1(\mathbf{x})$ are both diffeomorphisms, then their composition $\Theta_0(\Theta_1(\mathbf{x}))$ is also a diffeomorphism.

The concept behind the diffeomorphic metric mapping algorithm comes from considering linear transformations of type $\Theta(\mathbf{x}) = \mathbf{x} + \epsilon\mathbf{u}(\mathbf{x})$, where $\mathbf{u}$ is some smooth perturbing field, and ϵ is a small parameter. For sufficiently small ϵ, these linear transformations are diffeomorphisms [185].

Using these above properties, diffeomorphic transformations can be generated by solving Eq. (126). Considering the solution update equation by Euler's method over small time step h, and defining Θ^t to be the time-discretised diffeomorphic field at time t, we see that Θ^t and Θ^{t+h} are related by a small-deformation (Eq. (127)). Therefore, using the composition property of diffeomorphisms, as Θ^t is a diffeomorphism, so Θ^{t+h} will also be a diffeomorphism under Eq. (127). Finally, as the initial condition for Θ is the identity function ($\Theta^0 = \mathbf{x}$), itself a diffeomorphism, evolution under Eq. (126) will yield a diffeomorphism for all time (assuming sufficiently small steps h).

$$\frac{\partial \Theta(\mathbf{x}, t)}{\partial t} = \mathbf{u}\big(\Theta(\mathbf{x}, t)\big) \quad \Theta(t = 0) = \mathbf{x} \tag{126}$$

$$\Theta^{t+h}\big(\Theta^{t}(\mathbf{x})\big) = \Theta^{t}(\mathbf{x}) + h\mathbf{u}^{t}\big(\Theta^{t}(\mathbf{x})\big) \tag{127}$$

However, Eq. (127) alone does not constrain the flow field ($\mathbf{u}(t)$). For an initial source image $\mathbf{S}$ to be transformed onto the target image $\mathbf{T}$ under the generated diffeomorphism Θ^{t_f}, diffeomorphic metric mapping methods constrain $\mathbf{u}(t)$ by optimising the image similarity between $\mathbf{T}$ and $\Theta^{t_f}(\mathbf{S})$, whilst also aiming to maintain the smoothness of Θ^{t_f}. Typical approaches can be found in [182, 183].

In this work, a specific approach is considered known as diffeomorphic density matching [184, 186]. Here, images are considered as probability density distributions, with the transformation aiming to preserve densities under the diffeomorphism, i.e. it is mass conserving. It should be noted that density matching methods follow a slightly different approach to that of the traditional metric mappings, with specific details found in [184, 186]. This mass conservation is a useful property for our own problem, where the number of ions throughout detector space should be locally preserved under the transformation. The algorithm is also fast. Therefore, it is this method that has been tried here, although that is not to say that alternative techniques might be more appropriate or produce better results. An example mapping solution to the problem of a translated square-shaped distribution is shown in Figure 60. Here, the existing implementation *ddmatch* has been used [187]. Both the source and target distributions have a density of one inside the purple square, and a density of zero outside. Positions sampled from the source distribution (blue) can then be transformed under the derived mapping (orange) as shown in Figure 60c. This density matching will be applied to slices of the model and experiment density distributions in detector space, and the calculated diffeomorphisms used to better align the detected ions

to the model.

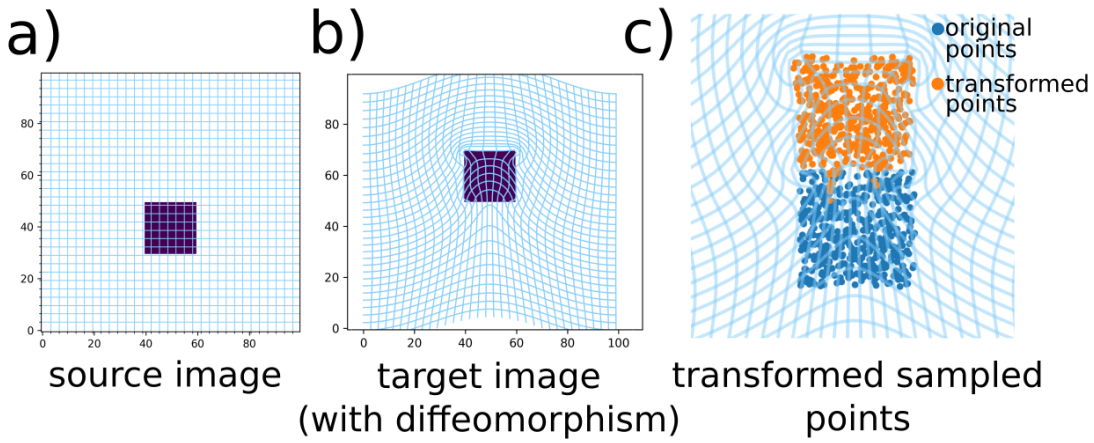


Figure 60: Diagram showing as calculated diffeomorphism for transforming (a) the source image (with blue position lines marking a regular grid) onto (b) the target image by the inexact density matching method outlined in [184]. (c) Transformation of points sampled from the source image (blue) under the derived transformation (orange). The blue lines show the local deformation of a regular grid in the original domain under the diffeomorphism.

3.12 Methodology Conclusions

The previous chapter has outlined the core theory behind a continuum model for specimen field evaporation. By using an implicit level set method to track the specimen surface, this model can handle changes in surface topology, as well as evaporation anisotropy due to crystallography and laser surface heating. Electrostatics have been efficiently solved using BEM, partially accelerated via a panel clustering method, avoiding meshing of the domain up to the detector. A proof-of-concept FEM-BEM coupled solver has also been demonstrated, showing how the effect of dielectric materials on the electrostatics could be accounted for. It has also been discussed how data can be simulated that is directly comparable to experiment. As will be seen, this simulated data can then be used to directly interpret and understand imaging distortions observed in experiment, as well as identify regions where trajectory overlap is likely occurring.

A reconstruction protocol has also been outlined for how a model's ion trajectory data can be used to drive the reconstruction procedure itself. While trajectory overlaps cannot currently be accounted for by the proposed protocol, closer examination of the trajectory mapping properties (Section 3.8.3) imply that sufficiently accurate evaporation models could potentially account for these multivalued regions i.e. assigning spatial uncertainty distributions to individual ions.

The following three chapters will consider results from applying these methods to both the simulation of typical APT microstructures and data reconstruction.

4 Two Dimensional Model

4.1 Summary of the 2D Model

Initially, a simplified 2D field evaporation model was developed to identify and test components for the coupled level set-BEM framework. Due to the reduced dimensionality, this 2D model is less computationally intensive. Therefore, optimisation is not as critical, allowing for rapid development and testing. While its results are not quantitatively comparable to experiment, its 2D nature makes it simple for users to set up simulations and perform qualitative experimental comparisons. This simplified model also provides a platform to test future extensions and improvements, without the numerical challenges encountered from moving to 3D.

4.2 Initialisation

The model initialisation process is outlined in Figure 61. In this work, the specimen surface geometry and internal phases have been initialised using an RGB image. Different colours in the input image correspond to the different material phases, which are assigned parameters stored in a database. The initial specimen surface is obtained via contour extraction. An additional phase-specific rotation parameter captures local grain misorientation for crystallographic phases.

Throughout this work, a level set grid of 128×128 has typically been used for 2D simulations. The grid voxel width has been set to 1 nm. This results in BEM surface panels of around 0.5 nm, roughly on the scale of APT's lateral resolution [188]. A virtual detector, described by a line segment of half length (radius) 0.038 m, has been placed 0.102 m from the specimen.

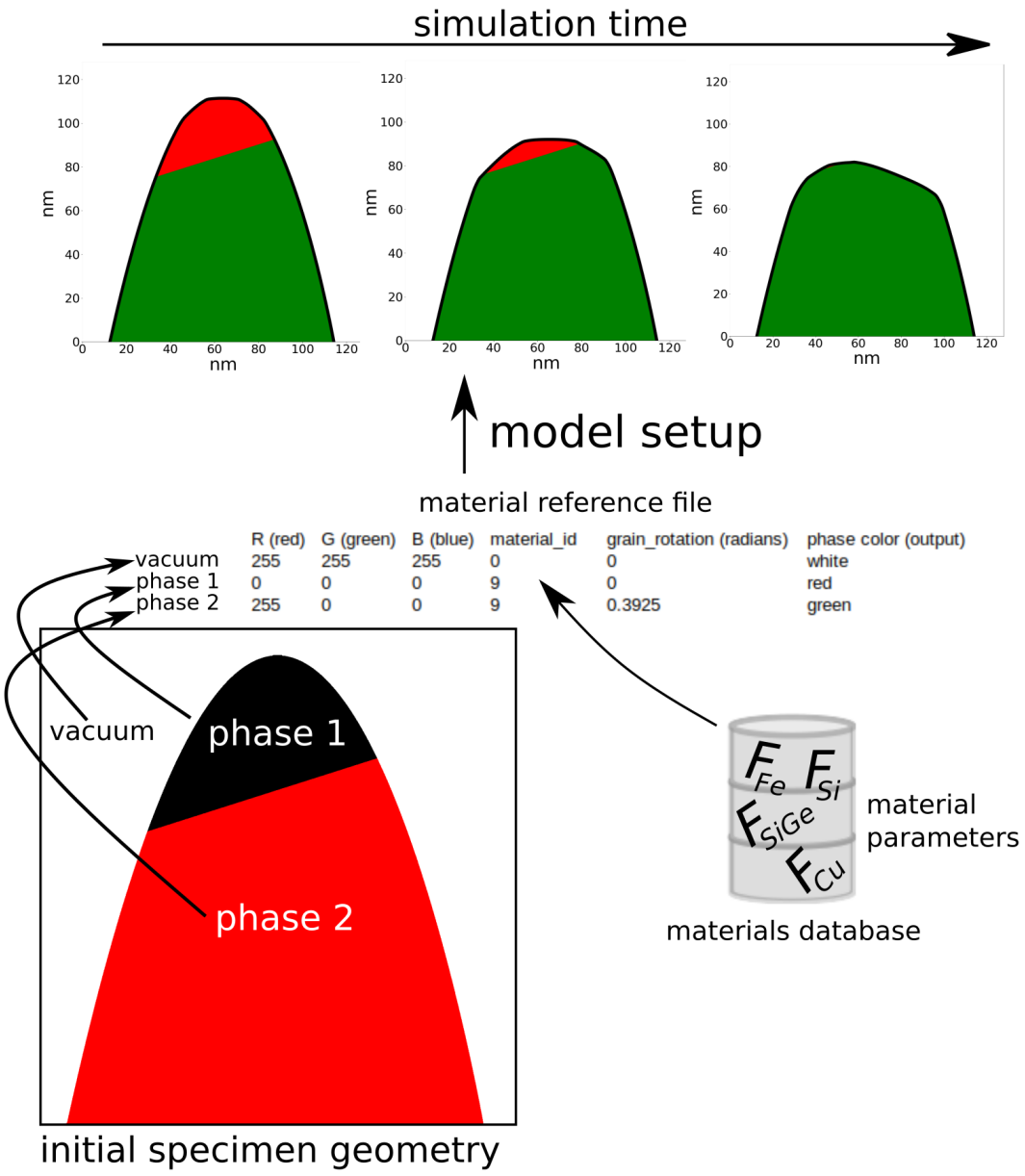


Figure 61: Illustration of the 2D model initialisation process. The initial model specimen is set up from an RGB image. Material phases, defined by image regions of constant RGB, are linked to physical parameters stored in a materials database.

4.3 Implementation

The level set grid is stored as a 2D array, with each voxel being assigned a local material phase type. When calculating the evaporation velocity at the surface, before its extension over the level set grid, the local evaporation parameters of a surface panel are determined by the assigned material phase of the level set voxel in which this panel's centre falls. On each model iteration, the level set field is modified according to Eq. (31).

Prior to the calculation of the electric field, the mesh shank extension is constructed (Section 3.4.3). Two different operational modes for solving the system electrostatics were implemented (Figure 62). A pure BEM mode, where the specimen is approximated as a conductor (Section 3.5.4), and a FEM-BEM mode capable of handling material phase dielectricity (Section 3.5.5). In the FEM-BEM coupling mode, the internal triangular mesh is constructed by the mesh generation program Triangle [154] at each model iteration. The internal mesh is constructed such that triangle edges conform with internal material boundaries.

The simulation will terminate if either a minimum apex height or a maximum number of iterations has been reached. Ion projection can be optionally enabled for simulations, where either a uniform projection (one ion per surface panel), or a realistic projection is performed (weighted by surface evaporation rate).

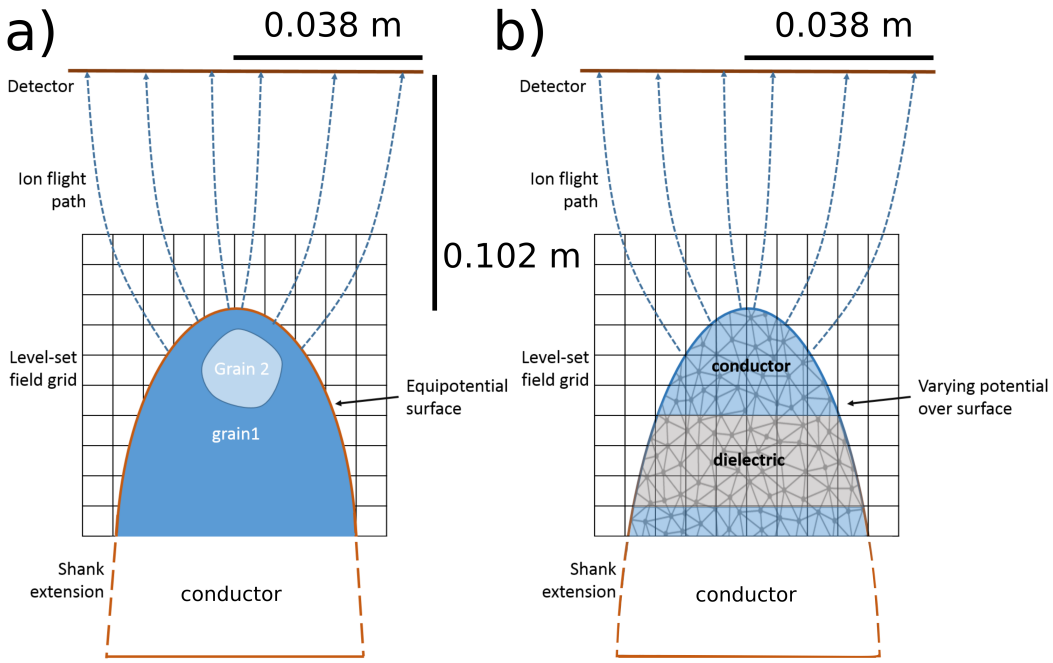


Figure 62: The different 2D model components. (a) Schematic for the pure BEM mode. Here the specimen surface is held at a constant potential. (b) Schematic for the FEM-BEM mode. Note the internal triangular mesh supporting the FEM solution. In FEM-BEM mode, only the specimen base is held at constant potential. Adapted from [133].

4.4 Multilayer Structures

A common specimen structure studied in APT are multilayer systems. These systems consist of a stack of different materials which frequently exhibit different evaporation behaviour. Their almost cylindrical symmetry around the analysis axis makes them one of the simplest multiphase systems to study and model [49, 75, 76, 77, 189]. Engineering applications of multilayer systems include electronics, LEDs, solar cells, and data storage.

As discussed in Section 3.5.1, previously proposed level set models [79, 80] have attempted to approximate the specimen surface evaporation rate via mean-curvature flow. A comparison is shown between curvature and electrostatic evaporation is considered for a specimen with a lower field phase (blue - Figure 63), and a higher field phase (red - Figure 64) compared to the bulk. In the low field example, the evaporation fields in the electrostatic-driven evaporation are $F_{\text{bulk}} = 30$ Vnm^{-1} and $F_{\text{layer}} = 20$ Vnm^{-1}, whilst the comparative curvature flow has a local curvature modifier ratio of $I_{\text{bulk}} : I_{\text{layer}} = 4 : 1$. These phase evaporation fields and curvature modifier values are reversed in the high field example.

While in both cases there are clear similarities in evolution, important differences can also be observed. One key difference is the formation of concave regions in the electrostatic model near interfaces, whilst under curvature flow the specimen surface remains convex for all time. While localised, the formation of these concavities can have major effects on ion trajectories and detector hit-map densities. Another difference is the formation of tangential discontinuities between the shank and apex. These discontinuities have been directly observed in experiment using electron microscopy, and have motivated modifications to mathematical projection models [42].

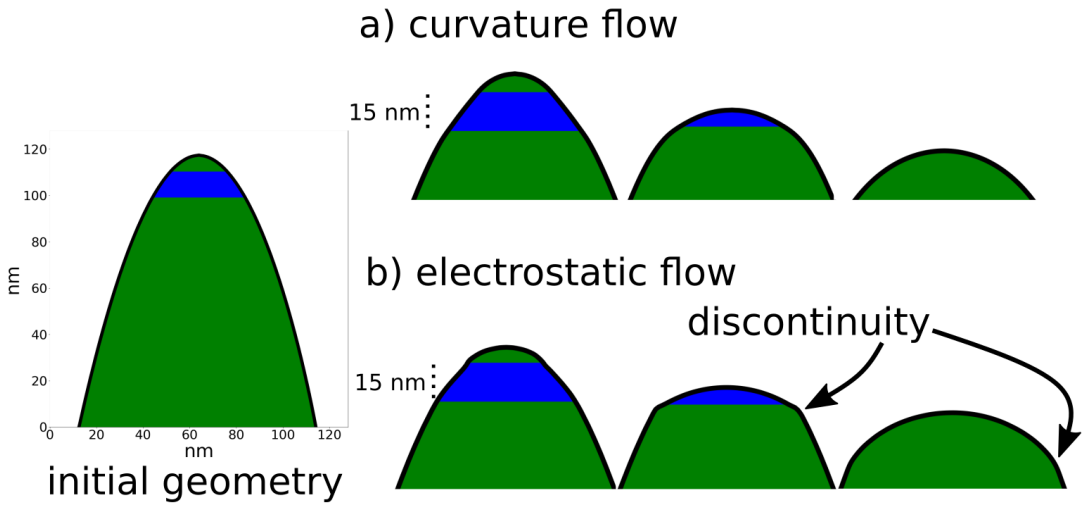


Figure 63: Comparison between curvature flow and electrostatic evaporation for a low field multilayer structure, where $F_{\text{bulk}} = 30$ Vnm^{-1} and $F_{\text{layer}} = 20$ Vnm^{-1}. Concave regions can be seen to form during the electrostatic evaporation. A tangential shank-apex discontinuity [42] also forms under electrostatic evaporation.

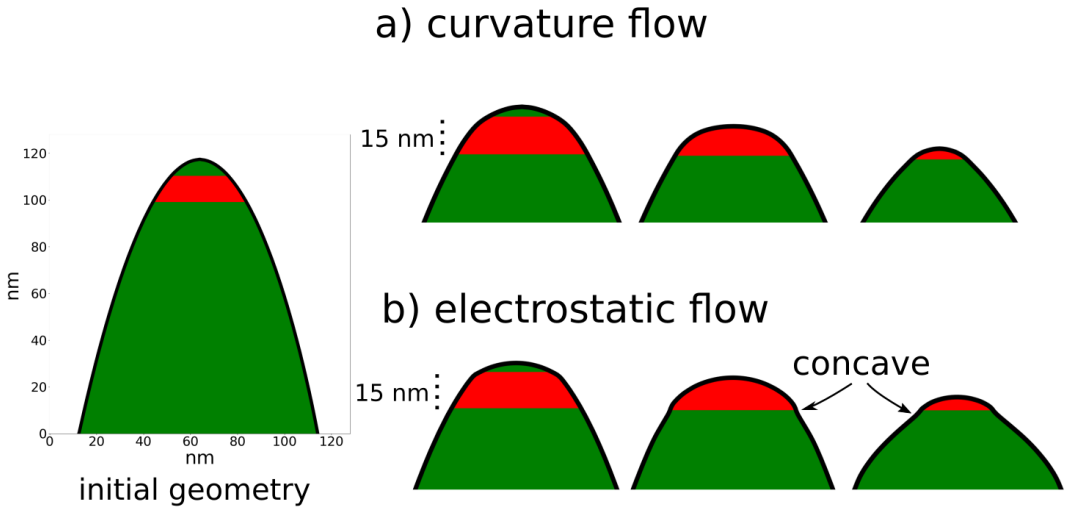


Figure 64: Comparison between curvature flow and electrostatic evaporation for a high field multilayer structure, where $F_{\text{bulk}} = 20$ Vnm^{-1} and $F_{\text{layer}} = 30$ Vnm^{-1}.

Following the simulated evaporation, ion trajectories can be calculated, and the resulting trajectory distortions investigated. Initially a comparison between the hitmap densities arising from both curvature and electrostatic evaporation of the low field system is considered (Figure 65). The concave surface region at the interface of the electrostatic model results in a local focusing of ion trajectories,

and a spike of increased hit density not present in the curvature-driven model. Later in this chapter, such interface density spikes will be observed in experimental data, verifying the electrostatic model's predictions (Section 4.6). Therefore, the curvature flow approximation is insufficient to accurately predict specimen field evaporation and charged optics.

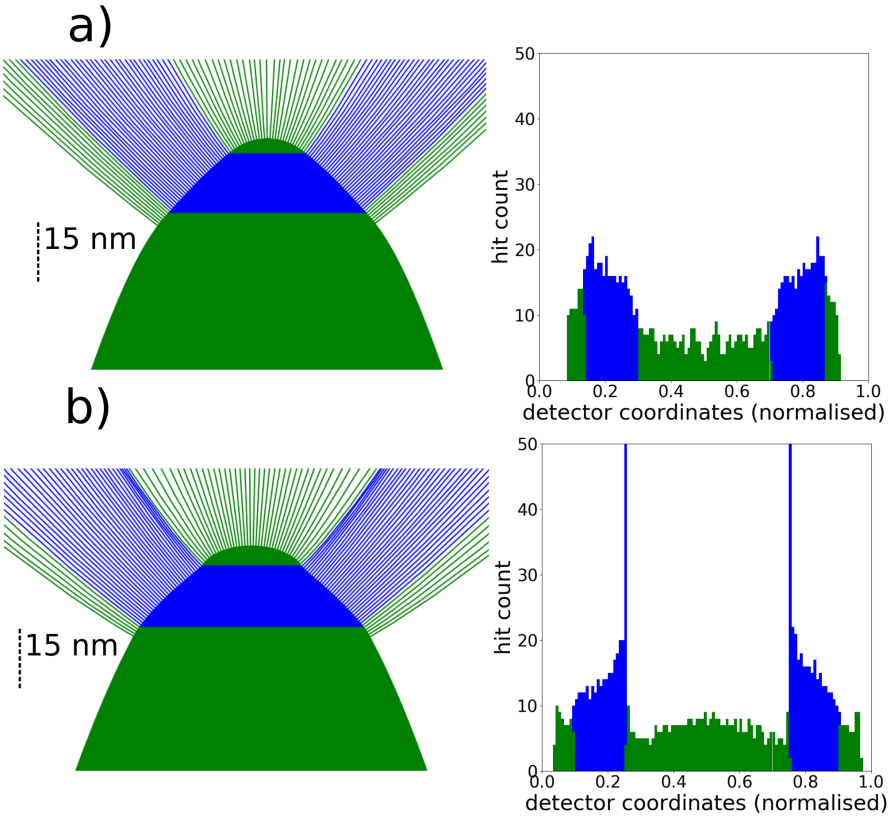


Figure 65: Ion projection during the evaporation of the low field multilayer from (a) the curvature-driven model and (b) the electrostatic-driven model. Major differences can be observed in the produced hitmap densities. Note that the spike in detector hit density for the electrostatic model is a real phenomenon, due to a local trajectory focusing surface concavity forming near the interface.

By calculating ion trajectories throughout the electrostatic-driven evaporation, local magnification and demagnification can be investigated. Here, lines of constant detector position can be calculated from sampled trajectories via the (2D) protocol in Section 3.8.4. These lines visualise the model estimated inverse trajectory mapping. A local bunching of lines implies high local magnification,

whilst a spreading of these lines implies demagnification due to trajectory focusing. This inverse mapping for the low field multilayer system under electrostatic-driven evaporation is visualised in Figure 66d. The initial bunching of the isolines arises from a reduction in the effective apex radius due to the evaporation of the underlying low field layer (blue). This is then followed by a spreading of isolines due to a blunting of the apex, resulting from preferential evaporation of the low field phase. These changes can be directly correlated to the simulated voltage curve (Figure 66e). The shape of this simulated voltage curve qualitatively agrees with an experimental analysis of a similar low field multilayer [49] (Figure 66f), serving to further verify the electrostatic model's predictions. Finally, it should be noted that the inverse trajectory mapping isolines span reveals how the FOV changes throughout the evaporation.

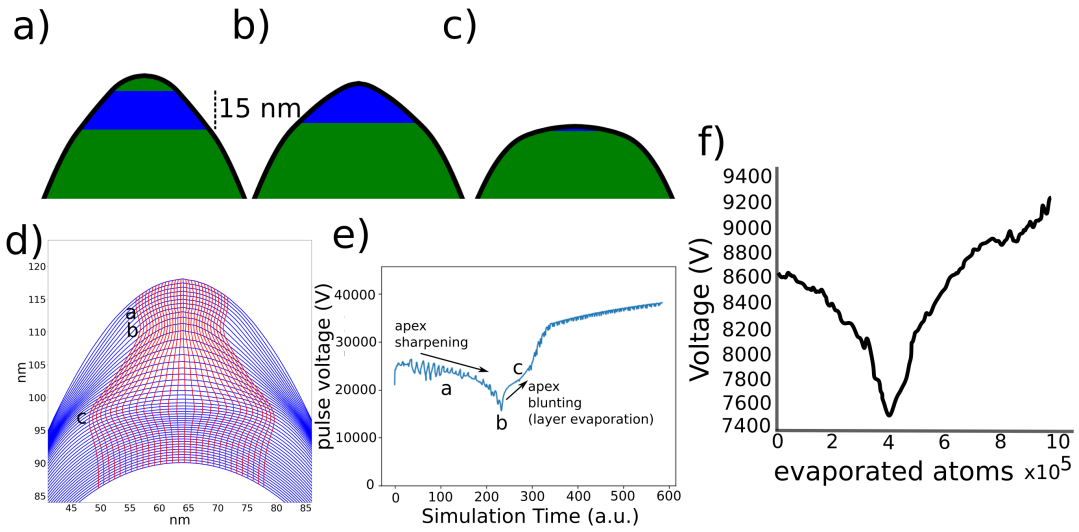


Figure 66: The inverse trajectory map for the low field multilayer system under electrostatic-driven evaporation. (a-c) Snapshots from its evaporation. (d) Visualisation of the trajectory map through isolines of constant detector position (red). (e) The simulated voltage curve. (f) Approximate reproduction from [49] showing an experimental voltage curve when passing through a low field multilayer.

4.5 High and Low Field Precipitates

In APT experiments, it is exceedingly common to analyse systems containing precipitates. These microstructures have been shown to introduce significant distortions into reconstructions [60, 61, 149, 190, 191], and the elimination of these is highly desirable for improving quantitative APT analysis [166]. Like with multilayers, precipitates can be both low or high field relative to the bulk.

A comparison is shown between the curvature and electrostatic evaporation for a low field precipitate in Figure 67b and 67d (where $F_{\text{bulk}} = 30$ Vnm^{-1} and $F_{\text{precipitate}} = 20$ Vnm^{-1}, and $I_{\text{bulk}} : I_{\text{precipitate}} = 2{:}1$), and a high field precipitate in Figure 67c and 67e (where $F_{\text{bulk}} = 20$ Vnm^{-1} and $F_{\text{precipitate}} = 30$ Vnm^{-1}, and $I_{\text{bulk}} : I_{\text{precipitate}} = 1{:}2$). As with the multilayer systems, whilst both the curvature and electrostatic models show qualitative similarities, important differences exist, in particular the formation of surface concavities in the electrostatic model.

The model inverse trajectory mapping can again be calculated (Figure 67f-g). The mapping in the high field case reveals a bunching of isolines within the precipitate, representing an increase in local magnification. Meanwhile the low field precipitate case reveals a spreading of isolines, implying local demagnification due to trajectory focusing. The local microstructure influences the apex shape and ion trajectories over the entire FOV, and reveals that microstructures cannot be assumed to introduce only local distortions in reconstructions. Another interesting, although subtle, observation is the slight rise in isolines following the initial evaporation of the high field precipitate (highlighted by the grey box in Figure 67f). This shows that in extreme cases, constant detector positions throughout time cannot always be assumed to correspond to surface positions of increasing depth.

It is worth briefly commenting on the stability of these inverse mapping isolines. In regions where there is trajectory focusing, the lines of constant detector position tend to fluctuate. While this is partially due to the increased gradients

(lower resolution) of the inverse mapping within these regions, particularly severe oscillations can also arise due to the presence of trajectory overlaps. These oscillations can be understood by considering the bijective assumption imposed during inverse mappings' construction (Section 3.8.4). By performing a straightforward interpolation, the lines of constant detector positions within the constructed inverse mapping can randomly jump between the multiple inverse solutions that exist wherever trajectory overlap is present.

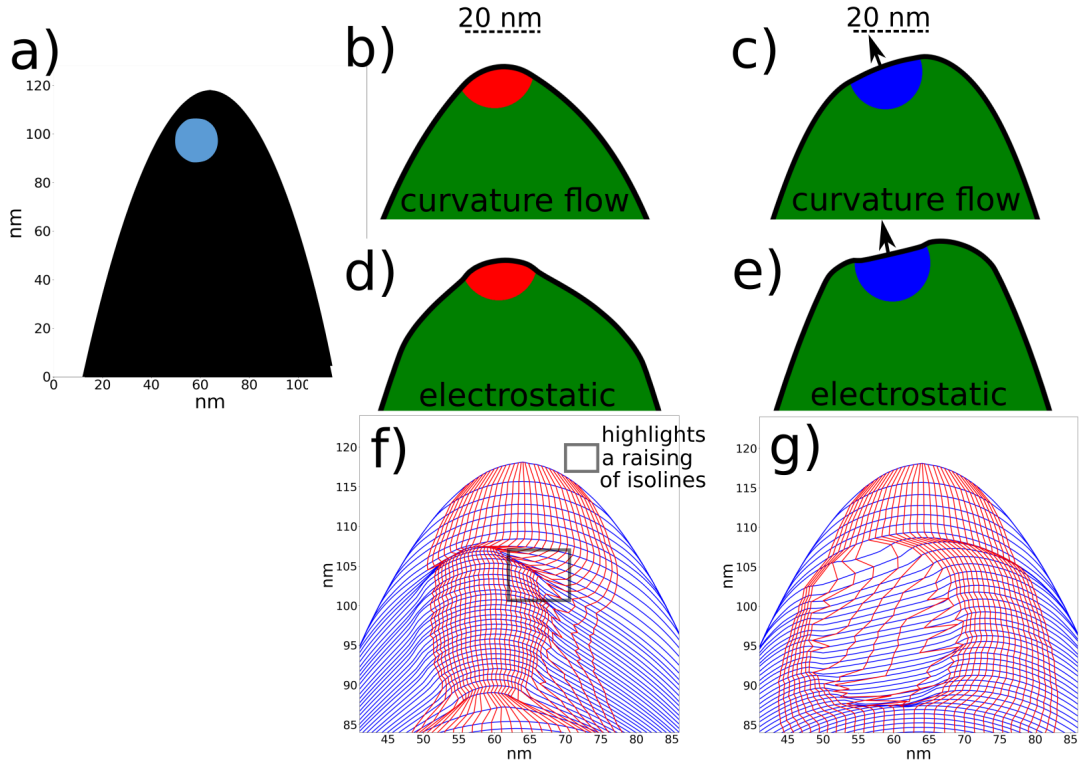


Figure 67: The inverse trajectory maps for the examined low field and high field precipitate. (a) Specimen geometry for the high field and low field examples. (b) High field precipitate following curvature flow ($I_{\text{bulk}} : I_{\text{precipitate}} = 1{:}2$). (c) Low field precipitate following curvature flow ($I_{\text{bulk}} : I_{\text{precipitate}} = 2{:}1$). (d) High field precipitate following electrostatic evaporation ($F_{\text{bulk}} = 20$ Vnm^{-1} and $F_{\text{precipitate}} = 30$ Vnm^{-1}). (e) Low field precipitate following electrostatic evaporation ($F_{\text{bulk}} = 30$ Vnm^{-1} and $F_{\text{precipitate}} = 20$ Vnm^{-1}). (f) The inverse trajectory map for the high field precipitate (bunching $\rightarrow$ magnification). (g) The inverse trajectory map for the low field precipitate (spreading $\rightarrow$ demagnification).

4.6 The Fin Field-Effect Transistor

An active area of APT research is the analysis of semiconductor device structures [51, 93, 98]. These structures typically consist of well defined phase geometries that can have differing evaporation behaviour and dielectricity. As a result, trajectory distortions are frequently problematic in their reconstructions.

In a study by Melkonyan et al. [51], a specimen structure representing an extracted region from a FinFET device was analysed, and its data qualitatively compared to an atomic-scale finite difference model's predictions. The point-projection reconstruction of the experimental data (Figure 68b) reveals a narrowing of the central fin that is absent from the true geometry (Figure 68a). This narrowing is an artefact of the evaporation process, and can be understood to arise from local trajectory focusing due to the lower evaporation field of the central fin compared to the surrounding material.

Assigning the central fin an evaporation field of $F_{\text{channel}} = 20$ Vnm^{-1} and the surrounding material a field of $F_{\text{bulk}} = 30$ Vnm^{-1}, the narrowing artefact of the central fin can be reproduced. The inverse trajectory mapping is shown in Figure 68d. The central spreading of the lines reveals a local demagnification of the central fin region. At the interface between the central fin (light blue) and surrounding material (red), there is a region of enhanced trajectory focusing and overlap (characterised by isoline fluctuations). Finally, outside of the central fin there is a region of high magnification where the bunching of isolines increases. The calculation of such inverse mappings that are directly comparable to experiments raises the question of whether such mappings could be applied to correct real distortions observed in reconstructions.

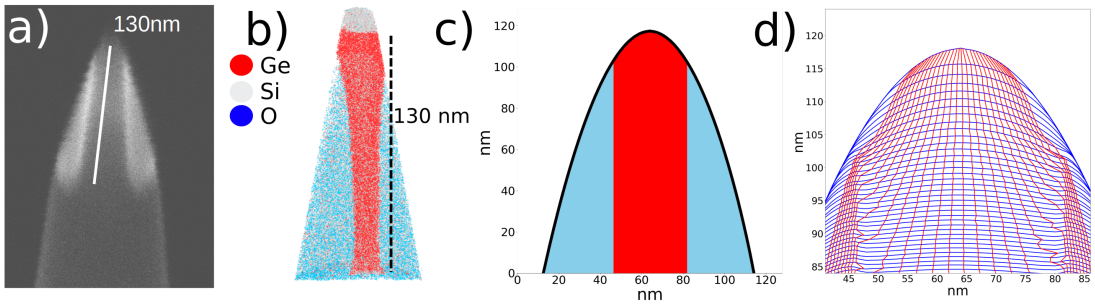


Figure 68: (a) True specimen geometry obtained via SEM [136]. (b) Point-projection reconstruction (constant shank mode) for the FinFET APT dataset. (c) Initial model geometry. (d) The inverse trajectory mapping for model evaporation fields of $F_{\text{channel}} = 20$ Vnm^{-1} and $F_{\text{bulk}} = 30$ Vnm^{-1}.

This narrowing artefact can also be understood by directly considering the simulated 1D detector density hitmaps. Ion trajectory calculation during the central fin's evaporation and corresponding density hitmap is shown in Figure 69. Ion trajectories originating from the central fin are focused due to the concave surface geometry, resulting in high ion density interface spikes on the detector. These same interfaces spikes can be observed in the experimental cross-sectional density profile in detector space (Figure 69c). In comparison, such spikes are absent in the simulated hitmaps derived under the curvature flow approximation (Figures 69d and 69e).

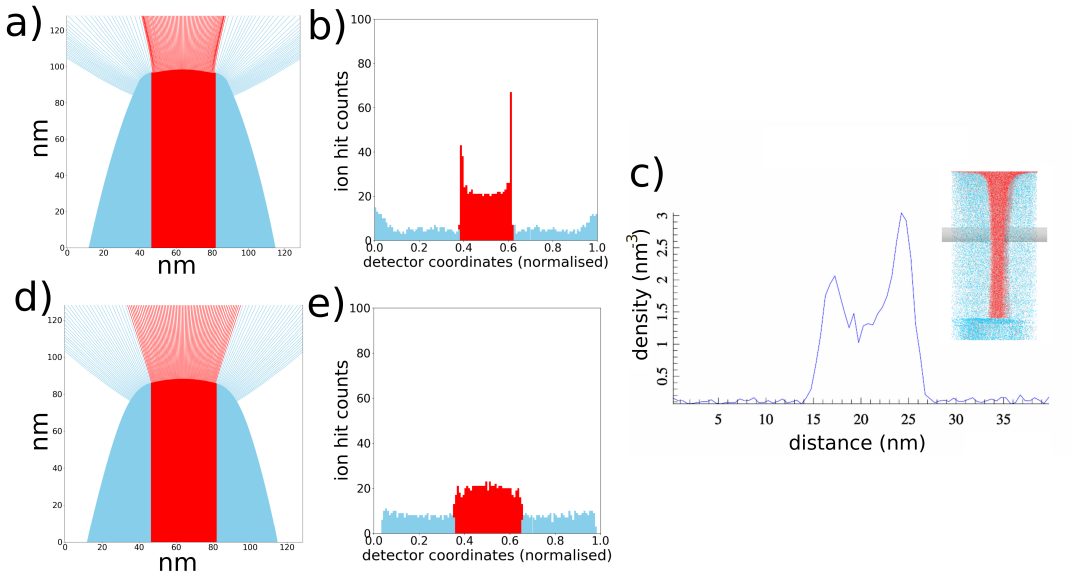


Figure 69: (a) An instance from the FinFET evaporation under the electrostatic field. (b) Corresponding simulated hitmap under electrostatic evaporation. (c) Cross-sectional density profile from the experimental FinFET dataset (detector space). Spikes in the ion hit density at interfaces show agreement between the electrostatic model predictions and experiment. (d) A frame under the curvature-driven approximation. (e) Corresponding simulated hitmap under curvature evaporation.

4.7 Dielectric Microstructures

The FEM-BEM coupling scheme is successful in reproducing electric field lensing and trajectory focusing arising for dielectric microstructures in finite difference models [63, 68]. This dielectric behaviour can be seen in Figure 70 for both a vertical multilayer (FinFET) structure, and a surface precipitate. It is worth noting that these lensing and focusing effects arise only when dielectric phases are exposed at the specimen surface. For completely internal dielectric phases, the conductor approximation still holds. These dielectric field lensing and trajectory focusing effects introduce an additional dependence on the internal phase geometries, implying that specimen field evaporation, charged optics, and the inverse trajectory mapping cannot necessarily be accurately predicted from the surface geometry evolution alone.

Previous simulations using the finite difference model [63] predicted that this field lensing should also result in local electric field strength enhancement at dielectric surfaces. However, the FEM-BEM coupling scheme fails to reproduce this field enhancement. A possible cause of this failure is the 2D approximation. Another explanation could be that the coupling scheme assumes boundary elements of constant potential. Therefore, close to the non-equipotential specimen surface, such constant potential panels might not accurately capture tangential field components. While this is likely not an issue for conductors, where surface tangential field components should be zero, this is not the case for dielectrics. Identifying the exact cause of this discrepancy will likely require the implementation of a 3D FEM-BEM coupling scheme, and higher-order or Galerkin BEM schemes.

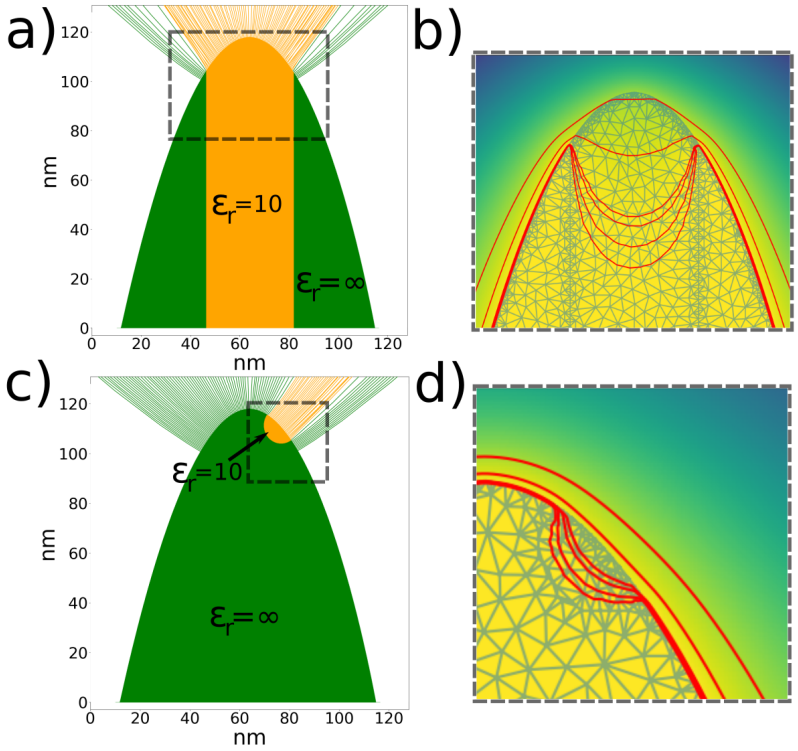


Figure 70: (a) The trajectory focusing arising due to dielectric effects from a vertical multilayer dielectric structure. (b) Electric potential surrounding the apex of this multilayer structure (equipotential field lines in red). (c) Trajectory focusing for a surface-exposed precipitate. (d) Electric potential (showing equipotential field lines in red) surrounding this same precipitate.

To gauge the practical computational efficiency when solving the full FEM-BEM coupled field solution compared to the BEM conductor approximation, a test system containing a large precipitate has been considered (Figure 71). The simulation has been run to a maximum apex height of 60 nm (see Figure 71b) for three different modes of operation:

- The FEM-BEM coupling scheme.
- A pure BEM scheme approximating the specimen as a conductor and ignoring dielectric effects.
- A hybrid mode where the FEM-BEM coupling scheme is used only when dielectric microstructures are surface exposed.

The simulation times for these different modes can be found in Table 1. These timings are highly dependent on the specimen shape and simulation parameters, e.g. the CFL fraction. The timing results for the test system show that, whilst solving for dielectrics is more computationally intensive, at practical resolutions the FEM-BEM coupling framework remains sufficiently fast in 2D to allow for full-scale dielectric evaporation simulations within minutes. The comparative computational complexities can be found in [133].

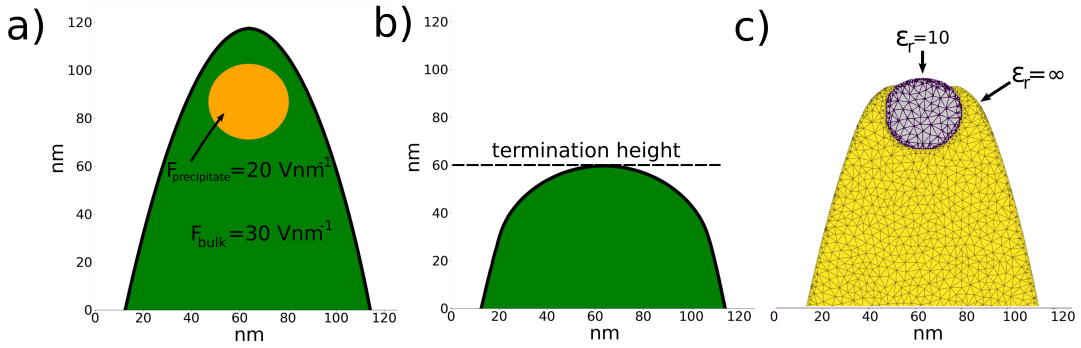


Figure 71: (a) Initial model specimen for the test system. (b) Final apex shape at simulation termination (c) Internal triangular mesh constructed in the FEM-BEM scheme for supporting the FEM solution showing phase dielectric values.

Method	Simulation times (seconds)
FEM-BEM	670
Pure BEM	100
hybrid	470

Table 1: Results for the collapse of the dielectric test system (Figure 71) under three different modes of electric field calculation. The resulting times are averaged over five runs (two sig. fig. timing precision set by standard deviations). All graphical outputs have been disabled.

4.8 Crystallographic Simulation

As previously discussed in Section 3.7.1, the underlying specimen crystal structure frequently results in the formation of specific surface facets during field evaporation. These facets can be directly observed via electron microscopy [50], and indirectly through pole structure density distortions within APT detector data and reconstructions [192].

Surface faceting can be incorporated in the 2D model via an anisotropic evaporation function. The anisotropy law applied in this work is defined in Eq. (91), obtained by promoting the previously constant evaporation fields to functions of surface angle. Different anisotropic evaporation fields can then be associated with different model phases and crystal grains.

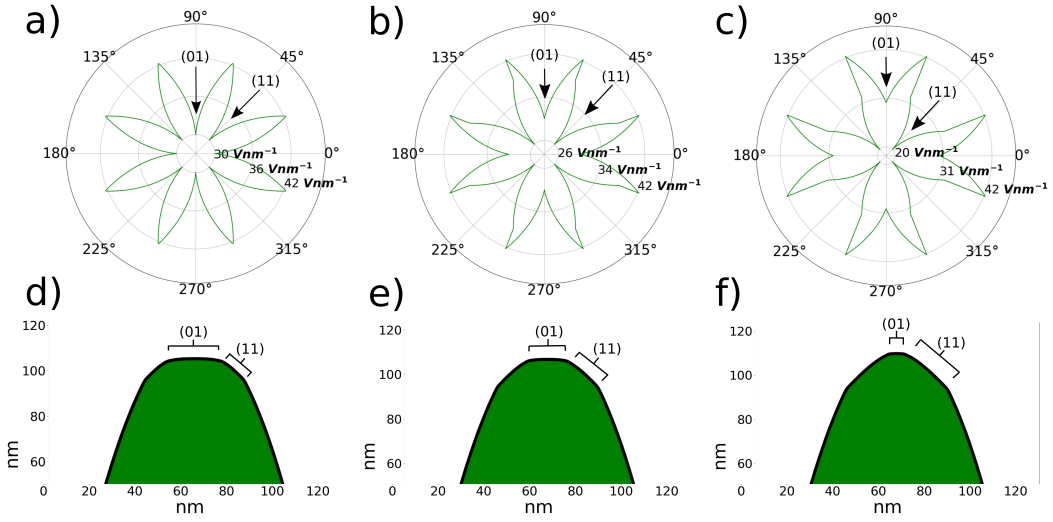


Figure 72: Effect of changing the anisotropic evaporation field function on steady-state apex facet sizes. Reducing a facet's evaporation field (the local minima in the polar plots) increases the relative facet size that forms during evaporation. At some critical ratio of the minima, certain facet's will be outcompeted and vanish (see Figures 72c and 72f).

Examples for the simulated evaporation of single grained materials under various anisotropy fields are shown in Figure 72. These examples show the effect on steady-state apex faceting from changing the anisotropic evaporation field

minima. It can be seen from these examples that the anisotropic evaporation function minima dictate the angles at which apex facets will form. Reducing the value of a facet's associated minima increases the relative size of the facet that forms. This relationship arises due to a reduction in a facet's relative evaporation field, corresponding to a relative increase in its local evaporation rate. It is known from crystal growth studies that facets propagating at faster velocities become larger in their asymptotic steady-state limit [193]. At some critical value for a facet's associated evaporation field minima, the facet was found to completely vanish, being outcompeted by the faster growth of its neighbours. The implication is that the faceted steady-state apex shape is dependent only on the anisotropic evaporation field's minima (Figure 72f), rather than its intermediate values. Therefore, these material-specific minima could potentially be determined through experiment by measuring the relative size of the surface facets that form through electron microscopy. This observation shares many similarities with Wulff's theorem for determining crystal equilibrium shapes, where facets with a higher relative surface free energy are smaller [159].

We can also consider the projection of ions off a faceted surface, and the trajectory distortions that arise. Such a projection is shown in Figure 73b, evaporated until steady-state under the anisotropic evaporation field in Figure 73a. The simulated hitmap, shown in Figure 73c, reveals regions of lower hit density, corresponding to projection off facet corners. While these hitmap density patterns appear very similar to the pole structure observed in both experiment and atomic models, there is a subtle yet important distinction: for atomic models these low density regions correspond to the facets themselves rather than their corners. This discrepancy arises due to atomic-scale evaporation ordering effects, and will be explored in further detail in Section 5.5, where a more direct comparison to atomic models is considered.

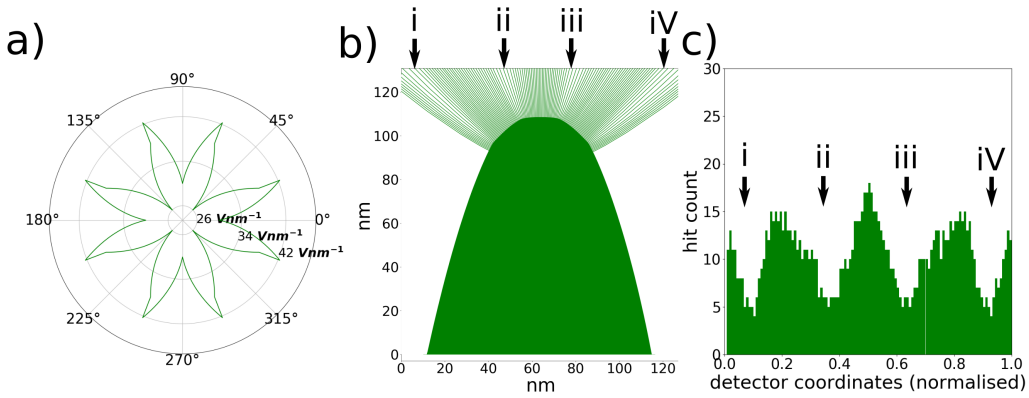


Figure 73: (a) The single grain's anisotropic evaporation field function. (b) Steady-state specimen evaporated under the same anisotropy function, with ion projection performed from its apex. (c) Corresponding simulated 1D hitmap. Roman numerals mark projected facet corners and their corresponding hitmap density sites.

We can also apply the model to considering polycrystalline systems. An example for simulated evaporation of a grain boundary under this modified anisotropic evaporation law is shown in Figure 74, where the two grains are misoriented by an angle of 22.5^o. The anisotropic evaporation fields for the green and red grain are shown in Figures 74a and 74b. It can be seen that the modified evaporation law successfully reproduces surface faceting, with facets forming at the local minima of the defined anisotropic evaporation field functions. A surface discontinuity occurs at the grain boundary interface.

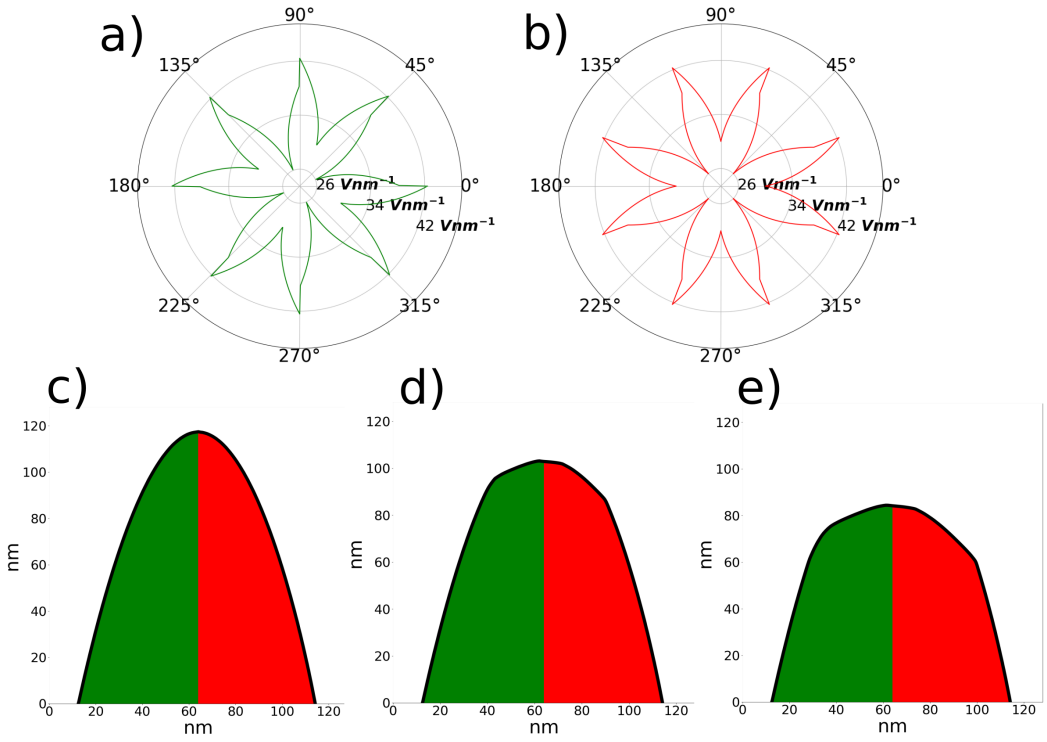


Figure 74: Polar plots for (a) green grain and (b) red grain anisotropic evaporation fields. (c-e) Simulated evaporation of a grain boundary at 22.5^o misorientation.

4.9 Incorporating Voids

It is well known that voids (cavities) can form inside materials during a variety of processes, e.g. material irradiation [194, 195]. Analysis of specimens containing voids is an interesting application of APT, particularly as these voids often fall close to the resolution limit of electron microscopy [111]. However, during their evaporation these cavities can induce extreme changes in the surface geometry, and therefore understanding the resulting distortions and artefacts in reconstructions is critical. As the level set method tracks the specimen surface implicitly as a contour within a scalar field, the merging and separation of the specimen surface is handled without having to consider explicit meshes. The simulation of a void using the 2D electrostatic model is shown in Figure 75.

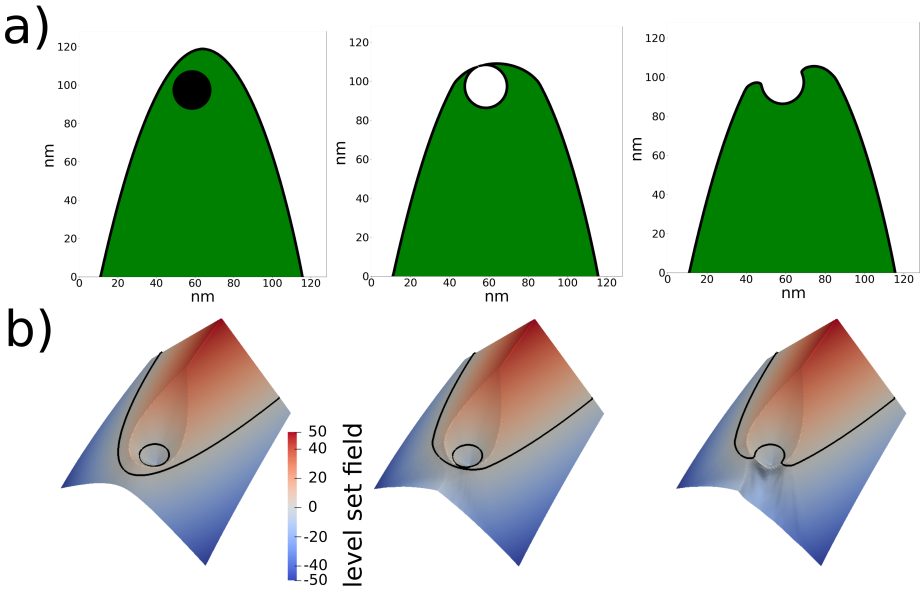


Figure 75: (a) Simulated evaporation of a circular void. (b) Corresponding evolution of the level set field throughout the void's evaporation.

The Figure 76a shows a uniform projection off the specimen apex midway through a void's evaporation. The trajectory calculations reveal that the void behaves as a converging lens to locally focus trajectories, even resulting in trajectory overlap. However, this uniform projection assumes that ions are evaporating

at the base of the void, where the surface field in the continuum model at least is much lower than the bulk evaporation field because of the void's extreme concave geometry.

A more realistic projection is to calculate trajectories only where the local field and evaporation rate is sufficiently high. This thresholded projection is shown in Figure 76a, with ion trajectories only calculated from where $\frac{||\mathbf{E}||}{F_{\text{bulk}}} > 0.5$. This thresholded projection discounts surface regions where the predicted evaporation rate is close to zero. Finally, an inverse trajectory mapping accounting for trajectory crossover can be calculated from this thresholded projection, and is given in Figure 76c. In order to represent this multivalued mapping, isolines of constant detector position can no longer be used. Instead a colour gradient visualises the corresponding detector coordinate. This visualisation of the inverse mapping reveals how ions originating from opposite sides of the void can arrive at exactly the same detector coordinate (see the green and purple regions found on both sides of the void). In order to apply such multivalued inverse mappings to driving reconstruction, the algorithm must be capable of handling ion positioning within these multivalued regions.

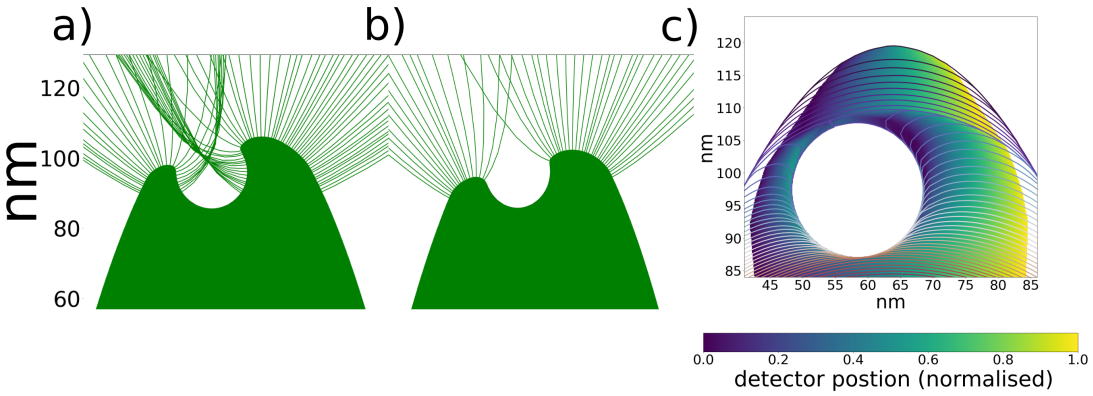


Figure 76: (a) Naive uniform ion projection off apex. (b) A thresholded uniform ion projection from the surface where $\frac{||\mathbf{E}||}{F_{\text{bulk}}} > 0.5$, ensuring trajectories are calculated only where there is evaporation. (c) Visualisation of the true multivalued inverse trajectory mapping for the void. Note that ions originating from different sides of the void can arrive at exactly the same detector coordinate(s).

4.10 Conclusions

In this chapter, results from the evaporation of different material systems using a 2D model have been analysed and discussed. While not quantitatively comparable to experiment, the model can provide a qualitative understanding to observed phenomena. It also serves as a simplified testing framework for the physics and algorithmic components required for accurate APT simulation, without the additional numerical and optimisation challenges presented by moving to 3D. Finally, it functions as an educational tool through an easier model setup and visualisation, aiding in the understanding of concepts such as inverse trajectory mappings, anisotropy functions, and curvature flow comparison.

Indeed, comparisons between electrostatic-driven and curvature-driven evaporation have revealed significant differences between shape evolution and trajectory distortions. This analysis confirms that the curvature approximation is insufficient to accurately predict APT experiment results, and that fully coupled electrostatic simulation is necessary. It has also been shown how crystallographic anisotropy and voids can be handled by the level set method, and how a FEM-BEM extension of the electrostatic solver can incorporate the effects of dielectric materials. The stability of inverse trajectory mappings has also been explored, including how inverse mappings can become multivalued due to the presence of trajectory crossover (Figure 76c).

A number of outstanding issues and challenges have been identified. Discrepancies exist between the results of atomic models [63], and the implemented FEM-BEM coupling for the predicted surface field of dielectrics. This discrepancy has potentially arisen due to the constant panel potential approximation of the implemented BEM. A higher-order linear or quadratic BEM could potentially resolve this, although major numerical challenges arise when handling corner panel nodes due to locally undefined surface normals [196].

In conclusion, the proposed 2D model presents a viable approach to perfor-

ming rapid APT simulation, successfully demonstrating nearly all the required concepts. Additionally, as we will see in the following section, nothing in theory is limiting its extension to full 3D. A large number of applicable methods for numerical optimisation [197, 198, 150, 132] and computational parallelisation [199, 200] heavily imply that highly efficient 3D simulation is achievable under this proposed framework.

5 Three Dimensional Model

Following the 2D prototype, a 3D model was developed using the established framework. However, to maintain computational efficiency, multiple algorithmic optimisations are required (these will include the panel clustering and adaptive panel sizes described in Sections 3.4.2 and 3.5.8). Together, these optimisations allow for 3D simulation in minutes, and direct quantitative comparison of model results with experimental data

5.1 Initialisation

Unlike in 2D, a single image is no longer sufficient to initialise the model specimen. Instead the model specimen surface and phase boundaries have been stored as triangular meshes. The initial signed distance level set field is computed from the specimen mesh and cached. Tools are provided to create specimen surfaces and phase meshes via analytical functions. However, meshes can also be generated for more general specimen geometries by contour extraction from a 3D voxel grid, such as those generated via electron tomography. Similar to the 2D model, user input matches phase meshes to material-specific physics parameters within a relational database. Euler rotation angles are also provided for each phase allowing for grain misorientation. Finally, a parameters file provides non-phase specific physical, geometric, and numerical simulation parameters.

In the following simulation examples, level set grid voxel sizes on the scale of a few nanometres have typically been used. A virtual detector has been placed 0.102 m from the specimen apex with radius 0.038 m, matching the instrument setup of the laser-assisted wide-angle atom probe (LaWaTAP) instrument. Like the LaWaTAP, no local electrode has been simulated, although one could be readily included into the model's electrostatic solution (Section 3.10.1).

5.2 Implementation

Prior to the level set simulation, the signed distance field is initialised by determining the shortest distance from the centre of each voxel to the specimen surface mesh. This is calculated by determining the closest distances between voxels' centres and the triangular mesh [201].

Once the level set field has been initialised, model evolution can begin. At each iteration, the surface is first extracted from the level set grid via marching cubes. The shank extension is then performed (Section 3.4.3), followed by an adaptive isotropic remeshing along the shank (Section 3.4.2). Finally, the surface electric field is solved via GMRES (Section 3.5.3). From this surface field, the surface evaporation rate of each panel is calculated (Eq. (3.1)), with point-in-polygon testing [173, 174] used to determine surface panels' associated phases. The velocity extension field is then constructed, and the level set field updated via the upwind scheme in Eq. (31) or its second-order variant [78]. This model iteration continues until one of the following termination conditions is reached: total number of iterations, minimum specimen height, or internal phase-specimen surface intersection.

Following completion of the simulated evaporation, the system's ion optics can be calculated. Here ions are either launched from surface panel corners, or randomly over the surface according to a MC approach (Section 3.9.2). These trajectories are calculated via an RK5 integrator [148]. At each RK5 iteration, the electric field is calculated at the ion's current position via the panel clustering method in Section 3.5.8.

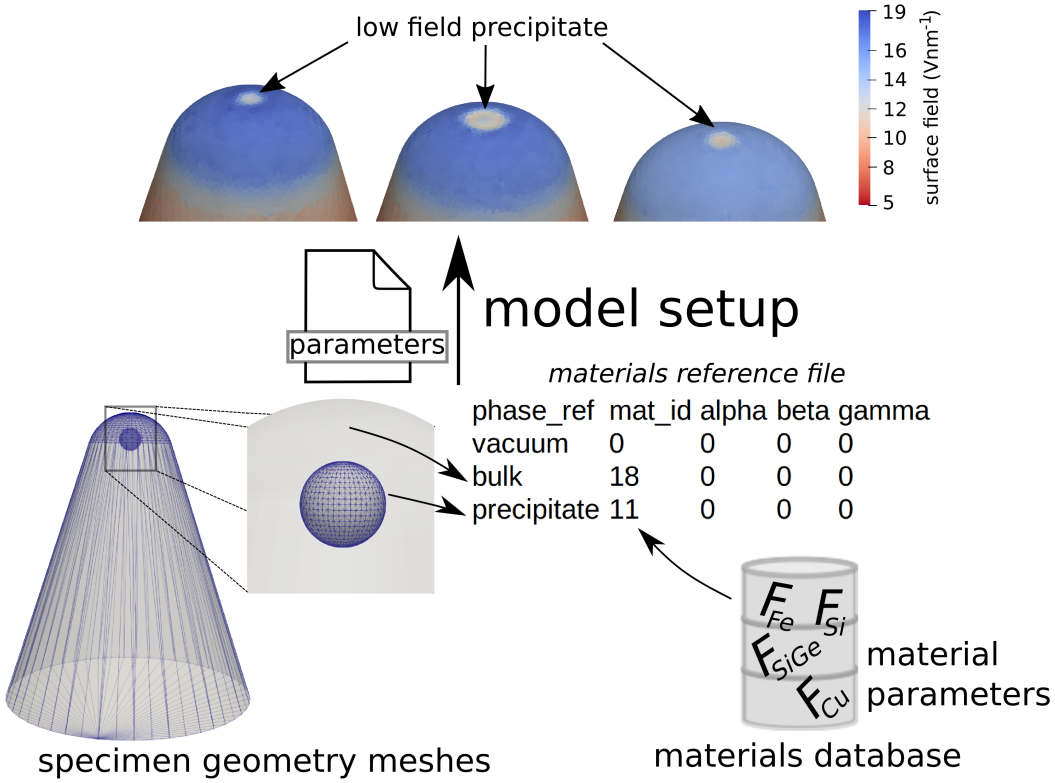


Figure 77: The 3D model initialisation process. The specimen surface and phase geometries are defined by triangular meshes. These meshes are then assigned phases according to physical parameters stored in a database.

5.3 Multiphase Evaporation

These examples demonstrate the evaporation of simple microstructure geometries featuring different evaporation fields. The first example considers the low field multilayer system in Figure 78a, with a bulk (red) evaporation field of $F_{bulk} = 45$ Vnm^{-1} and low field layer (blue) evaporation field of $F_{layer} = 33$ Vnm^{-1}. This initial specimen geometry has an apex radius of 35 nm and a shank angle of 14^o. The level set grid has dimensions $84 \times 84 \times 125$, with a grid cell width of 3 nm. Here ion trajectories have been calculated under the linear transfer function with $\kappa = 0.8$ (Section 3.10.2). The total simulation runtime was 9 minutes. The simulation results at various instances are shown in Figure 78.

The inverse trajectory mapping visualisation, represented by the red constant detector position isolines, show similar changes in magnification and FOV to the comparative 2D example (Section 4.4). Despite evaporation field differences and geometric changes, the local Jacobian remained positive, indicating that spatial overlap of ions due to trajectory crossover does not occur. The detector density hitmaps at model instances have also been calculated via the flux method (Section 3.9.3). The ringlike structures that arise in these hitmaps are characteristic of multilayer system evaporation in experiment [49].

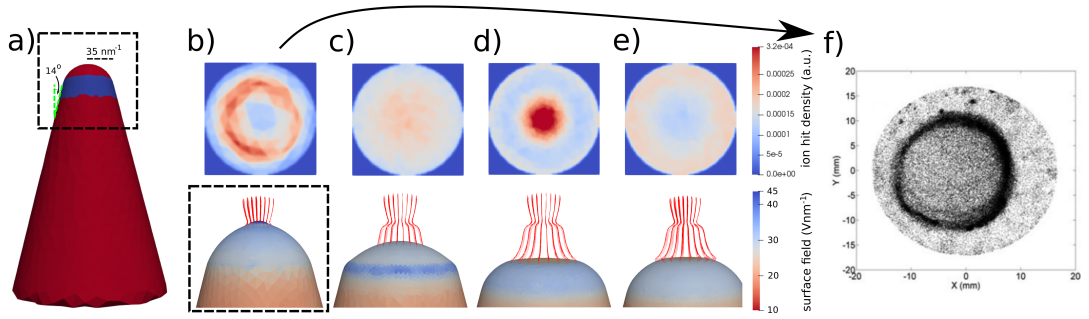


Figure 78: (a) Multilayer model initial geometry. (b-e) Specimen surface instances with the corresponding density detector maps calculated via the flux method (Section 3.9.3). The red isolines show constant detector positions of the inverse trajectory mapping. (f) Corresponding experimental density hitmap for a similar multilayer structure (reprinted from E. A. Marquis, B. P. Geiser, T. J. Prosa, and D. J. Larson. Journal of Microscopy, 241:225–233, 2011., with the permission of John Wiley & Sons, Inc.).

The second example considered is a low field Cu precipitate in an Fe matrix. Atomic-scale simulation of this system predicts that spatial overlap of Cu and Fe ions should occur at the precipitate-bulk interface [202]. A precipitate diameter of 17 nm has been simulated, such that interfaces can be resolved at a sufficiently high resolution to capture any potential trajectory overlap effects. The initial specimen model with an apex radius 35 nm and shank angle 18.5^o is shown in Figure 79a. The Fe matrix has been assigned an evaporation field of $F_{\mathrm{Fe}} = 35$ Vnm^{-1} [23], whilst the low field Cu precipitate has an evaporation field of $F_{\mathrm{Cu}} = 30$ Vnm^{-1} [23]. For this simulation, a $168 \times 168 \times 193$ level set grid, with cell widths of 1.5 nm, has been used. The total run time at this resolution, including ion projection, was 63 minutes. In this example, trajectories have been simulated over the entire instrument flight path without any transfer function.

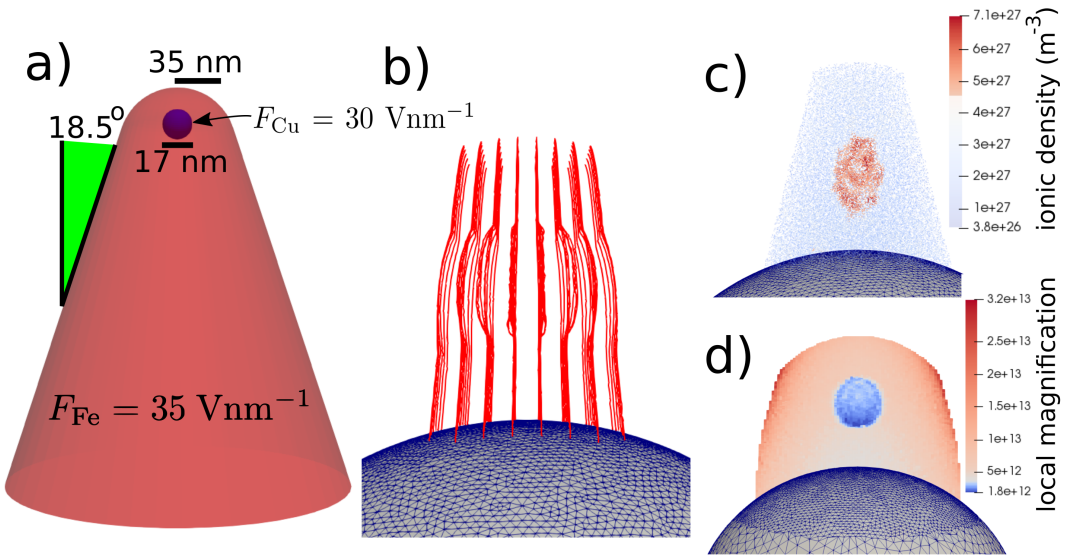


Figure 79: (a) Model precipitate initial geometry. (b) The inverse trajectory mapping (red lines show constant detector positions). (c) Density within the point-projection reconstruction. (d) Cross-section of the local magnification (Jacobian determinant) of specimen material. Note the significant demagnification of the low field precipitate.

Simulation results are shown in Figure 79. Throughout the simulation, the local Jacobian remained positive, implying that trajectory overlap did not occur. This is not unsurprising when considering the sub-nanometre scale at which interface mixing is present in the comparative atomic-scale simulation [202]. This is both beyond the numerical resolution limit of our simulation ($\sim$ 1.5 nm), as well as beyond the limit where the continuum approximation breaks down. At such sub-nanometre scales, trajectory deflections from surface terraces and ordered evaporation effects start to dominate due to the underlying crystallographic geometry. While higher numerical resolutions could be achieved through a future adaptive grid implementation, accurately capturing interface mixing at such sub-nanometre scales will likely require a multiscale modelling approach.

With no modelled trajectory crossover, the estimated inverse trajectory mapping is bijective (visualised in Figure 79b). A synthetic dataset has also been directly generated via the MC approach in Section 3.9.2. Its reconstruction via the point-projection protocol (Section 2.4.2) is shown in Figure 79c. An opti-

mum ICF of $\xi = 1.0$ has been estimated via a least squares fitting, similar to that in [100]. The reconstruction reveals a narrowing of the low field phase and an increased density, typical of low evaporation field phases [202, 61, 66]. This narrowing distortion can be understood to arise due to local demagnification of the precipitate, which can be seen from the visualised local magnification cross-section (Figure 79d).

5.4 Laser-Assisted Evaporation

In experiment, the analysis of semiconductors and insulators typically requires the application of laser pulsing to thermally reduce the surface evaporation barrier. Current instrument optics requires the laser to be incident on only one side of the specimen, and therefore its application results in anisotropic heating and evaporation over the apex [24, 203]. In Section 3.7.2, two models attempt to account for laser action: a steady-state heating model, and a surface heating model. Estimates for specimen cooling times compared to the laser pulse frequency [160] imply that the surface heating assumption is perhaps the more physical model (at least for conductors). However, neither model should be considered an accurate predictor for realistic laser-assisted evaporation.

First the surface heating model is considered (Eq. (93)). By considering field evaporation theory [108], the expression relating β to temperature T is given by $\beta = \frac{C}{kT}$, where k is the Boltzmann constant, and a typical value for C is 1.3 eV [204]. Therefore, a $\beta_{base} = 200$ approximately corresponds to 75 K, whilst $\beta_{max} = 40$ is approximately 375 K. These define a typical temperature range in experiment [160], and as such these model β values have been used here. The results from simulated evaporation under the surface heating model is shown in Figure 80. Visualisation of the estimated inverse trajectory mapping in Figure 80c shows apex blunting, and a slight FOV drift away from the side of laser incidence. Density hitmap simulation also shows an increased ion density on the side of laser incidence, agreeing well with the density artefacts observed in experiment [24, 203].

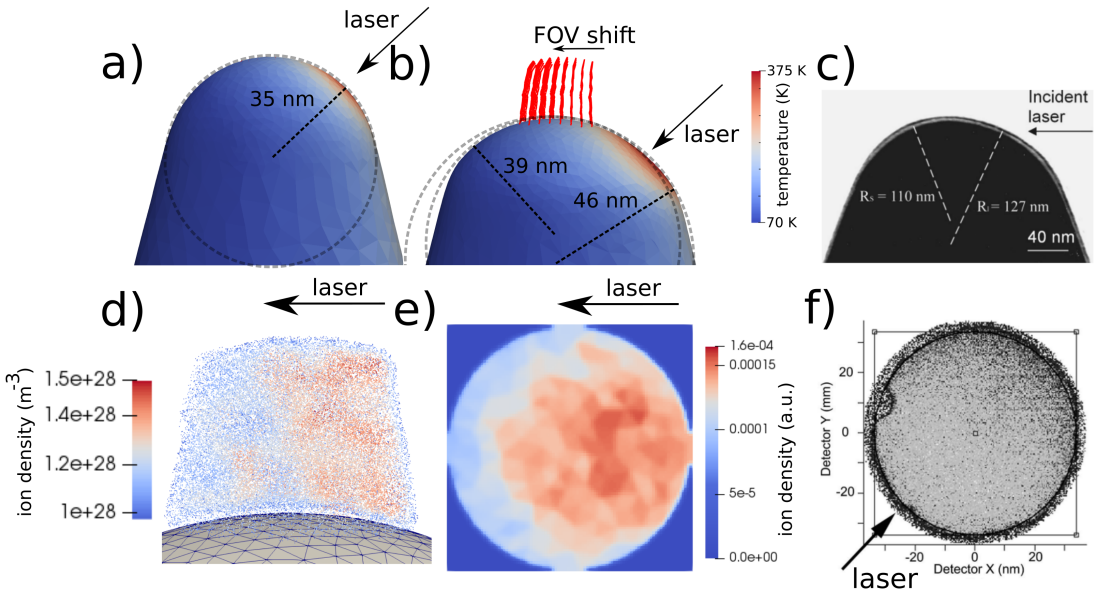


Figure 80: Results from evaporation under the surface heating laser model. (a) Initial specimen apex prior to evaporation. (b) Specimen apex following a period of laser-assisted evaporation. Blunting can be observed. (c) TEM of an experimental specimen apex (steel) after laser-assisted evaporation [205]. (d) Point-projection reconstruction of synthetic data showing local density. (e) Density detector hitmap during evaporation (calculated via flux method). (f) Corresponding experimental detector hitmap [205]. Experimental subfigures (c, f) reprinted from G. Sha, A. Cerezo, and G. D. W. Smith. Applied Physics Letters, 92(043503), 2008., with the permission of AIP Publishing.

Next, the steady-state heating model is considered (Eq. (92)). Unlike the instantaneous model, the applied laser power is a direct input parameter that determines the maximum surface temperature reached. Here our previous estimate for a typical laser incidence $||\mathbf{P}|| = 0.35$ MWm^{-2} will be used. Again $\beta_{base} = 200$ is used, corresponding to a base temperature of around 75 K. Solving the system in Figure 81, a maximum surface temperature is predicted of $\sim$ 3500 K, much greater than that estimated by experiment ($\sim$ 300 K) [160]. While the modelled specimen geometry does not have a realistic shank length, increasing its length would move the fixed base temperature further from the apex, and so could not account for this overprediction in temperature. Additionally, simulating evaporation under this temperature distribution does not predict an observable evaporation anisotropy (see Figures 81b-c) like that in experiment [24, 203]. Gi-

ven this brief analysis, the implication is that the proposed steady-state heating assumption is a less accurate model for experiment.

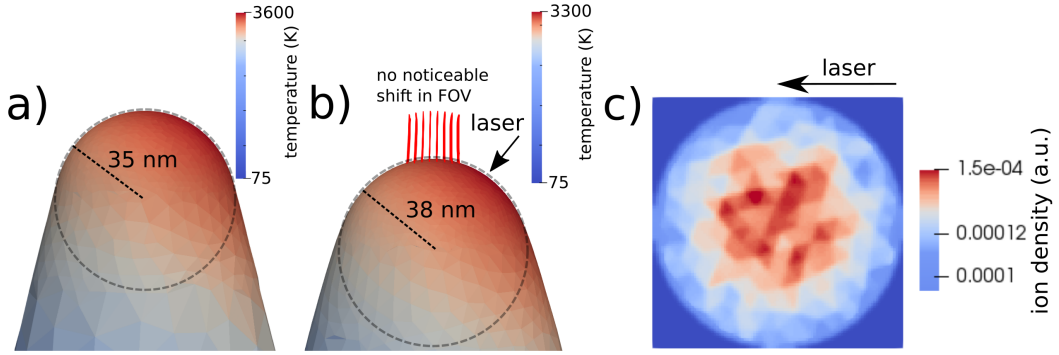


Figure 81: Results from evaporation under the steady-state laser model (a) Initial specimen apex prior to evaporation. (b) Specimen apex following a period of laser-assisted evaporation. Unlike Figure 80, no anisotropic apex blunting is observable. (c) Predicted density detector hitmap. Any hit density anisotropy is undetectable.

While neither model accurately reproduces the nonlinear effects observed in experiment [163, 162, 164], owing to an oversimplification of the physical process, they demonstrate that laser heating models can be readily integrated into the simulation framework.

5.5 Three Dimensional Crystallography

It has previously been discussed in Section 3.7.1 how surface faceting arises due to underlying specimen crystallography. Here, a modified evaporation law was suggested that produced surface faceting. This modification will now be compared to predictions made by TAPSim [67]: an atomic-scale simulator. Due to the simulation mesh conforming to the crystallographic lattice, faceting arises naturally in TAPSim, and so it is a useful tool for constraining the appropriate continuum model laws.

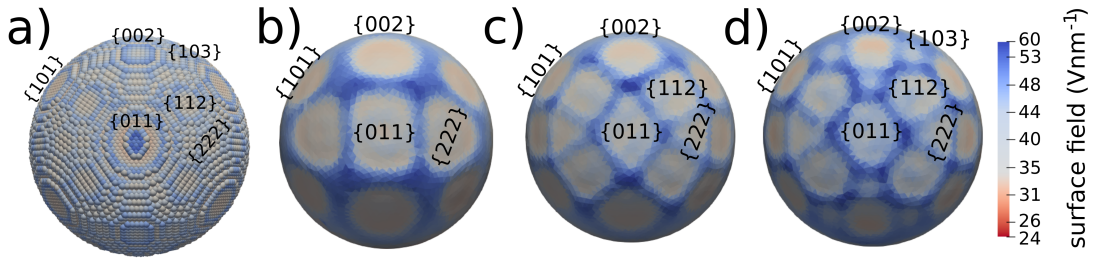


Figure 82: (a) Steady-state apex of a W bcc atomic-scale emitter oriented along [011]. (b) Continuum simulation of similarly oriented emitter. Note the incorrect square (non-diad) shape of the {011} facets. (c) Same simulation adding {112} facets. The central facet now matches the atomic model, but the {002} facet shapes are still incorrect. (d) Same simulation but adding {103} facets. The {002} facets now also match (tetrads).

In this work, a pure Tungsten (W) specimen has been simulated using an atomic-scale evaporation field of 57.1 Vnm^{-1}. Tungsten has a body-centred cubic (bcc) lattice, and this structure will be reflected in the resulting facets. The emitter crystallography is oriented such that $[0, 1, 1]$ is along the analysis axis. This atomic-scale simulation has been performed at 0 K to produce the strongest faceting. The steady-state TAPSim emitter shape is shown in Figure 82a, where the major system pole types have been labelled [23]. Given the positioning of these poles, appropriate anisotropy functions using the continuum law in Section 3.7.1 can then be constructed. The Figures 82b-d show the effect of adding increasingly higher-order poles to the continuum model. It can be seen

that the symmetry of particular facets [23] (e.g. (002) being a tetrad and (011) being a diad) arises from the positions and sizes of its neighbouring facets.

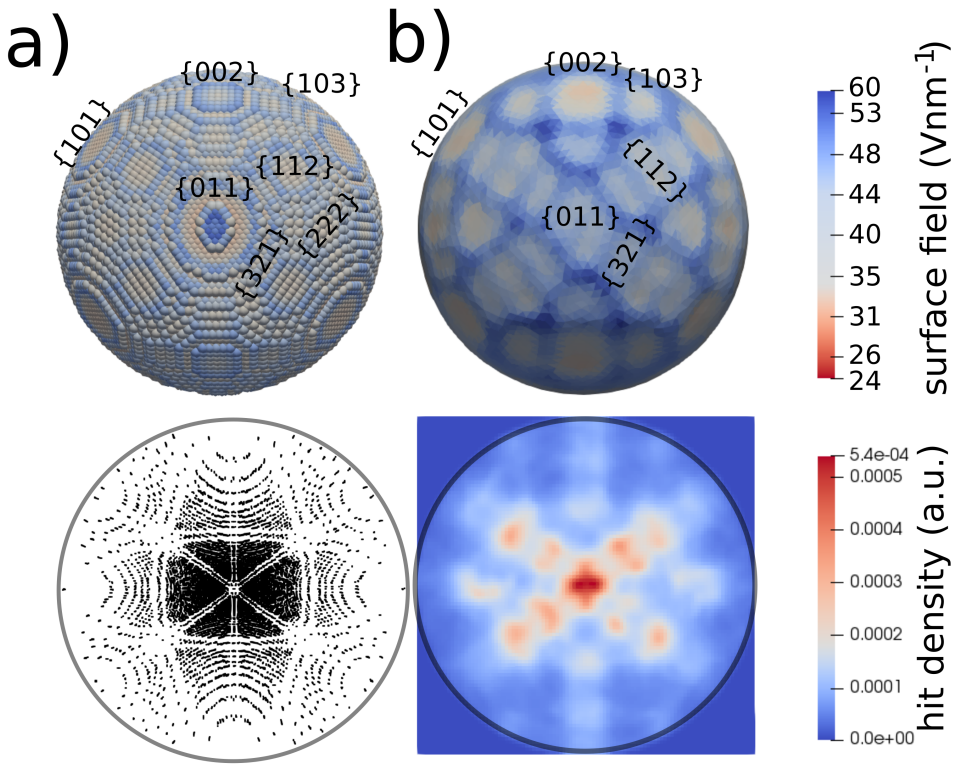


Figure 83: (a) Atomic-scale simulation of W (bcc structure) and its corresponding detector hitmap [67]. Note that poles and zone-lines appear as low density features in the hitmap. The local magnification increases towards the edge of the FOV. (b) Continuum simulation of the same bcc structure. The corresponding hitmap predicts high density regions where the atomic model predicted low density features.

While the specimen faceted shapes agree qualitatively, this alone does not confirm similar trajectory behaviour. Predicted hitmaps from the TAPSim model and continuum model are shown in Figure 83. No transfer function has been used for the charged optics. It can be seen that while a high hit density region is predicted by both models at the detector's centre, there are some significant differences in the predicted density patterns. The continuum model predicts high density hit regions on facets, rather than the low density poles and zone-lines predicted by the atomic model. It should be noted that the atomic model predictions agree well with experiment (see Figure 34), implying that the inaccuracy

lies with the continuum model.

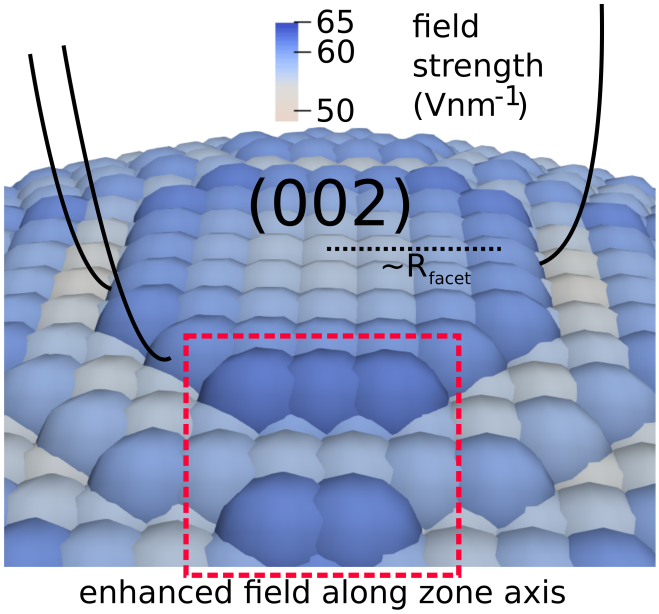


Figure 84: Diagram showing the close up of a [002] facet on the W emitter. Higher field strengths can be observed at the terraces. Example trajectories for evaporated ions are deflected away from the terrace. Generated using TAPSim [67].

This discrepancy in predicted hit density is not surprising as the low density pole structure is well understood to arise due to atomic-scale terracing and evaporation ordering effects [55, 206, 68]. During field evaporation, the most likely surface atom candidates for evaporation are those exposed to the highest surface electric field and with the fewest neighbouring bonds. Both higher surface fields and lower bonding configurations are found at atomic terraces, and so there tends to be an increased evaporation probabilities at these. This field enhancement can be understood due to the sudden increase in surface curvature at a terrace (Section 3.5.1). As the crystallographic surface normal at terraces is angled, atoms evaporating from a terrace are repelled away from the terrace and its facet's centre (see Figure 84). The electric field strength at a terrace increases as its facet's size decreases, due to a smaller facet radius (R_{facet}) corresponding to a higher curvature, and therefore higher field. Therefore, evaporated ions are increasingly deflected away from a facet's centre as its size decreases. The result

is a higher magnification surrounding surface facets, and a corresponding lower detector hit density. A similar surface field enhancement effect and deflection of trajectories occurs along zone axes, also due to an increase in local curvature and lower-than-average bonding configurations (Figure 84).

In summary, whilst the continuum model captures qualitatively similar surface faceting to that observed in experiment, the predicted ion trajectories and detector densities mismatch those observed in atomic-scale models and experiment. This is understood to be due to absence of atomic-scale evaporation ordering effects and crystallographic geometry. Therefore, it is highly likely that accurate pole structure cannot be reproduced by continuum modelling alone, and will instead require a multiscale modelling approach.

5.6 Void Structures

Like with the 2D implementation (see Section 4.9), multiple surfaces can be tracked implicitly in the level set field, allowing for the simulation of void structures. A void simulation has been performed on a $126 \times 126 \times 145$ level set grid, with a cell width of 2 nm. Here a void structure has been simulated similar to those observed in irradiated Tungsten [195, 111]. The simulated void has a radius of 7 nm, and is surrounded by a 3.5 nm thick Re layer (a similar shell-void thickness ratio to that observed in [111]). The W bulk has been assigned an evaporation field of $F_{\mathrm{W}} = 52\ \mathrm{Vnm}^{-1}$, and the Re layer a field of $F_{\mathrm{Re}} = 45\ \mathrm{Vnm}^{-1}$ [23]. Further details of the simulated specimen geometry are shown in Figure 85a. Different instances of the specimen surface during its evaporation are shown in Figures 85b-d. The focusing and subsequent crossing over of the Re ion trajectories due to the void surface concavity can be seen in Figure 85d. The Figures 85e-g show the synthetic data reconstruction displaying different local information (chemistry, density, Re composition). While the higher density region due to trajectory focusing appears as a prolate spheroid, the local Re composition reveals an hourglass shape.

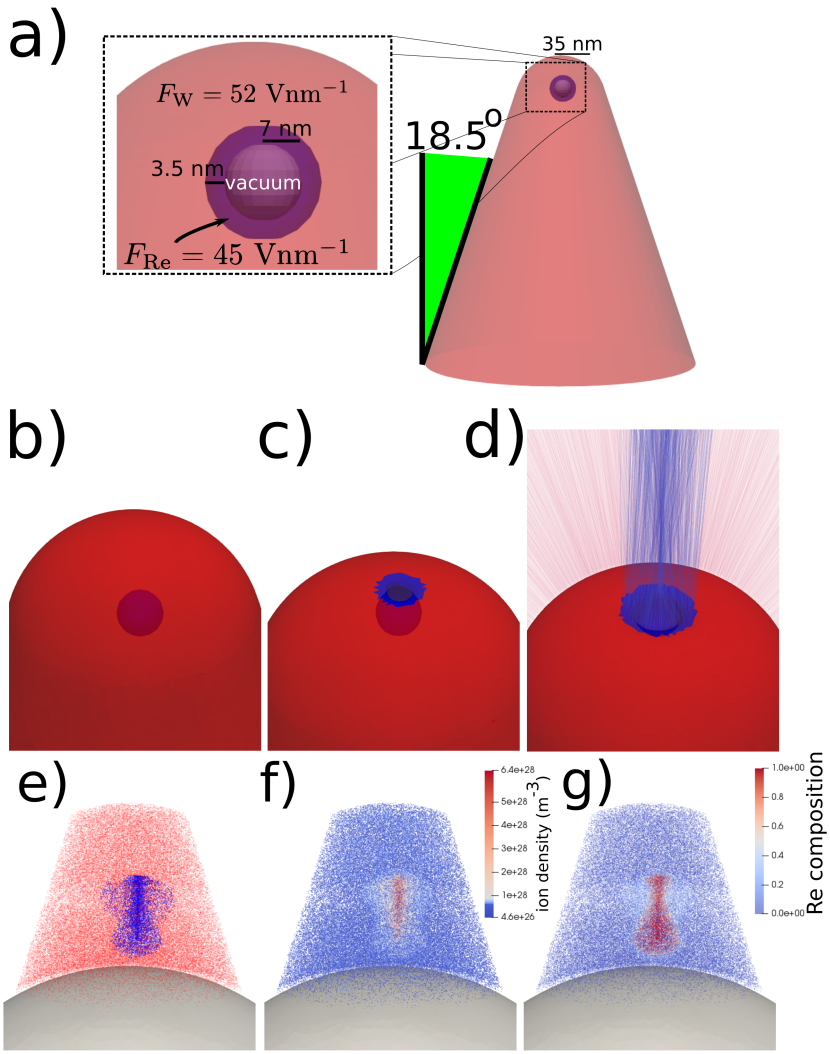


Figure 85: (a) The geometric setup for the simulated void structure. (b-d) Simulated evaporation of the void at different simulation times. The final instance also shows the focusing of ion trajectories originating from within the void concavity. (e) Point-projection reconstruction of the synthetic data. (f) Local reconstruction density. (g) Local Re composition.

However, some outlying numerical issues exist. In particular, there is noticeable drift and deformation of the void surface towards the specimen surface just prior to their intersection (Figure 86). It's possible that this drift could be reduced through an extension velocity construction via the fast marching method [198, 112], or through an adaptive grid implementation. There is also a fundamental limit in temporal resolution that can be achieved by the model at

the instant of initial void evaporation, due to a breakdown of the continuum approximation. Here the geometry is changing very rapidly with the evaporation of individual atoms, and when the void initially opens, atomic-scale evaporation ordering and trajectories are very dependent on the local crystallographic geometry [207].

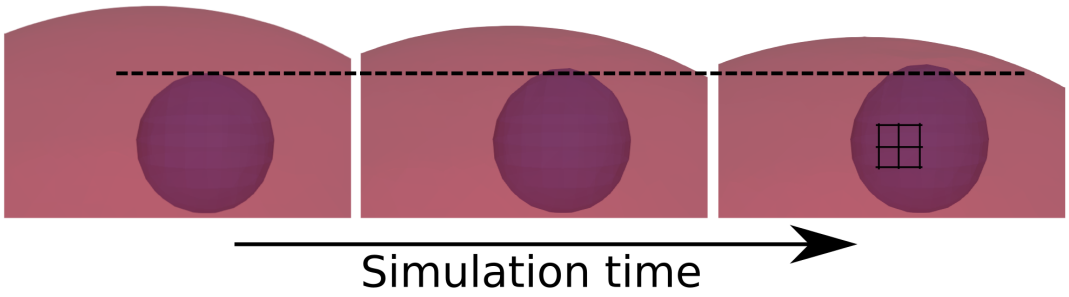


Figure 86: Void close up showing undesirable numerical drift towards the specimen surface prior to its intersection. While some drift is not unsurprising due to discretisation, especially on the scale of the level set grid (shown by the black grid), a level set extension velocity construction via the fast marching method could aid in its minimisation [198, 112].

This example demonstrates that voids can be incorporated into the 3D model, and successfully reproduce experimental results such as increased local densities due to trajectory focusing [195, 111]. However, numerical issues exist (Figure 86), and like with the crystallographic simulations (Section 5.5), care should be taken regarding when and where the continuum approximation breaks down. Accurate simulation of the initial evaporation into voids will likely require a multiscale modelling approach.

5.7 Electron Tomography Initialisation

So far all initial model geometries considered have been constructed using analytic functions. However, these analytically defined geometries will never be a perfect match to true experimental geometries. It is also possible to define realistic model geometries using data from correlative experimental techniques, such as electron tomography (ET) or atomic force microscopy (AFM). Here, ET data has been opted for due to providing direct information regarding the internal geometries of material phases.

In this work, all tomograms have been constructed from a TEM tilt series via the SIRT algorithm (Section 2.6.1) implementation within the ASTRA toolbox [208]. The output for these reconstructions is a 3D scalar image, where the physical interpretation of a particular local contrast depends on the imaging mode used. The specimen surface and internal phase meshes can then be extracted as isocontours of this voxel field via marching cubes (Section 2.6.3). Currently, this requires the user to manually defining a threshold value for the extracted surface.

The first specimen geometry considered is that of an Al-Mg-Si alloy containing MgSi precipitates, likely resulting from dealloying of $MgSi_2$ precipitates. A full 360^o TEM tilt series was obtained in HAADF-STEM mode[2]. The specimen surface was extracted with the normalised contrast value of 0.4, and the precipitates with a value of 0.63. The ET lateral cross-section with the marked extracted contours is shown in Figure 87a-b, and the resulting extracted 3D mesh geometries shown in Figure 87c. The material bulk is Al, and so has an experimentally measured evaporation field of $F_{\mathrm{Al}} = 19$ Vnm^{-1}. The effective evaporation field to use for the MgSi precipitates is unknown. However, the experimental evaporation fields for the pure elements are $F_{\mathrm{Mg}} = 21$ Vnm^{-1} and $F_{\mathrm{Si}} = 33$ Vnm^{-1}, both of which are higher field than F_{Al}. Therefore, an averaged value for the phase of $F_{\mathrm{MgSi}} = 27$ Vnm^{-1} has been assumed. The simulation has been performed on a

[2]TEM tilt series and ET reconstruction performed by Thomas Slater, Diamond Light Source.

$36 \times 38 \times 303$ level set grid, with a cell width of 3 nm. The total simulation time, including ion projection, took 26 minutes.

The estimated trajectory mapping is visualised in Figure 87c. Throughout the simulation, the Jacobian determinant remains positive implying that no trajectory overlap was present. In this example, ion trajectories have been calculated directly up to the detector without the use of an instrument transfer function or local electrode. Hence the image compression and subsequent FOV is underestimated compared to what is typical in a LEAP or LaWaTAP instrument.

The predicted apex shape and corresponding density hitmap at position D in Figure 87c are given in Figure 87d-e. It can be seen that the local magnification is increased within the neighbourhood of a high field precipitate (blue) due to a higher positive curvature. By considering the detector hitmap, we observe that higher magnification approximately corresponds to a lower hitmap density. Here, the marked higher density band corresponds to a region of lower magnification surrounding the precipitate boundary, due to negative specimen surface curvature. This region of positive curvature (low detector density), followed by a region of negative curvature (high detector density), is characteristic of interfaces between phases of differing evaporation field (see Figures 69a-b).

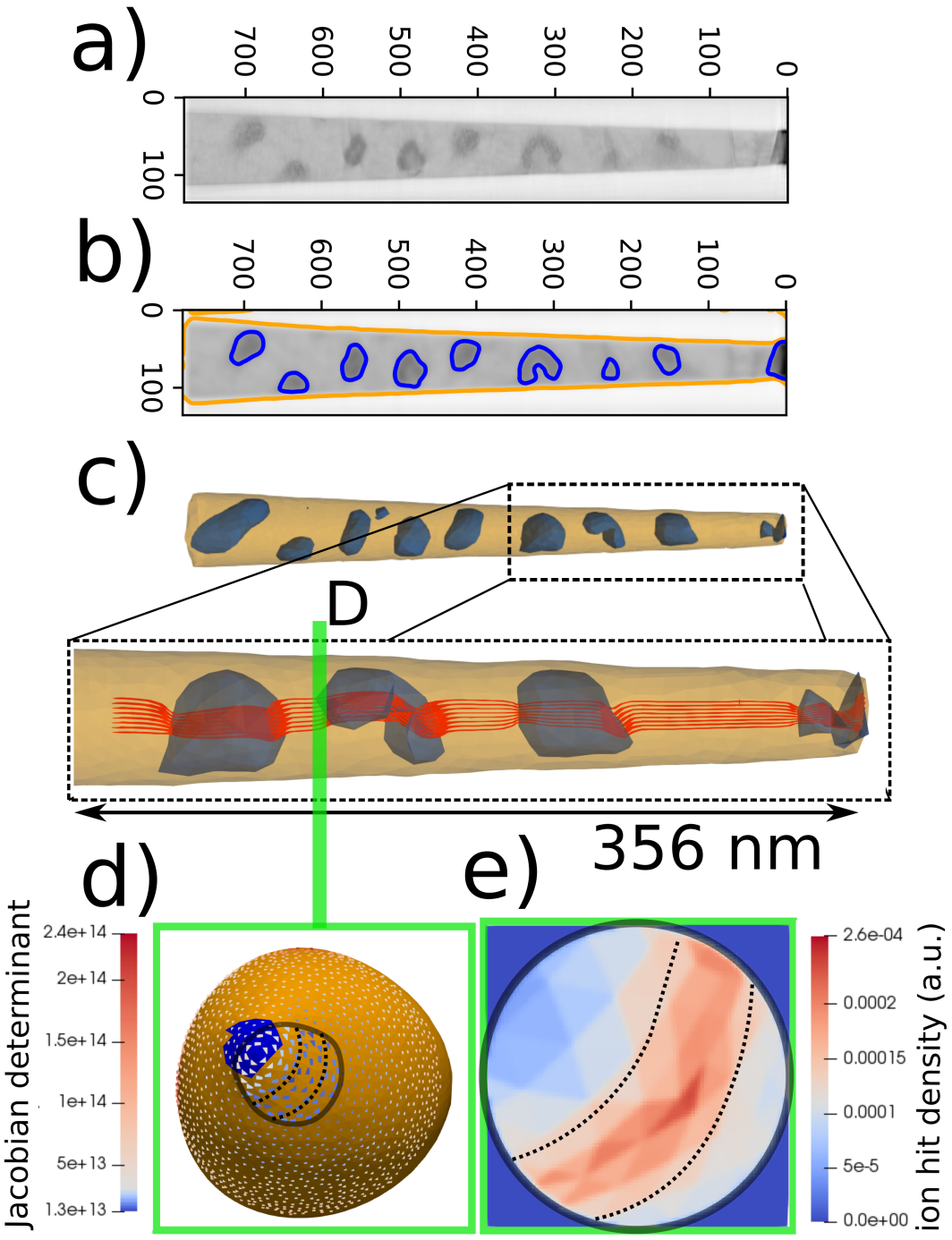


Figure 87: (a) Lateral cross-section of the ET scalar field. (b) Same cross-section but showing isocontour extraction, with the specimen surface in orange and the precipitates in blue. (c) Final specimen geometry following clean up, with an inset showing the predicted trajectory mapping. (d) Specimen surface at model instance D showing local magnification (Jacobian determinant). Unlike previous simulations, the initial geometry is asymmetric which is reflected in its steady state. The grey ring marks the surface patch within the FOV (detector). (e) Predicted detector density map at instance D. Note that a higher magnification approximately corresponds to a lower hitmap density.

5.8 Towards Data-Driven Evaporation

Finally, the potential to determine the model evaporation rate directly from the detector data will be explored, instead of estimating these from the calculated electric field. An advantage of such an approach is that it could avoid introducing physical errors from the assumed rate equation (Eq. (21)), e.g. from laser-assisted evaporation. This derivation can be achieved by solving the matrix system in Eq. (115) that describes the transfer of evaporation fluxes under the trajectory mapping onto the detector. When solving this system, panels outside of the FOV have an assumed evaporation rate of zero (this will introduce localised errors at the FOV boundary). This rectangular matrix equation can then be solved for the surface panel evaporation rates ($\mathbf{R_e}$) by computing the linear least squares solution. In order to guarantee its convergence, the detector must be sufficiently discretised to ensure that the linear system is not underconstrained.

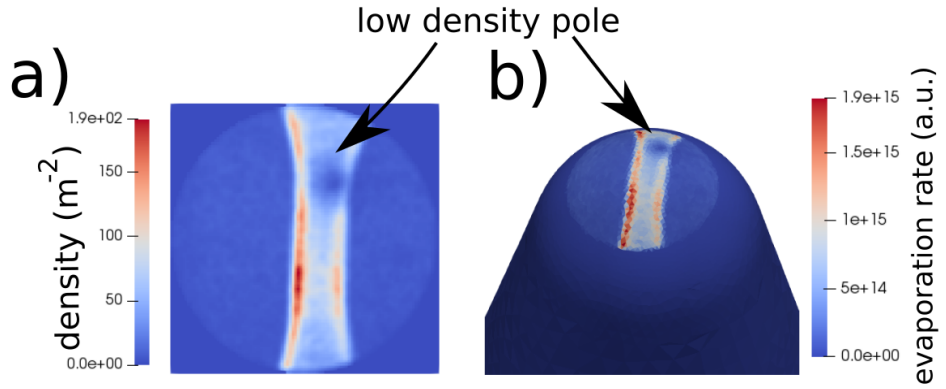


Figure 88: (a) Density hitmap from the FinFET experiment featuring the higher density central fin structure [51]. (b) Back-projection of the detected evaporation rate onto the same specimen surface via solving Eq. (115).

The first example considers deriving the local surface evaporation rate from real experimental hitmap data. The detector density hitmap, shown in Figure 88a, is midway through the evaporation of a vertical layer (FinFET) structure (Section 6.4). The back-projected evaporation rate onto an assumed hemispherical apex geometry is shown in Figure 88b. As will be seen, this hemispher-

ical apex assumption is unrealistic for the FinFET halfway through evaporation (Section 6.4). However, this method works for any assumed static specimen geometry, with Figure 89 showing the result for a surface concavity with a uniform detection density.

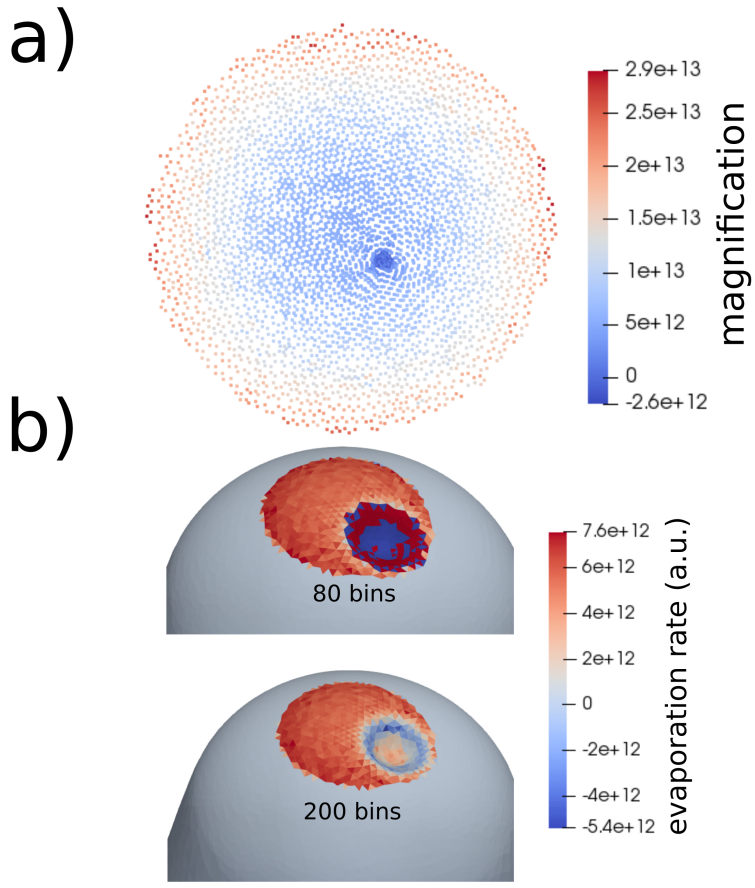


Figure 89: (a) Local magnification projected onto the detector for a local concavity. (b) Back-projected surface evaporation rates at two detector grid resolutions (80×80 bins vs 200×200 bins), assuming uniform detector density (1 m^{-2}). The solution within the concavity in the lower resolution case breaks down from ill-conditioning because of being locally underconstrained. The higher resolution case successfully converges, although unphysical negative evaporation rates arise, potentially due to assuming an unphysical hitmap density. Resolving this might require solving for the evaporation rate under a positivity constraint.

While in theory this back-projection method should be able to account for trajectory focusing effects arising from surface concavities, the linear system was found to be ill-conditioned within concavities unless a sufficiently high detector grid resolution is used (Figure 89). An adaptive detector binning, increasing in

resolution within reduced magnification regions, could ensure a well-conditioned problem even under extreme changes in local magnification.

This data-estimated evaporation rate could potentially be used to construct the velocity extension field for the level set method. However, a number of outlying problems must first be solved. This approach does not provide a satisfactory definition of evaporation rate outside of the FOV due to missing information, and so like other directly coupled methods [85, 86], some constraint must be imposed regarding surface evolution outside of the FOV. One possibility could be to use a hybrid method, where model predicted evaporation rates are used outside of the FOV. This direct method is also reliant on accurately estimating ion trajectories. During a data-driven simulation, any errors would likely accumulate, resulting in the model diverging away from the true specimen evolution of experiment. Therefore, it is highly likely that correlative experimental data, e.g. ET, would still be required to constrain and validate model evolution.

5.9 Conclusions

In this chapter, results from the 3D model implementation have been presented, extending the previous 2D conductor model from Section 4. A number of examples have been considered, including the evaporation of multiphase materials, voids, laser-assisted evaporation, and crystallographic anisotropy. The evaporation of a real needle-shaped geometry for a Mg-Si-Al alloy was also predicted through initialising the specimen model from ET data. The model successfully reproduces a wide range of distortions present in experiment, and simulation results can be quantitatively compared to this experimental data. While exact computation times depends on the model resolution, simulations run in minutes for grid cell widths of a few nm, potentially a thousand times faster than comparable atomic-scale simulations [74].

The current 3D implementation assumes that the modelled specimen is highly

conductive. While there is evidence that this is not an unreasonable approximation, given the high surface electric fields and typical material values for dielectric breakdown [144, 145, 146, 147], a model extension to handle dielectrics through a FEM-BEM coupling or multidomain-BEM [141] would add significant flexibility. Such an extension could also prove a useful tool for determining the validity of the classical dielectric approximation under the high field strengths present in experiment.

Two simple laser models have also been considered, with the surface heating model producing qualitatively comparable behaviour to the laser-assisted evaporation of a conductive steel in experiment (Figure 80). However, neither model can reproduce the complicated laser-assisted evaporation phenomena of dielectric materials predicted by theory, and observed in experiment [163, 162, 164]. While temperature distribution estimation could be decoupled from specimen evolution [83], accurate laser dynamics will require a direct coupling where Maxwell's equations are solved dynamically throughout the simulation via finite-difference time-domain methods [162] or fast multipole-accelerated BEM [209].

The simulation of a bcc emitter produced comparable surface faceting to that observed for an atomic model, with both models exhibiting comparable facet symmetries. However, the continuum approximation was unable to reproduce the correct structure distortions due to lacking atomic-scale geometry and evaporation ordering effects [206]. Accounting for these atomic-scale effects, whilst also maintaining model efficiency, will likely require a multiscale modelling approach. This could either be through comparable atomic-scale simulation for the evaporation of a few atomic planes, deriving some trajectory modifier function over continuum model facets, or through a direct continuum-atomistic coupling via adaptive grid methods [210]. For general crystallographic distortions, the most promising approach could be via hybrid physics-machine learning models [211], trained on a databank of comparable atomic and continuum simulations. Such multiscale

and hybrid models could also potentially capture and correct for ion mixing at interfaces arising due to atomic-scale evaporation ordering effects [46, 61].

A large number of possible methods exist for further improvement and optimisation of model numerics. An adaptive grid level set method could allow for simulation resolution to be increased surrounding phase interfaces [200]. A parallel-in-time multigrid method [199], and a level set narrow band approach [197] would also allow for more efficient solution of the level set equation. A fast marching velocity extension construction could improve subgrid resolution, and avoid the need for field reinitialisation [198, 112]. Implementing a level set method on an irregular unstructured grid via a finite volume or finite element method could also be considered [212], allowing the grid to better conform with the phase geometries observed in experiment. The electrostatic solver's accuracy and conditioning could also be improved through a higher-order collocation or Galerkin BEM [213, 214]. The BEM could also be further accelerated through BEM compression techniques such as a fast multipole method [131], and through Krylov subspace recycling to allow solver calculations to be recycled between model iterations [215]. Subspace recycling could also prove useful in further accelerating current atomic model implementations [67].

Despite these limitations and potential improvements, the existing 3D model is a highly useful tool for interpreting and understanding experimental data. Simulation of full-size specimen geometries can be performed in minutes, compared to the days-to-months currently required for equivalent atomic-scale simulations [74, 136]. For the first time, direct comparison with experiment can be performed through simulated evaporation of real specimen geometries observed in experiment. This fast correlative simulation sets the stage for applying such models to directly drive the reconstruction of experimental APT data, where the predicted inverse trajectory mapping can be utilised to attempt the correction of multiphase distortions.

6 Exploring Model-Driven Reconstruction

The development of a fast 3D model for specimen field evaporation raises the prospect of using such a model to directly drive reconstruction. In Section 3.11, a protocol was outlined for calibrating the model to experimental data, and using this calibrated model to subsequently reconstruct the data. This chapter will demonstrate several results from such reconstructions, including two experimental semiconductor datasets.

6.1 Setup and Workflow

The proposed reconstruction workflow is outlined in Figure 90. The initial steps consist of gathering the APT data, and setting up the 3D specimen model using correlative imaging data (here electron microscopy) gathered prior to APT analysis. Fixed parameters are provided, including the instrument detector radius and flight path. Using initial guesses for model parameters, the model is evaporated and trajectory mapping calculated. Next the user provides the detector space landmark positions (Section 3.11.2), matching up specific positions in the experimental detected ion sequence to the appearance or disappearance of corresponding model phases projected onto the detector. This allows for the experimental and model detector spaces to be calibrated in depth. Finally, the model trajectory mapping can be applied to drive the reconstruction of the experimental APT data (Section 3.11.1). This reconstruction procedure is typically performed iteratively, tuning both the specimen alignment and additional instrument compression parameters (Section 3.11.4), and the model evaporation parameters (Section 3.11.5). Note that by splitting up these calibration steps, the model simulation steps (highlighted in yellow) only need to be rerun when tuning physical evaporation parameters. In this work, both optimisation steps have been performed via an (adaptive) regular grid search, allowing for easy visualisation

and interpretation. However, other global (or potentially local) optimisation methods, such as random search [216], should be just as applicable. Finally, once model parameters have been optimised, the optional generalised alignment procedure (Section 3.11.10) can be performed. The final result from this workflow is a calibrated APT reconstruction, driven by the generalised specimen model.

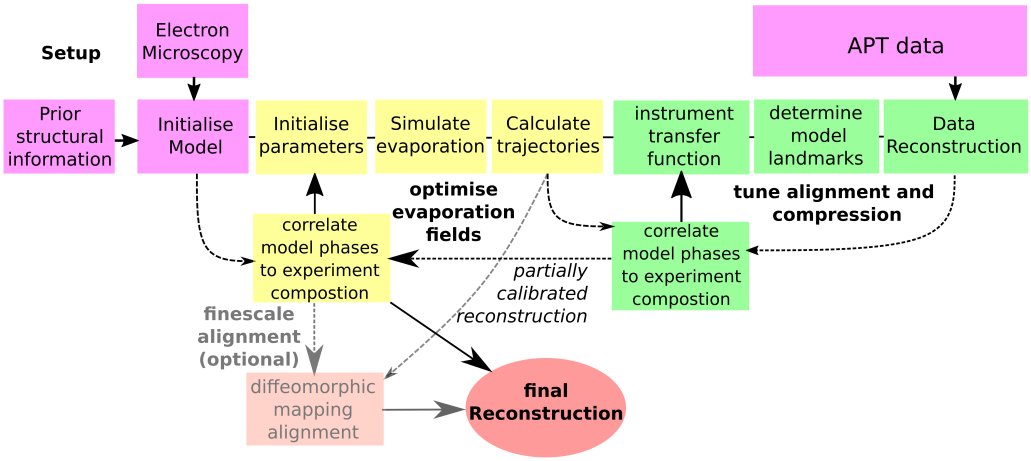


Figure 90: Outline for the proposed complete reconstruction workflow. The coloured regions breakdown the workflow into various blocks. Arrows imply the flow of data.

6.2 Reconstruction of a Synthetic Dataset

In order to test the numerical stability of the reconstruction protocol, it is insightful to generate synthetic data and then reconstruct this using the same generator model. To demonstrate the protocol's relative stability in the presence of surface concavities and trajectory focusing from low field inhomogeneities, the ET data set for the Al-Mg-Si alloy (Section 5.7) has been revisited, but instead assuming low field values for precipitates. A level set grid size of $39 \times 42 \times 297$ has been used, with the bulk field of $F_{\text{bulk}} = 17$ Vnm^{-1} and precipitates a field of $F_{\text{precipitate}} = 13$ Vnm^{-1}. In order to achieve a larger FOV, a detector radius of $R_{\text{det}} = 0.1$ m has been assumed. Ion trajectories have been calculated fully to the detector, with no instrument transfer function applied. The estimated inverse trajectory mapping from the simulated evaporation is shown in Figure 91. Throughout the simulated analysis, the Jacobian determinant remained positive over the entire FOV, confirming that no trajectory crossover is predicted to have occurred (at least over the grid resolution of 3 nm). The total simulation time took 28 minutes including ion projection.

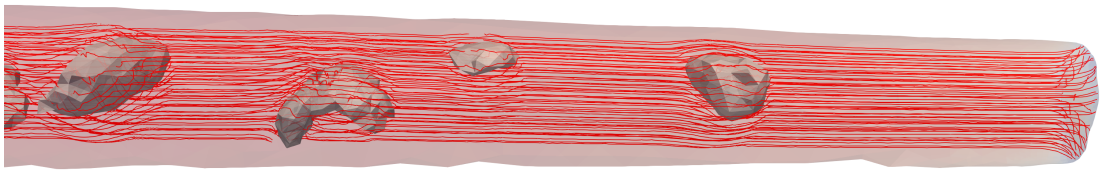


Figure 91: Visualisation of the estimated inverse trajectory mapping via constant detector position lines (red). Reprinted from C. Fletcher, M. P. Moody, and D. Haley. Journal of Physics D: Applied Physics, 53(475303), 2020., with the permission of IOP Publishing.

A synthetic dataset has been generated using the MC method in Section 3.9.2, with a constant ionic volume of $v_{\text{ion}} = 0.5$ nm^3. For the point-projection reconstruction, an initial cap radius of $R_0 = 22.5$ nm and shank angle of $\alpha = 1.9^o$ was determined via a least-squares fitting of the Bas specimen model to the ET

surface geometry (Figure 92a). From this constrained Bas geometry, the image compression factor (ξ) throughout the model's evaporation was determined by solving the linear system described in [100] via least squares (Figure 92b). Here, an average best fit value for the image compression was determined of $\xi = 1.16$. It is this ICF that is used for the comparative projection-based reconstruction.

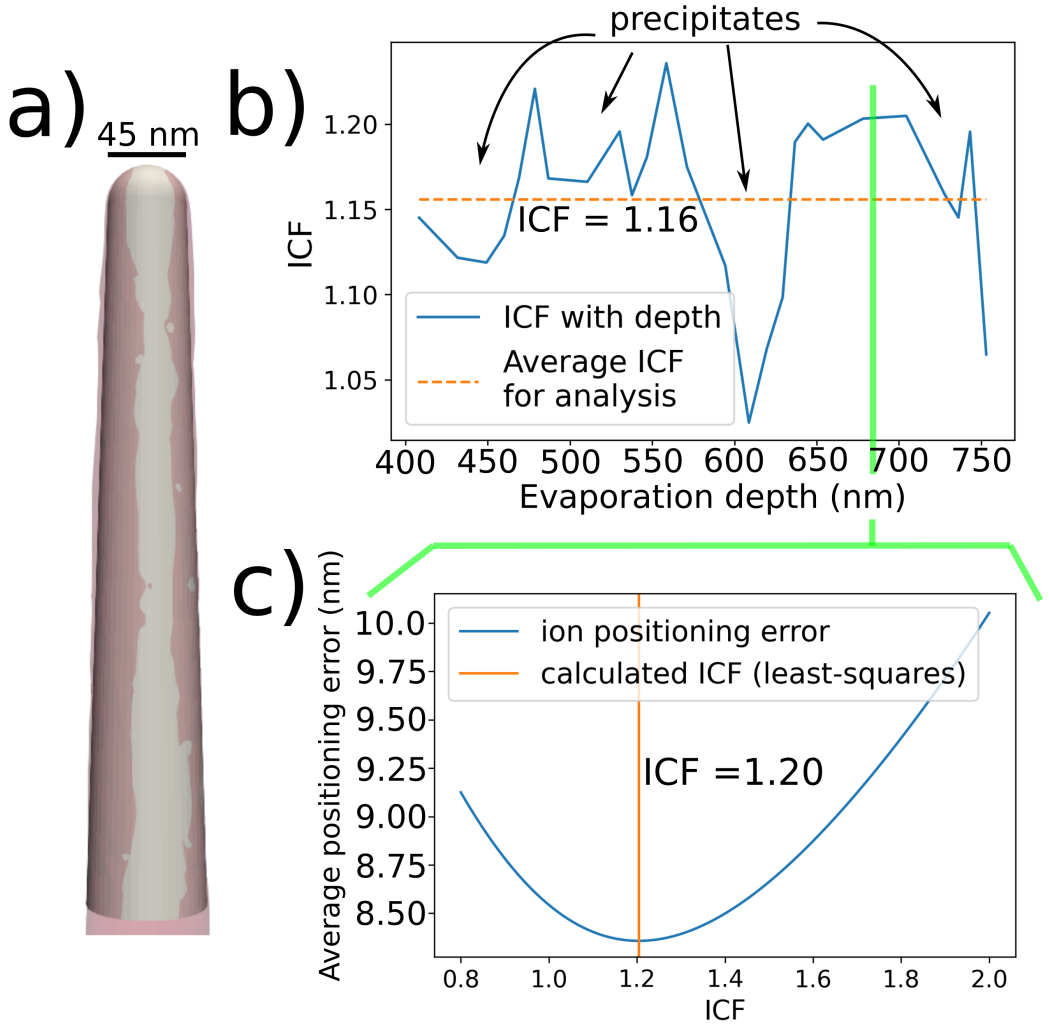


Figure 92: (a) The fitted hemispherical Bas model (grey) to the ET geometry (red) following a period of evaporation. (b) Calculation of image compression parameter (ξ) throughout the specimen evaporation. The sudden decreases in the instantaneous ICF can be attributed to passing through low field precipitates. The time-averaged model ICF of 1.16 is marked by the orange dashed line. (c) Inset showing the average positioning error, between initial launch positions and the back projection, against the least-squares calculated ICF at the evaporation depth marked by the green bar in b).

Model-driven reconstruction can also be performed on the synthetic data, via the landmarking method in Section 3.11.2, and compared back to this point-projection reconstruction. Due to the same model being used for both data generation and reconstruction, model alignment and parameter tuning is not required. The two reconstructions are shown in Figure 93, with the exact placement of landmarks visualised in Figure 93c. It can be seen that within the model-driven reconstruction (Figure 93b) there is a significant improvement in the correlation of model microstructure and precipitate ions. In comparison, the precipitates within the point-projection reconstruction (Figure 93a) are laterally demagnified compared to the model geometry. This demagnification of low field precipitates is widespread in experiment [61, 47], arising due to the local focusing of ion trajectories.

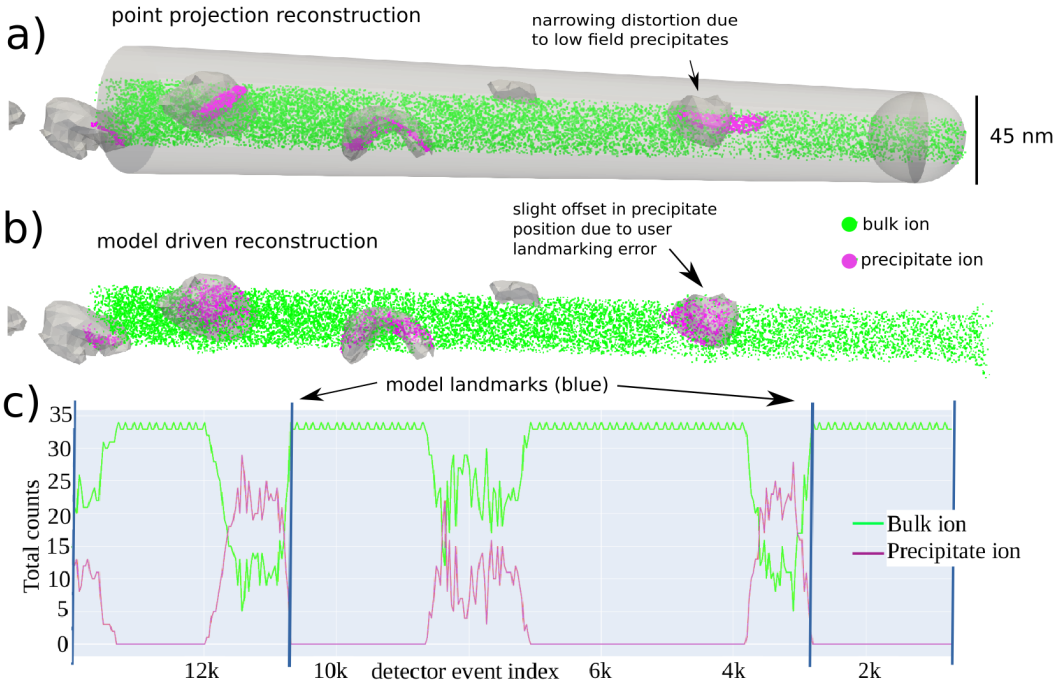


Figure 93: (a) Point-projection reconstruction with parameters of $R_0 = 22.5$ nm, $\alpha = 1.9^o$, and $\xi = 1.16$. A lateral demagnification (narrowing) of precipitate ions can be observed. (b) The model-driven reconstruction of the same synthetic dataset. (c) Binned histogram of ion positions in the detected evaporation sequence (detector space depth). Selected landmarks are highlighted such that corresponding model instances are snapped to these detector space depth positions by selection of appropriate ionic volumes. Reprinted from C. Fletcher, M. P. Moody, and D. Haley. Journal of Physics D: Applied Physics, 53(475303), 2020., with the permission of IOP Publishing.

The strong correlation between precipitate ions (purple) within the model-driven reconstruction and the original phase geometries (Figure 93b) implies that the reconstruction protocol is numerically stable, even with strong local demagnification. Now that the protocol's numerical stability has been validated, we can consider the reconstruction of experimental data under this same protocol.

6.3 The Multilayer Reconstruction

A typical multiphase material system studied using APT are multilayer structures. Here the specimen typically consists of a stack of layers with different compositions, and subsequent evaporation mechanics. Previous examples for these systems (Sections 4.4 and 5.3) have shown that the evaporation of layered phases with differing fields introduces changes to both the local magnification and FOV throughout analyses. This raises the question of whether such a model could be used to reverse these distortions within real APT data. The reconstruction of synthetic data in Section 6.2 confirmed that the reconstruction protocol is numerically stable. However, additional challenges now arise due to a lack of knowledge regarding the specimen alignment, chamber optics, and material evaporation physics.

The raw ET data for the multilayer system[3] is shown in Figure 94a. Here, due to a loss of edge contrast, the phase meshes corresponding to layers have had to be extrapolated to intersect with the specimen surface (Figure 9). The model initialisation procedure from the raw ET data is outlined in Figure 94. It should be noted that, whilst the evaporation field $F_{\mathrm{Ge}} = 29$ Vnm^{-1} is known from experiment [23], the effective evaporation fields for the two binary $\mathrm{Si}_X\mathrm{Ge}_{1-X}$ phases are unknown. These fields will have to be constrained via parameter tuning. Simple linear interpolation from the known monatomic evaporation fields for $F_{\mathrm{Ge}} = 29$ Vnm^{-1} and $F_{\mathrm{Si}} = 33$ Vnm^{-1} gives estimates for the phase effective fields of $\overline{F}_{\mathrm{Si}_{0.3}\mathrm{Ge}_{0.7}} = 30.2$ Vnm^{-1} and $\overline{F}_{\mathrm{Si}_{0.15}\mathrm{Ge}_{0.85}} = 29.5$ Vnm^{-1}. It is currently unclear just how accurate this assumption will be. To maximise similarity within the relevant region, only the layered section of the reconstruction (marked ROI in Figure 94) is considered during optimisation. As the $\mathrm{Si}_{0.15}\mathrm{Ge}_{0.85}$ phase lies outside of this ROI, its evaporation field will be fixed at its estimated value. Simulation

[3]ET performed by Hugo Bender, Paromita Kundu and Olivier Richard, and APT performed by Masoud Dialameh, all based at IMEC, Leuven.

was performed on a $41 \times 44 \times 130$ level set grid, with cell widths of 1.4 nm.

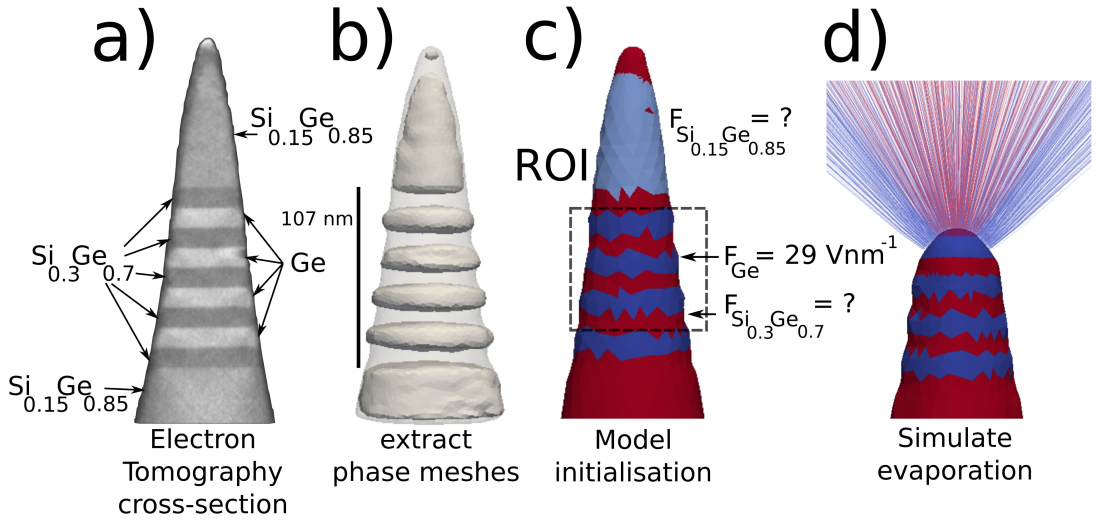


Figure 94: (a) Cross-section of the raw ET data (background removed). (b) Contour extracted surface and phase meshes. Due to edge contrast loss, phase meshes have been extended to intersect the specimen surface. (c) Initialised model with labelled effective evaporation fields (two unknown). (d) Once evaporation fields are defined, simulated evaporation can be performed.

Next, suitable landmarks must be defined to calibrate the model and experiment detector spaces in depth. Here, the initial detection of the evaporation of pure Ge layers (blue) has been used (Figure 95).

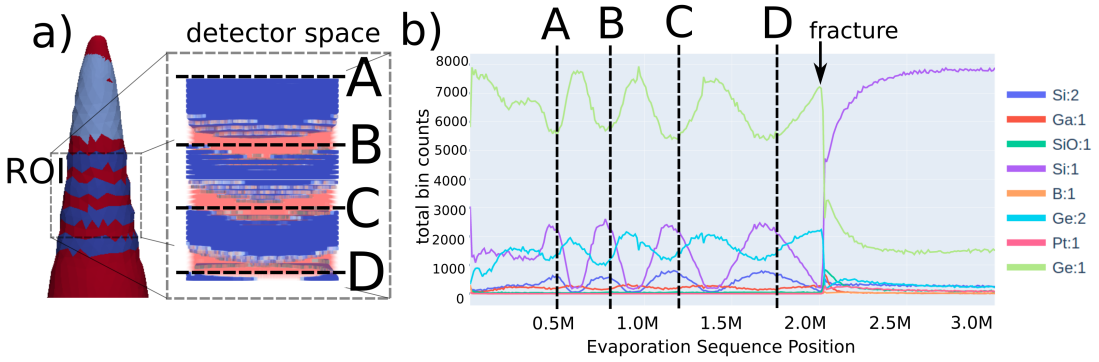


Figure 95: (a) Shows model predicted detector space within the Region Of Interest (ROI). Model landmarks are positioned where Ge (blue) layers enter the FOV. (b) Binned histogram of ion depth positions in detector space, with experimental landmark positions marking the initial evaporation of Ge layers.

With depth calibration complete, data reconstruction can proceed by following

the protocol outlined in Figure 90. During parameter optimisation, 12 simulations have been performed with varying $F_{Si_{0.3}Ge_{0.7}}$ evaporation field values, taking a total time of 4 hours. Figure 96a visualises the 1D grid of explored physical model parameters (effective evaporation fields). This sweep identifies an optimum evaporation field of $F_{Si_{0.3}Ge_{0.7}} = 30.3$ Vnm^{-1}, defining a best fit model. While this is in reasonable agreement with the estimated value of 30.2 Vnm^{-1}, further analyses are required to determine the general validity of this approximation. The plots in Figure 96b-d show the partial optimisation for the model alignment and instrument compression, with the optimum parameters identified. Finally, a comparison between the model-driven reconstruction and point-projection reconstruction is shown in Figures 96e. For the point-projection reconstruction, a shank angle of $\alpha = 8.9$ and initial radius of $R_0 = 9$ nm were determined by a least-squares fitting of the Bas model to the ET geometry, whilst an ICF $\xi = 1.6$ was found to ensure good correlation with the ET measured multilayer spacing. Within the point-projection reconstruction, the microstructural layers are distorted and tilted. In comparison, the model-driven reconstruction has successfully corrected this tilting, better correlating with the true microstructure observed by ET. This result confirms that the proposed protocol can successfully reduce microstructure distortions in comparison to projection-based reconstruction.

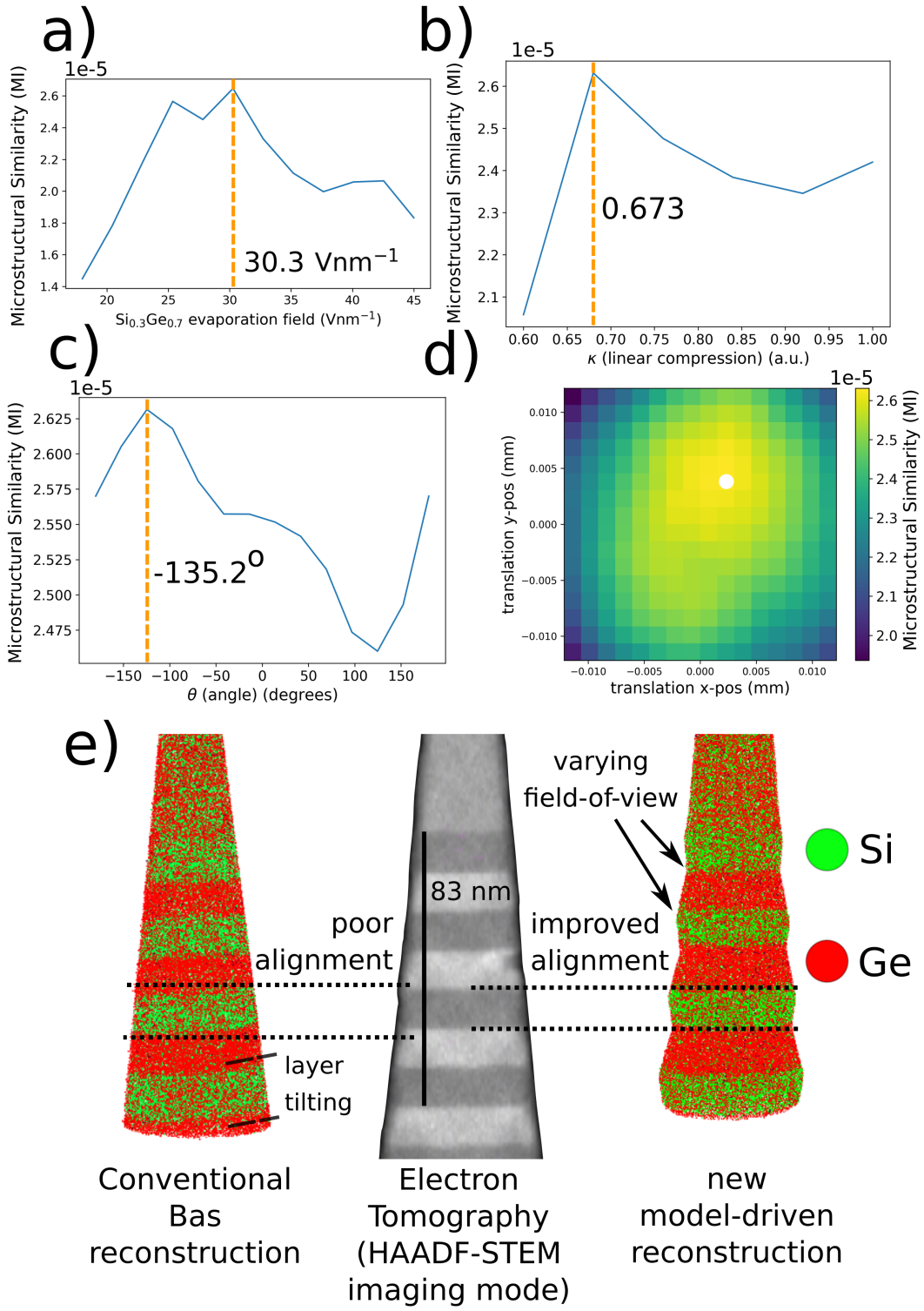


Figure 96: (a) Regular grid search over $F_{\mathrm{Si_{0.3}Ge_{0.7}}}$ in detector space under the MI metric. (b-d) Plots for the partial optimisations over the instrument compression (κ), and rigid body alignment parameters (θ, $\vec{\mathbf{r}}$). (e) Comparison between point-projection reconstruction and calibrated model-driven reconstruction. The tilting distortions present in the Bas reconstruction have been successfully corrected for.

It should be noted that while the model successfully aligns to the experimental data, correcting for the tilting artefacts, the current model's evaporation physics is not entirely realistic. Unlike in experiment, the laser heating effect has not been incorporated, which is known to cause apex blunting (Section 5.4). Simulation results of a multilayer system with matching evaporation fields in Figure 97a-b reveals that this laser blunting reproduces similar layer tilting and density effects to that observed in experiment (Figure 97c-d). Additionally, the distribution of Si charge-state ions over the detector, a function of the apex surface field, is also correlated to the experiment laser direction (Figure 97e). These results strongly imply that the observed tilting is very likely also due to the laser, and not just specimen misalignment. Provided further model constraints from experiment, such as the relative orientation between the ET and APT data, models for the laser could be directly incorporated into these simulations and reconstruction.

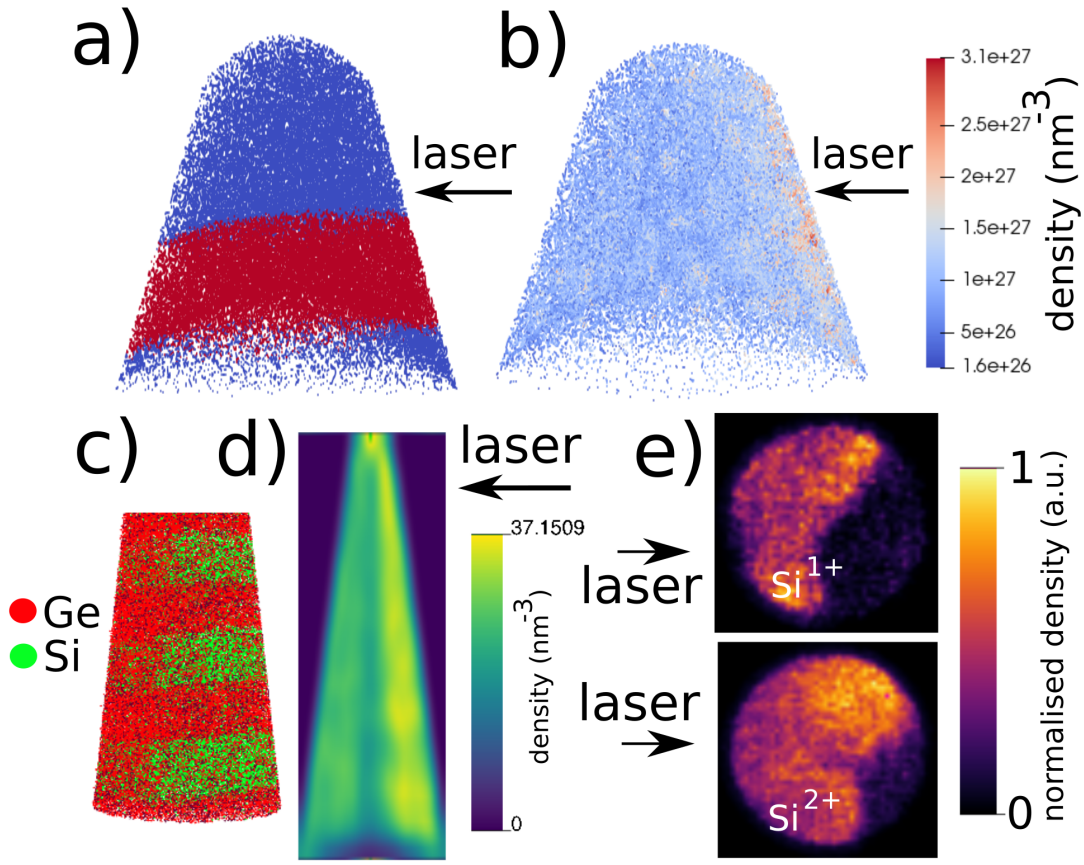


Figure 97: (a) Simulated reconstruction of a multilayer system with uniform evaporation fields under laser illumination. (b) Corresponding local density. (c) Tilting of layers in experimental dataset. (d) Density throughout the experimental point-projection reconstruction. (e) Distributions of Si charge-state ions. Si^{+1} appears biased towards the side of laser illumination, where the surface field is reduced due to blunting.

Regardless of the laser's omission, the model-driven reconstruction protocol has successfully reduced microstructural distortions within the multilayer dataset by best matching to the given model. However, in this example, evaporation field differences are small and the system is largely cylindrically symmetric. The next experimental system to be considered, the fin field-effect transistor (FinFET), will explore the protocol's performance under large evaporation field differences and structural asymmetry.

6.4 The FinFET Reconstruction

The FinFET is a modern transistor device that has largely replaced the traditional MOSFET design over the last decade (see Figure 1). Through a more spatially complex and efficient 3D structure, FinFETs take up a smaller volume and allow for faster switching times. However, its complex structure and size encroaches on the atomic scale, meaning that traditional analysis techniques such as TEM and SIMS are becoming increasingly limited for imaging such devices. The near atomic-scale spatial resolution of APT makes it a prime candidate for analysing the spatial composition of next-generation nanodevices [170, 11]. Therefore, correcting spatial distortions in such structures is a critical step towards wide-scale industrial application of APT.

Unlike the multilayer dataset, only standard SEM and TEM was available for the analysed FinFET[4]. Therefore, the specimen model had to be set up from the available micrographs (Figures 98a-b), whilst combining prior knowledge of the specimen geometry [51]. The Bas reconstruction is given in Figures 98c-d (with an initial radius $R_0 = 20$ nm, constant shank angle $\alpha = 15^o$, and $\xi = 1.6$), and reveals a narrowing artefact and increased density of the central fin region. This distortion is well understood from atomic-scale modelling, arising due to differing material evaporation fields [51]. Therefore, the question arises of whether a well-calibrated continuum model can directly correct for such distortions.

By qualitatively comparing the phase maps between the APT experimental data and the model through Figures 98e-f, the off-axis rotation of the central fin could be estimated as 3.5^o. This angle was used to set up the initial specimen model (shown in Figures 98h). Like with the multilayer structure in Section 6.3, a more accurate specimen model could be directly initialised from ET. A $84 \times 84 \times 134$ simulation grid was used, with cell widths of 3 nm.

[4]APT performed by Davit Melkonyan, and electron microscopy performed by Olivier Richard, both based at IMEC, Leuven.

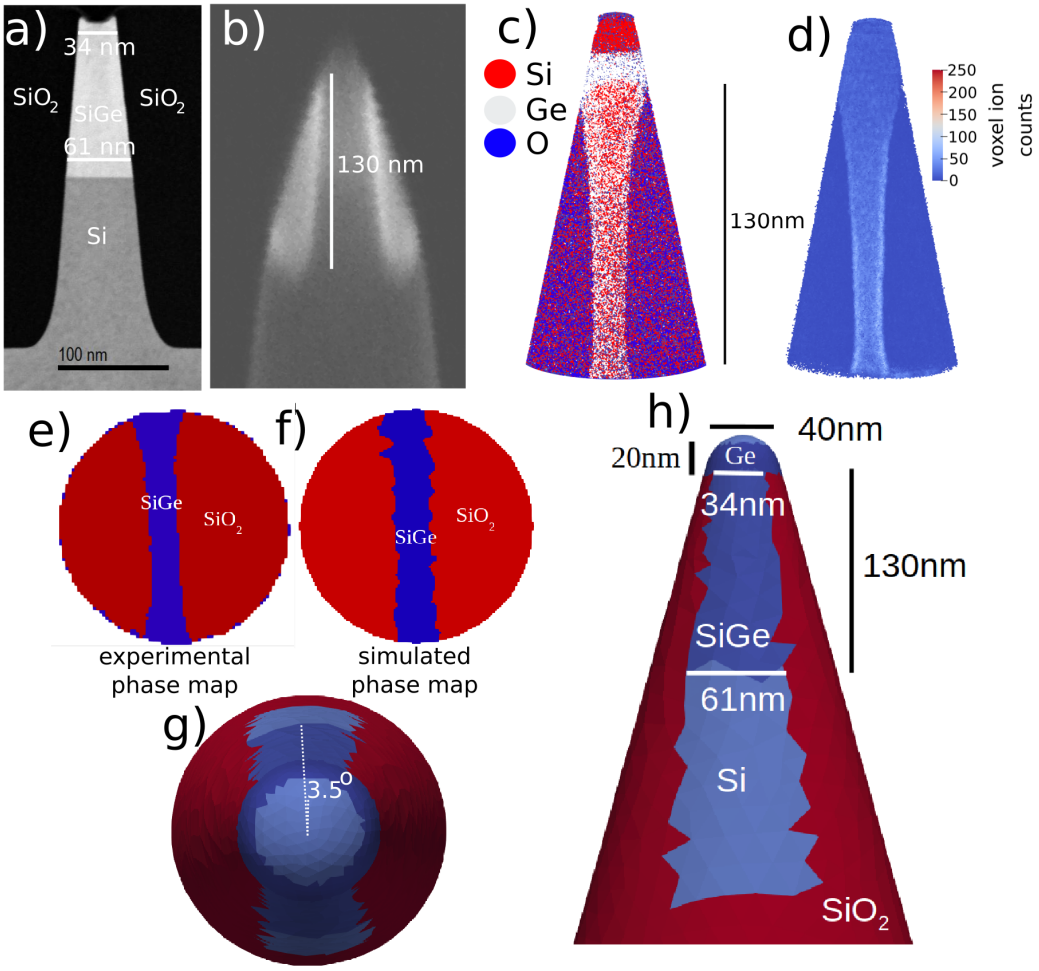


Figure 98: (a) DF-STEM imaging of specimen. (b) Denoised SEM image post-milling. (c) Bas reconstruction of APT data showing species. (d) Local density within Bas reconstruction. (e) Experimental phase map at maximum channel demagnification (determined from detector composition histogram via k-means clustering). (f) Corresponding model phase map. (g) Top-down view of specimen model showing central fin tilting. (h) Lateral view of FinFET specimen model. Figure has been adapted from [136].

Like with the multilayer example, suitable landmarks must be provided to depth calibrate the model and experiment detector spaces. The landmark positions are shown in Figure 99a, with their corresponding model surface states in Figure 99b-d.

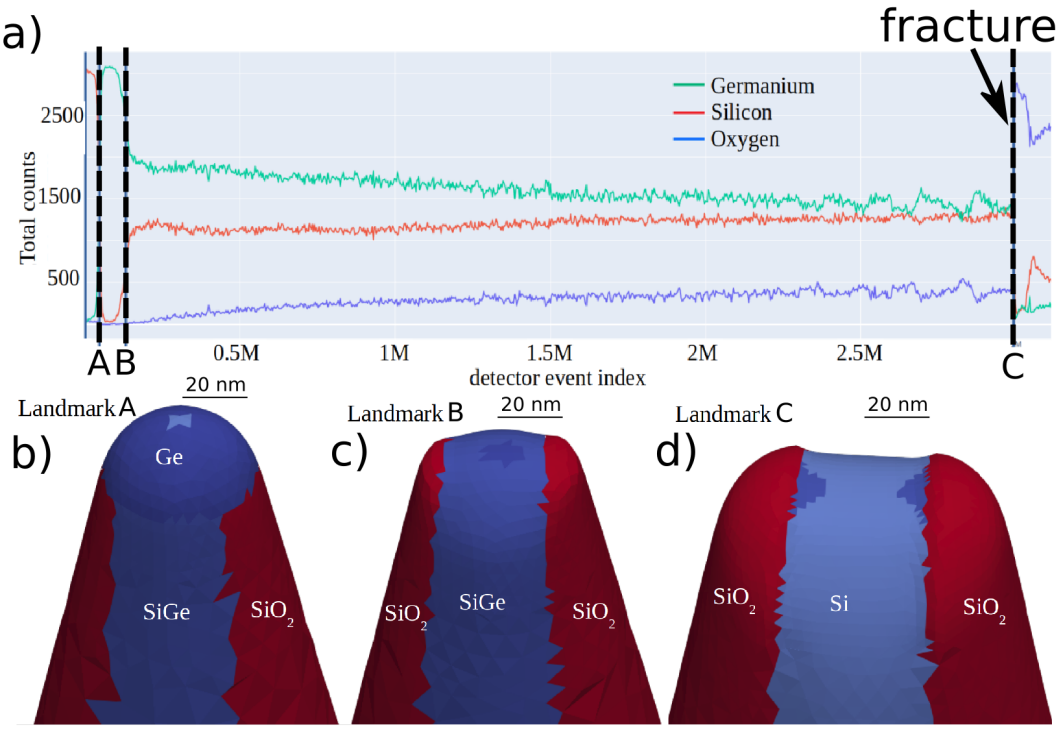


Figure 99: (a) Histograms (200 bins) for major ionic species showing landmark positions in the experimental evaporation sequence. (b-d) Model surface states at marked landmarks B-D. Figure adapted from [136].

The regular grid search for the F_{SiGe} and $F_{\mathrm{SiO_2}}$ evaporation field parameters is visualised in both detector space (Figure 100a) and sample space (Figure 100b). In both spaces, a line of maximum similarity can be observed, corresponding to an evaporation field ratio of F_{SiGe}:$F_{\mathrm{SiO_2}}$ = 1:1.6. This ratio agrees well with the parameter range predicted by Melkonyan et al. [51]. While maxima can be identified in the sample space similarity measurements, these potentially arise due to numerical instabilities within this space, caused by the extreme demagnification of the central fin (a hypothesis supported by considering the detector space similarity in Figure 100a). However, to ensure maximisation of the produced microstructure similarity, the optimum model parameters in sample space have been selected (blue star in Figure 100), such that $F_{\mathrm{SiGe}} = 35.0$ Vnm^{-1} and $F_{\mathrm{SiO_2}} = 59.0$ Vnm^{-1}.

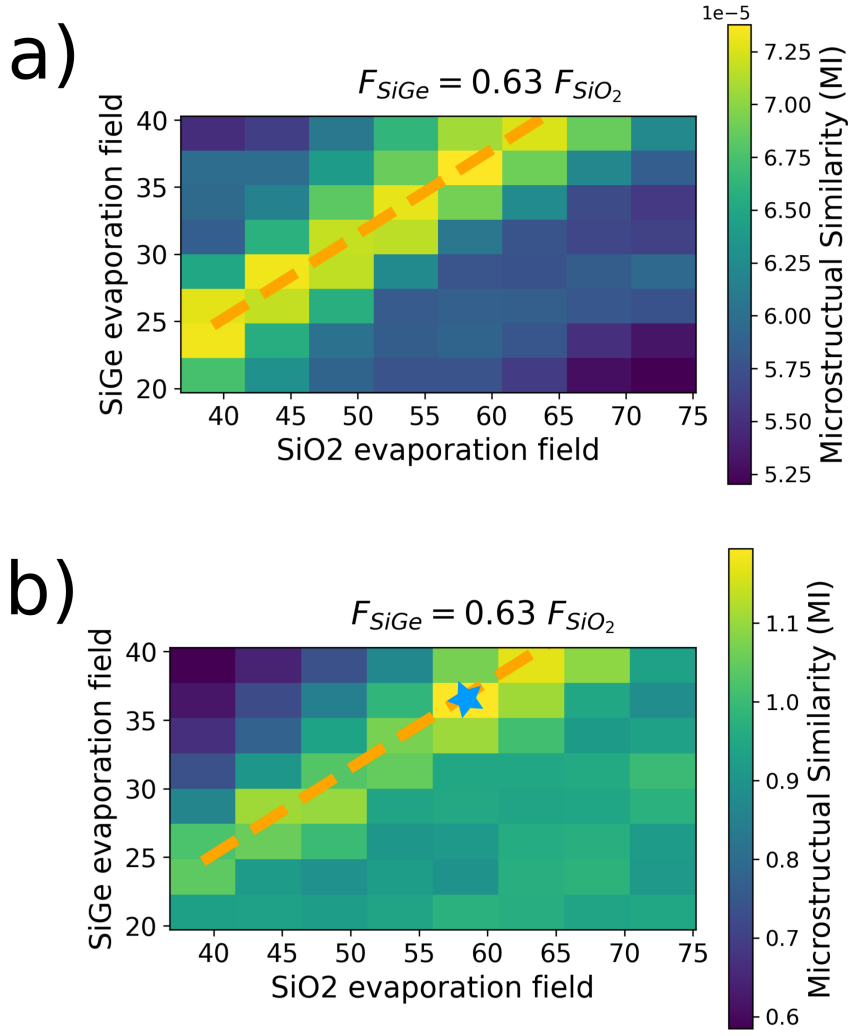


Figure 100: Visualisation of 8×8 regular grid search over $F_{\mathrm{SiO_2}}$ and F_{SiGe} measuring microstructure similarity via mutual information (MI) in both (a) detector space and (b) sample space. The optimum model parameters are highlighted by the blue marker.

Due to the experiment's cylindrical asymmetry and mapping instability, a relatively high resolution for the alignment grid search is required. Therefore, an adaptive grid search has been performed across three search grids of ever finer resolution, with the next grid centred on the previous grid's identified maximum. This adaptive grid alignment is performed for each physics model in the explored ensemble. The Figures 101a-c show the partial optimisation of the spatial alignment and image compression parameters from both the initial (coarse) and final (fine) grid, using the model with optimum evaporation field parameters. While

this adaptive search ensures faster convergence, care must be taken through maintaining a sufficient grid resolution at each stage to ensure that the true global maximum is identified.

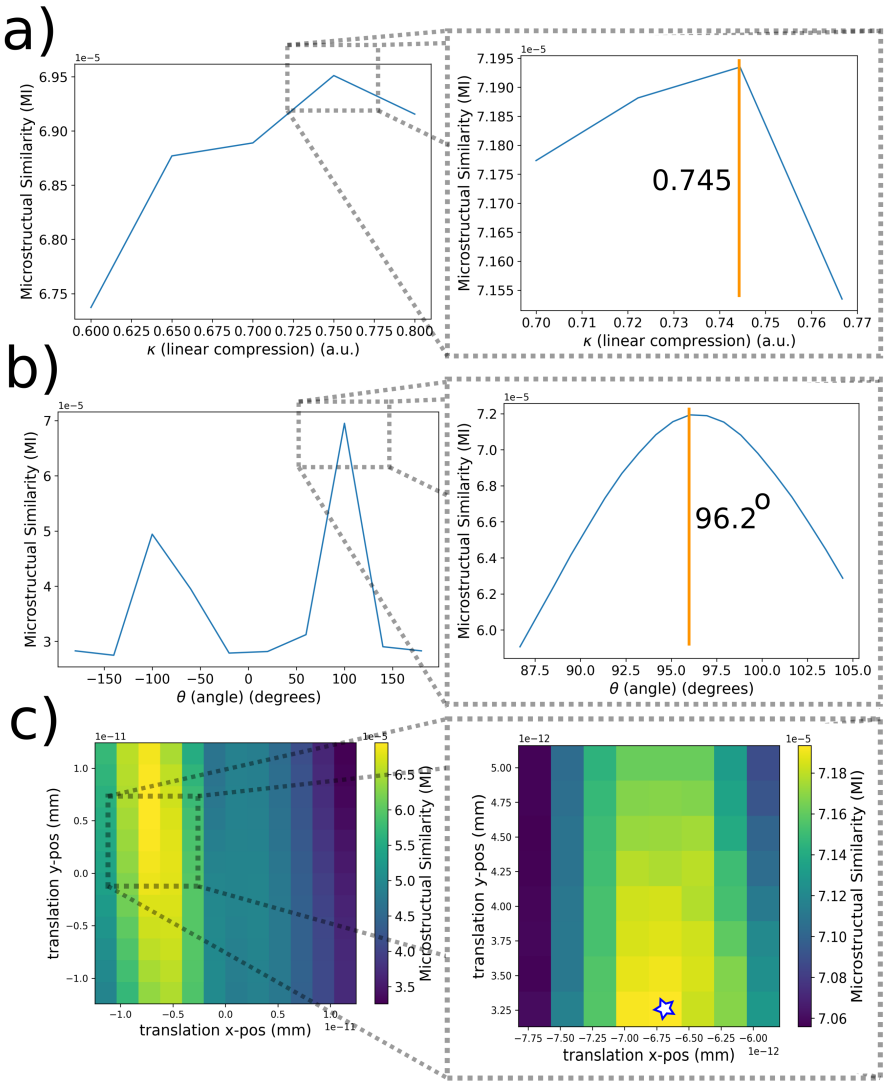


Figure 101: (a) Partial MI maximisation of the image compression (κ). (b) Partial MI maximisation of rotation around the analysis axis (θ). (c) Partial MI maximisation of the translation vector ($\vec{\mathbf{r}}$).

The parameter optimised model-driven reconstruction chemistry and local density for the FinFET structure is shown in Figures 102. This new reconstruction exhibits a significantly improved correlation against the initial SEM and model microstructure compared with the point-projection reconstruction (Figure 98). However, residual distortions still remain as density spikes at vertical

interfaces. While these interface artefacts could partially be due to physical model error at the interfaces, e.g. from unaccounted trajectory crossover and atomic-scale evaporation effects, neither of these can really explain the interface curvature artefacts, and the severity and locality of the observed density distortions. Instead, the major cause of these higher interface densities is very likely due to miscalibration of the model estimated trajectory mapping at vertical interfaces.

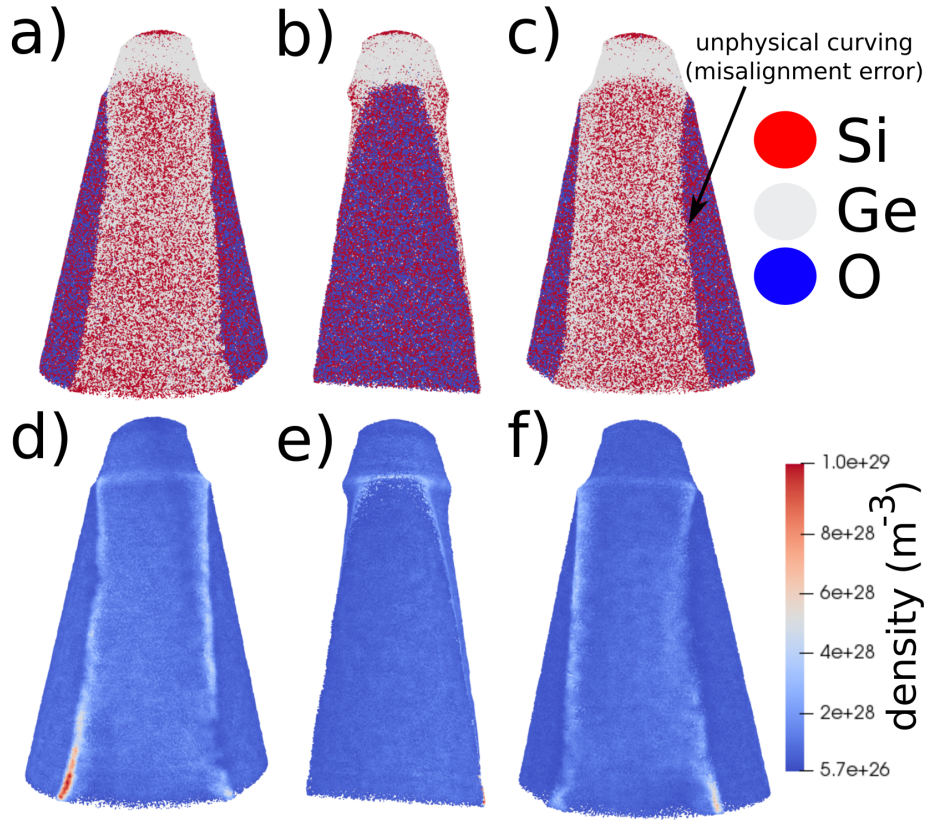


Figure 102: (a-c) Different rotations of the FinFET reconstruction showing local chemistry. Residual calibration errors can be observed by a curving of the central fin interfaces. (d-f) Matching rotations showing local density (calculated via KDE). Residual density distortions can be observed close to vertical interfaces.

A visualisation of local magnification over the specimen surface nearing the end of the simulated evaporation is shown in Figure 103b. The high demagnification of the central fin region makes model alignment in detector space highly unstable, as even small offsets of final ion detector positions can correspond to large offsets of their estimated initial launch positions. As a result, even small

model misalignments within demagnified detector space regions can produce significant distortions in the final reconstruction. Additionally, there is also almost certainly error in the initially assumed model geometry used in its reconstruction because of the underconstrained prior information (Figures 98a-b). Therefore, the implication is that obtaining an accurate model calibration through constrained parameter variation alone is incredibly challenging in the presence of significant demagnification.

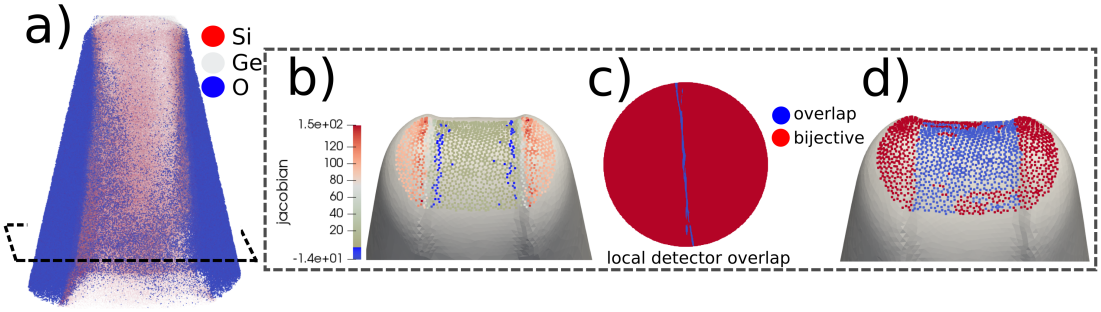


Figure 103: (a) Experimental reconstruction filtered for Oxygen (blue). It can be seen that the Oxygen concentration within the central fin increases nearing its base. (b) Local magnification near the end of the simulated FinFET evaporation. Blue points show the region of negative magnification (local inversion). (c) Region of ion overlap on the detector (blue) due to trajectory crossover. (d) Back-projection of this overlap region back onto specimen surface under the inverse mapping, predicting ion mixing within the central fin, and explaining the experimental presence of Oxygen there.

However, previously in Section 3.11.10, it was shown how diffeomorphic metric mappings can determine an optimum transformation to align two density distributions. This raises the question of whether these transformations can be applied to align the model-driven reconstruction detector space densities. The Figure 104 shows the effect of the diffeomorphic mapping being applied to a model and experiment detector density map at some time. It can be seen that the transformed model detector density under this mapping (Figure 104d) is a significantly better match to the experiment hitmap (Figure 104b) than the original model (Figure 104a). By applying these transformations throughout the entire depth-calibrated detector space in 2D slices, the model's outputted de-

tector positions for the forward trajectory mapping can be transformed under the determined diffeomorphisms. This transformation can be considered to be aligning the experimental data back onto the model.

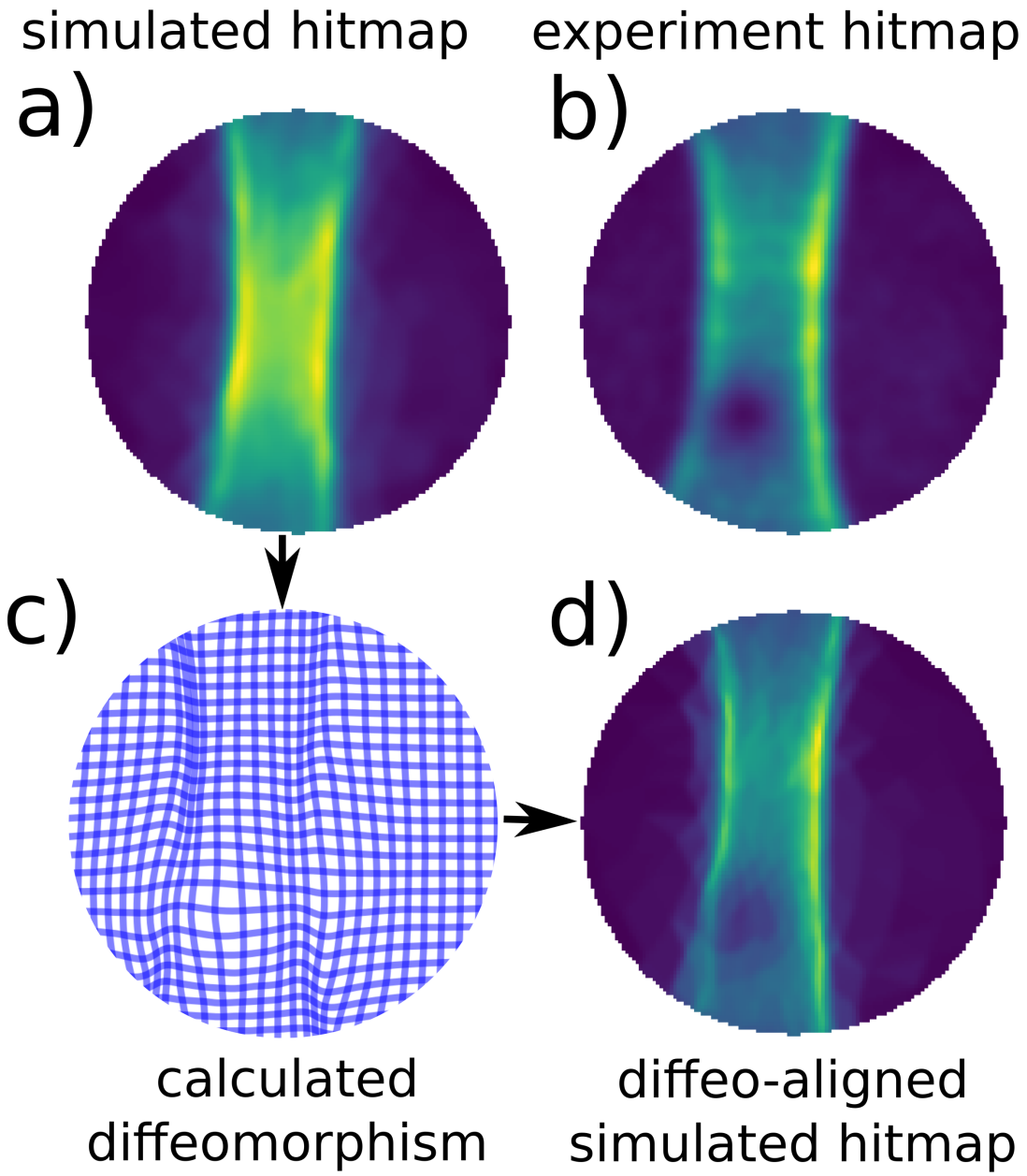


Figure 104: (a) The model density detector map at an instance in time. (b) The experiment density detector map at the same instance (via depth calibration). (c) The determined alignment transformation. (d) The transformed model density detector map. The low density pole has been partially accounted for. Alignment performed using the open-source code *ddmatch* [187].

The final reconstruction, following application of the diffeomorphic density matching, is shown in Figure 105. It can be seen that the residual interface curvature distortions present in Figure 102 have been significantly reduced, and that there is now a good correlation between the microstructure in both the final reconstruction and model. Interface density distortions have also been reduced. This reduction can be quantified by 1D histograms of the local ion voxel densities for the different reconstructions (Figure 105c). Here, local reconstruction voxel densities have been determined by a 3D histogram on a $100 \times 100 \times 100$ spatial voxel grid spanning each reconstruction, with edge voxels filtered out. The histogram associated with the projection-based reconstruction (green) is bimodal, and possesses a tail that stretches out to much higher densities. These two distribution modes can be understood to loosely correspond to the two phases present (lower density mode from the SiO_2 phase; higher density mode from the central SiGe phase). In comparison, the diffeomorphism-aligned model reconstruction distribution (orange) is only uni-modal, and features a smaller density spread and significantly attenuated distribution tail (associated with the anomalous vertical interface densities). These distributions strongly imply that both the multiphase and interface density artefacts present in the projection-based reconstruction have largely been corrected for through the diffeomorphism-aligned model-driven reconstruction approach. While vertical interface density distortions still remain, their presence is not surprising given the extreme focusing of the central fin region (Figure 103c), and the occurrence of trajectory crossover. Employing an adaptive detector space discretisation when performing model alignment, where resolution is locally increased within high demagnification regions, could help reduce numerical alignment errors introduced from Cartesian grid discretisation.

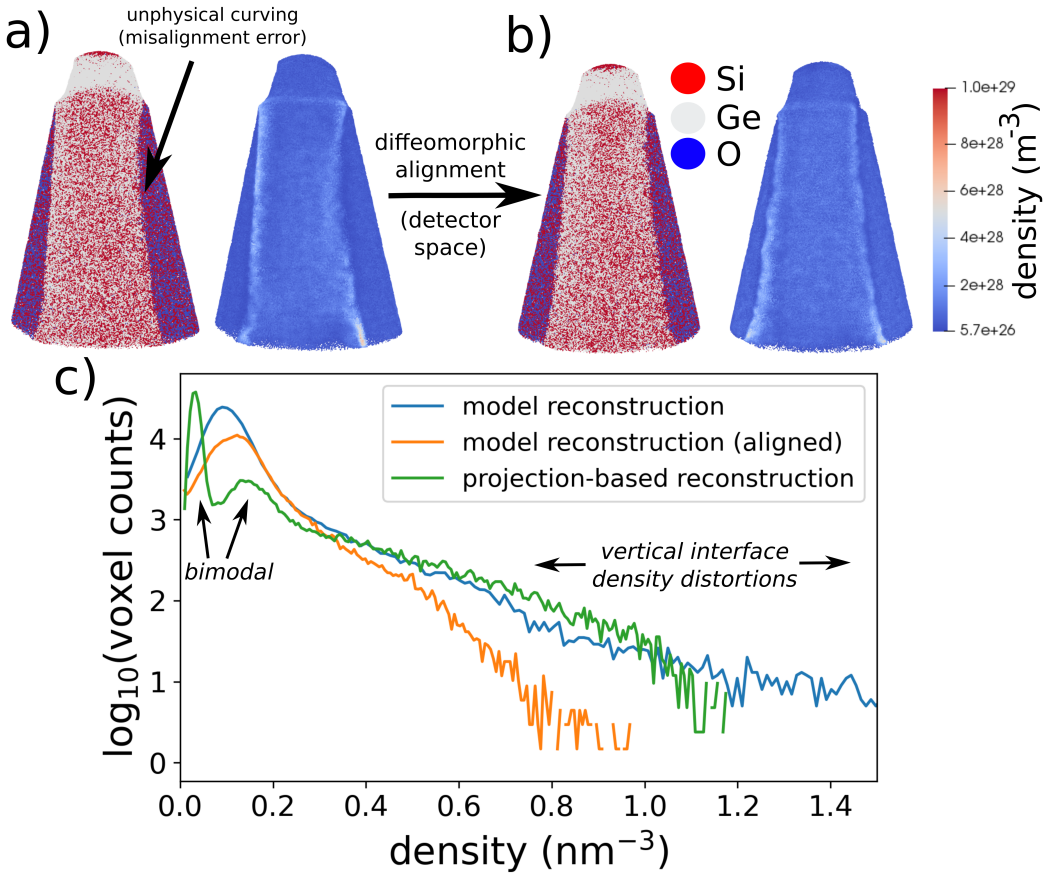


Figure 105: (a) Front-facing orientation of parameter-constrained reconstruction showing local composition and density. (b) Same orientation of reconstruction following interface alignment via the diffeomorphic density matching transformation. (c) Histogram for local voxel densities (200 bins) for the different reconstructions. It can be seen that the diffeomorphism-aligned model-driven reconstruction boasts a reduced density spread, particularly at the higher densities associated with vertical interfaces.

The FinFET system is a rather extreme example in terms of material evaporation field differences. The lower field of the central fin results in trajectory focusing and extreme demagnification, challenging the model alignment to its limits. However, even in this extreme case, the model-driven reconstruction protocol has successfully managed to reduce microstructural distortions compared to a traditional projection-based reconstruction.

6.5 Discussion and Conclusions

In this chapter, model-driven reconstruction via the protocol outlined in Figure 90 has been explored. This included a round trip test, where the same model was used for both synthetic data generation and reconstruction, confirming that numerical errors are relatively small. Next, the model-driven reconstruction of two experimental semiconductor datasets was considered: a multilayer and a FinFET-like system. By comparing to electron microscopy, as well as considering the variation in local reconstruction density, a quantifiable reduction in artefacts and density distortions has been observed. Finally, the application of diffeomorphic density matching transformations was considered in order to perform fine-scale alignment at vertical interfaces in the FinFET dataset.

Currently, only the composition is being used during model parameter optimisation. However, in theory the model phase and experimental density should also correlate under MI, and so could contribute to the problem's similarity measure. Information from the experiment voltage curve could aid in constraining effective evaporation fields.

A number of outlying issues and uncertainties remain with this reconstruction process. It was seen in Section 5.5 that the continuum approximation alone cannot account for pole structure artefacts. Additionally, the correct physics for modelling the laser interaction and dielectric behaviour at such length scales and field strengths is unknown. In order to partially account for these effects, future models could potentially be driven directly from the APT data (see Section 5.8). This could also reduce the need for expensive parameter tuning, and potentially enable the reconstruction of more challenging microstructures. However, given the problem's complicated surface physics, its large number of degrees of freedom, and extreme multiscale nature, data integration against correlative experimental techniques will almost certainly be a necessity in order to fully constrain the model, and validate reconstruction integrity.

7 General Conclusions and Future Work

In this work, a continuum model for predicting the changing geometry of field emitters in APT experiments has been developed. The specimen surface has been tracked as a contour within a scalar field via a level set method, which is evolved according to the local specimen surface evaporation rate. The electric field over the specimen surface and along ion trajectories has been calculated by solving a boundary integral equation, efficiently handling the large computational domain. This framework also allows for evaporation multiphysics to be incorporated, including a FEM-BEM coupling for dielectricity, crystallographic anisotropy, internal cavities, and laser heating dynamics.

Comparing to experimental results, the model's predictions have been shown to typically be in good agreement. Crucially, unlike previous modelling approaches, the developed framework provides a significant increase in computational efficiency, albeit at a loss of accuracy, allowing for simulation of specimens that directly resemble those in real experiments.

By considering properties of the ion trajectory mapping between the specimen surface and detector, it was shown that the mapping can be accurately estimated by sampling ion trajectories. It was also shown that the presence of ion trajectory crossover leads to multivalued regions in the inverse mapping. A local surface magnification was also defined in terms of the Jacobian determinant, allowing for efficient prediction of detector density hitmaps. This mapping estimation via trajectory sampling avoids the currently computationally intractable problem of calculating individual trajectories for every detection event.

Finally, the reconstruction of simulated and experimental datasets was demonstrated using the predictions from calibrated emitter models. The experimental datasets included a semiconductor multilayer and FinFET device. For both systems, the model-driven reconstruction exhibited a quantifiable reduction in microstructural distortions through improved correlation with correlative elec-

tron microscopy. Concepts have been borrowed from Computational Anatomy, particularly the idea of aligning imaging data to a 'best-known' specimen model. This approach provides additional image stability under the guaranteed presence of physical model errors. The proposed protocol should be applicable to many experimental semiconductor systems.

While the protocol successfully corrects APT distortions, a number of further developments are required to move towards true atomic-scale tomography [166]. In my opinion, the six major future work directions are given below. It should be noted that these are interdependent.

- *Data-driven model evaporation:* Constraining the level set velocity extension field from the APT detector space density. Such an approach could be used to account for difficult-to-model evaporation drivers, e.g. the laser. However, this constraint can only be applied to the surface patch within the FOV. Further improvements to the instrument FOV, as well as to correlative techniques [105, 101], could help resolve this missing information problem.

- *Multiscale evaporation models:* It has readily been discussed how the continuum model cannot account for crystallographic trajectory deflections and ion mixing due to a disrupted surface evaporation sequence [46, 61, 49, 68]. In order to incorporate and attempt to reverse these effects, an extensive multiscale modelling approach is required that can account for the physics over the relevant length scales. This could use both concurrent modelling - the domain decomposition and direct coupling of different resolution models [217, 72] (e.g. atomic models at interfaces), and sequential modelling - where estimated parameters using one model form the input to another [70, 218]. Additional improvements to the individual modelling approaches are likely still required before any multiscale approach could be applied quantitatively.

- *Positioning error estimation:* Due to atomic-scale evaporation being fundamentally driven by random processes, atomic-scale resolution using current detector technology is almost certainly impossible [101]. However, compositional accuracy could be improved through integrating local models for predicting ion positioning uncertainties [219] into the reconstruction procedure. This could lead to probability density representations of reconstructions, rather than as point clouds.

- *Hybrid physics-machine learning:* The accuracy of specimen evaporation models are limited by the included physics. Integrating physical and machine learning models could correct for missing or inaccurate multiscale physics, whilst potentially providing increased computational efficiency through problem dimensionality reduction [211]. Such an approach could also allow for efficient integration of continuum and machine learning models, and potentially avoid the requirement for prior specimen geometry knowledge

- *Fast Poisson Solvers:* Currently, the problem's electrostatic domain does not accurately reflect that in experiment. The biased instrument chamber has been omitted, as well as any detector voltage bias, and specimen shank and holder. This is problematic for accurately predicting realistic compression of ion trajectories. The fundamental challenge here is building a highly efficient Poisson solver that can handle the domain's 10^9 variations in length scale, whilst also being solved throughout the moving boundary problem. The validity of assuming that chamber electrostatics remain unchanged throughout multiphase evaporation is unclear [176]. Possible acceleration methods include BEM compression techniques [131], Krylov subspace recycling [215], as well as novel meshfree solvers [220].

- *Application to FIM:* Field ion microscopy (FIM) is a precursor technique to APT where atomic surface positions are observed indirectly via an imaging

gas. Recently FIM has received a renewed interest due to its theoretical atomic-scale resolution and $\sim 100\%$ effective detection efficiency [221, 222, 223]. However, multiphase distortions of ionised imaging gas trajectories will still occur, and could be corrected for via a model-driven approach.

For almost 30 years, APT reconstruction has remained largely unchanged. The model-driven reconstruction approach outlined in this thesis provides a novel and physical approach to APT image generation. It has been shown that this method is capable of correcting for large-scale trajectory distortions introduced from the approximations of projection-based approaches [17]. This method could account for trajectory crossover, improving interface compositional accuracy. Such model-driven correction of multiphase distortions may prove a critical step towards true atomic-scale atom probe tomography.

References

[1] G. E. Moore. Cramming More Components onto Integrated Circuits. *Electronics*, 38(8):114–117, 1965.

[2] WSTS. Semiconductor Industry Green Book. Technical report, 2015.

[3] W. P. Maszara and M. R. Lin. FinFETs - Technology and circuit design challenges. *European Solid-State Device Research Conference*, pages 3–8, 2013.

[4] B. Nikolic. The Manufacturing Process. In *EE141: Digital Integrated Circuits*, pages 33–62. Berkeley, 2000.

[5] Sony. Semiconductor Device Failure Analysis. In *Semiconductor Quality and Reliability Handbook*, chapter 3. Sony, 2016.

[6] E. I. Muehldorf and A. D. Savkar. LSI Logic Testing - An Overview. *IEEE Transactions on Computers*, C-30(1):1–17, 1981.

[7] Panasonic. Failure Mechanism of Semiconductor Devices. Technical Report T04007BE-3, 2009.

[8] R. Fernández, R. Rodríguez, M. Nafría, X. Aymerich, B. Kaczer, and G. Groeseneken. FinFET and MOSFET preliminary comparison of gate oxide reliability. *Microelectronics Reliability*, 46(9-11):1608–1611, 2006.

[9] M. H. Chiang, J. N. Lin, K. Kim, and C. T. Chuang. Random dopant fluctuation in limited-width FinFET technologies. *IEEE Transactions on Electron Devices*, 54(8):2055–2060, 2007.

[10] K. Takeuchi, A. Nishida, and T. Hiramoto. Random fluctuations in scaled MOS devices. *International Conference on Simulation of Semiconductor Processes and Devices*, pages 79–85, 2009.

[11] International Roadmap Committee. Metrology. In *International for Devices and Systems*. IEEE, 2018.

[12] R. G. Forbes. Field evaporation theory: a review of basic ideas. *Applied Surface Science*, 87-88(94):1–11, 1995.

[13] G. L. Kellogg. Measurement of activation energies for field evaporation of tungsten ions as a function of electric field. *Physical Review B - Condensed Matter and Materials Physics*, 29(8), 1984.

[14] G. L. Kellogg and T. T. Tsong. Pulsed-laser atom-probe field-ion microscopy. *Journal of Applied Physics*, 51(2):1184–1193, 1980.

[15] F. Vurpillot, B. Gault, A. Vella, M. Bouet, and B. Deconihout. Estimation of the cooling times for a metallic tip under laser illumination. *Applied Physics Letters*, 88(9), 2006.

[16] A. Cerezo, T. J. Godfrey, and G. D. W. Smith. Application of a position-sensitive detector to atom probe microanalysis. *Review of Scientific Instruments*, 59(6):862–866, 1988.

[17] P. Bas, A. Bostel, B. Deconihout, and D. Blavette. A general protocol for the reconstruction of 3D atom probe data. *Applied Surface Science*, 87/88:298–304, 1995.

[18] D. Blavette, A. Bostel, J. M. Sarrau, B. Deconihout, and A. Menand. An atom probe for three-dimensional tomography. *Nature*, 363(6428):432–435, 1993.

[19] T. F. Kelly and M. K. Miller. Invited review article: Atom probe tomography. *Review of Scientific Instruments*, 78(3), 2007.

[20] O. Nishikawa and M. Klmoto. Toward a scanning atom probe - computer simulation of electric field. *Applied Surface Science*, 7677:424–430, 1994.

[21] T. F. Kelly, P. P. Camus, D. J. Larson, L. M. Holzman, and S. S. Bajikar. On the many advantages of local-electrode atom probes. *Ultramicroscopy*, 62(1-2):29–42, 1996.

[22] B. A. Mamyrin, V. I. Karataev, D. V. Shmikk, and V. A. Zagulin. The mass-reflectron, a new nonmagnetic time-of-flight mass spectrometer with high resolution. *Journal of Experimental and Theoretical Physics*, 37(1):45–48, 1973.

[23] B. Gault, M. P. Moody, J. M. Cairney, and S. P. Ringer. *Atom Probe Microscopy*. Springer, New York, 1st edition, 2012.

[24] G. Sha, A. Cerezo, and G. D.W. Smith. Field evaporation behavior during irradiation with picosecond laser pulses. *Applied Physics Letters*, 92(4):2006–2009, 2008.

[25] A. Cerezo, T. J. Godfrey, C. R. M. Grovenor, M. G. Hetherington, R. M. Hoyle, J. P. Jakubovics, J. A. Liddle, G. D. W. Smith, and G. M. Worrall. Surface analysis with a position-sensitive atom probe. *Journal of Microscopy*, 154(3):215–225, 1989.

[26] H. N. Southworth and J. M. Walls. The projection geometry of the field-ion image. *Surface Science*, 75(1):129–140, 1978.

[27] J. M. Walls and H. N. Southworth. Magnification in the field-ion microscope. *Journal of Physics D: Applied Physics*, 12(5):657–667, 1979.

[28] D. Blavette, J. M. Sarrau, A. Bostel, and J. Gallot. Direction et distance d'analyse à la sonde atomique. *Revue de Physique Appliquee*, 17(7):435–440, 1982.

[29] B. P. Geiser, D. J. Larson, E. Oltman, S. S. A. Gerstl, D. A. Reinhard, T. F. Kelly, and T. J. Prosa. Wide-Field-of-View Atom Probe Reconstruction. *Microscopy and Microanalysis*, 15(Suppl 2):292–293, 2009.

[30] B. Gault, D. Haley, F. De Geuser, M. P. Moody, E. A. Marquis, D. J. Larson, and B. P. Geiser. Advances in the reconstruction of atom probe tomography data. *Ultramicroscopy*, 111(6):448–457, 2011.

[31] F. De Geuser and B. Gault. Reflections on the Projection of Ions in Atom Probe Tomography. *Microscopy and Microanalysis*, 23(2):238–246, 2017.

[32] D. J. Larson, T. J. Prosa, R. M. Ulfig, B. P. Geiser, and T. F. Kelly. *Local Electrode Atom Probe Tomography: A User's Guide*. Springer, New York, 2013.

[33] A. Cerezo, P. J. Warren, and G. D. W. Smith. Some aspects of image projection in the field-ion microscope. *Ultramicroscopy*, 79(1-4):251–257, 1999.

[34] B. Gault, F. De Geuser, L. T. Stephenson, M. P. Moody, B. C. Muddle, and S. P. Ringer. Estimation of the reconstruction parameters for atom probe tomography. *Microscopy and Microanalysis*, 14(4):296–305, 2008.

[35] P. J. Warren, A. Cerezo, and G. D. W. Smith. Observation of atomic planes in 3DAP analysis. *Ultramicroscopy*, 73(1-4):261–266, 1998.

[36] N. D. Wallace, A. V. Ceguerra, A. J. Breen, and S. P. Ringer. On the Retrieval of Crystallographic Information from Atom Probe Microscopy Data via Signal Mapping from the Detector Coordinate Space. *Ultramicroscopy*, 189:65–75, 2018.

[37] P. J. Warren, A. Cerezo, and G. D. W. Smith. Towards 3D lattice reconstruction with the Position Sensitive Atom Probe. *Microscopy and Microanalysis*, 4(S2):86–87, 1998.

[38] B. Gault, F. De Geuser, L. T. Stephenson, M. P. Moody, B. C. Muddle, and S. P. Ringer. Estimation of the Reconstruction Parameters for Atom Probe Tomography. *Microscopy and Microanalysis*, 14(4):296–305, 2008.

[39] B. P. Geiser, T. F. Kelly, D. J. Larson, J. Schneir, and J. P. Roberts. Spatial Distribution Maps for Atom Probe Tomography. *Microscopy and Microanalysis*, 13:437–447, 2007.

[40] D. Haley, P. A. J. Bagot, and M. P. Moody. DF-Fit: A Robust Algorithm for Detection of Crystallographic Information in Atom Probe Tomography Data. *Microscopy and Microanalysis*, 25(2):331–337, 2019.

[41] L. Yao, M. P. Moody, J. M. Cairney, D. Haley, A. V. Ceguerra, C. Zhu, and S. P. Ringer. Crystallographic structural analysis in atom probe microscopy via 3D Hough transformation. *Ultramicroscopy*, 111(6):458–463, 2011.

[42] D. J. Larson, B. P. Geiser, T. J. Prosa, R. M. Ulfig, and T. F. Kelly. Non-Tangential Continuity Reconstruction in Atom Probe Tomography Data. *Microscopy and Microanalysis*, 17(S2):740–741, 2011.

[43] D. J. Larson, B. P. Geiser, T. J. Prosa, S. S. A. Gerstl, D. A. Reinhard, and T. F. Kelly. Improvements in planar feature reconstructions in atom probe tomography. *Journal of Microscopy*, 243(1):15–30, 2011.

[44] B. Gault, S. T. Loi, V. J. Araullo-Peters, L. T. Stephenson, M. P. Moody, S. L. Shrestha, R. K. W. Marceau, L. Yao, J. M. Cairney, and S. P. Ringer. Dynamic reconstruction for atom probe tomography. *Ultramicroscopy*, 111(11):1619–1624, 2011.

[45] F. Vurpillot, M. Gruber, G. Da Costa, I. Martin, L. Renaud, and A. Bostel. Pragmatic reconstruction methods in atom probe tomography. *Ultramicroscopy*, 111(8):1286–1294, 2011.

[46] F. Vurpillot, D. J. Larson, and A. Cerezo. Improvement of multilayer analyses with a three-dimensional atom probe. *Surface and Interface Analysis*, 36:552–558, 2004.

[47] F. De Geuser, W. Lefebvre, F. Danoix, F. Vurpillot, B. Forbord, and D. Blavette. An improved reconstruction procedure for the correction of local magnification effects in three-dimensional atom-probe. *Surface and Interface Analysis*, 39:268–272, 2007.

[48] J. P. Barnes, A. Grenier, I. Mouton, S. Barraud, G. Audoit, J. Bogdanowicz, C. Fleischmann, D. Melkonyan, W. Vandervorst, S. Duguay, N. Rolland, F. Vurpillot, and D. Blavette. Atom probe tomography for advanced nanoelectronic devices: Current status and perspectives. *Scripta Materialia*, 148:91–97, 2017.

[49] E. A. Marquis, B. P. Geiser, T. J. Prosa, and D. J. Larson. Evolution of tip shape during field evaporation of complex multilayer structures. *Journal of Microscopy*, 241:225–233, 2011.

[50] S. Du, T. Burgess, S. Tjing Loi, B. Gault, Q. Gao, P. Bao, L. Li, X. Cui, W. Kong Yeoh, H. Hoe Tan, C. Jagadish, S. P. Ringer, and R. Zheng. Full tip imaging in atom probe tomography. *Ultramicroscopy*, 124:96–101, 2013.

[51] D. Melkonyan, C. Fleischmann, L. Arnoldi, J. Demeulemeester, A. Kumar, J. Bogdanowicz, F. Vurpillot, and W. Vandervorst. Atom probe tomography analysis of SiGe fins embedded in SiO2: Facts and artefacts. *Ultramicroscopy*, 179:100–107, 2017.

[52] D. J. Rose. On the magnification and resolution of the field emission electron microscope. *Journal of Applied Physics*, 27(3):215–220, 1956.

[53] H. D. Beckey, H. Krone, and F. W. Roellgen. Comparison of tips, thin wires and sharp metal edges as emitters for field ionization mass spectrometry. *Journal of Physics E: Scientific Instruments*, 1(2):118–120, 1968.

[54] P. J. Birdseye and D. A. Smith. The electric field and the stress on a field-ion specimen. *Surface Science*, 23(1):198–210, 1970.

[55] R. Smith and J. M. Walls. Ion trajectories in the field-ion microscope. *Journal of Physics D: Applied Physics*, 11:409–419, 1978.

[56] P. J. Birdseye, D. A. Smith, and G. D. W. Smith. Analogue investigations of electric field distribution and ion trajectories in the field ion microscope. *Journal of Physics D: Applied Physics*, 7(12):1642–1651, 1974.

[57] O. Dimond. *Modelling the Reconstruction of 3D Atom Probe Data*. PhD thesis, University of Oxford, 1999.

[58] F. Vurpillot, A. Bostel, and D. Blavette. The shape of field emitters and the ion trajectories in three-dimensional atom probes. *Journal of Microscopy*, 196(December):332–336, 1999.

[59] F. Vurpillot, A. Bostel, E. Cadel, and D. Blavette. The spatial resolution of 3D atom probe in the investigation of single-phase materials. *Ultramicroscopy*, 84:213–224, 2000.

[60] F. Vurpillot, A. Bostel, and D. Blavette. Trajectory overlaps and local magnification in three-dimensional atom probe. *Applied Physics Letters*, 76(21):3127–3129, 2000.

[61] F. Vurpillot, A. Cerezo, D. Blavette, and D. J. Larson. Modeling Image Distortions in 3DAP. *Microscopy and Microanalysis*, 10(3):384–390, 2004.

[62] B. P. Geiser, D. J. Larson, S. S. A. Gerstl, D. A. Reinhard, T. F. Kelly, T. J. Prosa, and J. D. Olson. A System for Simulation of Tip Evolution Under Field Evaporation. *Microscopy and Microanalysis*, 15(S2):302–303, 2009.

[63] C. Oberdorfer and G. Schmitz. On the field evaporation behavior of dielectric materials in three-dimensional atom probe: A numeric simulation. *Microscopy and Microanalysis*, 17(1):15–25, 2011.

[64] N. Rolland, F. Vurpillot, S. Duguay, and D. Blavette. A Meshless Algorithm to Model Field Evaporation in Atom Probe Tomography. *Microscopy and Microanalysis*, 21(6):1649–1656, 2015.

[65] J. P. Barnes and P. Hut. A hierarchical O(N log N) force-calculation algorithm. *Nature*, 324(6096):446–449, 1986.

[66] C. Oberdorfer, S. M. Eich, and G. Schmitz. A full-scale simulation approach for atom probe tomography. *Ultramicroscopy*, 128:55–67, 2013.

[67] C. Oberdorfer. TAPSim, 2014.

[68] C. Oberdorfer. *Numeric Simulation of Atom Probe Tomography*. PhD thesis, University of Münster, 2014.

[69] N. Sukumar. Voronoi cell finite difference method for the diffusion operator on arbitrary unstructured grids. *International Journal for Numerical Methods in Engineering*, 57(1):1–34, 2003.

[70] L. Yao, T. Withrow, O. D. Restrepo, W. Windl, and E. A. Marquis. Effects of the local structure dependence of evaporation fields on field evaporation behavior. *Applied Physics Letters*, 107(24):1–14, 2015.

[71] T. Withrow, C. Oberdorfer, W. Windl, and E. A. Marquis. Coupling Molecular Dynamics and Finite Element Simulations to Investigate the Nearest

Neighbor Dependence of Field Evaporation. *Microscopy and Microanalysis*, 23(S1):646–647, 2017.

[72] C. Oberdorfer, T. Withrow, L. J. Yu, K. Fisher, E. A. Marquis, and W. Windl. Influence of surface relaxation on solute atoms positioning within atom probe tomography reconstructions. *Materials Characterization*, 146(January):324–335, 2018.

[73] T. P. Withrow. *Computational Modeling of Atom Probe Tomography*. PhD thesis, The Ohio State University, 2018.

[74] M. Kühbach, A. Breen, M. Herbig, and B. Gault. Building a Library of Simulated Atom Probe Data for Different Crystal Structures and Tip Orientations Using TAPSim. *Microscopy and Microanalysis*, 25(2):320–330, 2019.

[75] N. Rolland, D. J. Larson, B. P. Geiser, S. Duguay, F. Vurpillot, and D. Blavette. An analytical model accounting for tip shape evolution during atom probe analysis of heterogeneous materials. *Ultramicroscopy*, 159:195–201, 2015.

[76] N. Rolland, F. Vurpillot, S. Duguay, and D. Blavette. Dynamic evolution and fracture of multilayer field emitters in atom probe tomography: A new interpretation. *European Physical Journal: Applied Physics*, 72(2), 2015.

[77] N. Rolland, F. Vurpillot, S. Duguay, B. Mazumder, J. S. Speck, and D. Blavette. New Atom Probe Tomography Reconstruction Algorithm for Multilayered Samples: Beyond the Hemispherical Constraint. *Microscopy and Microanalysis*, 23(2):247–254, 2017.

[78] J. A. Sethian. *Level Set Methods and Fast Marching Methods: Evolving Interfaces in Computational Geometry, Computer Vision and Materials Science*. Cambridge University Press, 2nd edition, 1999.

[79] D. Haley, M. P. Moody, and G. D. W. Smith. Level set methods for modelling field evaporation in atom probe. *Microscopy and Microanalysis*, 19(6):1709–17, 2013.

[80] D. Haley, P. A. J. Bagot, and M. P. Moody. Extending continuum models for atom probe simulation. *Materials Characterization*, 146:299–306, 2018.

[81] Z. Xu, D. Li, W. Xu, A. Devaraj, R. Colby, S. Thevuthasan, B. P. Geiser, and D. J. Larson. Simulation of heterogeneous atom probe tip shapes evolution during field evaporation using a level set method and different evaporation models. *Computer Physics Communications*, 189:106–113, 2015.

[82] R. Malladi, J. A. Sethian, and B. C. Vemuri. Shape modeling with front propagation: a level set approach. *IEEE Trans. on Pattern Analysis and Machine Intelligence*, 17(2):158–175, 1995.

[83] C. Hatzoglou and F. Vurpillot. A Mesoscopic Field Evaporation Model. *Microscopy and Microanalysis*, 25(S2):286–287, 2019.

[84] D. Beinke, C. Oberdorfer, and G. Schmitz. Towards an accurate volume reconstruction in atom probe tomography. *Ultramicroscopy*, 165:34–41, 2016.

[85] D. Beinke and G. Schmitz. Atom Probe Reconstruction With a Locally Varying Emitter Shape. *Microscopy and Microanalysis*, 25:1–8, 2019.

[86] D. Beinke, F. Bürger, H. Solodenko, R. Acharya, H. Klauk, and G. Schmitz. Extracting the shape of nanometric field emitters. *Nanoscale*, 12(4):2820–2832, 2020.

[87] A. Alpers, R. J. Gardner, S. König, R. S. Pennington, C. B. Boothroyd, L. Houben, R. E. Dunin-Borkowski, and K. Joost Batenburg. Geometric

reconstruction methods for electron tomography. *Ultramicroscopy*, 128:42–54, 2013.

[88] P. Gilbert. Iterative Methods for the Three-dimensional Reconstruction of an Object from Projections. *Journal of Theoretical Biology*, 36:105–117, 1972.

[89] P. A. Penczek. Fundamentals of Three-Dimensional Reconstruction from Projections. In *Methods in Enzymology*, volume 482, chapter 1, pages 1–33. Elsevier, 1 edition, 2010.

[90] P. Ercius, O. Alaidi, M.J. Rames, and G. Ren. Electron Tomography: A Three-Dimensional Analytic Tool for Hard and Soft Materials Research. *Advanced Materials*, 27(38):5638–5663, 2015.

[91] T. C. Petersen and S. P. Ringer. Electron tomography using a geometric surface-tangent algorithm: Application to atom probe specimen morphology. *Journal of Applied Physics*, 105(10), 2009.

[92] I. Arslan, E. A. Marquis, M. Homer, M. A. Hekmaty, and N. C. Bartelt. Towards better 3-D reconstructions by combining electron tomography and atom-probe tomography. *Ultramicroscopy*, 108(12):1579–1585, 2008.

[93] A. Grenier, S. Duguay, J. P. Barnes, R. Serra, G. Haberfehlner, D. Cooper, F. Bertin, S. Barraud, G. Audoit, L. Arnoldi, E. Cadel, A. Chabli, and F. Vurpillot. 3D analysis of advanced nano-devices using electron and atom probe tomography. *Ultramicroscopy*, 136:185–192, 2014.

[94] A. Devaraj, R. Colby, F. Vurpillot, and S. Thevuthasan. Understanding atom probe tomography of oxide-supported metal nanoparticles by correlation with atomic-resolution electron microscopy and field evaporation simulation. *Journal of Physical Chemistry Letters*, 5(8):1361–1367, 2014.

[95] W. Guo, B. T. Sneed, Y. Meng, D. A. Cullen, J. Zuo, and J. D. Poplawsky. Recent Progress of Correlative Transmission Electron Microscopy and Atom Probe Tomography for Materials Characterization. *Microscopy and Microanalysis*, 23(S1):692–693, 2017.

[96] I. Mouton, T. Printemps, A. Grenier, N. Gambacorti, E. Pinna, M. Tiddia, A. Vacca, and G. Mula. Toward an accurate quantification in atom probe tomography reconstruction by correlative electron tomography approach on nanoporous materials. *Ultramicroscopy*, 182:112–117, 2017.

[97] I. Mouton, S. Katnagallu, S. K. Makineni, O. Cojocaru-Mirédin, T. Schwarz, L. T. Stephenson, D. Raabe, and B. Gault. Calibration of Atom Probe Tomography Reconstructions Through Correlation with Electron Micrographs. *Microscopy and Microanalysis*, 25(2):301–308, 2019.

[98] A. Grenier, S. Duguay, J. P. Barnes, R. Serra, N. Rolland, G. Audoit, P. Morin, P. Gouraud, D. Cooper, D. Blavette, and F. Vurpillot. Three dimensional imaging and analysis of a single nano-device at the ultimate scale using correlative microscopy techniques. *Applied Physics Letters*, 106(21), 2015.

[99] R. Kirchhofer. *Development of a Dynamic Atom Probe*. PhD thesis, Colorado School of Mines, 2014.

[100] D. Haley, T. C. Petersen, S. P. Ringer, and G. D. W. Smith. Atom probe trajectory mapping using experimental tip shape measurements. *Journal of Microscopy*, 244(2):170–180, 2011.

[101] T. Kelly, R. Dunin-Borkowski, and J. Meyer. Project Tomo: Toward Atomic-scale Analytical Tomography. *Microscopy and Microanalysis*, 26(S2):2618–2621, 2020.

[102] Z. Saghi, G. Divitini, B. Winter, R. Leary, E. Spiecker, C. Ducati, and P. A. Midgley. Compressed sensing electron tomography of needle-shaped biological specimens – Potential for improved reconstruction fidelity with reduced dose. *Ultramicroscopy*, 160(1):230–238, 2016.

[103] M. Duchamp, A. Ramar, A. Kovács, T. Kasama, F. J. Haug, S. B. Newcomb, C. Ballif, and R. E. Dunin-Borkowski. Conventional and 360 degree electron tomography of a micro-crystalline silicon solar cell. *Journal of Physics: Conference Series*, 326(1), 2011.

[104] E. Gómez-de Mariscal, M. Maška, A. Kotrbová, V. Pospíchalová, P. Matula, and A. Muñoz-Barrutia. Deep-Learning-Based Segmentation of Small Extracellular Vesicles in Transmission Electron Microscopy Images. *Scientific Reports*, 9(1):1–10, 2019.

[105] J. Op de Beeck, C. Fleischmann, W. Vandervorst, and K. Paredis. Nanoscale Localization of an Atom Probe Tip through Electric Field Mapping. *The Journal for Physical Chemistry*, 124(11):6371–6378, 2020.

[106] T. T. Tsong and E. W. Müller. Effects of static-field penetration and atomic polarization on the capacity of a capacitor, field evaporation, and field ionization processes. *Physical Review*, 181(2):530–534, 1969.

[107] H. J. Kreuzer and K. Nath. Field evaporation. *Surface Science*, 183(3):591–608, 1987.

[108] M. K. Miller and R. G. Forbes. Field Evaporation and Related Topics. In *Atom-Probe Tomography: The Local Electrode Atom Probe*, pages 111–187. Springer, New York, 1 edition, 2014.

[109] R. G. Forbes. An alternative theoretical approach to field evaporation rate sensitivities. *Surface Science*, 46(2):577–601, 1974.

[110] M. Gruber, F. Vurpillot, A. Bostel, and B. Deconihout. Field evaporation: A kinetic Monte Carlo approach on the influence of temperature. *Surface Science*, 605(23-24):2025–2031, 2011.

[111] M. J. Lloyd, R. G. Abernethy, M. R. Gilbert, I. Griffiths, P. A. J. Bagot, D. Nguyen-Manh, M. P. Moody, and D. E. J. Armstrong. Decoration of voids with rhenium and osmium transmutation products in neutron irradiated single crystal tungsten. *Scripta Materialia*, 173:96–100, 2019.

[112] D. L. Chopp. Another Look at Velocity Extensions in the Level Set Method. *SIAM Journal on Scientific Computing*, 31(5):3255–3273, 2009.

[113] J. A. Sethian and J. Strain. Crystal Growth and Dendritic Solidification. *Journal for Computational Physics*, 98:231–253, 1992.

[114] M. Garzon, D. Adalsteinsson, L. Gray, and J. A. Sethian. A coupled level set-boundary integral method for moving boundary simulations. *Interfaces and Free Boundaries*, 7(3):277–302, 2005.

[115] M. Sussman, P. Smereka, and S. Osher. A Level Set Approach for Computing Solutions to Incompressible Two-Phase Flow. *Journal of Computational Physics*, 114(1):146–159, 1994.

[116] E. Rouy and A. Tourin. A Viscosity Solutions Approach to Shape-From-Shading. *SIAM Journal on Numerical Analysis*, 29(3):867–884, 1992.

[117] C. W. Shu and S. Osher. Efficient implementation of essentially non-oscillatory shock-capturing schemes. *Journal of Computational Physics*, 77(2):439–471, 1988.

[118] W. E. Lorensen and H. E. Cline. Marching cubes: A high resolution 3D surface construction algorithm. *Computer Graphics*, 21(4):163–169, 1987.

[119] T. Lewiner, H. Lopes, A. W. Vieira, and G. Tavares. Efficient Implementation of Marching Cubes' Cases with Topological Guarantees. *Journal of Graphics Tools*, 8(2):1–15, 2003.

[120] W. Dijkstra. Condition numbers in the boundary element method: shape and solvability. Technical report, Eindhoven, Technische Universiteit, Eindhoven, 2008.

[121] M. Botsch and L. Kobbelt. A remeshing approach to multiresolution modeling. *ACM International Conference Proceeding Series*, 71:185–192, 2004.

[122] S. Loriot, M. Rouxel-Labbé, J. Tournois, and I. O. Yaz. Polygon Mesh Processing. In CGAL Editorial Board, editor, *CGAL User and Reference Manual*. Board, CGAL Editorial, 5.0.3 edition, 2020.

[123] P. P. Pebay and T. J. Baker. A Comparison Of Triangle Quality Measures. In *Proceedings of the National Academy of Sciences*, pages 9653–9657. Plenum Press, 1991.

[124] L. Gillott. The effect of pulsed fields on ion trajectories in the field ion microscope. *Journal of Physics E: Scientific Instruments*, 7:1012–1014, 1974.

[125] G. Green. 22. An Essay on the Application of mathematical Analysis to the theories of Electricity and Magnetism. *Journal fur die Reine und Angewandte Mathematik*, 1852(44):356–374, 1852.

[126] M. A. Grayson. The heat equation shrinks embedded plane curves to round points. *Journal of Differential Geometry*, 26(2):285–314, 1987.

[127] M. A. Grayson. Shortening Embedded Curves. *The Annals of Mathematics*, 129(1):71, 1989.

[128] W. W. Mullins. Two-dimensional motion of idealized grain boundaries. *Journal of Applied Physics*, 27(8):900–904, 1956.

[129] K. Bhattacharya. On the dependence of charge density on surface curvature of an isolated conductor. *Physica Scripta*, 91(3):1–17, 2016.

[130] F. Vurpillot, A. Bostel, and D. Blavette. A new approach to the interpretation of atom probe field-ion microscopy images. *Ultramicroscopy*, 89(1-3):137–144, 2001.

[131] Y. J. Liu, S. Mukherjee, N. Nishimura, M. Schanz, W. Ye, A. Sutradhar, E. Pan, N. A. Dumont, A. Frangi, and A. Saez. Recent Advances and Emerging Applications of the Boundary Element Method. *Applied Mechanics Reviews*, 64(3):030802, 2012.

[132] L. Yijun. *Fast Multipole Boundary Element Method: Theory and Applications in Engineering*. Cambridge University Press, Cambridge, 1st edition, 2009.

[133] C. Fletcher, M. P. Moody, and D. Haley. Fast modelling of field evaporation in atom probe tomography using level set methods. *Journal of Physics D: Applied Physics*, 52(435305), 2019.

[134] F. Glück and D. Hilk. Electric potential and field calculation of charged BEM triangles and rectangles by Gaussian cubature. *Progress In Electromagnetics Research B*, 74:1–21, 2017.

[135] P. Jabłoński. Integral and geometrical means in the analytical evaluation of the BEM integrals for a 3D Laplace equation. *Engineering Analysis with Boundary Elements*, 34(3):264–273, 2010.

[136] C. Fletcher, M. P. Moody, and D. Haley. Towards model-driven reconstruction in atom probe tomography. *Journal of Physics D: Applied Physics*, 53(475303), 2020.

[137] P. Souzangar. *Efficient Numerical Modeling of Snom Tips*. PhD thesis, ETH Zurich, 2016.

[138] Y. Liu and T. J. Rudolphi. Some identities for fundamental solutions and their applications to weakly-singular boundary element formulations. *Engineering Analysis with Boundary Elements*, 8(6):301–311, 1991.

[139] B. Gault, M. P. Moody, J. M. Cairney, and S. P. Ringer. *Atom Probe Microscopy*. Springer, New York, 2012.

[140] G. Aiello, S. Alfonzetti, E. Dilettoso, and N. Salerno. An iterative solution to FEM-BEM algebraic systems for open-boundary electrostatic problems. *IEEE Transactions on Magnetics*, 43(4):1249–1252, 2007.

[141] M. Ramšak and L. Škerget. 3D multidomain BEM for solving the Laplace equation. *Engineering Analysis with Boundary Elements*, 31(6):528–538, 2007.

[142] Q. Zhang. *Rigorous nonlinear electrostatic simulation of Atom Probe Tomography*. PhD thesis, Georgia Institute of Technology, 2020.

[143] M. G. Larson and F. Bengzon. The Finite Element Method in 2D. In *The Finite Element Method: Theory, Implementation, and Applications*, chapter 4, pages 71–111. Springer, 2013.

[144] F. Vurpillot, A. Gaillard, G. Da Costa, and B. Deconihout. A model to predict image formation in Atom probe Tomography. *Ultramicroscopy*, 132:152–157, 2013.

[145] E. P. Silaeva, L. Arnoldi, M. L. Karahka, B. Deconihout, A. Menand, H. J. Kreuzer, and A. Vella. Do dielectric nanostructures turn metallic in high-electric dc fields? *Nano Letters*, 14(11):6066–6072, 2014.

[146] L. Arnoldi, E. P. Silaeva, A. Gaillard, F. Vurpillot, I. Blum, L. Rigutti, B. Deconihout, and A. Vella. Energy deficit of pulsed-laser field-ionized and field-emitted ions from non-metallic nano-tips. *Journal of Applied Physics*, 115(203705), 2014.

[147] L. Arnoldi, E. P. Silaeva, F. Vurpillot, B. Deconihout, E. Cadel, I. Blum, and A. Vella. Role of the resistivity of insulating field emitters on the energy of field-ionised and field-evaporated atoms. *Ultramicroscopy*, 159:139–146, 2015.

[148] J. R. Dormand and P. J. Prince. A reconsideration of some embedded Runge-Kutta formulae. *Journal of Computational and Applied Mathematics*, 15(2):203–211, 1986.

[149] E. A. Marquis and F. Vurpillot. Chromatic aberrations in the field evaporation behavior of small precipitates. *Microscopy and Microanalysis*, 14(6):561–570, 2008.

[150] W. Hackbusch and Z. P. Nowak. On the fast matrix multiplication in the boundary element method by panel clustering. *Numerische Mathematik*, 54(4):463–491, 1989.

[151] D. J. R. Meagher. Octree Encoding: A New Technique for the Representation, Manipulation and Display of Arbitrary 3-D Objects by Computer. Technical Report IPL-TR-80-111, Rensselaer Polytechnic Institute, 1980.

[152] N. Nishimura. Fast multipole accelerated boundary integral equation methods. *Applied Mechanics Reviews*, 55(4):299, 2002.

[153] Y. Mi and M. H. Aliabadi. A Taylor expansion algorithm for integration of 3D near-hypersingular integrals. *Communications in Numerical Methods in Engineering*, 12(1):51–62, 1996.

[154] J. R. Shewchuk. Triangle: Engineering a 2D quality mesh generator and Delaunay triangulator. In *1st Workshop on Applied Computational Geometry*, pages 203–222, 1996.

[155] L. C. Morrow, J. R. King, T. J. Moroney, and S. W. McCue. Moving boundary problems for quasi-steady conduction limited melting. *SIAM Journal on Applied Mathematics*, 79(5):2107–2131, 2019.

[156] Y. Wei, Z. Peng, M. Kühbach, A. Breen, M. Legros, M. Larranaga, F. Mompiou, and B. Gault. 3D nanostructural characterisation of grain boundaries in atom probe data utilising machine learning methods. *PLOS ONE*, 14(11):1–19, 2019.

[157] M. Burger, F. Haußer, C. Stöcker, and A. Voigt. A level set approach to anisotropic flows with curvature regularization. *Journal of Computational Physics*, 225(1):183–205, 2007.

[158] Y. Giga and N. Požár. A level set crystalline mean curvature flow of surfaces. *Adv. Differential Equations*, 21(7-8):631–698, 2016.

[159] T. L. Einstein. Equilibrium Shape of Crystals. In *Handbook of Crystal Growth: Second Edition*, volume 1, pages 215–264. Elsevier, 2014.

[160] F. Vurpillot, J. Houard, A. Vella, and B. Deconihout. Thermal response of a field emitter subjected to ultra-fast laser illumination. *Journal of Physics D: Applied Physics*, 42(12), 2009.

[161] D. J. Larson, T. J. Prosa, R. M. Ulfig, B. P. Geiser, and T. F. Kelly. Appendix A: Data File Formats. In *Local Electrode Atom Probe Tomography*. Springer, New York, 2013.

[162] T. F. Kelly, A. Vella, J. H. Bunton, J. Houard, E. P. Silaeva, J. Bogdanowicz, and W. Vandervorst. Laser pulsing of field evaporation in atom probe tomography. *Current Opinion in Solid State and Materials Science*, 18(2):81–89, 2014.

[163] A. Vella. On the interaction of an ultra-fast laser with a nanometric tip by laser assisted atom probe tomography: A review. *Ultramicroscopy*, 132:5–18, 2013.

[164] R. Hanus. *Laser-tip interactions in the laser-assisted atom probe tomography technique: the case of III-V semiconductors*. PhD thesis, Liège, 2018.

[165] P. Felfer and J. M. Cairney. A computational geometry framework for the optimisation of atom probe reconstructions. *Ultramicroscopy*, 169:62–68, 2016.

[166] T. F. Kelly. Atomic-scale analytical tomography. *Microscopy and Microanalysis*, 23(1):34–45, 2017.

[167] H. Weyl. The method of orthogonal projection in potential theory. *Duke Mathematical Journal*, 7(1):411–444, 1940.

[168] E. A. Coddington and N. Levinson. Existence and Uniqueness of Solutions. In W. T. Martin and E. H. Spanier, editors, *Theory of Ordinary Differential Equations*, chapter 1, pages 22–32. McGraw-Hill Book Company, New York Toronto London, 1 edition, 1955.

[169] P. Daskalopoulos and K. A. Lee. All Time Smooth Solutions of the One-Phase Stefan Problem and the Hele-Shaw Flow. *Communications in Partial Differential Equations*, 29(1-2):71–89, 2005.

[170] A. D. Giddings, S. Koelling, Y. Shimizu, R. Estivill, K. Inoue, W. Vandervorst, and W. K. Yeoh. Industrial application of atom probe tomography to semiconductor devices. *Scripta Materialia*, 2017.

[171] J. Wambsganss. Gravitational lensing in astronomy. *Living Reviews in Relativity*, 1(12), 1998.

[172] M. Botsch, L. Kobbelt, M. Pauly, P. Alliez, and B. Levy. Parameterisation. In *Polygon Mesh Processing*, pages 71–73. A K Peters, Natick, 1 edition, 2010.

[173] T. Möller and B. Trumbore. Fast, Minimum Storage Ray/Triangle Intersection. *Journal of Graphics Tools,*, 2(1):21–28, 1997.

[174] J. D. Foley, A. van Dam, S. K. Feiner, and J. Hughes. *Computer Graphics: Principles and Practice*. Addison-Wesley, Boston, 1995.

[175] V. A. Epanechnikov. Non-parametric estimation of a multivariate probability density. *Theory of Probability and Applications*, 14(1):153–158, 1969.

[176] S. Tjing, B. Gault, S. P. Ringer, D. J. Larson, and B. P. Geiser. Electrostatic simulations of a local electrode atom probe : The dependence of tomographic reconstruction parameters on specimen and microscope geometry. *Ultramicroscopy*, 132:107–113, 2013.

[177] Y. J. Liu and N. Nishimura. The fast multipole boundary element method for potential problems: A tutorial. *Engineering Analysis with Boundary Elements*, 30(5):371–381, 2006.

[178] M. P. Moody, F. Tang, B. Gault, S. P. Ringer, and J. M. Cairney. Atom probe crystallography: Characterization of grain boundary orientation relationships in nanocrystalline aluminium. *Ultramicroscopy*, 111(6):493–499, 2011.

[179] A. Melbourne, G. Ridgway, and D. J. Hawkes. Image similarity metrics in image registration. *Medical Imaging 2010: Image Processing*, 7623(1):762335, 2010.

[180] H. A. Sturges. The Choice of a Class Interval. *Journal of the American Statistical Association*, 21(153):65–66, 1926.

[181] B. B. Avants, C. L. Epstein, M. Grossman, and J. C. Gee. Symmetric diffeomorphic image registration with cross-correlation: Evaluating automated labeling of elderly and neurodegenerative brain. *Medical Image Analysis*, 12(1):26–41, 2008.

[182] M. F. Beg, M. I. Miller, A. Trouvé, and L. Younes. Computing large deformation metric mappings via geodesic flows of diffeomorphisms. *International Journal of Computer Vision*, 61(2):139–157, 2005.

[183] J. Ashburner. A fast diffeomorphic image registration algorithm. *NeuroImage*, 38(1):95–113, 2007.

[184] M. Bauer, S. Joshi, and K. Modin. Diffeomorphic density matching by optimal information transport. *SIAM Journal on Imaging Sciences*, 8(3):1718–1751, 2015.

[185] G. E. Christensen, R. D. Rabbitt, M. I. Miller, S. C. Joshi, U. Grenander, T. Coogan, and D. C. Van Essen. Topological Properties of Smooth Anatomic Maps. In *Information Processing in Medical Imaging*, pages 101–112. Kluwer Academic Publishers, Boston, 1995.

[186] C. Rottman, M. Bauer, K. Modin, and S. Joshi. Weighted Diffeomorphic Density Matching with Applications to Thoracic Image Registration. In *Proc. 5th MICCAI Workshop on Mathematical Foundations of Computational Anatomy (MFCA)*, 2015.

[187] K. Modin. ddmatch, 2017.

[188] B. Gault, M. P. Moody, F. De Geuser, and A. La Fontaine. Spatial Resolution in Atom Probe Tomography M icroscopy M icroanalysis Spatial Resolution in Atom Probe Tomography. *Microscopy and Microanalysis*, 16:99–110, 2010.

[189] F. Vurpillot, N. Rolland, R. Estivill, S. Duguay, and D. Blavette. Accuracy of analyses of microelectronics nanostructures in atom probe tomography. *Semiconductor Science and Technology*, 31(7), 2016.

[190] C. Hatzoglou, B. Radiguet, and P. Pareige. Experimental artefacts occurring during atom probe tomography analysis of oxide nanoparticles in metallic matrix: Quantification and correction. *Journal of Nuclear Materials*, 492:279–291, 2017.

[191] S. H. Kim, K. Jang, P. W. Kang, J. P. Ahn, J. B. Seol, C. M. Kwak, C. Hatzoglou, F. Vurpillot, and P. P. Choi. Characterization of Pd and Pd@Au core-shell nanoparticles using atom probe tomography and field evaporation simulation. *Journal of Alloys and Compounds*, 831:154721, 2020.

[192] D. J. Larson, B. Gault, B. P. Geiser, F. De Geuser, and F. Vurpillot. Atom probe tomography spatial reconstruction: Status and directions. *Current Opinion in Solid State and Materials Science*, 17(5):236–247, 2013.

[193] G. Russo and P. Smereka. A level-set method for the Evolution of Faceted Crystals. *SIAM Journal on Scientific Computing*, 21(6):2073–2095, 2000.

[194] M. K. Miller, L. Longstreth-Spoor, and K. F. Kelton. Detecting density variations and nanovoids. *Ultramicroscopy*, 111(6):469–472, 2011.

[195] M. Dagan, L. R. Hanna, A. Xu, S. G. Roberts, G. D. W. Smith, B. Gault, P. D. Edmondson, P. A. J. Bagot, and M. P. Moody. Imaging of radiation damage using complementary field ion microscopy and atom probe tomography. *Ultramicroscopy*, 159:387–394, 2015.

[196] C. L. Chan and A. Chandra. An algorithm for handling corners in the boundary element method: Application to conduction-convection equations. *Applied Mathematical Modelling*, 15(5):244–255, 1991.

[197] D. Adalsteinsson and J. A. Sethian. A Fast Level Set Method for Propagating Interfaces. *Journal for Computational Physics*, 118:267–277, 1994.

[198] D. Adalsteinsson and J. A. Sethian. The fast Construction of extension Velocities in Level Set Methods. *The Journal of Computational Physics*, 148:2–22, 1999.

[199] D. Ruprecht and R. Krause. Explicit parallel-in-time integration of a linear acoustic-advection system. *Computers and Fluids*, 59:72–83, 2012.

[200] M. Mirzadeh, A. Guittet, C. Burstedde, and F. Gibou. Parallel level-set methods on adaptive tree-based grids. *Journal of Computational Physics*, 322:345–364, 2016.

[201] D. Eberly. Distance Between Point and Circle or Disk in 3D. In *Geometric Tools Documentation*, chapter Mathematic, pages 1–11. Creative Commons, 1999.

[202] D. Blavette, F. Vurpillot, P. Pareige, and A. Menand. A model accounting for spatial overlaps in 3D atom-probe microscopy. *Ultramicroscopy*, 89(1-3):145–153, 2001.

[203] S. Koelling, N. Innocenti, A. Schulze, M. Gilbert, A. K. Kambham, and W. Vandervorst. In-situ observation of non-hemispherical tip shape formation during laser-assisted atom probe tomography. *Journal of Applied Physics*, 109(10), 2011.

[204] M. K. Miller and R. G. Forbes. Chapter 3: Field Evaporation and Related Topics. In *Atom-Probe Tomography: The Local Electrode Atom Probe*, chapter 3, pages 111–187. Springer, 2014.

[205] G. Sha, A. Cerezo, and G. D. W. Smith. Field evaporation behavior during irradiation with picosecond laser pulses. *Applied Physics Letters*, 92(043503), 2008.

[206] F. Vurpillot, D. Blavette, and A. Menand. Trajectories of field emitted ions in 3D atom- probe. *The European Journal for Applied Physics*, 6:217–221, 1999.

[207] X. Wang, C. Hatzoglou, B. Sneed, Z. Fan, W. Guo, K. Jin, D. Chen, H. Bei, Y. Wang, W. J. Weber, Y. Zhang, B. Gault, K. L. More, F. Vurpillot, and J. D. Poplawsky. Interpreting nanovoids in atom probe tomography data for accurate local compositional measurements. *Nature Communications*, 11(1):1–11, 2020.

[208] W. van Aarle, W. J. Palenstijn, J. De Beenhouwer, T. Altantzis, S. Bals, K. J. Batenburg, and J. Sijbers. The ASTRA Toolbox: A platform for advanced algorithm development in electron tomography. *Ultramicroscopy*, 157(2015):35–47, 2015.

[209] S. Boutami, A. Glière, B. Stout, J. Hazart, and M. Fall. Multilevel fast multipole method based on a potential formulation for 3D electromagnetic scattering problems. *Journal of the Optical Society of America A*, 30(6):1273, 2013.

[210] P. Yang, L. Zhang, Y. Tang, L. Gong, Y. Zhao, and J. Yang. An atomic-continuum multiscale modeling approach for interfacial thermal behavior between materials. *Applied Mathematical Modelling*, 38(14):3373–3379, 2014.

[211] J. Willard, X. Jia, S. Xu, M. Steinbach, and V. Kumar. Integrating Physics-Based Modeling with Machine Learning: A Survey. *arXiv*, 1(1):1–34, 2020.

[212] S. Groß, V. Reichelt, and A. Reusken. A finite element based level set method for two-phase incompressible flows. *Computing and Visualization in Science*, 9(4):239–257, 2006.

[213] D. B. Ingham and J. A. Ritchie. The Linear Boundary Element Solution of Laplace's Equation with Dirichlet Boundary Conditions. *Mathematical and Computer Modelling*, 15(3):195–204, 1991.

[214] L. J. Gray and G. H. Paulino. Symmetric galerkin boundary integral formulation for interface and multi-zone problems. *International Journal for Numerical Methods in Engineering*, 40(16):3085–3101, 1997.

[215] M. L. Parks, E. De Sturler, G. Mackey, D. D. Johnson, and S. Maiti. Recycling Krylov subspaces for sequences of linear systems. *SIAM Journal on Scientific Computing*, 28(5):1651–1674, 2006.

[216] J. Bergstra and Y. Bengio. Random search for hyper-parameter optimization. *Journal of Machine Learning Research*, 13:281–305, 2012.

[217] R. E. Miller and E. B. Tadmor. The Quasicontinuum Method: Overview, applications and current directions. *Journal of Computer-Aided Materials Design*, 9(3):203–239, 2002.

[218] M. Ashton, A. Mishra, J. Neugebauer, and C. Freysoldt. Ab initio Description of Bond Breaking in Large Electric Fields. *Physical Review Letters*, 124(17):176801, 2020.

[219] S. Chen, X. Yao, C. Zheng, and W. H. Duan. Quantification of evaporation induced error in atom probe tomography using molecular dynamics simulation. *Ultramicroscopy*, 182:28–35, 2017.

[220] A. Gopal and L N. Trefethen. Solving laplace problems with corner singularities via rational functions. *SIAM Journal on Numerical Analysis*, 57(5):2074–2094, 2019.

[221] M. Dagan, B. Gault, G. D. W. Smith, P. A. J. Bagot, and M. P. Moody. Automated Atom-By-Atom Three-Dimensional (3D) Reconstruction of Field Ion Microscopy Data. *Microscopy and Microanalysis*, 23:255–268, 2017.

[222] S. S. Katnagallu, B. Gault, B. Grabowski, J. Neugebauer, D. Raabe, and A. Nematollahi. Advanced data mining in field ion microscopy. *Materials Characterization*, 146:307–318, 2017.

[223] B. Klaes, R. Lardé, F. Delaroche, C. Hatzoglou, S. Parvianien, J. Houard, G. Da Costa, A. Normand, M. Brault, B. Radiguet, and F. Vurpillot. Development of Wide Field of View Three-Dimensional Field Ion Microscopy and High-Fidelity Reconstruction Algorithms to the Study of Defects in Nuclear Materials. *Microscopy and Microanalysis*, 27(2):365–384, 2021.

8 Appendix A: Variation in Evaporation Parameters

The average frequency of evaporation for an individual atom can be described by the Arrhenius relationship in Eq. (128) [23].

$$p_i = p_0 \; e^{-\frac{Q_i}{kT}} \tag{128}$$

Here ν_0 is some trial frequency dependent on the lattice frequency, and Q is the atomic-specific evaporation barrier. When considering a population of surface atoms, its average evaporation rate is proportional to the sum of probabilities for all surface atoms that are candidates for evaporation (Eq. (129)). These candidate atoms typically have different evaporation barriers depending on their local surface position and configuration. For large populations, this sum can be well approximated by an integral over Q (Eq. (130)).

$$< R_e > = \sum_{i}^{N} p_0 \; e^{-\frac{Q_i}{kT}} \tag{129}$$

$$= \int_{-\infty}^{\infty} \rho(Q) e^{-\frac{Q}{kT}} dQ \tag{130}$$

Here $\rho(Q)$ is a kind of density of surface states giving the number of candidate surface atoms with evaporation barrier Q. While such an integral could potentially be calculated numerically, a simplified form can be obtained by making assumptions regarding the exact form of $\rho(Q)$. The Figure 106 shows an approximate copy from [70] for the relative distribution of atomic-specific evaporation fields calculated from an atomic model. The plot shows particular dominant modes corresponding to different subpopulations of surface atoms, characterised by

their local configuration and environment. As the evaporation fields govern the evaporation barrier, this relative distribution is directly related to $\rho(Q)$.

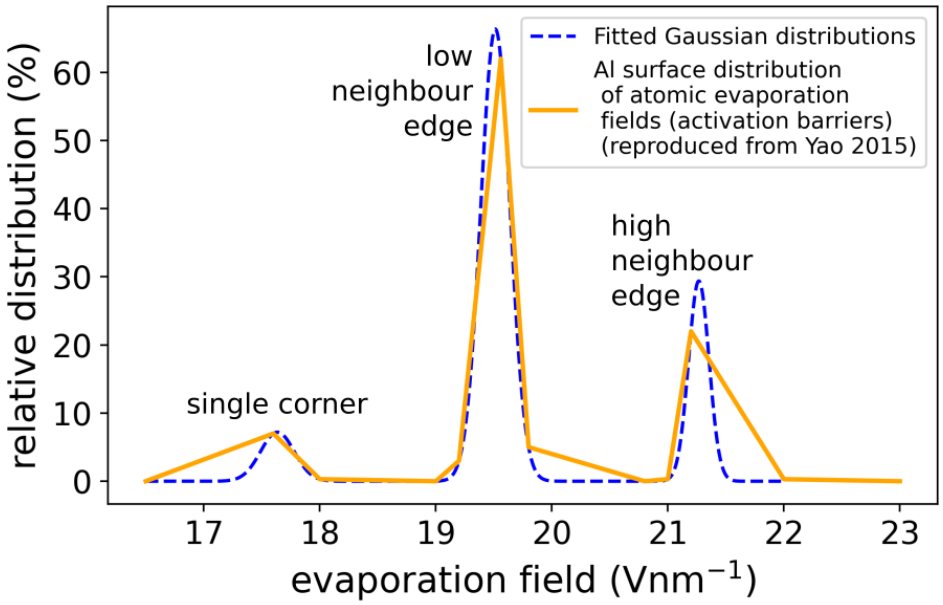


Figure 106: An approximate reproduction from [70] for a distribution of surface atom evaporation fields (activation barriers), determined by an atomic model. Gaussian distributions have been fitted to its three modes, highlighting its approximation via a mixture model.

The form of the distribution implies that $\rho(Q)$ could potentially be reasonably approximated a Gaussian mixture model (Eq. (131)).

$$\rho(Q) = \sum_{i}^{M} \frac{\omega_i}{\sigma_i \sqrt{2\pi}} e^{-\frac{1}{2}\frac{(Q-Q_i)^2}{\sigma_i^2}} \tag{131}$$

Here Q is the mean evaporation barrier associated with a mode i, σ_i defines the variation in evaporation barriers associated with mode i, and ω_i give the number of atoms within each mode's subpopulation. Inserting this form for $\rho(Q)$ into Eq. (130), and performing the integral substitution $Q' = Q - Q_i$, we obtain Eq. (132).

$$< R_e > = \sum_i^M \frac{\omega_i}{\sigma_i\sqrt{2\pi}} \int e^{-\frac{1}{2}\frac{(Q-Q_i)^2}{\sigma_i^2}} e^{-\frac{Q}{kT}} dQ$$
$$= \sum_i^M \frac{\omega_i}{\sigma_i\sqrt{2\pi}} \int e^{-\frac{1}{2}\frac{(Q')^2}{\sigma_i^2}} \big(1 - \frac{Q'}{kT} + \frac{1}{2}\frac{(Q')^2}{(kT)^2} + ...\big) dQ' e^{-Q_i/kT} \tag{132}$$

We now have an infinite series of integral terms of the form given in Eq. (133).

$$\frac{1}{\sigma_i\sqrt{2\pi}} \frac{1}{(kT)^n} \int e^{-\frac{1}{2}\frac{Q'^2}{\sigma_i^2}} (Q')^n dQ' \tag{133}$$

Such terms can be solved by the integral identity in Eq. (134).

$$\int \frac{1}{\sigma\sqrt{2\pi}} e^{-\frac{1}{2\sigma^2}x^2} x^n dx = \begin{cases} (n-1)!!\ \sigma^n & \text{for n even} \\ 0 & \text{for n odd} \end{cases} \tag{134}$$

Where !! denotes the double factorial. Grouping together like terms, we eventually obtain the following power series form for the averaged evaporation rate. Noting that for $\sigma_i << kT$, we can then obtain the following approximate form.

$$< R_e > = \sum_i^M \omega_i \big(1 - \frac{1}{2}\left(\frac{\sigma_i}{kT}\right)^2 + \frac{1}{6}\left(\frac{\sigma_i}{kT}\right)^4 + ...\big) e^{-\frac{Q_i}{kT}} \tag{135}$$
$$\approx \sum_i^M \omega_i \big(1 - \frac{1}{2}\left(\frac{\sigma_i}{kT}\right)^2\big) e^{-\frac{Q_i}{kT}} \tag{136}$$

Therefore, assuming there is a dominant evaporation mode like in Figure 106 for atoms with low neighbour counts, or that the surface field is controlled, an Arrhenius law like that assumed in Eq. (21) is likely a reasonable approximation.

9 Appendix B: The Exterior BEM Problem

The boundary integral equation can be split into integrals over an outer boundary Γ_+ (a sphere with radius R_+ centred on the specimen) and inner boundary Γ_-.

$$u = \int_{\Gamma_+} Gq \; d\Gamma - \int_{\Gamma_+} Fu \; d\Gamma - \int_{\Gamma_-} Gq \; d\Gamma + \int_{\Gamma_-} Fu \; d\Gamma \tag{137}$$

Taking Γ_+ away to infinity, the first two components of Eq. (138) vanish by imposing the following boundary condition.

$$\lim_{R_+ \to \infty} \Big[\int_{\Gamma_+} Gq \; d\Gamma - \int_{\Gamma_+} Fu \; d\Gamma \Big] = 0 \tag{138}$$

Applying Eq. (138), and assuming for a field point $\mathbf{x}$ that $d(\mathbf{x}, \Gamma_+) >> d(\mathbf{x}, \Gamma_-)$,a relation between u and q in 3D is derived (Eq. (141)).

$$\int_{\Gamma_+} (G) \; [q] \; d\Gamma = \int_{\Gamma_+} (F) \; [u] \; d\Gamma \tag{139}$$

$$\Big(\frac{1}{4\pi R_+}\Big) \; [q] \; 4\pi R_+^2 \approx \Big(- \frac{1}{4\pi R_+^2}\Big) \; [u] \; 4\pi R_+^2 \tag{140}$$

$$q \approx -\frac{u}{R_+} \tag{141}$$

The 3D Green's function $G(\mathbf{x}, \mathbf{y})$ drops to zero as the distance between $\mathbf{x}$ and $\mathbf{y}$ increases. Therefore, both u and q tend to zero at infinity. However, in 2D both u and q are non-zero at infinity. The boundary integral equation for the exterior problem is now given by Eq. (142).

$$u = \int_{\Gamma_-} Fu \; d\Gamma - \int_{\Gamma_-} Gq \; d\Gamma \tag{142}$$

10 Appendix C: 3D BEM Analytic Integrals

The 3D integration kernels are given in Eq. (143).

$$
\begin{aligned}
G(\mathbf{x},\mathbf{y}) &= \frac{1}{4\pi}\frac{1}{||\mathbf{x}-\mathbf{y}||} \\
\frac{\partial G(\mathbf{x},\mathbf{y})}{\partial n} &= -\frac{1}{4\pi}\frac{(\mathbf{x}-\mathbf{y})\cdot\mathbf{n_y}}{||\mathbf{x}-\mathbf{y}||^3} \\
\frac{\partial G(\mathbf{x},\mathbf{y})}{\partial x_l} &= -\frac{1}{4\pi}\frac{(\mathbf{x}-\mathbf{y})\cdot\mathbf{n_x}}{||\mathbf{x}-\mathbf{y}||^3} \\
\frac{\partial^2 G(\mathbf{x},\mathbf{y})}{\partial n\,\partial x_l} &= \frac{1}{4\pi}\left[-3\frac{(\mathbf{x}-\mathbf{y})\cdot\mathbf{n_x}\;(\mathbf{x}-\mathbf{y})\cdot\mathbf{n_y}}{||\mathbf{x}-\mathbf{y}||^5} + \frac{\mathbf{n_x}\cdot\mathbf{n_y}}{||\mathbf{x}-\mathbf{y}||^3}\right]
\end{aligned}
\tag{143}
$$

For a given triangle panel Γ_j with corners $(\mathbf{a},\mathbf{b},\mathbf{c})$, and the collocation field point at the centre of Γ_i, the diagonal BEM matrix elements are given by the analytical formulas in Eq. (148) and Eq. (149).

$$\mathbf{a_1} = \mathbf{b}-\mathbf{a} \quad \mathbf{a_2} = \mathbf{c}-\mathbf{b} \quad \mathbf{a_3} = \mathbf{a}-\mathbf{c} \tag{144}$$

$$\mathbf{ax} = \mathbf{a}-\mathbf{x} \quad \mathbf{bx} = \mathbf{b}-\mathbf{x} \quad \mathbf{cx} = \mathbf{c}-\mathbf{x} \tag{145}$$

$$n_1 = \mathbf{bx}\cdot\mathbf{a_1}/||\mathbf{a_1}|| \quad n_2 = \mathbf{cx}\cdot\mathbf{a_2}/||\mathbf{a_2}|| \quad n_3 = \mathbf{ax}\cdot\mathbf{a_3}/||\mathbf{a_3}|| \tag{146}$$

$$n_4 = \mathbf{ax}\cdot\mathbf{a_1}/||\mathbf{a_1}|| \quad n_5 = \mathbf{bx}\cdot\mathbf{a_2}/||\mathbf{a_2}|| \quad n_6 = \mathbf{cx}\cdot\mathbf{a_3}/||\mathbf{a_3}|| \tag{147}$$

$$L_1 = \log\Big(\frac{||\mathbf{bx}||+n_1}{||\mathbf{ax}||+n_4}\Big) \quad L_2 = \log\Big(\frac{||\mathbf{cx}||+n_2}{||\mathbf{bx}||+n_5}\Big) \quad L_3 = \log\Big(\frac{||\mathbf{ax}||+n_3}{||\mathbf{cx}||+n_6}\Big) \tag{148}$$

$$G_{ij} = \frac{1}{6\pi}\sum_i^3 \frac{L_i}{||\mathbf{a}_i||} \tag{149}$$

$$F_{ij} = -\frac{3}{2} \tag{150}$$

Derivation of these matrix elements' analytical forms can be found in [135]. It is more efficient to calculate off-diagonal elements numerically (Appendix D).

11 Appendix D: 3D BEM Numerical Integrals

Integration of the 3D BEM kernels has been performed using the 7-point quadrature method in [134]. The integration scheme is defined in terms of Barycentric coordinates. For a triangle panel Γ_{abc}, defined by the corner points $(\mathbf{x}_a, \mathbf{x}_b, \mathbf{x}_c)$, Barycentric coordinates $(\lambda_a, \lambda_b, \lambda_c)$ provide a local coordinate system over the panel. An arbitrary panel coordinate can then be expressed via Eq. (151).

$$\mathbf{x} = \lambda_a \mathbf{x}_a + \lambda_b \mathbf{x}_b + \lambda_c \mathbf{x}_c \quad \text{where } \lambda_a + \lambda_b + \lambda_c = 1 \quad \lambda_a, \lambda_b, \lambda_c \geq 0 \tag{151}$$

When calculating the BEM kernel integrals in 3D, we are evaluating a surface integral of the form in Eq. (152).

$$I = \int_{\Gamma_{abc}} f(\mathbf{x}) \; d^2\mathbf{x} \tag{152}$$

Here $f(\mathbf{x})$ is the integrated scalar field. The integration formula is then given by Eq. (153), with the exact Barycentric coordinates and weights in Table 2.

$$I = \sum_{i}^{7} \omega_i f(\mathbf{a}_i) \tag{153}$$

$\mathbf{x}$	λ_a	λ_b	λ_c	ω
$\mathbf{a_1}$	1/3	1/3	1/3	9/40
$\mathbf{a_2}$	1/3 + 2(1 - $\sqrt{15}$)/21	1/3 - (1 - $\sqrt{15}$)/21	1/3 - (1 - $\sqrt{15}$)/21	155 + $\sqrt{15}$/1200
$\mathbf{a_3}$	1/3 - (1 - $\sqrt{15}$)/21	1/3 + 2(1 - $\sqrt{15}$)/21	1/3 - (1 - $\sqrt{15}$)/21	155 + $\sqrt{15}$/1200
$\mathbf{a_4}$	1/3 - (1 - $\sqrt{15}$)/21	1/3 - (1 - $\sqrt{15}$)/21	1/3 + 2(1 - $\sqrt{15}$)/21	155 + $\sqrt{15}$/1200
$\mathbf{a_5}$	1/3 + 2(1 + $\sqrt{15}$)/21	1/3 - (1 + $\sqrt{15}$)/21	1/3 - (1 + $\sqrt{15}$)/21	155 - $\sqrt{15}$/1200
$\mathbf{a_6}$	1/3 - (1 + $\sqrt{15}$)/21	1/3 + 2(1 + $\sqrt{15}$)/21	1/3 - (1 + $\sqrt{15}$)/21	155 - $\sqrt{15}$/1200
$\mathbf{a_7}$	1/3 - (1 + $\sqrt{15}$)/21	1/3 - (1 + $\sqrt{15}$)/21	1/3 + 2(1 + $\sqrt{15}$)/21	155 - $\sqrt{15}$/1200

Table 2: Barycentric coordinates and weights for the quadrature scheme.

12 Appendix E: The FEM-BEM Coupling

In this appendix, the FEM-BEM coupling will be constructed from the weak formulation in Eq. (74). The first step is to construct the solution and test function in terms of a set of basis functions $\psi_i(\mathbf{x})$, centred on particular nodes $\mathbf{x}_i$ in space.

$$\begin{aligned} \nu(\mathbf{x}) &= \sum_i \nu_i \psi_i(\mathbf{x}) \\ u(\mathbf{x}) &= \sum_j u_j \psi_j(\mathbf{x}) \\ q(\mathbf{x}) &= \sum_J q_j \psi_j(\mathbf{x}) \end{aligned} \tag{154}$$

Plugging these basis expansions into the weak formulation given in Eq. (74), we arrive at the FEM matrix equation (Eq. (156)).

$$\sum_i \sum_j \nu_i \underbrace{\left[\int_{\mathbf{X}^+} \nabla\psi_i \cdot \nabla\psi_j \; d\mathbf{x}^2 \right]}_{A_{ij}} u_j = \sum_i \sum_j \nu_i \underbrace{\left[\int_\Gamma \; \psi_i(\mathbf{x}) \; \psi_j(\mathbf{x}) \right]}_{C_{ij}} q_j \tag{155}$$

$$\begin{aligned} \boldsymbol{\nu} \cdot \mathbf{A} \cdot \mathbf{u}^{fem} &= \boldsymbol{\nu} \cdot \mathbf{C} \cdot \mathbf{q}^{fem} \\ \mathbf{A} \cdot \mathbf{u}^{fem} &= \mathbf{C} \cdot \mathbf{q}^{fem} \end{aligned} \tag{156}$$

Here $\mathbf{A}$ is the FEM problem matrix, and $\mathbf{C}$ is the Neumann boundary condition matrix. Their exact form depends on the basis functions used. Elements of $\mathbf{q}^{fem}$ are zero for any node not on Γ. Here, triangle basis functions have been used over the FEM domain $\mathbf{X}^+$ [143]. The domain has been discretised into triangle elements, with nodes located at element corners.

In the problem at hand, particular FEM nodes in the interior domain have Dirichlet boundary conditions, i.e. fixed u_i (Eq. (74)). Assuming these Dirichlet

nodes do not fall on the boundary, this condition can be enforced by the addition of a loading vector of node potentials ($\mathbf{b}$), giving Eq. (157). For nodes where there is an enforced Dirichlet boundary condition, the corresponding row of $\mathbf{A}$ is replaced with that of the identity matrix $\mathbf{I}$, and the corresponding element of $\mathbf{b}$ is replaced with its enforced potential value.

$$\mathbf{A} \cdot \mathbf{u}^{fem} = \mathbf{C} \cdot \mathbf{q}^{fem} + \mathbf{b} \tag{157}$$

In order to couple the BEM problem over the exterior domain $\mathbf{X}^-$ to the FEM problem over the interior domain $\mathbf{X}^+$, a relation is required between the respective boundary potential values ($\mathbf{u}^{fem}$ and $\mathbf{u}^{bem}$) within each problem. However, in the BEM problem the potential is assumed to be constant over each element, while in the FEM problem it is assumed to vary linearly. Considering Figure 107, it can be seen that in 2D, BEM nodes fall at boundary element centres, whilst FEM nodes fall at element corners. Therefore, it seems reasonable to assume that a potential value from $\mathbf{u}_{bem}$ can be approximated as the averaged values of $\mathbf{u}_{fem}$ from the corners of the same element (described by the matrix $\mathbf{T}$ in Eq. 158).

$$\begin{aligned} \mathbf{u}^{bem} &= \mathbf{T} \cdot \mathbf{u}^{fem} \\ T_{ij} &= \frac{1}{2}(\delta_{i,j} + \delta_{i,j-1} + \delta_{i-N+1,j}) \quad i,j \in (1,N) \end{aligned} \tag{158}$$

Using this relation, we can formulate the coupled FEM-BEM matrix equation. Here elements underscored with $\mathbf{X}^+$ denotes association with nodes in the open interior domain, whilst those underscored with Γ denotes association with nodes on the boundary. A sign flip has occurred to the coupling matrix component due to the FEM and BEM problem boundaries having opposing normal directions (see Figure 107).

$$\underbrace{\left(\begin{bmatrix} \mathbf{A}_{\mathbf{X}^+\mathbf{X}^+} & \mathbf{A}_{\Gamma\mathbf{X}^+} \\ \mathbf{A}_{\mathbf{X}^+\Gamma} & \mathbf{A}_{\Gamma\Gamma} \end{bmatrix} + \begin{bmatrix} \mathbf{0} & \mathbf{0} \\ \mathbf{0} & \mathbf{C} \cdot \boldsymbol{P}^{-1} \cdot \boldsymbol{F} \cdot \mathbf{T} \end{bmatrix} \right)}_{\mathbf{A}'} \cdot \begin{bmatrix} \mathbf{u}_{\mathbf{X}^+}^{fem} \\ \mathbf{u}_{\Gamma}^{fem} \end{bmatrix} = \begin{bmatrix} \mathbf{b}_{\mathbf{X}^+} \\ \mathbf{0} \end{bmatrix} \tag{159}$$

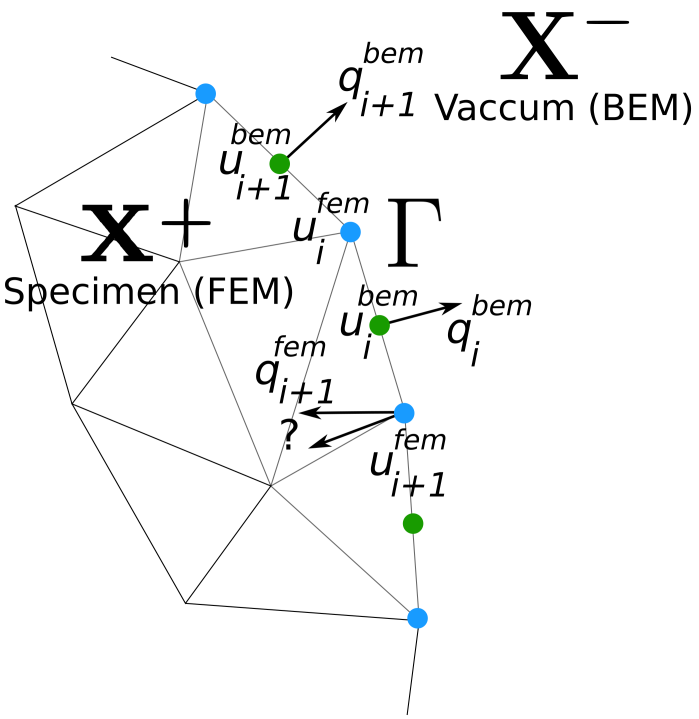


Figure 107: Diagram showing the relation of FEM and BEM boundary nodes. The surface normal ambiguity at panel corners (FEM nodes) is also highlighted.

Here $\mathbf{F}$ and $\mathbf{P}$ are the BEM matrix elements from Eq. (68). The coupling matrix $\mathbf{C}$ is calculated by integrating over the boundary (Eq. 160). Here the relation of indices i and j to the FEM and BEM elements is illustrated in Figure 107.

$$
\begin{aligned}
C_{ij} &= \int_{\Gamma} \epsilon(\mathbf{x})\ \psi_i(\mathbf{x})\ \psi_j(\mathbf{x})\ d\mathbf{x} \\
&= \epsilon_i\ [\delta_{i+1,j} + \delta_{i-N+1,j}] \int_0^{a_i} \frac{a_i - x}{a_i} \frac{x}{a_i}\ dx \quad i,j \in (1,N) \\
&= \epsilon_i\ [\delta_{i+1,j} + \delta_{i-N+1,j}]\ \frac{a_i}{2}
\end{aligned}
\tag{160}
$$

Here ϵ_i is the relative permittivity associated with the FEM element edged by BEM element Γ_i with length a_i.

The FEM problem matrix ($\mathbf{A}$) is constructed from the solution for an individual FEM element ($\mathbf{\Omega}_k$) with corner nodes ($\mathbf{x}_\alpha$, $\mathbf{x}_\beta$, $\mathbf{x}_\gamma$), relative permittivity $\epsilon(\mathbf{\Omega}_k)$, and area A.

$$
M_{ij}(\mathbf{x}_\alpha, \mathbf{x}_\beta, \mathbf{x}_\gamma) = \int_{\mathbf{\Omega}_k} \nabla\psi_i \cdot \nabla\psi_j\ d\mathbf{x}^2 \quad i,j \in (\alpha,\beta,\gamma) \tag{161}
$$

$$
\mathbf{M}(\mathbf{\Omega}_k) = \epsilon(\mathbf{\Omega}_k) \frac{A}{||\mathbf{J}||}
\begin{pmatrix}
(\mathbf{x}_\gamma - \mathbf{x}_\beta)\cdot(\mathbf{x}_\gamma - \mathbf{x}_\beta) & (\mathbf{x}_\beta - \mathbf{x}_\gamma)\cdot(\mathbf{x}_\gamma - \mathbf{x}_\alpha) & (\mathbf{x}_\gamma - \mathbf{x}_\beta)\cdot(\mathbf{x}_\beta - \mathbf{x}_\alpha) \\
(\mathbf{x}_\beta - \mathbf{x}_\gamma)\cdot(\mathbf{x}_\gamma - \mathbf{x}_\alpha) & (\mathbf{x}_\gamma - \mathbf{x}_\alpha)\cdot(\mathbf{x}_\gamma - \mathbf{x}_\alpha) & (\mathbf{x}_\alpha - \mathbf{x}_\gamma)\cdot(\mathbf{x}_\beta - \mathbf{x}_\alpha) \\
(\mathbf{x}_\gamma - \mathbf{x}_\beta)\cdot(\mathbf{x}_\beta - \mathbf{x}_\alpha) & (\mathbf{x}_\alpha - \mathbf{x}_\gamma)\cdot(\mathbf{x}_\beta - \mathbf{x}_\alpha) & (\mathbf{x}_\beta - \mathbf{x}_\alpha)\cdot(\mathbf{x}_\beta - \mathbf{x}_\alpha)
\end{pmatrix}
\tag{162}
$$

$$
\mathbf{J} = \begin{pmatrix}
(\mathbf{x}_\beta - \mathbf{x}_\alpha)_0 & (\mathbf{x}_\beta - \mathbf{x}_\alpha)_1 \\
(\mathbf{x}_\gamma - \mathbf{x}_\alpha)_0 & (\mathbf{x}_\gamma - \mathbf{x}_\alpha)_1
\end{pmatrix}
\tag{163}
$$

Derivation of this single element solution can be found in [143]. Given this single FEM element solution ($\mathbf{M}$), elements of the problem matrix A_{ij} can be constructed by summing up the contribution of FEM elements containing both corner nodes $\mathbf{x}_i$ and $\mathbf{x}_j$. This summation over element contributions to construct A_{ij} is expressed algorithmically as

Result: A_{ij}

for *k in FEM elements* **do**
    $\mathbf{M} = \mathbf{M}(\mathbf{\Omega}_k)$
    for *a in (1, 2, 3)* **do**
        for *b in (1, 2, 3)* **do**
            $i = \mathrm{Conn}(k, a)$
            $j = \mathrm{Conn}(k, b)$
            $A_{ij} += M_{ab}$
        end
    end
end

Here $(\alpha, \beta, \gamma) = \mathrm{Conn}(k)$ gives the indices of the corner nodes of FEM element $\mathbf{\Omega}_k$ (i.e. the connectivity matrix).

13 Appendix F: The Multipole Expansion

Consider a particular cluster Γ^c. The aim is to find an approximation that holds where the distance from this cluster to field point $\mathbf{z}$ is much further than the interdistances between panels, i.e. $||\mathbf{z}-\mathbf{y}_c|| >> R_c$.

$$\sum_{j}^{\Gamma^c} \int_{\Gamma_j} K_l(\mathbf{z},\mathbf{y}) q_j d^2\mathbf{y} \approx M_l(\mathbf{z},\mathbf{y}_c,R_c) \tag{164}$$

To obtain this approximation, the kernel $K_l(\mathbf{z},\mathbf{y})$ is Taylor expanded around $\mathbf{y}_c$.

$$K_l(\mathbf{z},\mathbf{y}) = \big[\frac{(\mathbf{z}-\mathbf{y}_c)\cdot\hat{\mathbf{e}}_l}{||\mathbf{z}-\mathbf{y}_c||^3}\big]+\big[\frac{1}{||\mathbf{z}-\mathbf{y}_c||^3}\hat{\mathbf{e}}_l-\frac{3}{||\mathbf{z}-\mathbf{y}_c||^5}(\mathbf{z}-\mathbf{y}_c)\cdot\hat{\mathbf{e}}_l(\mathbf{z}-\mathbf{y}_c)\big]\cdot(\mathbf{y}-\mathbf{y}_c)+... \tag{165}$$

Here $\hat{\mathbf{e}}_l$ are the Cartesian coordinate unit vectors, indexed by $l \in \{1,2,3\}$. As $\frac{R_c}{||\mathbf{z}-\mathbf{y}_c||} > \frac{\mathbf{y}-\mathbf{y}_c}{||\mathbf{z}-\mathbf{y}_c||}$, defining $\epsilon = \frac{\mathbf{y}-\mathbf{y}_c}{||\mathbf{z}-\mathbf{y}_c||}$ we can rewrite Eq. (166) in increasing powers of $\epsilon(\mathbf{y},\mathbf{z},\mathbf{y}_c)$.

$$\begin{aligned} K_l(\mathbf{z},\mathbf{y}) = \frac{1}{||\mathbf{z}-\mathbf{y}_c||^2}\Bigg[&\frac{(\mathbf{z}-\mathbf{y}_c)\cdot\hat{\mathbf{e}}_l}{||\mathbf{z}-\mathbf{y}_c||}+ \\ &\big(\frac{1}{||\mathbf{z}-\mathbf{y}_c||}\hat{\mathbf{e}}_l - 3\frac{(\mathbf{z}-\mathbf{y}_c)}{||\mathbf{z}-\mathbf{y}_c||}\cdot\hat{\mathbf{e}}_l\frac{(\mathbf{z}-\mathbf{y}_c)}{||\mathbf{z}-\mathbf{y}_c||}\big)\cdot\epsilon(\mathbf{y},\mathbf{z},\mathbf{y}_c\big)+\mathcal{O}(\epsilon)\Bigg] \end{aligned} \tag{166}$$

Truncating to some order in ϵ then provides a far-field approximation for $K_l(\mathbf{z},\mathbf{y})$. By using such an approximation, integrals over panels are now independent of $\mathbf{z}$. Expanding all of a cluster's panels around its $\mathbf{y}_c$ enables a single expansion for the integral (Eq. (164)) to be obtained. This expansion (Eq. (167)), and its coefficients (Eqs. (168) and (169)), can then be precomputed prior to field evaluation.

$$M_l(\mathbf{z}, \mathbf{y}_c, R_c) = \frac{(\mathbf{z}-\mathbf{y}_c)\cdot\hat{\mathbf{e}}_l}{||\mathbf{z}-\mathbf{y}_c||^3}K_0 + \frac{1}{||\mathbf{z}-\mathbf{y}_c||^3}\hat{\mathbf{e}}_l\cdot\mathbf{K_1} - 3\frac{(\mathbf{z}-\mathbf{y}_c)\cdot\hat{\mathbf{e}}_l}{||\mathbf{z}-\mathbf{y}_c||^5}(\mathbf{z}-\mathbf{y}_c)\cdot\mathbf{K}_1 \tag{167}$$

$$K_0 = \sum_j^{\Gamma^c} q_j \int_{\Gamma_j^c} d^2\mathbf{y} \tag{168}$$

$$\mathbf{K_1} = \sum_j^{\Gamma^c} q_j \int_{\Gamma_j^c} (\mathbf{y}-\mathbf{y}_c)\; d^2\mathbf{y} \tag{169}$$

Throughout this work, the multipole expansion has been truncated to first order. Higher order expansions quickly become unmanageable in Cartesian coordinates by requiring tensor algebra. If higher accuracy is desired, it is more common to consider a spherical harmonic form [132].

14 Appendix G: BEM System for Mixed Boundary Conditions

The implemented BEM method results in a matrix equation, given in Eq. (170), relating panel potentials $\mathbf{u}$ to normal fluxes $\mathbf{q}$.

$$\mathbf{F} \cdot \mathbf{u} = \mathbf{P} \cdot \mathbf{q} \tag{170}$$

In general, the boundary conditions can be a mix of Dirichlet and Neumann. Taking Γ_D to be the boundary subset which is Dirichlet, and Γ_N the subset which is Neumann, the Eq. (170) can be expanded into blocks corresponding to these subsets (Eq. (171)).

$$\begin{pmatrix} \mathbf{F}_{DD} & \mathbf{F}_{ND} \\ \mathbf{F}_{DN} & \mathbf{F}_{NN} \end{pmatrix} \cdot \begin{pmatrix} \mathbf{u}_D \\ \mathbf{u}_N \end{pmatrix} = \begin{pmatrix} \mathbf{P}_{DD} & \mathbf{P}_{ND} \\ \mathbf{P}_{DN} & \mathbf{P}_{NN} \end{pmatrix} \cdot \begin{pmatrix} \mathbf{q}_D \\ \mathbf{q}_N \end{pmatrix} \tag{171}$$

Under this nomenclature, the known vector quantity on the boundary is $(\mathbf{u}_D, \mathbf{q}_N)$. Therefore, the matrix equation is rearranged to Eq. (172). This system can now be readily solved via GMRES.

$$\underbrace{\begin{pmatrix} \mathbf{P}_{DD} & -\mathbf{F}_{ND} \\ \mathbf{P}_{DN} & -\mathbf{F}_{NN} \end{pmatrix}}_{\mathbf{A}} \cdot \underbrace{\begin{pmatrix} \mathbf{q}_D \\ \mathbf{u}_N \end{pmatrix}}_{\mathbf{x}} = \underbrace{\begin{pmatrix} \mathbf{F}_{DD} & -\mathbf{P}_{ND} \\ \mathbf{F}_{DN} & -\mathbf{P}_{NN} \end{pmatrix} \cdot \begin{pmatrix} \mathbf{u}_D \\ \mathbf{q}_N \end{pmatrix}}_{\mathbf{b}} \tag{172}$$

15 Appendix H: Continuity of Laplace's Equation under Boundary Perturbations

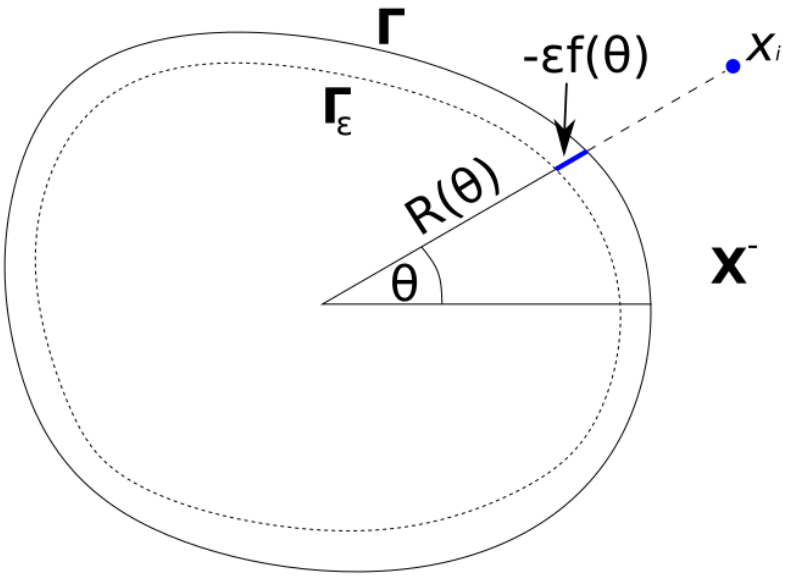


Figure 108: Diagram for the exterior Laplace's problem under boundary perturbation. Here, the problem boundary Γ is perturbed to become Γ_ϵ. Point $\mathbf{x}_i$ exists both in the original and perturbed domains.

Consider the solution to $\nabla^2 u = 0$ on domain $\mathbf{X}$. Its boundary (Dirichlet) can be parameterised as $R(\theta)$ for $0 \leq \theta < 2\pi$ (assuming the boundary remains single-valued with respect to θ). Now, consider a perturbation of this domain such that its new boundary is $R(\theta) - \epsilon f(\theta)$. Note that we are free to pick any small value for ϵ we wish. We can now define the following change in variables (Eq. (173)).

$$\begin{aligned} \eta &= r + \epsilon f(\theta) \\ \psi &= \theta \end{aligned} \tag{173}$$

In this new coordinate system, the perturbed domain in (η, ψ) coordinates are identical to the original domain in the original (r, θ) coordinate system. We can

then derive an expression for partial derivatives relating these via the chain rule.

$$\frac{\partial}{\partial r} = \frac{\partial}{\partial \eta} \tag{174}$$

$$\frac{\partial}{\partial \theta} = +\epsilon \frac{\partial f}{\partial \theta}\frac{\partial}{\partial \eta} + \frac{\partial}{\partial \psi} \tag{175}$$

Now, we consider this perturbed domain solution in the original (r, θ) coordinate system. This can then be expressed in (η, ψ).

$$\nabla^2 u = 0 \tag{176}$$

$$\frac{1}{r}\frac{\partial}{\partial r}\left(r\frac{\partial u}{\partial r}\right) + \frac{1}{r^2}\frac{\partial^2 u}{\partial \theta^2} = 0$$

$$\frac{1}{\eta - \epsilon f}\frac{\partial}{\partial \eta}\left((\eta - \epsilon f)\frac{\partial}{\partial \eta}\right)u + \frac{1}{(\eta - \epsilon f)^2}\left(\epsilon \frac{\partial f}{\partial \theta}\frac{\partial}{\partial \eta} + \frac{\partial}{\partial \psi}\right)^2 u = 0$$

$$\eta\frac{\partial}{\partial \eta}\left(\eta\frac{\partial u}{\partial \eta}\right) - 2\eta\epsilon f\frac{\partial^2 u}{\partial \eta^2} - \epsilon f\frac{\partial u}{\partial \eta} + \epsilon^2 f^2\frac{\partial^2 u}{\partial \eta^2}$$

$$+\epsilon^2\left(\frac{\partial f}{\partial \theta}\right)^2\frac{\partial^2 u}{\partial^2 \eta} + 2\epsilon\frac{\partial f}{\partial \theta}\frac{\partial^2 u}{\partial \eta \partial \psi} + \epsilon\frac{\partial^2 f}{\partial \theta^2}\frac{\partial u}{\partial \eta} + \frac{\partial^2 u}{\partial \psi^2} = 0 \tag{177}$$

$$[\frac{1}{\eta}\frac{\partial}{\partial \eta}\left(\eta\frac{\partial u}{\partial \eta}\right) + \frac{1}{\eta^2}\frac{\partial^2 u}{\partial \psi^2}]+$$

$$\epsilon[-\frac{2}{\eta}f\frac{\partial^2 u}{\partial \eta^2} - \frac{f}{\eta^2}\frac{\partial u}{\partial \eta} + \frac{2}{\eta^2}\frac{\partial f}{\partial \theta}\frac{\partial^2 u}{\partial \eta \partial \psi} + \frac{1}{\eta^2}\frac{\partial^2 f}{\partial \theta^2}\frac{\partial u}{\partial \eta}]+$$

$$\epsilon^2[\frac{f^2}{\eta^2}\frac{\partial^2 u}{\partial \eta^2} + \frac{1}{\eta^2}\left(\frac{\partial f}{\partial \theta}\right)^2\frac{\partial^2 u}{\partial^2 \eta}] = 0 \tag{178}$$

Examining Eq. (178), we assume the trial solution for u in Eq. (179). Note that we do not yet know if this trial solution is valid.

$$u = u_0 + \sum_{n=1}^{\infty} \epsilon^n u_n \tag{179}$$

Plugging the perturbation expansion into Eq. (178), and letting $\epsilon \to 0$, we can see that u_0 must be the base solution for the unperturbed system given our earlier observation regarding domain identity. Therefore, u_0 is just the unperturbed solution to Laplace's equation. Next we consider the higher powers of ϵ. Noting that Eq. (178) must hold for all values of ϵ, it can be seen that terms associated with the same power of ϵ in Eq. (178) must sum together to equal zero. We end up with the following recurrence relations for the terms associated with powers of ϵ (Eqs. (180) and (181)).

$$\begin{aligned} \epsilon \quad & [\frac{1}{\eta}\frac{\partial}{\partial\eta}\left(\eta\frac{\partial u_1}{\partial\eta}\right) + \frac{1}{\eta^2}\frac{\partial^2 u_1}{\partial\psi^2}]+ \\ [-\frac{2}{\eta}f\frac{\partial^2 u_0}{\partial\eta^2} - \frac{f}{\eta^2}\frac{\partial u_0}{\partial\eta} + \frac{2}{\eta^2}\frac{\partial f}{\partial\theta}\frac{\partial^2 u_0}{\partial\eta\partial\psi} + \frac{1}{\eta^2}\frac{\partial^2 f}{\partial\theta^2}\frac{\partial u_0}{\partial\eta}] &= 0 \end{aligned} \tag{180}$$

$$\begin{aligned} \epsilon^n \quad & [\frac{1}{\eta}\frac{\partial}{\partial\eta}\left(\eta\frac{\partial u_n}{\partial\eta}\right) + \frac{1}{\eta^2}\frac{\partial^2 u_n}{\partial\psi^2}]+ \\ [-\frac{2}{\eta}f\frac{\partial^2 u_{n-1}}{\partial\eta^2} - \frac{f}{\eta^2}\frac{\partial u_{n-1}}{\partial\eta} + \frac{2}{\eta^2}\frac{\partial f}{\partial\theta}\frac{\partial^2 u_{n-1}}{\partial\eta\partial\psi} + \frac{1}{\eta^2}\frac{\partial^2 f}{\partial\theta^2}\frac{\partial u_{n-1}}{\partial\eta}]+ \\ [\frac{f^2}{\eta^2}\frac{\partial^2 u_{n-2}}{\partial\eta^2} + \frac{1}{\eta^2}\left(\frac{\partial f}{\partial\theta}\right)^2\frac{\partial^2 u_{n-2}}{\partial^2\eta}] &= 0 \end{aligned} \tag{181}$$

This relation expresses the n-th term of Eq. (179) as the solution to Poisson's equation, with an additional inhomogeneous part depending on the previously solved series terms. For Poisson's equation, it is known that a solution must exist over the domain. Additionally, the solution is unique (to a constant). Therefore, we know that each u_n has a unique solution (to a constant). Therefore, due to this uniqueness property, Eq. (179) describes the true solution under the domain perturbation. For any point $\mathbf{x}$ in both the unperturbed and perturbed domains, $|u(\mathbf{x}) - u_0(\mathbf{x})|$ is described by a polynomial of ϵ, i.e. Eq. (179). As a result, the solution to Laplace's equation is continuous with respect to smooth boundary variations.